



UNIVERSITAT DE
BARCELONA

Cell-adhesive nanopatterns for musculoskeletal tissue engineering

Ignasi Casanellas Mercado

ADVERTIMENT. La consulta d'aquesta tesi queda condicionada a l'acceptació de les següents condicions d'ús: La difusió d'aquesta tesi per mitjà del servei TDX (www.tdx.cat) i a través del Dipòsit Digital de la UB (diposit.ub.edu) ha estat autoritzada pels titulars dels drets de propietat intel·lectual únicament per a usos privats emmarcats en activitats d'investigació i docència. No s'autoritza la seva reproducció amb finalitats de lucre ni la seva difusió i posada a disposició des d'un lloc aliè al servei TDX ni al Dipòsit Digital de la UB. No s'autoritza la presentació del seu contingut en una finestra o marc aliè a TDX o al Dipòsit Digital de la UB (framing). Aquesta reserva de drets afecta tant al resum de presentació de la tesi com als seus continguts. En la utilització o cita de parts de la tesi és obligat indicar el nom de la persona autora.

ADVERTENCIA. La consulta de esta tesis queda condicionada a la aceptación de las siguientes condiciones de uso: La difusión de esta tesis por medio del servicio TDR (www.tdx.cat) y a través del Repositorio Digital de la UB (diposit.ub.edu) ha sido autorizada por los titulares de los derechos de propiedad intelectual únicamente para usos privados enmarcados en actividades de investigación y docencia. No se autoriza su reproducción con finalidades de lucro ni su difusión y puesta a disposición desde un sitio ajeno al servicio TDR o al Repositorio Digital de la UB. No se autoriza la presentación de su contenido en una ventana o marco ajeno a TDR o al Repositorio Digital de la UB (framing). Esta reserva de derechos afecta tanto al resumen de presentación de la tesis como a sus contenidos. En la utilización o cita de partes de la tesis es obligado indicar el nombre de la persona autora.

WARNING. On having consulted this thesis you're accepting the following use conditions: Spreading this thesis by the TDX (www.tdx.cat) service and by the UB Digital Repository (diposit.ub.edu) has been authorized by the titular of the intellectual property rights only for private uses placed in investigation and teaching activities. Reproduction with lucrative aims is not authorized nor its spreading and availability from a site foreign to the TDX service or to the UB Digital Repository. Introducing its content in a window or frame foreign to the TDX service or to the UB Digital Repository is not authorized (framing). Those rights affect to the presentation summary of the thesis as well as to its contents. In the using or citation of parts of the thesis it's obliged to indicate the name of the author.

Tesi doctoral

Cell-adhesive nanopatterns for musculoskeletal tissue engineering

Ignasi Casanellas Mercado



UNIVERSITAT_{DE}
BARCELONA

Cell-adhesive nanopatterns for musculoskeletal tissue engineering

Programa de doctorat en Nanociències



Ignasi Casanellas Mercado

Directors:

Prof. Josep Samitier Martí

Dra. Anna Lagunas Targarona

Tutor: Prof. Josep Samitier Martí

Barcelona, 2022



UNIVERSITAT DE
BARCELONA

Nothing shocks me. I'm a scientist.

- Dr. Indiana Jones

Acknowledgements

First of all, I would like to acknowledge and thank the directors of this thesis, my supervisors: Prof. Josep Samitier and Dr. Anna Lagunas.

Josep, thank you for believing in me since that first chat at the 11th floor of Tower I, all those years ago, and offering me a place in your group. Thanks for the opportunity, for making time, for pushing while listening, and for never saying “no”.

Anna, thank you for being there every step of the way. I was lucky to have you steering me, especially through the early days (years). Thank you for navigating the fine line between supervisor and friend.

Many thanks to Dr. Clara Alcon for her invaluable guidance around the lab (especially with getting a Western blot done before revision deadlines). Also, thank you Clara for your uplifting demeanour and your down-to-earth approach to life and science.

Thanks to all the “seniors” I have encountered at the lab throughout this time: Maria José, Mònica, Joan, Loris, Romén, Arantxa and David C., for creating a supporting environment where it was okay to make mistakes, ask questions, and learn. Thanks for making excellent research coexist with excellent people.

Thanks to Miriam Funes for all the shopping and storing, and for keeping the lab running for people like me to come in and find things ready to play; and to David Izquierdo for the training on substrate fabrication and giving science a personal touch.

Thanks to Andrea, Roberto, Maider and Adrianna, fellow PhDs, for being there along the way and making me see that I wasn't alone in the ordeal. Thanks also to the next-generation PhD Students in the group: Albert, Enrico, Jessica, Francesc, Inês, Sujey, Fernando and Aishwarya. Doing a PhD could be described as the journey from always being the youngest person in the room to joining the adults (scientifically, at least). You made this process very easy.

To Dr. Lídia Bardia and Dr. Anna Lladó, many thanks for shedding some light in the sometimes-dark world of confocal microscopy. Thanks also to Dr. Pietro Delcanale for running super-resolution microscopy trials and introducing me to the technique.

I would like to thank Prof. Núria Montserrat for her early encouragement and her guidance in the condensate transplantation experiments. Likewise, many thanks to Prof. Pere Roca-Cusachs

and Dr. Zanetta (Jenny) Kechagia for the chance to collaborate and kindly discussing some of the work.

Thanks to Prof. Matthew Dalby for granting my long-harboured wish of carrying out a research stay at his lab in Glasgow – plans unfortunately thwarted by Covid. Nevertheless, thank you Matt for the opportunity, the interest and the understanding.

I would like to acknowledge the people who work behind the scenes to make science, and so much more, possible. The cleaning and maintenance people, the waiters and cooks at the cafeteria, the security guards (thanks for opening the door for me after hours and on the occasional weekend)... People we don't usually think of when talking about science but without whom research centres and universities could not work, thank you.

Finally, I want to thank the people in my life who helped and supported me outside of the lab. Moltes gràcies als meus pares i germans, per donar estructura a la vida des de sempre; i a l'Ariadna, arribada durant la realització d'aquesta tesi, per instigar-nos a treballar per deixar-te un món millor.

Last but definitely not least: Infinite thanks to my wife, Nupur, for making every day a better day. Finishing our theses side by side made this difficult period so much easier, and I can't wait to see where the next step will take us. Also, many thanks to you (almost-Dr. Nagar now) for your invaluable help with R coding!

Table of Contents

Acknowledgements	5
Abstract	11
Publications	13
List of Abbreviations	15
Chapter 1: Introduction	19
1.1. The extracellular matrix	21
1.2. Cell-matrix adherence and mechanotransduction	22
1.2.1. Integrin receptors as sensors of adhesion	22
1.2.2. Integrin adhesions as mechanotransducers	24
1.2.3. Adhesion signal transformation into biological responses	26
1.3. Tailoring nanoscale cell-matrix interactions	28
1.3.1. Ligand presentation	28
1.3.2. Substrate stiffness	29
1.3.3. Nanotopography	31
1.4. Dendrimer-nanopatterned cell culture substrates	31
1.5. Repairing musculoskeletal tissues	34
1.6. Objectives	39
1.7. Chapter abstracts	40
1.8. References	42
Chapter 2: Materials and methods	57
2.1. Production of PLLA-coated substrates	59
2.2. Nanopatterning of RGD-Cys-D1 dendrimers	59
2.3. Cell culture	61
2.4. Live imaging	62
2.5. Protrusion measurements	62
2.6. Single and collective cell segmentation and tracking	63
2.7. Trajectory graphs	63
2.8. Track analysis	63
2.9. Actin staining and spread analysis	64

2.10.	Blocking cell-substrate interactions with dendrimers in solution	64
2.11.	Blocking cell-cell interactions through N-cadherin and gap junctions	65
2.12.	Immunostaining	65
2.13.	Analysis of integrin clustering	66
2.14.	Cell viability in condensates	67
2.15.	Analysis of internuclear distance	67
2.16.	Western blot assay	67
2.17.	RNA extraction and retrotranscription	69
2.18.	qPCR and data analysis	69
2.19.	Analysis of condensate area and Cx43 GJIC	70
2.20.	Neurobiotin assay	71
2.21.	Condensate transplantation	72
2.22.	Myosin inhibition	72
2.23.	Analysis of focal adhesions and nuclear shape	72
2.24.	Analysis of YAP nuclear translocation	73
2.25.	Analysis of differentiation to tendon and bone	74
2.26.	Statistics	74
2.27.	References	75
Chapter 3: Dynamics of stem cell migration and condensation		77
3.1.	Introduction	79
3.2.	Results	83
3.2.1.	Cell morphology	83
3.2.2.	Single cell migration	85
3.2.3.	Mesenchymal condensation	89
3.2.4.	Supracellular organization on protein coatings	91
3.2.5.	Collective cell migration	92
3.2.6.	Blocking cell-substrate and cell-cell interactions	93
3.3.	Discussion	97
3.3.1.	The intersection between nanopatterned ligands and a protein coating	97
3.3.2.	Nanoscale ligand density modulates stem cell migration	98
3.3.3.	Nanoscale ligand density modulates condensation	99
3.3.4.	Condensation on fibronectin as the emergence of topological defects	100

3.3.5. Condensation through contact inhibition and following of locomotion	101
3.4. References	106
Chapter 4: Condensate structure and intercellular communication	117
4.1. Introduction	119
4.2. Results	123
4.2.1. Condensate structure and stability	123
4.2.2. Gap junction intercellular communication	127
4.2.3. Condensate transplantation assay	131
4.2.4. Integrin blocking and myosin inhibition	133
4.3. Discussion	135
4.3.1. Ligand density regulates condensate structure, stability and GJIC	135
4.3.2. Substrate adhesion continually regulates GJIC across condensate layers	139
4.4. References	142
Chapter 5: Adhesion, nuclear shape and differentiation to musculoskeletal lineages	151
5.1. Introduction	153
5.2. Results	156
5.2.1. Nuclear remodelling, cytoskeletal morphology and adhesion size	156
5.2.2. Differentiation to cartilage, tendon and bone	162
5.2.3. Lineage commitment through adherence and nuclear shape	166
5.2.4. Freezing mesenchymal condensates	168
5.3. Discussion	169
5.3.1. Adhesion area modulates nuclear morphology	169
5.3.2. Optimal ligand densities to promote differentiation	171
5.3.3. YAP-mediated mechanotransduction in chondrogenesis	172
5.3.4. Local ligand density modulates differentiation through adhesion size and distribution	173
5.4. References	176
Chapter 6: Conclusions	185
Resum en català (Summary in Catalan)	189
List of Figures	194

List of Tables	197
List of Videos	198
List of Equations	199

Abstract

Traditionally described as the smallest unit of life, cells continuously modulate their behaviour according to the environment they find themselves in – and to the company they keep. Of course, this phenomenon is also inherent to human beings, as we sense our surroundings through highly specialized systems (our five senses) that act as signal sensors and transducers. Through these systems we are able to experience the world around us, interact with it and, to the best of our abilities, try to remodel it to fit our purposes, just as the cells that compose us do.

The question of how exactly cells sense their environment (including the extracellular matrix and neighbouring cells) and respond to it has fascinated scientists for decades. We know that environmental inputs can drive cells into distinct paths such as division, differentiation, and even malignancy, representing a paramount regulator of cell function in a myriad of physiological settings. Therefore, by deepening our fundamental understanding of cell-matrix interactions, researchers also contribute to the development of therapies or devices to tackle injury and disease across our bodies.

Since cells have micrometric sizes, their interactions with the surrounding matrix take place primarily at the nanoscale. Protein receptors at the cell membrane bind to ligands present in extracellular proteins; these adhesions have intracellular repercussions and regulate parameters such as cell shape, cytoskeletal organization or gene expression. In this thesis, we produce nanopatterns of cell-binding ligands and employ them as *in vitro* platforms for mesenchymal stem cells, in culture media inducers of differentiation towards cartilage, tendon or bone. We analyse cell movement dynamics, the formation of early tissue structures and their mechanical properties and stability, intercellular communication, and cell differentiation to each of the lineages. We also explore mechanotransduction mechanisms that may explain our observations. Through this work we aim to unveil fundamental cell-matrix interactions driving the development of musculoskeletal tissues, which are some of the most frequently injured in the body and among the main causes of disability around the world.

Publications

The following scientific articles were generated, completely or partially, from the work presented in this thesis:

- Casanellas I, Lagunas A, Tsintzou I, Vida Y, Collado D, Pérez-Inestrosa E, Rodríguez-Pereira C, Magalhaes J, Gorostiza P, Andrades JA, Becerra J, Samitier J. Dendrimer-based uneven nanopatterns to locally control surface adhesiveness: a method to direct the chondrogenic differentiation of mesenchymal stem cells. *Journal of Visualized Experiments* (131): e56347 (2018), doi: [10.3791/56347](https://doi.org/10.3791/56347)
- Casanellas I, García-Lizarribar A, Lagunas A, Samitier J. Producing 3D biomimetic nanomaterials for musculoskeletal system regeneration. *Frontiers in Bioengineering and Biotechnology* 6: 128 (2018), doi: [10.3389/fbioe.2018.00128](https://doi.org/10.3389/fbioe.2018.00128)
- Casanellas I, Lagunas A, Vida Y, Pérez-Inestrosa E, Andrades JA, Becerra J, Samitier J. Matrix nanopatterning regulates mesenchymal differentiation through focal adhesion size and distribution according to cell fate. *Biomimetics* 4(2): 43 (2019), doi: [10.3390/biomimetics4020043](https://doi.org/10.3390/biomimetics4020043)
- Rodríguez-Pereira C, Lagunas A, Casanellas I, Vida Y, Pérez-Inestrosa E, Andrades JA, Becerra J, Samitier J, Blanco FJ, Magalhaes J. RGD-dendrimer-poly(L-lactic) acid nanopatterned substrates for the early chondrogenesis of human mesenchymal stromal cells derived from osteoarthritic and healthy donors. *Materials* 13(10): 2247 (2020), doi: [10.3390/ma13102247](https://doi.org/10.3390/ma13102247)
- Casanellas I, Lagunas A, Vida Y, Pérez-Inestrosa E, Andrades JA, Becerra J, Samitier J. The Janus role of adhesion in chondrogenesis. *International Journal of Molecular Sciences* 21(15): 5269 (2020), doi: [10.3390/ijms21155269](https://doi.org/10.3390/ijms21155269)
- Casanellas I, Lagunas A, Vida Y, Pérez-Inestrosa E, Rodríguez-Pereira C, Magalhaes J, Andrades JA, Becerra J, Samitier J. Substrate ligand density modulates gap junction intercellular communication during mesenchymal cell condensation. *bioRxiv* (2021), doi: [10.1101/2021.04.28.441739](https://doi.org/10.1101/2021.04.28.441739)
- Casanellas I, Vida Y, Pérez-Inestrosa E, Samitier J, Lagunas A. Dynamics of stem cell migration and condensation on nanopatterned adhesive ligands. *Manuscript in preparation*

List of Abbreviations

2D: Two-dimensional

3D: Three-dimensional

18 β GA: 18 β -glycyrrhetic acid

ACI: Autologous chondrocyte implantation

AFM: Atomic force microscopy

ALP: Alkaline phosphatase

CDH2: Cadherin-2, N-cadherin

CFL: Contact following of locomotion

CIL: Contact inhibition of locomotion

COL-I: Collagen-I

COL-2: Collagen-II

cPLA2: Cytosolic phospholipases A2

Cx: Connexin

Cx43: Connexin 43

CT-Cx43: C-terminal Cx43

d_{\min} : Minimum interparticle distance

DMSO: Dimethyl sulfoxide

E-cadherin: Epithelial cadherin

ECM: Extracellular matrix

ER: Endoplasmic reticulum

FA: Focal adhesion

F-actin: Filamentous actin

FAK: Focal adhesion kinase

FB: Fibrillar adhesion

FBS: Foetal bovine serum

FN: Fibronectin

FX: Focal complex

GDF5: Growth differentiation factor 5

GJ: Gap junction

GJA1: Gap junction alpha 1

GJIC: Gap junction intercellular communication

GTPase: Guanosine triphosphate hydrolase

hAMSC: Human adipose-derived MSC

hMSC: Human MSC

INM: Inner nuclear membrane

iPSC: Induced pluripotent stem cell

LINC: Linker of nucleoskeleton and cytoskeleton

MKL1: Megakaryoblastic leukaemia 1

mRNA: Messenger ribonucleic acid

MRTFA: Myocardin related transcription factor A

MSC: Mesenchymal stem cell, Multipotent stromal cell, Medicinal signalling cell

N-cadherin: Neural cadherin

NCAM: Neural cell adhesion molecule

NPC: Nuclear pore complex

NSI: Nuclear shape index

ONM: Outer nuclear membrane

OSX: Osterix

PAMAM: Polyamidoamine

PBS: Phosphate-buffered saline

PEG: Polyethylene glycol

PLA: Polylactic acid

PLLA: Poly-L-lactic acid

P/S: Penicillin-Streptomycin

PXN: Paxillin

rcf: Relative centrifugal force

RGD: Arginine – Glycine – Aspartate

RGDS: Arginine – Glycine – Aspartate – Serine

rpm: Revolutions per minute

S₀: Substrate zero

S₁₈: Substrate eighteen

S₄₅: Substrate forty-five

S₉₀: Substrate ninety

SCX: Scleraxis

S_{FN}: Substrate fibronectin

SOX9: RY-Box Transcription Factor 9

STM: Scanning tunnelling microscopy

TNMD: Tenomodulin

UV: Ultraviolet

VCL: Vinculin

XPS: X-ray photoelectron spectroscopy

YAP: Yes-Associated Protein

ZO-1: Zonula occludens-1

Chapter 1

Introduction

1.1. The extracellular matrix

In a biological context, the extracellular matrix (ECM) refers to a cell's immediate micro- and nano-environment. The ECM constitutes a cell's physical and chemical support, providing it with the necessary components and cues to sustain its life and guide its behaviour. Its composition is highly variable depending on the specific tissue or cell state¹. In a native mammalian physiological setting, the ECM is a tightly packed mesh that can contain hundreds of proteins, together with enzymes and growth factors². *In vitro*, the ECM includes any substrate or material on which cells are cultured, plus the products they secrete.

Cells are constantly interacting with the extracellular matrix by probing it, remodelling it and in turn being affected by its chemical and mechanical signals. These cues are sensed by receptor proteins, transduced and transmitted in the cell, where they can regulate enzymatic reactions (cell metabolism), transcriptional regulatory proteins (gene expression) and cytoskeletal proteins (cell shape and movement), thus affecting cell behaviour in virtually its whole range of biological processes³. In turn, cells modulate the ECM by applying forces to rearrange and unfold it, and by secreting ECM components that progressively alter its chemical composition. This cycle, guided by cell contractility and biochemical signals (both intracellular, such as transcription factor transportation to the nucleus, and extracellular, such as growth factor secretion for paracrine signalling), acts as a feedback loop continuously regulating cell function⁴.

The interplay between cells and the ECM during development and disease is today one of the main lines of scientific research, as an interdisciplinary field that involves not only cellular and molecular biology but also physics, biochemistry, materials science, engineering and informatics. Deepening our knowledge into how cells sense, respond to, and remodel the ECM allows us to better understand the driving factors of tissue and organ formation in healthy conditions, as well as their malfunction and deterioration due to disease or ageing. This knowledge can then be applied in the design of new biomaterials or cell therapies for tissue regeneration; as well as more comprehensive *in vitro* models for drug or therapy testing (potentially accelerating their development process and reducing the need for animal models).

The interactions between cells and their surroundings take place largely at the nanoscale, through molecules such as matrix ligands, membrane receptors and cytoplasmic proteins^{4,5}. Hence, the pursuit of a complete understanding of cell behaviour necessarily involves the use of nanoscale tools such as nanofabrication and nanopatterning to produce ECM-like biomaterials,

as well as nanoscopy techniques to observe and measure biochemical processes at this scale. In this thesis, cell culture substrates were unevenly nanopatterned with a common ECM ligand at biologically relevant densities. Mesenchymal stem cells were seeded on the substrates and induced to undergo the initial stages of musculoskeletal tissue formation, involving processes such as individual and collective cell migration, condensation, differentiation and intercellular communication. By precisely tailoring cell-substrate local adherence, we shed light on the regulatory framework of cell-ECM nanoscale interactions in early tissue development.

An important distinction to be made is that cells *in vivo* always reside in a three-dimensional environment (and might perceive different kinds of ECM in different directions, for instance if they reside at tissue interfaces), whereas many *in vitro* systems are two-dimensional in that they are designed as surfaces on which cells “crawl”, rather than volumetric spaces in which they “flow”. Most of the studies cited below were indeed performed on this kind of substrates (as is also the case of this thesis), which has led to some questioning of their physiological relevance⁶. However, while they do not recreate a complete matrix for cells to interact with, 2D studies provide important knowledge on specific mechanisms by which cells sense, integrate and respond to their immediate surroundings. They are also generally simpler systems that allow to fine tune the cellular environment and closely observe cell response to it^{7,8}. In this case, in order to modulate local cell-matrix adherence, the use of unevenly nanopatterned ligands is a useful recreation, while arguably reductionist, of conditions cells might find *in vivo*.

1.2. Cell-matrix adherence and mechanotransduction

1.2.1. Integrin receptors as sensors of adhesion

Cell-matrix adherence and mechanical sensing, and its effects on cell behaviour, has been extensively studied and reviewed, although many questions remain unanswered^{5,9-12}. This section is a summary of the main concepts on cellular adhesion and mechanotransduction, the underlying biological mechanisms regulating cell response in this thesis.

Adherent cells tend to attach to an array of ECM proteins such as fibronectin, vitronectin or collagen. Fibronectin in particular is widely used in research laboratories to functionalize cell culture substrates; cells plated on fibronectin-coated surfaces typically exhibit a high percentage of adherence and a spreading morphology. In 1984, Pierschbacher and Ruoslahti discovered RGDS

as the fibronectin sequence responsible for cell attachment (with the serine residue described as “not essential”) and found that other proteins also bind to cells through RGD-containing domains¹³, opening the possibility to modulate cell adhesion *in vitro* using synthetic RGD peptides, rather than whole proteins. Integrins were subsequently identified as the family of membrane receptors driving cell-RGD recognition¹⁴.

Integrins are comprised of two transmembrane subunits, α and β , each with an intracellular and an extracellular domain. The two subunits are held together by extracellular non-covalent bonds, and project outwards of the cell by as much as 20 nm³. There are 18 kinds of α and 8 kinds of β subunits; they can combine to form a total of 24 known heterodimers (integrin types), of which 8 bind to RGD. Other integrins bind to ligands in collagen, laminin, E-cadherin or osteopontin, and up to 12 integrin heterodimers can bind to more than one ligand type^{15,16} (Fig. 1.1). Some integrin types are ubiquitous, while others are specific to a tissue or cell lineage³. Fibronectin-binding integrins containing the β_1 subunit have been described as the ones driving adhesion formation and growth, allowing the site to withstand large forces, while $\alpha\beta_3$ integrins initiate mechanotransduction^{17,18}. Cells adapt to inputs such as substrate rigidity by engaging different integrin types, either separately or in competition, with varying binding and unbinding rates¹⁹.

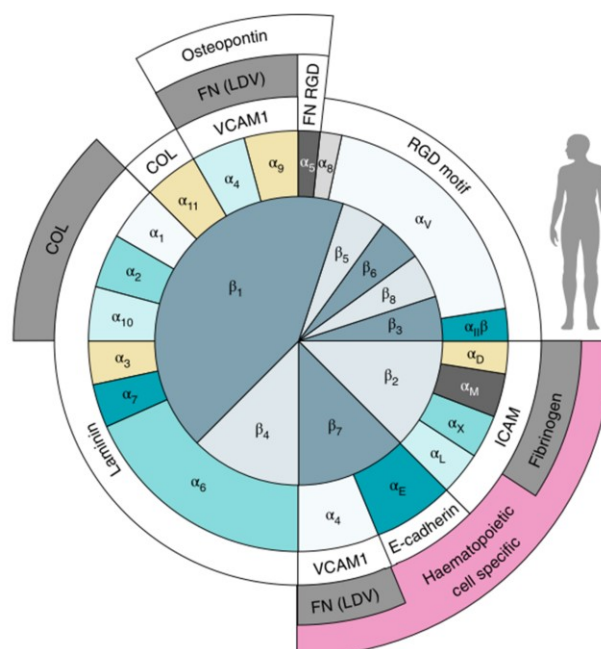


Figure 1.1. Types and ligands of integrin receptors. The 24 known integrin types and their corresponding main extracellular ligands in mammals. Adapted with permission from Moreno-Layseca *et al.* (2019)¹⁶

Integrins are constantly internalized into the cytoplasm and recycled to the membrane through various routes¹⁶. With a lengthy half-life time of 12 to 24 hours, they can undergo this cycle many times, remaining immobilized at adhesion sites for under 80 seconds in each binding event²⁰. The trafficking process acts as a regulator of integrin function, as it tightly controls integrin availability and location at the membrane. It plays a crucial part in cell migration, allowing for new adhesions to be quickly formed and destroyed to sense the matrix for directional cues. Integrins are generally endocytosed at the back of the cell and recycled at the front in the direction of cellular movement, although trafficking exists in several directions within the cell²¹.

1.2.2. Integrin adhesions as mechanotransducers

The transient adhesions that cells form to probe their surroundings are known as nascent adhesions or focal complexes (FXs), small clusters of integrins tethered to ECM ligands in a force-independent process^{22,23}. Nascent adhesions of a similar size (100 nm) and integrin number (50) form on substrates regardless of stiffness, stabilised by cytoplasmic protein talin²⁴, seemingly recruited by focal adhesion kinase (FAK)²⁵. In addition to talin, kindlins also play a role in the activation of certain integrin types, although their specific function is not yet fully described^{26,27}. Talin activates integrins by binding to their cytoplasmic β tail, switching the extracellular domain of the receptor to an extended conformation with higher affinity for ECM ligands (inside-out regulation)^{28,29}. While integrin subunits are parallel to each other in the resting state, upon ligand binding the cytoplasmic end of the β subunit migrates along the membrane away from the α , resulting in a conformational change that further increases ligand affinity and allows the support of tensions at an angle (non-perpendicular to the membrane)^{30–32} (Fig. 1.2).

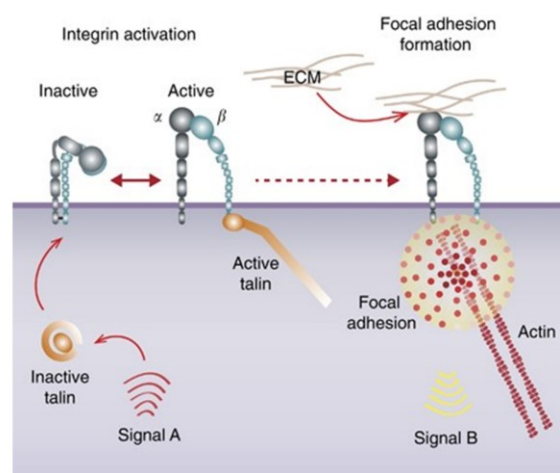


Figure 1.2. Integrin conformational states. Integrin activation entails the extension of the extracellular domains and the separation of the two subunits at the plasma membrane. Activation is regulated by inside-

out signals (cytoplasmic activators binding to the receptor's tails) or outside-in signals (extracellular ligands attaching). In each case, integrin activation results in subsequent chemical or mechanical signals at the other side of the membrane. Integrins thus mediate communication in both directions, in and out of the cell. Adapted under a Creative Commons license (CC BY-NC 3.0) from Hamidi, Pietilä and Ivaska (2016)³³.

Nascent adhesions can either disassemble or, if integrin clustering continues in response to extracellular cues (outside-in regulation), grow into focal adhesions (FAs). As adhesions grow, they transmit proportionally higher forces, up to a maximum threshold at which they would destabilize^{34,35}. Talin, bound directly to integrins and F-actin on each side, serves as the primary transducer of forces between the cell membrane and the cytoskeleton. Unfolding of the first three talin rods exposes vinculin-binding domains, triggering its recruitment, which in turn prevents talin refolding³⁶. This reinforcement of the talin-actin bond by vinculin occurs when tensions reach 5 pN and allows the adhesion to sustain larger forces, causing further unfolding of talin and a progressive increase in tension and adhesion size³⁷. Vinculin attaches to actin by an asymmetric catch-bond, the lifetime of which increases with the load it bears, so this structure remains stable under high tensions³⁸. The amount of tension sustained at the talin section of adhesions is thus regulated by the number of protein molecules recruited^{39,40}. Focal adhesions can further mature into fibrillar adhesions (FBs), which are large clusters of $\alpha 5\beta 1$ integrins attached to fibronectin RGD ligands in the ECM^{10,16}.

Integrin-mediated adhesions sustain bidirectional tensions thanks to integrin association to the actin cytoskeleton through the adhesome, a complex of interconnected cytoplasmic proteins recruited to the adhesion site, including paxillin, vinculin, α -actinin and zyxin, among others⁴¹⁻⁴³. FAs effectively link the ECM and the cytoplasm, reaching the cell nucleus and allowing for mechanical signals to be exchanged in both directions^{42,44-46} (Fig. 1.3).

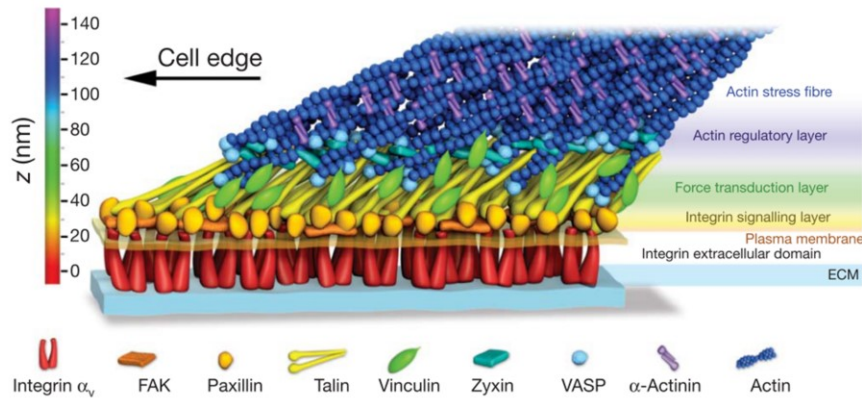


Figure 1.3. Nanoscale architecture of focal adhesions. The adhesome complex links clustered integrin receptors with the cytoskeleton. Adapted with permission from Kanchanawong *et al.* (2010)⁴¹

1.2.3. Adhesion signal transformation into biological responses

While cells probe and remodel their immediate surroundings with inside-out forces, outside-in signals from the matrix and adjacent cells regulate cell movement, morphology, metabolism and gene expression, with this interplay driving a myriad of biological processes such as tissue and organ development⁴. Tensions generated at integrin adhesions are propagated through the cytoskeleton and can reach the linker of nucleoskeleton and cytoskeleton (LINC) complex at the nuclear membrane, stretching it and enlarging its pores. Larger pores then facilitate passage of molecules such as transcriptional regulators⁴⁷. Moreover, the LINC complex is connected to chromatin through the mechanosensitive lamin protein network^{48–50}. Dynamic changes of chromatin conformation in response to deformations of the nuclear membrane regulates cellular adaptation to mechanical inputs⁵¹. Tensions originated by probing cells with the integrin ligand RGD can induce chromatin stretching, affecting gene transcription⁵².

Direct force propagation into the nucleus is not the only way by which integrin mechanotransduction affects cell behaviour^{10,53,54}. Altering membrane morphology or cytoskeletal dynamics can have downstream repercussions on biochemical signalling pathways such as Rho-family GTPases (paramount in cell spreading and migration)^{55,56}, as well as on transcriptional regulators such as YAP/TAZ and MKL1, ultimately regulating gene expression^{50,57,58}. The LINC complex also interacts with mechanosensitive signalling factors such as β -catenin, mediating their translocation⁵⁹. In addition, nuclear translocation of cytoplasmic proteins depends on their size, surface properties and mechanical stability. Force-mediated unfolding of

proteins such as transcription factor MRTFA makes them more flexible and facilitates their transportation through the nuclear membrane^{47,60} (Fig. 1.4).

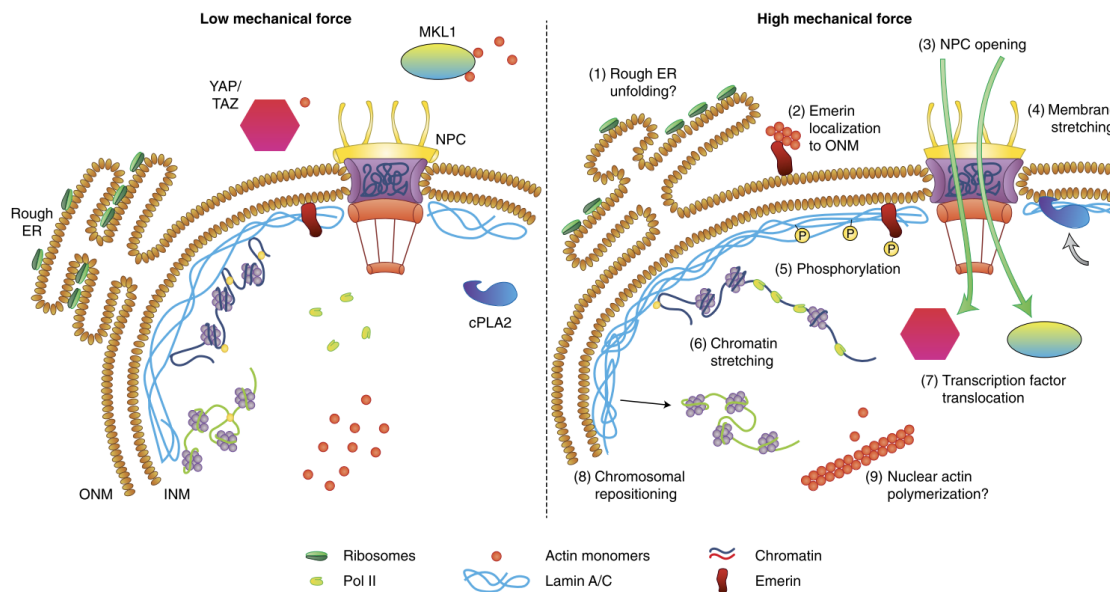


Figure 1.4. Proposed mechanisms of nuclear mechanotransduction. (1) Stretching of the nuclear membrane could alter the conformation of the rough endoplasmic reticulum (ER), exposing more ribosomes to the cytoplasm. (2) Force application promotes translocation of emerin from the inner nuclear membrane (INM) to the outer nuclear membrane (ONM), modulating chromatin organization and facilitating actin polymerization at the ONM. (3) Increased membrane tension could open nuclear pore complexes (NPCs) and modulate their permeability. (4) Stretching of the nuclear membrane recruits cPLA2 to the INM. (5) Force transmission to the nucleus results in post-translational modification and altered dynamics of lamin A/C and INM proteins, such as emerin (see also (2)), which can modulate the mechanical properties of the nucleus and induce downstream signalling. (6) External forces can induce chromatin stretching, altering polymerase and transcription factor accessibility and activity. (7) Nuclear-pore opening and sequestration at the nuclear envelope can modulate localization and activity of transcription factors. (8) Forces acting on the nucleus may reposition chromatin domains, altering their transcriptional activity. (9) Mechanically induced polymerization of nuclear actin can modulate the export and activity of the transcriptional regulator MKL1, and affect other nuclear processes that require monomeric actin. Reproduced with permission from Kirby and Lammerding (2018)⁵³.

Finally, while integrin mediation is the most well-studied mechanotransduction path and the one driving cell response in this thesis, it is not the only one⁶¹. Piezo channels were described a decade ago as highly conserved plasma membrane channels that turn active or inactive in response to forces such as shear stress or membrane stretching⁶². Like integrins, they interact closely with the cytoskeleton⁶³ and are a two-way street, with intracellular signals regulating their activity and sensitivity⁶⁴. Piezo channels are a regulator of cell function in many mammalian physiological settings such as hearing, neuron sensing, blood vessel integrity, wound healing,

metabolism, touch sensation and proprioception, as well as development^{65–70}. Other mechanosensitive membrane channels have been identified, namely from the two-pore potassium (K2P) and hyperosmolarity-gated calcium-permeable (OSCA/TMEM63) families^{71–73}.

1.3. Tailoring nanoscale cell-matrix interactions

Given the importance of nanoscale cell-matrix interactions in modulating global cell behaviour, in the past decades there have been sustained efforts to develop *in vitro* systems that allow their tailoring, be it to observe cell response to specific cues or to induce a desired cellular phenotype^{7,74,75}. Adhesion-mediated cell response depends primarily on the substrate's functionalization (ligand presentation) and mechanical properties, reviewed here.

1.3.1. Ligand presentation

The density, order and type of biochemical ligands in the cellular substrate have been widely studied regarding their effects on cell behaviour. Over the past two decades, advances in fabrication technologies have allowed for the production of cell culture materials in which ligand presentation can be precisely tuned at the nanoscale^{76–82}. To investigate integrin-mediated response, extracellular ligands can be patterned on biologically inert substrates such as polyethylene glycol (PEG) or poly-lactic acid (PLA), so that the resulting cell behaviour can be attributed to ligand sensing. Block-copolymer micelle nanolithography was used to generate hexagonal patterns of gold nanodots coated with cyclic RGD peptides. Although each nanodot contained multiple peptides, it constituted one single binding site for the cell, given its 8-nm size similar to that of integrins. This system revealed that interligand spacings above a 58 to 73 nm threshold inhibit cell attachment and spreading on the substrate, due to impaired integrin clustering⁸³. Large nanopacings thus prevent the recruitment of adhesion proteins and the formation of focal adhesions⁸⁴, as well as cell protrusion and migration⁸⁵. When seeded on gradients of varying interligand distance, cells polarize and migrate towards the region of shorter spacing⁸⁶. Finally, researchers measured the force required to detach cells from the substrate at different ligand densities. This force was 14 times higher on substrates with an interligand spacing of 50 nm than of 90 nm, although ligand surface density is only 3 times greater in the former. This is due to cells being able to generate mature focal adhesions only on the substrates of shorter spacing⁸⁷. To decouple the effects of ligand spacing from the inherent cell spreading that it

mediates, MSCs were seeded on cell-sized island of RGD nanopatterns, revealing that ligand spacing regulates differentiation independently of cell size⁸⁸.

Beyond interligand spacing, other factors such as ligand disposition are paramount in modulating cell response. At mean interparticle distances greater than 70 nm, disordered nanopatterns sustain cell adherence, and particularly cell spreading, much better than ordered ones. This is because disordered patterns present local interligand spacings shorter than 70 nm, where cells can attach and spread, even if the global average spacing is greater than the threshold (because other local spacings present even larger values). Interestingly, cells present similar morphologies on ordered and disordered patterns with a short mean interligand spacing (58 nm), showcasing the biological relevance of the 70-nm approximate threshold for effective adhesion formation⁸⁹. The observation that cells respond positively to disordered ligand dispositions opened the door to the use of uneven rather than highly ordered nanopatterned cell culture substrates, potentially facilitating their production in research laboratories. In this thesis we employ nanopatterned substrates with a liquid-like order and we name them according to the percentage of surface area that contains mean interligand spacings below 70 nm. It should be noted that the 70-nm threshold to sustain adhesion formation holds true only on stiff substrates, as discussed in the next section.

Although RGD remains the most widely used ligand in sensing studies, several other ligands can also engage integrin receptors and potentially affect cell differentiation⁹⁰. Substrates have also been designed with more than one cell ligand, intended to modulate adhesion and induce differentiation, showing that integrin crosstalk with other molecules such as growth factors is also a factor to be considered when designing cell culture platforms^{91–93}.

1.3.2. Substrate stiffness

Cells sense ECM stiffness through the cytoskeletal forces that result upon applying pressure to it or pulling from its ligands, as the ECM resists deformation⁹⁴. It was recently demonstrated that cells actually sense substrate rigidity through the varying rate of force loading at adhesions⁹⁵. Thus, integrins act as a mediator not only of adherence signals such as ligand density and spacing, but also of the ECM's mechanical properties^{9,12}.

Engler and colleagues were among the first to demonstrate that tuning substrate stiffness (within an elastic regime) is sufficient to induce mesenchymal differentiation towards tissues with native stiffness in the same range as the substrate. Moreover, if cells are cultured on a substrate

for several days, they become committed to the fate determined by substrate stiffness, which is not overridden even by posterior chemical stimuli inducers of another lineage. Cells on stiffer substrates form more punctuate paxillin adhesions and more organized F-actin fibres, and present increased cortical stiffness. Inhibiting F-actin contractility erases the effect of substrate stiffness on cell differentiation, showing that it is indeed transmitted through cytoskeletal tensions⁹⁶.

The fact that stiffness is detected through the same receptors as adhesiveness explains why both parameters, studied independently, tend to have similar effects on cell behaviour. For instance, cells respond to stiffer substrates by engaging more integrins and generating larger adhesions; and tend to migrate towards stiffer areas of substrates (durotaxis) as they do towards more adherent ones (haptotaxis). This paradigm opens the door to designing biomaterials focusing on functionalization (ligand presentation) rather than, or alongside, the mechanical properties of the substrate or scaffold⁹⁷. Therefore, researchers have developed *in vitro* platforms to control both substrate stiffness and ligand nanopatterning as independent variables, in order to decouple the effects of each factor and study the relation between them. For this purpose, cell culture substrates are frequently based on hydrogels such as polyacrylamide, the stiffness (Young's modulus) of which can be modulated through the concentration of crosslinker, providing different degrees of polymerization. Hydrogels can then be functionalized with proteins or ligands at the corresponding densities^{98–100}. Using fibronectin-coated polyacrylamide hydrogels revealed that the substrate's Young's modulus determines cell differentiation only at an intermediate protein concentration, whereas at low and high protein densities MSCs respond according to ligand availability but independently of substrate stiffness¹⁰¹.

Nanopatterned hydrogels of varying stiffness and ligand density were used to describe how integrin adhesions mediate the combination of both inputs together, in what is known as the molecular clutch model. By this model, the 70-nm threshold to sustain large adhesions is relevant only for stiff substrates, whereas cells on soft substrates generate adhesions at large rather than small interligand spacings. This is due to individual clutches (each ligand-integrin-talin-actin sequence) being able to withstand only a certain amount of tension before they trigger a mechanosensing signal to recruit more integrin receptors. On stiff substrates, as tension builds, the presence of free ligands around the site allows for further integrin clustering and the formation of a larger adhesion with more clutches, which in turn can collectively sustain higher loads. With low ligand densities, integrins cannot be recruited and the existing clutches disengage due to overbearing loads. However, on softer substrates where individual clutches do not sustain

such large forces, clutches are more likely to pass the mechanosensing force threshold if there are no other clutches nearby to share the applied load. A high ligand density on a soft substrate will result in an even distribution of low tensions among clutches, preventing them from activating integrin recruitment and thus impairing adhesion growth. Therefore, the model shows that there is an optimal substrate rigidity that promotes adhesion growth, and that this rigidity increases with ligand density. The specific threshold values depend on factors such as cell type¹⁰².

Molecular clutch dynamics regulate cellular mechanotransduction events¹⁰³ and differentiation: Soft hydrogels with a high interligand nanospacing allow for more integrin molecules to be recruited at ligand sites, thus inducing mechanotransduction and MSC osteogenesis similarly to stiffer substrates¹⁰⁴.

1.3.3. Nanotopography

Cell behaviour and differentiation is affected by other environmental factors such as substrate topography, which are largely independent of local adherence and thus fall outside of the framework of this thesis. In an early study, Dalby and colleagues reported that surface nanotopography determines the ability of cells seeded on it to attach and spread, affecting their cytoskeletal conformation¹⁰⁵. They subsequently demonstrated the induction of bone mineralization solely through a rearrangement of substrate nanotopography with 100-nm deep pillars^{106,107}. Other topographical features can also drive cell behaviour: Groove-ridge patterns with a periodicity of 650 nm increase MSC differentiation to both adipocytes and osteocytes¹⁰⁸ and also facilitate iPSC differentiation¹⁰⁹, whereas aligned fibrous nanostructures induce cellular elongation and differentiation towards myogenic lineages¹¹⁰. In our case however, topography is not altered by dendrimer nanopatterning, given their small height (around 4 nm) compared to the topographical features of the aforementioned studies^{111,112}.

1.4. Dendrimer-nanopatterned cell culture substrates

The Nanobioengineering Group at IBEC has previously developed cell culture substrates nanopatterned with cell-binding ligands in the form of dendrimers, synthesized by Prof. Yolanda Vida and Prof. Ezequiel Pérez-Inestrosa at the University of Málaga¹¹¹⁻¹¹³. Dendrimers are polymeric macromolecules composed by a repetitive sequence of monomers, also called branching units, extending radially from the molecule's core¹¹⁴. Each of the monomers at the outer layer of the dendrimer can be covalently functionalized. Rather than precisely controlling

the sites of ligand binding on the substrate, the method used here consists in submerging low-charged biocompatible surfaces, such as gold or poly-L-lactic acid (PLLA), in an aqueous solution of polyamidoamine (PAMAM) G1 dendrimers functionalized with the cell-adhesive peptide RGD (Fig. 1.5a). Although each dendrimer presents eight copies of the RGD ligand, it provides a single site for integrin receptor binding, given that the integrin-RGD complex is up to 12 nm in size¹¹⁵, while dendrimers present a smaller diameter of 4-5 nm.

Dendrimers adsorb on the submerged substrate until an equilibrium is reached between surface dendrimer density and dendrimer concentration in solution¹¹⁶. The adsorption process is initially governed by the electrostatic charges between dendrimers and the surface (hence the use of a low-charged substrate to facilitate adsorption). As dendrimers deposit on the surface, further adsorption becomes progressively more difficult due to repulsion between dendrimers. Thus, final dendrimer density on the substrate depends not only on the initial concentration of the solution, but also on the time of functionalization and the dynamics of the surface-solution equilibrium¹¹⁷ (Fig. 1.5b). Since we fixed the time of functionalization to 16 h and always employ PLLA substrates, we modulate surface ligand density by adjusting the concentration of dendrimer in solution. Because of the aforementioned factors, final surface density does not increase linearly with initial dendrimer concentration (Table 1.1).

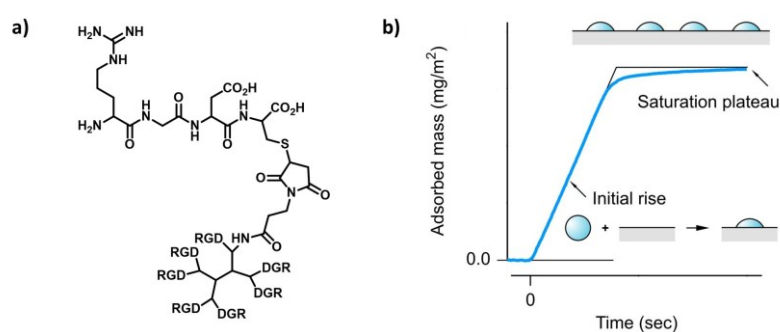


Figure 1.5. Dendrimer surface adsorption. **a)** Molecular structure of a PAMAM G1 dendrimer functionalized with 8 RGD groups. One RGD is shown full and the rest are abbreviated. **b)** Example of mass adsorption from a liquid solution onto a surface over time.

The main advantages of this protocol are its relative ease and speed compared to other nanopatterning methods, that it does not require any specialized nanofabrication equipment, and that it facilitates the large-scale or bulk production of substrates in the laboratory, thus being fully compatible with regular cell culture protocols. Moreover, since dendrimers can be functionalized with different molecules through an amide bond, it can be extended to the study of ligands other

than RGD. As a counterpart, it does not allow to precisely modulate the nanoscale organization (spatial disposition) of ligands, although the liquid-like order in which dendrimers adsorb can be predicted and characterized. The protocol could also realistically be expanded to produce substrates with micropatterned ligand-containing sections amid a ligand-free surface.

Previous studies functionalized dendrimers with cell-interacting moieties in their outer sphere, and deposited them onto surfaces^{118,119}. These substrates were used to study cell adhesion^{120,121}, morphology^{122,123} and migration^{124,125}. However, the lack of precise surface characterization in these studies makes it difficult to establish a correlation between dendrimer surface configuration and cell response. Dendrimer-nanopatterned substrates were characterized at the Nanobioengineering Group through atomic force microscopy (AFM), scanning tunnelling microscopy (STM) and X-ray photoelectron spectroscopy (XPS)^{111–113}. Since dendrimers are unevenly distributed in the nanopatterns, quantifying the mean interligand distance over a large substrate would not be representative of ligand density available to cells at local sites. Instead, AFM height images were thresholded to obtain particle positions, from which local minimum interparticle distances (d_{\min}) were calculated. These were plotted in the z-axis of particle position maps and the corresponding contour plots were constructed. We then take the average percentage area covered with ligands at a spacing lower than 70 nm (the threshold for an efficient cell adherence on stiff substrates, as discussed above) as the defining characteristic of each substrate. In this way, we obtain substrates with three levels of global adherence: low (only 18% of the surface area covered with dendrimers at less than 70 nm), intermediate (45% of the area considered as adherent) and high (90% of adherent area). We also name each kind of nanopatterned substrate according to this number: S_{18} , S_{45} and S_{90} , respectively (Fig. 1.6, Table 1.1).

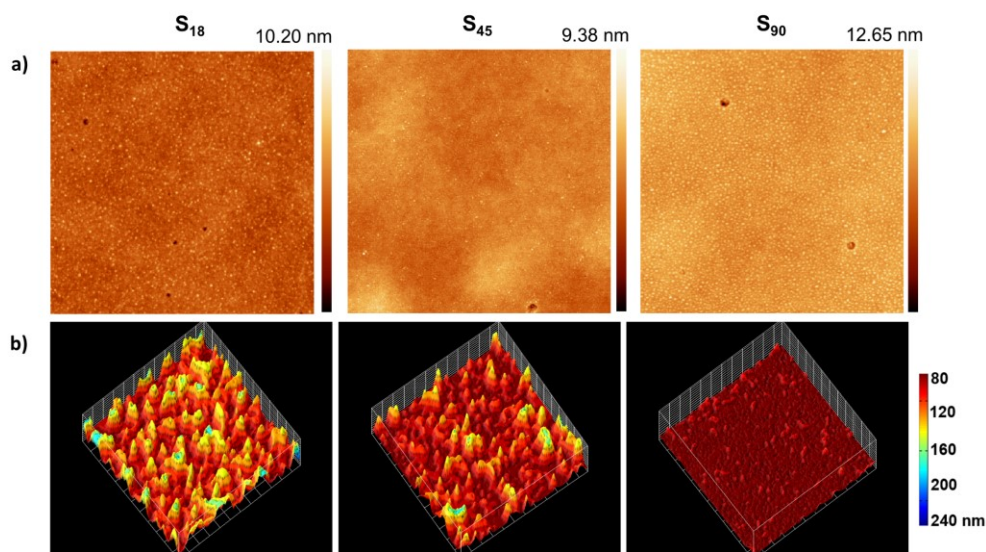


Figure 1.6. Uneven nanopatterns of RGD dendrimers. **a)** Representative atomic force microscopy (AFM) images of nanopatterned substrates. The colour legend indicates height, from 0 nm to the corresponding maximum values. **b)** Three-dimensional renderings of nanopatterned substrates showing minimum interparticle distance (d_{\min}) contour plots, as indicated by the colour legend and substrate heights. Adapted with permission from Lagunas *et al.* (2017)¹¹¹.

Table 1.1. Nanopatterns characterization. Data retrieved from Lagunas *et al.* (2017)¹¹¹

Nanopatterned substrate	Dendrimer C _i (% w/w)	Mean interligand distance (nm)	% adherent area ($d_{\min} < 70$ nm)
S ₉₀	2.5×10^{-8}	58 ± 1	90 ± 2
S ₄₅	10^{-8}	63 ± 8	45 ± 7
S ₁₈	4×10^{-9}	71 ± 5	18 ± 11

1.5. Repairing musculoskeletal tissues

The musculoskeletal system is a group of tissues that physically support the human body, allow it to move and protect vital organs. Musculoskeletal tissues include bone, ligament, cartilage, tendon and muscle. Skeletal bones confer the body with its stable three-dimensional structure, sustaining other tissues. Adjacent bones are connected by ligaments at the joints (such

as elbows and knees), where articular cartilage prevents direct friction between them. Tendons connect bones to skeletal muscle, allowing us to voluntarily flex our joints¹²⁶.

Musculoskeletal conditions are the leading cause of disability worldwide^{127,128}. Cartilage, tendon and bone are among the most frequently injured tissues in the body^{129–132}. While many musculoskeletal conditions can be managed in primary care or through conservative therapies (such as lifestyle modifications or tailored exercise), some of them require surgical intervention¹³³. In these cases, and especially in tissues with a limited capacity of self-repair such as cartilage and tendon, there is a need for improved cell-based therapies to promote regeneration. Up to 30% of tendon injuries require surgery after unsuccessful conservative therapies, but patients still face prolonged recovery periods and high rates of re-injury alongside high levels of pain^{134,135}. In order to repair cartilage damage, there are three main surgical techniques: microfracture, which induces the production of fibrocartilage (more brittle and prone to re-injury) rather than hyaline cartilage¹³⁶; mosaicplasty, in which whole sections of cartilage tissue are removed from healthy areas and implanted into the injured sites¹³⁷; and autologous chondrocyte implantation (ACI), which consists of extracting chondrocytes from the patient and then injecting them to induce tissue formation¹³⁸. A variation of the last one is matrix-induced autologous chondrocyte implantation (MACI), in which cells are implanted into the tissue loaded in a biomaterial, such as a biodegradable hydrogel¹³⁹. In severe cases, whole joint replacement might be required.

While the aforementioned techniques can be suitable for locally injured cartilage, they are not indicated for cases of extensive damage such as osteoarthritis (OA), a prevalent musculoskeletal disease entailing the progressive degradation of articular cartilage. OA results in subsequent damage to the subchondral bone, causing significant pain and mobility loss^{140,141}. Chondrocytes extracted from a donor dedifferentiate in culture, limiting the possibilities for expansion (to increase the number of available cells) before implantation¹⁴². Thus, current treatments for OA are mostly palliative, as they only attempt to temporarily reduce the symptoms without solving the disease. Being available for extraction, expansion and differentiation, stem cells emerge as a promising alternative.

During embryonic development, the mesenchyme is a transient structure comprised of loosely attached cells in a protein-rich extracellular matrix (ECM). As the main pool of undifferentiated cells in the mesodermal germ layer, the mesenchyme originates most of the body's connective tissues, including those of the musculoskeletal system such as cartilage, tendon and bone. Mesenchymal Stem Cells, also known as Multipotent Stromal Cells or Medicinal

Signalling Cells (MSCs)¹⁴³ are the only reminiscence of mesenchyme still present in the stroma (connective tissue) of adult organisms; they are available for extraction and purification from tissues such as fat and bone marrow¹⁴⁴. MSCs are characterized by their self-renewal capacity and their multipotent differentiation potential, properties that are sustained in their niche within the corresponding adult tissue^{145–148}. The International Society for Cellular Therapy proposed three conditions that cells should fulfil to be categorised as MSCs *in vitro*: Be adherent to plastic culture substrates; express certain protein markers at the cell surface (CD105, CD73 and CD90, indicative of stemness) but not express certain others (such as CD45, CD34, CD14/CD11b and CD79 α /CD19, specific of differentiated cell types); and have the capacity to differentiate to osteoblasts, adipocytes and chondroblasts (as a measure to determine their multipotent potential)¹⁴⁹.

MSCs hold potential for translation to therapies in clinical scenarios, one of the main reasons being that their use is considered more ethically acceptable than that of embryonic stem cells (ESCs). Since they are generally restricted to differentiation towards mesodermal lineages, MSCs are also safer than ESCs for clinical applications; for instance, they do not form teratomas¹⁵⁰. However, some reports show that MSCs can differentiate to non-mesodermal fates such as hepatocytes, pancreatic cells and neurons^{151–153}. These properties of MSCs, together with the fact that they are angiogenic and antiapoptotic, make them a promising choice to promote the regeneration of connective tissues such as cartilage, tendon and bone^{154–156}. Moreover, MSCs are immunomodulators capable of reducing the immune response, which gives them great potential as inducers of tolerance in cell and organ transplantation procedures, in which they could help resolve the important issue of rejection¹⁵⁷. Since MSCs tend to migrate towards wounded or diseased tissue, they could be used as vectors to deliver therapeutic compounds and for gene therapy applications¹⁵⁸. This is also facilitated by the fact that MSCs are relatively easy to transfect using both viral and non-viral vectors (the latter ones with a lower transduction efficiency, but safer for potential clinical use)¹⁵⁰.

Due to their promising therapeutic properties, extensive research has been conducted on the use of MSCs to treat lesions and degenerative diseases of musculoskeletal tissues. While adult MSCs can be obtained from tissues such as bone marrow, adipose-derived MSCs are considered advantageous thanks to their higher number and easier extraction from the patient or donor¹⁵⁹. The main hurdle for their use in a clinical setting is that their differentiation is difficult to modulate; past studies show that MSC implantation *in vivo* can be ineffective or lead to complications such as calcification, fibrogenesis, or the formation of heterotopic tissues^{160–163}.

MSCs should therefore be precisely directed towards the desired tissue prior to and during implantation¹³⁹. Recent research in this sense verses mostly on the use of scaffolds or hydrogels that mimic the chemical and mechanical properties of native tissue, so that cells will adapt to the tailored environment by forming the corresponding target tissue^{142,164–171}. For instance, one single population of MSCs can differentiate towards the osteogenic and chondrogenic fates in parallel, depending on whether cells are seeded on a nanopatterned poly(ϵ -caprolactone) surface or embedded into a hyaluronan hydrogel, respectively¹⁷². This approach is particularly relevant in tissue engineering strategies that aim to reproduce native conditions as a model *in vitro*, or to generate a final construct to implant in the patient.

Another strategy to design MSC-based regenerative therapies is to take cells only until the early stages of differentiation (predifferentiation), rather than to a fully developed tissue that might be more difficult to integrate into the damaged environment *in vivo*¹⁷³. For instance, bone- and adipose-derived MSCs that are fully differentiated to chondrocytes *in vitro* can then mineralize and generate undesired bone grafts when implanted *in vivo*^{174–176}. On the other hand, MSCs predifferentiated to chondrogenesis or osteogenesis, and then encapsulated in hydrogels with the aim to generate adjoining cartilage and bone tissues, generate constructs more similar to native tissue if they undergo 7 rather than 14 days of predifferentiation¹⁷⁷. Therefore, there is interest for engineered materials that guide the initial steps of stem cell differentiation towards musculoskeletal lineages. In order to tune substrate properties to each of these tissues, more fundamental knowledge is needed about the extracellular cues that mediate cell functions in each case. In this thesis we analyse the impact of nanoscale ligand density on MSC behaviour and differentiation towards cartilage, tendon and bone.

The design of appropriate stem cell carrier matrices, based on the physiology of the native tissue and stem cell requirements, is of capital importance for cell differentiation and transplantation. A platform that allows cells to undertake the initial stages of development in a similar manner as in native conditions will stand a better chance of translation to regenerative therapies of that tissue. Relevant factors in early morphogenesis, which should be considered in the design of biomaterials, include spatial cell positioning and intercellular interactions. One of the first steps in the development of many tissues is mesenchymal condensation, in which MSCs come together to form multicellular clusters that will set the foundations of development¹⁷⁸ (Fig. 1.7).

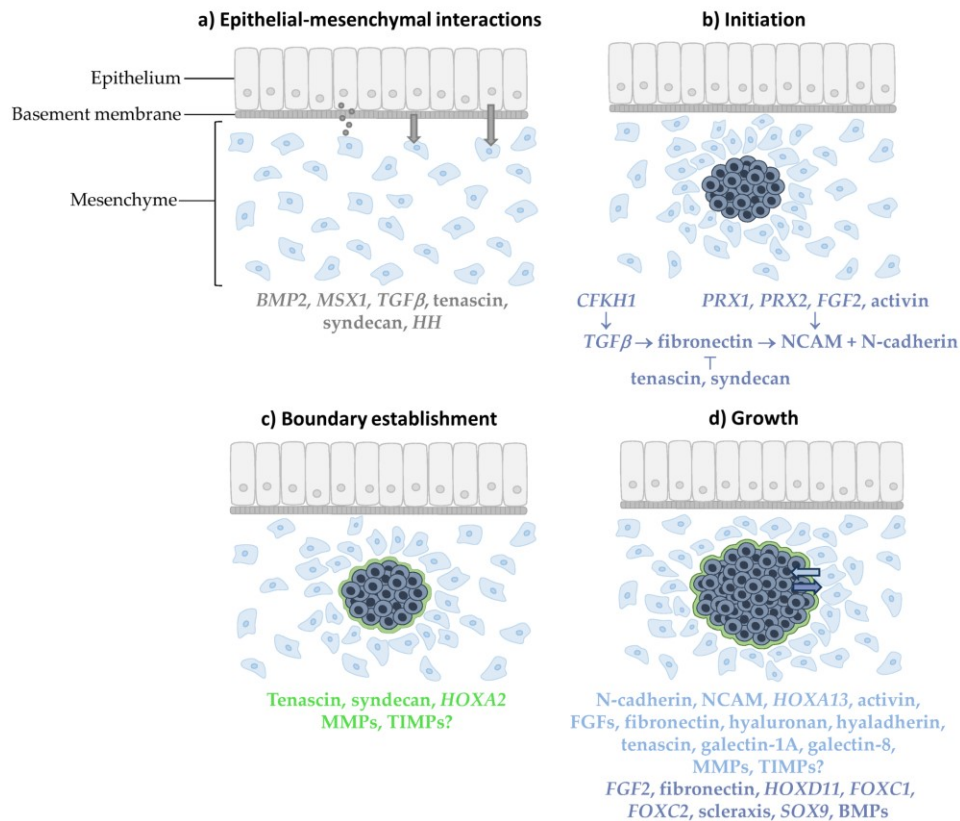


Figure 1.7 Mesenchymal condensation. **a)** Mesenchymal cells are first induced by epithelial signalling molecules through diffusion, close interaction with the basement membrane or direct cell–cell interaction. **b)** Condensation is then initiated by a signalling pathway involving neural cell adhesion molecules (NCAM) and N-cadherin. **c)** A boundary surrounding the condensed cells is then established which permits **d)** growth of the condensation from incoming cells that adhere to the condensation and cells undergoing proliferation within the condensation. Signalling molecules involved in each step are color-coded for the location in which they appear. Grey, dark blue, green, and light blue correspond to epithelial cells, condensed cells, the condensation boundary, and mesenchymal cells, respectively. Reproduced under a Creative Commons license (CC BY 4.0) from Giffin, Gaitor and Franz-Odenaal (2019)¹⁷⁸.

Condensation is an important step in the formation of musculoskeletal tissues, in particular cartilage and bone. This process is mediated by complex intercellular mechanical and chemical communication networks. Since signalling in multicellular networks is strongly influenced by the system architecture, the cell carrier should allow the establishment and maintenance of cell-cell interactions during the different stages of MSC differentiation. With this end, we apply surface nanopatterning to modulate cell-biomaterial nanoscale adherence and provide the initial architectural requirements to better mimic the native structure of musculoskeletal tissues.

1.6. Objectives

The objectives of this thesis are as follows:

- Determine whether and how nanoscale local ligand density regulates mesenchymal condensation during early cartilage formation.
- Study how local ligand density modulates the structure of prechondrogenic condensates, as well as their mechanical stability.
- Unveil the effects of local ligand density on intercellular communication networks in prechondrogenic condensates, and the principles of the biological mechanism driving this regulation.
- Identify the nanopattern configuration that promotes the differentiation of mesenchymal stem cells towards three musculoskeletal lineages: cartilage, tendon and bone.
- Find how cell-substrate adhesion and cellular morphology mediate differentiation to musculoskeletal tissues according to local ligand density and cell fate.
- Overall, advance in the development of *in vitro* platforms to induce effective cell differentiation towards cartilage, tendon and bone.

1.7. Chapter abstracts

After the Introduction and Methods (Chapter 2), this thesis is structured in three chapters where we employ dendrimer-nanopatterned substrates to modulate and study cell behaviour in developmental settings of musculoskeletal tissues:

Chapter 3: Dynamics of stem cell migration and condensation

Single and collective cell migration are an essential part of biological processes such as tissue development, wound healing, and disease. In the first stages of cartilage formation, mesenchymal stem cells gather into clusters that set the structural bases for subsequent steps in morphogenesis. This process of mesenchymal condensation is limited by the ability of cells to migrate across the extracellular environment and establish cell-cell contacts. We live-imaged the onset of chondrogenesis on nanopatterns of cell-adhesive matrix ligand and found that local ligand density modulates both single and collective stem cell migration through directionality and velocity, impacting the rate of cell-cell collisions. The progressive transition from single cells to multicellular condensates is also guided by cell-cell contacts mediated by N-cadherin and gap junctions. While cells on nanopatterned substrates present an amoeboid mode of migration, those on protein coatings show mesenchymal morphologies and tend to form a nematic-like monolayer with topological defects. We pose that, once two cells collide on nanopatterned substrates, mesenchymal condensation is regulated by the balance between contact inhibition of locomotion (cells resuming single migration) and contact following of locomotion (cells establishing a new condensation unit).

Chapter 4: Condensate structure and intercellular communication

Gap junction intercellular communication (GJIC) provides a continuous and efficient flow of biological information during tissue formation and is essential to sustain homeostasis and function in living organisms. This mode of intercellular communication is particularly important in avascular tissues such as cartilage. We use nanopatterned substrates to study how local ligand density modulates the structure, mechanical stability and protein network architecture within multicellular mesenchymal condensates in early chondrogenesis. We show that nanopatterns of high ligand density facilitate condensate growth and generate condensates that are more stable in culture, as well as increasing cell compaction in them. These results are not explained by cadherin-mediated cell-cell adhesions. We then demonstrate that high local ligand density nanopatterns promote gap junction protein expression and improve the architecture of the

intercellular protein network. By a tracer uptake assay, we demonstrate that high local ligand density promotes GJIC in mesenchymal condensates. We then design a condensate transplantation assay and show that cell sensing of ligand density is a continuous process, with cells responding to changing substrate conditions even if they are not in direct contact with it. Finally, we confirm that substrate information is sensed by integrin adhesions and propagated into the forming tissue through cytoskeletal contraction.

Chapter 5: Adhesion, cell shape and differentiation to musculoskeletal lineages

Injuries and conditions of musculoskeletal tissues such as cartilage, tendon and bone are among the main causes of disability worldwide; there is an urgent need for improved cell-based regenerative therapies of these tissues. As an application of nanopatterned substrates to guide stem cells towards musculoskeletal fates, here we induce cell differentiation to each of these three lineages to unveil the optimal local ligand density that promotes it. Nanopatterns of high local ligand density promote chondrogenic differentiation through nuclear translocation of a mechanosensitive transcriptional activator. The same nanopattern configuration also promotes osteogenesis, although in this case cells form smaller adhesions than on low- and medium-density substrates. Tenogenesis is seemingly not affected by substrate ligand density. Given that tension exerted from cell membrane receptors is transmitted by the cytoskeleton to the cell nucleus, we analyse nuclear morphology on each condition according to cell fate. For chondrogenesis, we find that cells respond to initial increases in adhesion size with elongated nuclei; as adhesion size increases, nuclei regain a circular shape. In the case of tenogenesis, there is no relation between adhesion size and nuclear circularity, indicating that adhesions are equally distributed around the cell on all substrates. For osteogenesis, we find that nuclear deformation increases with decreasing adhesion size. We pose that cell response to nanoscale ligand density depends on both size and distribution of integrin adhesions around the cell, in a different manner for each of the three analysed lineages, and that nuclear stretching modulates the observed effects on differentiation.

1.8. References

1. Frantz, C. *et al.* The extracellular matrix at a glance. *J. Cell Sci.* **123**, 4195–4200 (2010).
2. Hynes, R. O. & Naba, A. Overview of the Matrisome — An Inventory of Extracellular Matrix Constituents and Functions. *Cold Spring Harb. Perspect. Biol.* **4**, a004903 (2012).
3. Alberts, B. *et al.* *Molecular Biology of the Cell.* (Garland Science, 2002). doi:10.1017/CBO9781107415324.004.
4. Vogel, V. & Sheetz, M. Local force and geometry sensing regulate cell functions. *Nat. Rev. Mol. Cell Biol.* **7**, 265–275 (2006).
5. Wolfenson, H., Yang, B. & Sheetz, M. P. Steps in Mechanotransduction Pathways that Control Cell Morphology. *Annu. Rev. Physiol.* **81**, 585–605 (2019).
6. Cukierman, E., Pankov, R., Stevens, D. R. & Yamada, K. M. Taking cell-matrix adhesions to the third dimension. *Science* **294**, 1708–1712 (2001).
7. Ruprecht, V. *et al.* How cells respond to environmental cues - insights from bio-functionalized substrates. *J. Cell Sci.* **130**, 51–61 (2017).
8. Xi, W., Saw, T. B., Delacour, D., Lim, C. T. & Ladoux, B. Material approaches to active tissue mechanics. *Nat. Rev. Mater.* **4**, 23–44 (2019).
9. Geiger, B., Spatz, J. P. & Bershadsky, A. D. Environmental sensing through focal adhesions. *Nat. Rev. Mol. Cell Biol.* **10**, 21–33 (2009).
10. Sun, Z., Guo, S. S. & Fässler, R. Integrin-mediated mechanotransduction. *J. Cell Biol.* **215**, 445–456 (2016).
11. Vogel, V. Unraveling the Mechanobiology of Extracellular Matrix. *Annu. Rev. Physiol.* **80**, 353–387 (2018).
12. Kechagia, J. Z., Ivaska, J. & Roca-Cusachs, P. Integrins as biomechanical sensors of the microenvironment. *Nat. Rev. Mol. Cell Biol.* **20**, 457–473 (2019).
13. Pierschbacher, M. D. & Ruoslahti, E. Cell attachment activity of fibronectin can be duplicated by small synthetic fragments of the molecule. *Nature* **309**, 30–33 (1984).
14. Ruoslahti, E. & Pierschbacher, M. D. New Perspectives in Cell Adhesion : RGD and Integrins. *Science* **238**, 491–497 (1987).

15. Barczyk, M., Carracedo, S. & Gullberg, D. Integrins. *Cell Tissue Res.* **339**, 269–280 (2010).
16. Moreno-Layseca, P., Icha, J., Hamidi, H. & Ivaska, J. Integrin trafficking in cells and tissues. *Nat. Cell Biol.* **21**, 122–132 (2019).
17. Roca-Cusachs, P., Gauthier, N. C. & Sheetz, M. P. Clustering of $\alpha 5\beta 1$ integrins determines adhesion strength whereas $\alpha v\beta 3$ and talin enable mechanotransduction. *Proc. Natl. Acad. Sci.* **106**, 16245–16250 (2009).
18. Tan, S. J. *et al.* Regulation and dynamics of force transmission at individual cell-matrix adhesion bonds. *Sci. Adv.* **6**, eaax0317 (2020).
19. Elosegui-Artola, A. *et al.* Rigidity sensing and adaptation through regulation of integrin types. *Nat. Mater.* **13**, 631–637 (2014).
20. Tsunoyama, T. A. *et al.* Super-long single-molecule tracking reveals dynamic-anchorage-induced integrin function. *Nat. Chem. Biol.* **14**, 497–506 (2018).
21. Paul, N. R., Jacquemet, G. & Caswell, P. T. Endocytic Trafficking of Integrins in Cell Migration. *Curr. Biol.* **25**, 1092–1105 (2015).
22. Zhang, X. *et al.* Talin depletion reveals independence of initial cell spreading from integrin activation and traction. *Nat. Cell Biol.* **10**, 1062–1068 (2008).
23. Choi, C. K. *et al.* Actin and α -actinin orchestrate the assembly and maturation of nascent adhesions in a myosin II motor-independent manner. *Nat. Cell Biol.* **10**, 1039–1050 (2008).
24. Changede, R., Xu, X., Margadant, F. & Sheetz, M. P. Nascent Integrin Adhesions Form on All Matrix Rigidities after Integrin Activation. *Dev. Cell* **35**, 614–621 (2015).
25. Lawson, C. *et al.* FAK promotes recruitment of talin to nascent adhesions to control cell motility. *J. Cell Biol.* **196**, 223–232 (2012).
26. Harburger, D. S., Bouaouina, M. & Calderwood, D. A. Kindlin-1 and -2 Directly Bind the C-terminal Region of Integrin Cytoplasmic Tails and Exert Integrin-specific Activation Effects. *J. Biol. Chem.* **284**, 11485–11497 (2009).
27. Haydari, Z., Shams, H., Jahed, Z. & Mofrad, M. R. K. Kindlin Assists Talin to Promote Integrin Activation. *Biophys. J.* **118**, 1977–1991 (2020).
28. Tadokoro, S. *et al.* Talin binding to integrin β tails: A final common step in integrin activation. *Science* **302**, 103–106 (2003).

Chapter 1

29. Haage, A. *et al.* Talin Autoinhibition Regulates Cell-ECM Adhesion Dynamics and Wound Healing In Vivo. *Cell Rep.* **25**, 2401–2416 (2018).
30. Kim, M., Carman, C. V & Springer, T. A. Bidirectional Transmembrane Signaling by Cytoplasmic Domain Separation in Integrins. *Science* **301**, 1720–1726 (2003).
31. Zhu, J., Zhu, J. & Springer, T. A. Complete integrin headpiece opening in eight steps. *J. Cell Biol.* **201**, 1053–1068 (2013).
32. Bachmann, M., Kukkurainen, S., Hytönen, V. P. & Wehrle-Haller, B. Cell adhesion by integrins. *Physiol. Rev.* **99**, 1655–1699 (2019).
33. Hamidi, H., Pietilä, M. & Ivaska, J. The complexity of integrins in cancer and new scopes for therapeutic targeting. *Br. J. Cancer* **115**, 1017–1023 (2016).
34. Balaban, N. Q. *et al.* Force and focal adhesion assembly: a close relationship studied using elastic micropatterned substrates. *Nat. Cell Biol.* **3**, 466–472 (2001).
35. Nicolas, A., Geiger, B. & Safran, S. A. Cell mechanosensitivity controls the anisotropy of focal adhesions. *Proc. Natl. Acad. Sci.* **101**, 12520–12525 (2004).
36. Yao, M. *et al.* The mechanical response of talin. *Nat. Commun.* **7**, 11966 (2016).
37. Yao, M. *et al.* Mechanical activation of vinculin binding to talin locks talin in an unfolded conformation. *Sci. Rep.* **4**, 4610 (2014).
38. Huang, D. L., Bax, N. A., Buckley, C. D., Weis, W. I. & Dunn, A. R. Vinculin forms a directionally asymmetric catch bond with F-actin. *Science* **357**, 703–706 (2017).
39. Gingras, A. R. *et al.* The structure of the C-terminal actin-binding domain of talin. *EMBO J.* **27**, 458–469 (2008).
40. Roberts, G. C. K. & Critchley, D. R. Structural and biophysical properties of the integrin-associated cytoskeletal protein talin. *Biophys. Rev.* **1**, 61–69 (2009).
41. Kanchanawong, P. *et al.* Nanoscale architecture of integrin-based cell adhesions. *Nature* **468**, 580–584 (2010).
42. Jahed, Z., Shams, H. & Mehrbod, M. *Mechanotransduction Pathways Linking the Extracellular Matrix to the Nucleus. International Review of Cell and Molecular Biology* vol. 310 (Elsevier Inc., 2014).
43. Horton, E. R. *et al.* Definition of a consensus integrin adhesome and its dynamics during

- adhesion complex assembly and disassembly. *Nat. Cell Biol.* **17**, 1577–1587 (2015).
44. Martino, F., Perestrelo, A. R., Vinarský, V., Pagliari, S. & Forte, G. Cellular mechanotransduction: From tension to function. *Front. Physiol.* **9**, 824 (2018).
 45. Kim, C., Ye, F. & Ginsberg, M. H. Regulation of integrin activation. *Annu. Rev. Cell Dev. Biol.* **27**, 321–345 (2011).
 46. Miller, A. E., Hu, P. & Barker, T. H. Feeling Things Out: Bidirectional Signaling of the Cell–ECM Interface, Implications in the Mechanobiology of Cell Spreading, Migration, Proliferation, and Differentiation. *Adv. Healthc. Mater.* **9**, 1–24 (2020).
 47. Elosegui-Artola, A. *et al.* Force Triggers YAP Nuclear Entry by Regulating Transport across Nuclear Pores. *Cell* **171**, 1397–1410 (2017).
 48. Maniotis, A. J., Chen, C. S. & Ingber, D. E. Demonstration of mechanical connections between integrins, cytoskeletal filaments, and nucleoplasm that stabilize nuclear structure. *Proc. Natl. Acad. Sci.* **94**, 849–854 (1997).
 49. Swift, J. *et al.* Nuclear Lamin-A Scales with Tissue Stiffness and Enhances Matrix-Directed Differentiation. *Science* **341**, 1240104 (2013).
 50. Ho, C. Y., Jaalouk, D. E., Vartiainen, M. K. & Lammerding, J. Lamin A/C and emerin regulate MKL1-SRF activity by modulating actin dynamics. *Nature* **497**, 507–511 (2013).
 51. Miroshnikova, Y. A., Nava, M. M. & Wickström, S. A. Emerging roles of mechanical forces in chromatin regulation. *J. Cell Sci.* **130**, 2243–2250 (2017).
 52. Tajik, A. *et al.* Transcription upregulation via force-induced direct stretching of chromatin. *Nat. Mater.* **15**, 1287–1296 (2016).
 53. Kirby, T. J. & Lammerding, J. Emerging views of the nucleus as a cellular mechanosensor. *Nat. Cell Biol.* **20**, 373–381 (2018).
 54. Humphries, J. D., Chastney, M. R., Askari, J. A. & Humphries, M. J. Signal transduction via integrin adhesion complexes. *Curr. Opin. Cell Biol.* **56**, 14–21 (2019).
 55. Böttcher, R. T. *et al.* Kindlin-2 recruits paxillin and Arp2/3 to promote membrane protrusions during initial cell spreading. *J. Cell Biol.* **216**, 3785–3798 (2016).
 56. Stutchbury, B., Atherton, P., Tsang, R., Wang, D. & Ballestrem, C. Distinct focal adhesion protein modules control different aspects of mechanotransduction. *J. Cell Sci.* **130**, 1612–1624 (2017).

Chapter 1

57. Muehlich, S. *et al.* Unravelling a new mechanism linking actin polymerization and gene transcription. *Nucleus* **7**, 121–125 (2016).
58. Panciera, T., Azzolin, L., Cordenonsi, M. & Piccolo, S. Mechanobiology of YAP and TAZ in physiology and disease. *Nat. Rev. Mol. Cell Biol.* **18**, 758–770 (2017).
59. Hamouda, M. S., Labouesse, C. & Chalut, K. J. Nuclear mechanotransduction in stem cells. *Curr. Opin. Cell Biol.* **64**, 97–104 (2020).
60. Infante, E. *et al.* The mechanical stability of proteins regulates their translocation rate into the cell nucleus. *Nat. Phys.* **15**, (2019).
61. Swaminathan, V. & Gloerich, M. Decoding mechanical cues by molecular mechanotransduction. *Curr. Opin. Cell Biol.* **72**, 72–80 (2021).
62. Coste, B. *et al.* Piezo1 and Piezo2 Are Essential Components of Distinct Mechanically Activated Cation Channels. *Science* **330**, 55–60 (2010).
63. Nourse, J. L. & Pathak, M. M. Seminars in Cell & Developmental Biology How cells channel their stress: Interplay between Piezo1 and the cytoskeleton. *Semin. Cell Dev. Biol.* **71**, 3–12 (2017).
64. Borbiri, I. & Rohacs, T. *Regulation of Piezo Channels by Cellular Signaling Pathways. Current Topics in Membranes* vol. 79 (Elsevier Ltd, 2017).
65. Parpaite, T. & Coste, B. Piezo channels. *Curr. Biol.* **27**, R250–R252 (2017).
66. Hyman, A. J., Tumova, S. & Beech, D. J. *Piezo1 Channels in Vascular Development and the Sensing of Shear Stress. Current Topics in Membranes* vol. 79 (Elsevier Ltd, 2017).
67. Duchemin, A.-L., Vignes, H. & Vermot, J. Mechanically activated piezo channels modulate outflow tract valve development through the Yap1 and Klf2- Notch signaling axis. *Elife* **8**, e44706 (2019).
68. Holt, J. R. *et al.* Spatiotemporal dynamics of PIEZO1 localization controls keratinocyte migration during wound healing. *Elife* **10**, e65415 (2021).
69. Ma, S. *et al.* A role of PIEZO1 in iron metabolism in mice and humans II II Article A role of PIEZO1 in iron metabolism in mice and humans. *Cell* **184**, 969–982 (2021).
70. Canales Coutiño, B. & Mayor, R. The mechanosensitive channel Piezo1 cooperates with Semaphorin to control neural crest migration. *Development* **148**, dev200001 (2021).
71. Brohawn, S. G., Su, Z. & Mackinnon, R. Mechanosensitivity is mediated directly by the lipid

- membrane in TRAAK and TREK1 K⁺ channels. *Proc. Natl. Acad. Sci.* **111**, 3614–3619 | (2014).
72. Murthy, S. E. *et al.* OSCA/TMEM63 are an evolutionarily conserved family of mechanically activated ion channels. *Elife* **7**, e41844 (2018).
 73. Kefauver, J. M., Ward, A. B. & Patapoutian, A. Discoveries in structure and physiology of mechanically activated ion channels. *Nature* **587**, 567–576 (2020).
 74. Griffin, M. F., Butler, P. E., Seifalian, A. M., Deepak M Kalaskar & Michelle. Control of stem cell fate by engineering their micro and nanoenvironment. *World J. Stem Cells* **7**, 37 (2015).
 75. Lagunas, A., Caballero, D. & Samitier, J. Influence of Controlled Micro- and Nanoengineered Environments on Stem Cell Fate. in *Advanced Surfaces for Stem Cell Research* (eds. Tiwari, A., Garipcan, B. & Uzun, L.) 87–141 (Hoboken: Wiley, 2016).
 76. Zhang, S. Fabrication of novel biomaterials through molecular self-assembly. *Nat. Biotechnol.* **21**, 1171–1178 (2003).
 77. Segalman, R. A. Patterning with block copolymer thin films. *Mater. Sci. Eng. Reports* **48**, 191–226 (2005).
 78. Christman, K. L., Enriquez-rios, V. D. & Maynard, H. D. Nanopatterning proteins and peptides. *Soft Matter* **2**, 928–939 (2006).
 79. Mendes, P. M., Yeung, C. L. & Preece, J. A. Bio-nanopatterning of Surfaces. *Nanoscale Res. Lett.* **2**, 373–384 (2007).
 80. Reynhout, I. C., Delaittre, G., Kim, H.-C., Nolte, R. J. M. & Cornelissen, J. J. L. M. Nanoscale organization of proteins via block copolymer lithography and non-covalent bioconjugation. *J. Mater. Chem. B* **1**, 3026–3030 (2013).
 81. Kam, L. C., Shen, K. & Dustin, M. L. Micro- and Nanoscale Engineering of Cell Signaling. *Annu. Rev. Biomed. Eng.* **15**, 305–326 (2013).
 82. Lagunas, A. *et al.* Synthesis of a polymethyl(methacrylate)-polystyrene-based diblock copolymer containing biotin for selective protein nanopatterning. *Polym. Chem.* **7**, 212–218 (2016).
 83. Arnold, M. *et al.* Activation of integrin function by nanopatterned adhesive interfaces. *ChemPhysChem* **5**, 383–388 (2004).
 84. Cavalcanti-Adam, E. A. *et al.* Lateral spacing of integrin ligands influences cell spreading and

Chapter 1

- focal adhesion assembly. *Eur. J. Cell Biol.* **85**, 219–224 (2006).
85. Cavalcanti-Adam, E. A. *et al.* Cell spreading and focal adhesion dynamics are regulated by spacing of integrin ligands. *Biophys. J.* **92**, 2964–2974 (2007).
 86. Arnold, M. *et al.* Induction of Cell Polarization and Migration by a Gradient of Nanoscale Variations in Adhesive Ligand Spacing. *Nano Lett.* **8**, 2063–2069 (2008).
 87. Selhuber-Unkel, C. *et al.* Cell Adhesion Strength Is Controlled by Intermolecular Spacing of Adhesion Receptors. *Biophys. J.* **98**, 543–551 (2010).
 88. Wang, X., Li, S., Yan, C., Liu, P. & Ding, J. Fabrication of RGD micro/nanopattern and corresponding study of stem cell differentiation. *Nano Lett.* **15**, 1457–1467 (2015).
 89. Huang, J. *et al.* Impact of order and disorder in RGD nanopatterns on cell adhesion. *Nano Lett.* **9**, 1111–1116 (2009).
 90. Kapp, T. G. *et al.* A comprehensive evaluation of the activity and selectivity profile of ligands for RGD-binding integrins. *Sci. Rep.* **7**, 39805 (2017).
 91. Sefkow-Werner, J. *et al.* Heparan sulfate co-immobilized with cRGD ligands and BMP2 on biomimetic platforms promotes BMP2-mediated osteogenic differentiation. *Acta Biomater.* **114**, 90–103 (2020).
 92. Posa, F. *et al.* Biomaterials Surface Co-presentation of BMP-2 and integrin selective ligands at the nanoscale favors $\alpha 5\beta 1$ integrin-mediated adhesion. *Biomaterials* **267**, 120484 (2021).
 93. Oliver-Cervelló, L. *et al.* An Engineered Biomimetic Peptide Regulates Cell Behavior by Synergistic Integrin and Growth Factor Signaling. *Adv. Healthc. Mater.* **10**, 2001757 (2021).
 94. Discher, D. E., Janmey, P. & Wang, Y.-L. Tissue cells feel and respond to the stiffness of their substrate. *Science* **310**, 1139–1143 (2005).
 95. Andreu, I. *et al.* The force loading rate drives cell mechanosensing through both reinforcement and cytoskeletal softening. *Nat. Commun.* **12**, 1–12 (2021).
 96. Engler, A. J., Sen, S., Sweeney, H. L. & Discher, D. E. Matrix Elasticity Directs Stem Cell Lineage Specification. *Cell* **126**, 677–689 (2006).
 97. Huebsch, N. *et al.* Harnessing traction-mediated manipulation of the cell/matrix interface to control stem-cell fate. *Nat. Mater.* **9**, 518–526 (2010).
 98. Tse, J. R. & Engler, A. J. Preparation of Hydrogel Substrates with Tunable Mechanical Properties.

- Curr. Protoc. Cell Biol.* **10.16**, 1–16 (2010).
99. Missirlis, D. & Spatz, J. P. Combined effects of PEG hydrogel elasticity and cell-adhesive coating on fibroblast adhesion and persistent migration. *Biomacromolecules* **15**, 195–205 (2014).
 100. Labouesse, C. *et al.* StemBond hydrogels control the mechanical microenvironment for pluripotent stem cells. *Nat. Commun.* **12**, 6132 (2021).
 101. Stanton, A. E., Tong, X., Lee, S. & Yang, F. Biochemical Ligand Density Regulates Yes-Associated Protein Translocation in Stem Cells through Cytoskeletal Tension and Integrins. *ACS Appl. Mater. Interfaces* **11**, 8849–8857 (2019).
 102. Oria, R. *et al.* Force loading explains spatial sensing of ligands by cells. *Nature* **552**, 219–224 (2017).
 103. Elosegui-Artola, A., Trepap, X. & Roca-Cusachs, P. Control of Mechanotransduction by Molecular Clutch Dynamics. *Trends Cell Biol.* **28**, 356–367 (2018).
 104. Zhang, M. *et al.* Controllable ligand spacing stimulates cellular mechanotransduction and promotes stem cell osteogenic differentiation on soft hydrogels. *Biomaterials* **268**, 120543 (2021).
 105. Dalby, M. J. *et al.* Fibroblast reaction to island topography: changes in cytoskeleton and morphology with time. *Biomaterials* **24**, 927–935 (2003).
 106. Dalby, M. J. *et al.* The control of human mesenchymal cell differentiation using nanoscale symmetry and disorder. *Nat. Mat* **6**, 997–1003 (2007).
 107. Allan, C. *et al.* Osteoblast response to disordered nanotopography. *Cell Eng. Micro/Nanoscale* **9**, 1–7 (2018).
 108. Abagnale, G. *et al.* Surface topography enhances differentiation of mesenchymal stem cells towards osteogenic and adipogenic lineages. *Biomaterials* **61**, 316–326 (2015).
 109. Abagnale, G. *et al.* Surface Topography Guides Morphology and Spatial Patterning of Induced Pluripotent Stem Cell Colonies. *Stem Cell Reports* **9**, 654–666 (2017).
 110. Newman, P. *et al.* Relationship between nanotopographical alignment and stem cell fate with live imaging and shape analysis. *Sci. Rep.* **6**, 37909 (2016).
 111. Lagunas, A. *et al.* Tailoring RGD local surface density at the nanoscale toward adult stem cell chondrogenic commitment. *Nano Res.* **10**, 1959–1971 (2017).

Chapter 1

112. Casanellas, I. *et al.* Dendrimer-based uneven nanopatterns to locally control surface adhesiveness: A method to direct chondrogenic differentiation. *J. Vis. Exp.* **131**, e56347 (2018).
113. Lagunas, A. *et al.* Large-scale dendrimer-based uneven nanopatterns for the study of local arginine-glycine-aspartic acid (RGD) density effects on cell adhesion. *Nano Res.* **7**, 399–409 (2014).
114. Turrin, C., Caminade, A., Rolland, O. & Majoral, J. Dendrimers and nanomedicine: multivalency in action. *New J. Chem.* **33**, 1809–1824 (2009).
115. Xiong, J. *et al.* Crystal Structure of the Extracellular Segment of Integrin $\alpha_v\beta_3$ in Complex with an Arg-Gly-Asp Ligand. *Science* **296**, 151–156 (2002).
116. Pericet-Camara, R., Cahill, B. P., Papastavrou, G. & Borkovec, M. Nano-patterning of solid substrates by adsorbed dendrimers. *Chem. Commun.* **3**, 266–268 (2007).
117. Migliorini, E., Weidenhaupt, M. & Picart, C. Practical guide to characterize biomolecule adsorption on solid surfaces (Review). *Biointerphases* **13**, 06D303 (2018).
118. Saovapakhiran, A., Emanuele, A. D., Attwood, D. & Penny, J. Surface Modification of PAMAM Dendrimers Modulates the Mechanism of Cellular Internalization. *Bioconjug. Chem.* **20**, 693–701 (2009).
119. Albertazzi, L., Fernandez-villamarin, M., Riguera, R. & Fernandez-megia, E. Peripheral functionalization of dendrimers regulates internalization and intracellular trafficking in living cells. *Bioconjug. Chem.* **23**, 1059–1068 (2012).
120. Mikhail, A. S., Jones, K. S. & Sheardown, H. Dendrimer-Grafted Cell Adhesion Peptide-Modified PDMS. *Biotechnol. Prog.* **24**, 938–944 (2008).
121. Kino-oka, M., Kim, J., Kurisaka, K. & Kim, M. Preferential growth of skeletal myoblasts and fibroblasts in co-culture on a dendrimer-immobilized surface. *J. Biosci. Bioeng.* **115**, 96–99 (2013).
122. Kim, M.-H. *et al.* Morphological regulation and aggregate formation of rabbit chondrocytes on dendrimer-immobilized surfaces with D-glucose display. *J. Biosci. Bioeng.* **107**, 196–205 (2009).
123. Lomba, M. *et al.* Cell adhesion on surface patterns generated by the photocrosslinking of hyperbranched polyesters with a trisdiazonium salt. *React. Funct. Polym.* **73**, 499–507 (2013).
124. Maheshwari, G., Brown, G., Lauffenburger, D. A., Wells, A. & Griffith, L. G. Cell adhesion and motility depend on nanoscale RGD clustering. *J. Cell Sci.* **113**, 1677–1686 (2000).

125. Kim, M.-H., Kino-oka, M., Kawase, M., Yagi, K. & Taya, M. Synergistic Effect of D-Glucose and Epidermal Growth Factor Display on Dynamic Behaviors of Human Epithelial Cells. *J. Biosci. Bioeng.* **104**, 428–431 (2007).
126. Walker, J. Skeletal system 2: structure and function of the musculoskeletal system. *Nurs. Times* **116**, 52–56 (2020).
127. Briggs, A. M. *et al.* Reducing the global burden of musculoskeletal conditions. *Bull. World Health Organ.* **96**, 366–368 (2018).
128. Cieza, A. *et al.* Global estimates of the need for rehabilitation based on the Global Burden of Disease study 2019: a systematic analysis for the Global Burden of Disease Study 2019. *Lancet* **396**, 2006–2017 (2020).
129. Butler, D. L., Juncosa, N. & Dressler, M. R. Functional efficacy of tendon repair processes. *Annu. Rev. Biomed. Eng.* **6**, 303–329 (2004).
130. Yang, G., Rothrauff, B. B. & Tuan, R. S. Tendon and Ligament Regeneration and Repair: Clinical Relevance and Developmental Paradigm. *Birth Defects Res. Part C Embryo Today* **99**, 203–222 (2013).
131. Wang, P. *et al.* Bone tissue engineering via nanostructured calcium phosphate biomaterials and stem cells. *Bone Res.* **2**, 14017 (2014).
132. Liu, Y., Suen, C. W., Zhang, J. fang & Li, G. Current concepts on tenogenic differentiation and clinical applications. *J. Orthop. Transl.* **9**, 28–42 (2017).
133. Fingar, K. R., Stocks, C., Weiss, A. J. & Steiner, C. A. Most Frequent Operating Room Procedures Performed in U.S. Hospitals, 2003-2012. *Healthcare Cost and Utilization Project, Agency for Healthcare Research and Quality* <http://www.hcup-us.ahrq.gov/reports/statbriefs/sb186-Operating-Room-Procedures-United-States-2012.pdf>. (2014).
134. Rees, J. D., Wilson, A. M. & Wolman, R. L. Current concepts in the management of tendon disorders. *Rheumatology* **45**, 508–521 (2006).
135. Wu, F., Nerlich, M. & Docheva, D. Tendon injuries: Basic science and new repair proposals. *EFORT Open Rev.* **2**, 332–342 (2017).
136. Song, S. J. & Park, C. H. Microfracture for cartilage repair in the knee: current concepts and limitations of systematic reviews. *Ann. Transl. Med.* **7**, S108–S108 (2019).
137. Bartha, L., Vajda, A., Duska, Z., Rahmeh, H. & Hangody, L. Autologous osteochondral

Chapter 1

- mosaicplasty grafting. *J. Orthop. Sports Phys. Ther.* **36**, 739–750 (2006).
138. Welch, T., Mandelbaum, B. & Tom, M. Autologous Chondrocyte Implantation: Past, Present, and Future. *Sports Med. Arthrosc.* **24**, 85–91 (2016).
139. Makris, E. A., Gomoll, A. H., Malizos, K. N., Hu, J. C. & Athanasiou, K. A. Repair and tissue engineering techniques for articular cartilage. *Nat. Rev. Rheumatol.* **11**, 21–34 (2015).
140. Jiang, Y. & Tuan, R. S. Origin and function of cartilage stem/progenitor cells in osteoarthritis. *Nat. Rev. Rheumatol.* **11**, 206–212 (2015).
141. Felson, D. T. An update on the pathogenesis and epidemiology of osteoarthritis. *Radiol. Clin. North Am.* **42**, 1–9 (2004).
142. Johnstone, B. *et al.* Tissue engineering for cartilage repair. *Eur. Cells Mater.* **25**, 248–267 (2013).
143. Caplan, A. I. Mesenchymal stem cells: Time to change the name! *Stem Cells Transl. Med.* **6**, 1445–1451 (2017).
144. Miwa, H. & Era, T. Tracing the destiny of mesenchymal stem cells from embryo to adult bone marrow and white adipose tissue via *pdgfra* expression. *Development* **145**, dev155879 (2018).
145. Nombela-Arrieta, C., Ritz, J. & Silberstein, L. E. The elusive nature and function of mesenchymal stem cells. *Nat. Rev. Mol. Cell Biol.* **12**, 126–131 (2011).
146. Brack, A. S. & Rando, T. A. Tissue-Specific Stem Cells: Lessons from the Skeletal Muscle Satellite Cell. *Stem Cell* **10**, 504–514 (2012).
147. Assis-Ribas, T., Forni, M. F., Winnischofer, S. M. B., Sogayar, M. C. & Trombetta-Lima, M. Extracellular matrix dynamics during mesenchymal stem cells differentiation. *Dev. Biol.* **437**, 63–74 (2018).
148. Donnelly, H., Salmeron-sanchez, M. & Dalby, M. J. Designing stem cell niches for differentiation and self-renewal. *J. R. Soc. Interface* **15**, 20180388 (2018).
149. Dominici, M. *et al.* Minimal criteria for defining multipotent mesenchymal stromal cells. The International Society for Cellular Therapy position statement. *Cytotherapy* **8**, 315–317 (2006).
150. Mundra, V., Gerling, I. C. & Mahato, R. I. Mesenchymal Stem Cell-Based Therapy. *Mol. Pharm.* **10**, 77–89 (2013).
151. Aurich, H. *et al.* Hepatocyte differentiation of mesenchymal stem cells from human adipose tissue in vitro promotes hepatic integration in vivo. *Gut* **58**, 570–581 (2009).

152. Marappagounder, D., Somasundaram, I., Dorairaj, S. & Sankaran, R. J. Differentiation of mesenchymal stem cells derived from human bone marrow and subcutaneous adipose tissue into pancreatic islet-like clusters in vitro. *Cell. Mol. Biol. Lett.* **18**, 75–88 (2013).
153. Ghorbani, S., Tiraihi, T. & Soleimani, M. Differentiation of mesenchymal stem cells into neuron-like cells using composite 3D scaffold combined with valproic acid induction. *J. Biomater. Appl.* **32**, 702–715 (2018).
154. Caplan, A. I. Adult Mesenchymal Stem Cells for Tissue Engineering Versus Regenerative Medicine. *J. Cell. Physiol.* **213**, 341–347 (2007).
155. Cuenca-López, M. D. *et al.* Adult stem cells applied to tissue engineering and regenerative medicine. *Cell. Mol. Biol. (Noisy-le-grand)*. **54**, 40–51 (2008).
156. Robert, A. W., Marcon, B. H., Dallagiovanna, B. & Shigunov, P. Adipogenesis, Osteogenesis, and Chondrogenesis of Human Mesenchymal Stem/Stromal Cells: A Comparative Transcriptome Approach. *Front. Cell Dev. Biol.* **8**, 561 (2020).
157. Manferdini, C. *et al.* Adipose-Derived Mesenchymal Stem Cells Exert Antiinflammatory Effects on Chondrocytes and Synoviocytes From Osteoarthritis Patients Through Prostaglandin E 2. *Arthritis Rheum.* **65**, 1271–1281 (2013).
158. Liang, X., Ding, Y., Zhang, Y., Tse, H. F. & Lian, Q. Paracrine mechanisms of mesenchymal stem cell-based therapy: Current status and perspectives. *Cell Transplant.* **23**, 1045–1059 (2014).
159. Xia, H. *et al.* Tissue repair and regeneration with endogenous stem cells. *Nat. Rev. Mater.* **3**, 174–193 (2018).
160. Butnariu-Ephrat, M., Robinson, D., Mendes, D. G., Halperin, N. & Nevo, Z. Resurfacing of Goat Articular Cartilage by Chondrocytes Derived From Bone Marrow. *Clin. Orthop. Relat. Res.* **330**, 234–243 (1996).
161. Gilbert, J. E. Current treatment options for the restoration of articular cartilage. *Am. J. Knee Surg.* **11**, 42–46 (1998).
162. Bari, C. De, Accio, F. D. & Luyten, F. P. Failure of In Vitro-Differentiated Mesenchymal Stem Cells From the Synovial Membrane to Form Ectopic Stable Cartilage In Vivo. *Arthritis Rheum.* **50**, 142–150 (2004).
163. Noël, D. *et al.* Short-Term BMP-2 Expression Is Sufficient for In Vivo Osteochondral Differentiation of Mesenchymal Stem Cells. *Stem Cells* **22**, 74–85 (2004).

Chapter 1

164. Walker, K. J. & Madihally, S. V. Anisotropic temperature sensitive chitosan-based injectable hydrogels mimicking cartilage matrix. *J. Biomed. Mater. Res. - Part B* **103**, 1149–1160 (2015).
165. Tamaddon, M. *et al.* Monomeric, porous type II collagen scaffolds promote chondrogenic differentiation of human bone marrow mesenchymal stem cells in vitro. *Sci. Rep.* **7**, 43519 (2017).
166. Liu, M. *et al.* Injectable hydrogels for cartilage and bone tissue engineering. *Bone Res.* **5**, 17014 (2017).
167. Cunniffe, G. M. *et al.* Tissue-specific extracellular matrix scaffolds for the regeneration of spatially complex musculoskeletal tissues. *Biomaterials* **188**, 63–73 (2019).
168. Bayrak, E. & Yilgor Huri, P. Engineering Musculoskeletal Tissue Interfaces. *Front. Mater.* **5**, 24 (2018).
169. Chen, Y., Lee, K., Yang, Y., Kawazoe, N. & Chen, G. PLGA-collagen-ECM hybrid meshes mimicking stepwise osteogenesis and their influence on the osteogenic differentiation of hMSCs. *Biofabrication* **12**, 025027 (2020).
170. Kuterbekov, M., Jonas, A. M., Glinel, K. & Picart, C. Osteogenic differentiation of adipose derived stromal cells: From bench to clinics. *Tissue Eng. Part B Rev.* **26**, 461–474 (2020).
171. Garot, C., Bettega, G. & Picart, C. Additive Manufacturing of Material Scaffolds for Bone Regeneration: Toward Application in the Clinics. *Adv. Funct. Mater.* **31**, 2006967 (2021).
172. Donnelly, H. *et al.* Bone and cartilage differentiation of a single stem cell population driven by material interface. *J. Tissue Eng.* **8**, 204173141770561 (2017).
173. Hellingman, C. A., Koevoet, W. & Osch, G. J. V. M. Van. Can one generate stable hyaline cartilage from adult mesenchymal stem cells? A developmental approach. *J. Tissue Eng. Regen. Med.* **6**, e1–e11 (2012).
174. Peltari, K. *et al.* Premature induction of hypertrophy during in vitro chondrogenesis of human mesenchymal stem cells correlates with calcification and vascular invasion after ectopic transplantation in SCID mice. *Arthritis Rheum.* **54**, 3254–3266 (2006).
175. Hennig, T. *et al.* Reduced chondrogenic potential of adipose tissue derived stromal cells correlates with an altered TGFbeta receptor and BMP profile and is overcome by BMP-6. *J. Cell. Physiol.* **211**, 682–691 (2007).
176. Scotti, C. *et al.* Recapitulation of endochondral bone formation using human adult

- mesenchymal stem cells as a paradigm for developmental engineering. *Proc. Natl. Acad. Sci.* **107**, 7251–7256 (2010).
177. Lam, J. *et al.* Generation of osteochondral tissue constructs with chondrogenically and osteogenically predifferentiated mesenchymal stem cells encapsulated in bilayered hydrogels. *Acta Biomater.* **10**, 1112–1123 (2014).
178. Giffin, J. L., Gaitor, D. & Franz-Odenaal, T. A. The forgotten skeletogenic condensations: A comparison of early skeletal development amongst vertebrates. *J. Dev. Biol.* **7**, 4 (2019).

Chapter 2

Materials and methods

Unless otherwise stated, all experimental procedures were conducted at the Nanobioengineering Group laboratory and Core Facilities at the Institute for Bioengineering of Catalonia (IBEC). Confocal microscopy was conducted at the Advanced Digital Microscopy (ADM) unit at the Institute for Research in Biomedicine (IRB Barcelona). Except for live imaging experiments, epifluorescence microscopy was conducted at the ADM and at the Molecular Imaging Platform (MIP) at the Molecular Biology Institute of Barcelona (IBMB). All facilities are located at the Barcelona Science Park (PCB).

2.1. Production of PLLA-coated substrates

Corning® glass microscopy slides of 7.5 x 2.5 cm (Sigma-Aldrich, 2947-75X25) were cut with a diamond-tip cutter to square pieces of 1.25 x 1.25 cm. A small L-shaped indentation was made on the lower side to distinguish it from the upper side in subsequent steps. Slides were washed thoroughly with deionized water (18 M Ω ·cm Milli-Q, Millipore) followed by 96% ethanol and air-dried.

A 2% m/v solution of 95/5 L-lactide/DL-lactide copolymer (PLLA, Corbion) was prepared by adding 200 mg of solid polymer to 10 ml of 1,4-dioxane (Sigma-Aldrich, 296309) in a pressure tube with a magnetic stirring bar. The tube was placed in a silicon oil (Thermo Fisher Scientific, 174665000) bath on a hot plate at 60°C with gentle stirring (300 rpm) overnight, and the solution was transferred to a 15-ml vial for storage at room temperature.

Glass substrates were spin-coated with the PLLA solution in a class 10,000 clean room (the MicroFabSpace at IBEC). Slides were placed on a hot plate at 60°C for at least 10 min to dry. Each slide was fixed on a spin-coater with vacuum (Laurell Tech, WS-650MZ 23NPP/LITE) and 200-250 μ l of PLLA solution were added with a Pasteur pipette, covering the whole surface (Fig. 2.1). Slides were coated with a two-step program: 5 s at 500 rpm with an acceleration of 300 rpm/s (to eliminate excess solution and spread the remaining solution homogeneously on the surface) followed by 30 s at 3000 rpm with an acceleration of 1500 rpm/s^{1,2}.

2.2. Nanopatterning of RGD-Cys-D1 dendrimers

All steps were performed in a sterile tissue culture hood, and only sterile materials, solutions and techniques were used. Spin-coated PLLA substrates were treated for 13 min under UV light (Fig. 2.1). Each substrate was placed in one well of a 12-well culture plate with tweezers (previously cleaned with ethanol and sterilized with UV light).

RGD-Cys-D1 dendrimers were kindly provided by Prof. Yolanda Vida and Prof. Ezequiel Pérez-Inestrosa (University of Málaga), shipped to IBEC in powder form and stored at -20°C until use. Deionized water was used to prepare RGD-functionalized dendrimer solutions. A stock solution was prepared by dissolving the solid dendrimer in water. An intermediate solution and three working solutions were prepared from it as detailed in Table 2.1. Dendrimer solutions were stored at -20°C for up to 6 months. They were always completely thawed and sonicated for 10 min in an ultrasound bath just before use.

Table 2.1. Preparation of RGD-Cys-D1 dendrimer solutions

Solution	Concentration (mg/ml)	Dendrimer (mg)	MQ water (ml)
A (stock)	0.77	5	6.494
	Concentration (% w/w)	Dendrimer (μl)	
B (intermediate)	10^{-5}	0.78 of Sol. A	6
C	2.5×10^{-8}	15 of Sol. B	5.985
D	10^{-8}	6 of Sol. B	5.994
E	4×10^{-9}	2.4 of Sol. B	5.998

Dendrimer solutions were filtered through a $0.22 \mu\text{m}$ Millex RB sterile syringe filter (Merck Millipore) attached to a syringe and applied directly on the substrates (2 ml/well, Fig. 2.1). If necessary, substrates were gently pushed to the bottom of the well with a pipette, taking care not to scrape the PLLA coating. Plates were sealed and left at room temperature overnight (16 h). Solutions were removed, substrates were washed with sterile deionized water and left to dry on air for a few minutes. They were stored at 4°C for up to one month in a sealed culture plate.

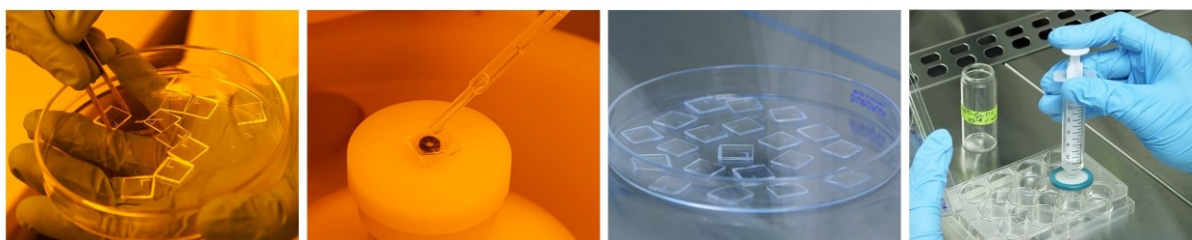


Fig. 2.1. Steps of substrate coating and nanopatterning. From left to right: Cut glass slides before coating, PLLA solution being placed on a slide attached to a spin coater, slides irradiated with UV light in a cell culture hood, and dendrimer solutions being applied on the slides through a syringe and filter. Adapted with permission from Casanellas *et al.* (2018)².

Fibronectin-coated substrates (S_{FN}) were produced by incubating PLLA substrates in fibronectin from bovine plasma solution (Sigma-Aldrich, F1141) 100 $\mu\text{g}/\text{ml}$ in phosphate buffered saline (PBS, Gibco, 21600-10) for 1 h at room temperature, just before cell seeding.

2.3. Cell culture

Human adipose-derived MSCs (ATCC, PCS-500-01) from a 38-year-old female donor were cultured in T75 flasks at 37°C and 5% CO_2 in growth medium, consistent of MSC Basal Medium (ATCC, PCS-500-030) supplemented with MSC Growth Kit Low Serum (ATCC, PCS-500-040) and 0.1% v/v penicillin-streptomycin (P/S, Invitrogen, 15140). Medium was replaced every 2-3 days. Passaging was carried out when cells reached 70-80% confluence. Cells were rinsed with PBS and trypsinised with 5 ml of trypsin-EDTA for 4 min at 37°C and 5% CO_2 . Trypsin was inactivated with 5 ml of growth medium, cells were rinsed off the flask, transferred to a 15-ml centrifuge tube and centrifuged for 5 min at 200-300 rcf. The supernatant was discarded and the pellet was resuspended in 5-10 ml of growth medium. Cells were counted in a Neubauer chamber by pipetting 10 μl of freshly resuspended solution into each of the two counting chambers. In each of the four quadrants (delimited by triple lines) of each chamber, cells were counted if they were completely contained within the quadrant or in contact with the upper or left sides, but not if they were outside of the quadrant or in contact with the lower or right sides. The sum of the cell count numbers of both chambers was divided by eight quadrants and multiplied by 10,000 to obtain the concentration of cells per ml in the cell suspension.

For passaging, 500,000 cells were seeded in each fresh T75 flask. For experiments other than live imaging, cells were trypsinised at passages 3 to 4, counted, resuspended in the corresponding medium (Table 2.2.) with 0.1% v/v P/S, and seeded on substrates at a density of 3,000 cells/ cm^2 in non-treated 12-well plates (VWR, 34-0947). Non-treated plates were used to favour adhesion to the fabricated substrates rather than to the bottom of the wells. 3 replicates of each condition were seeded. Medium was replaced every 2-3 days.

Table 2.2 Differentiation media.

Lineage	Commercial name	Maker, reference	
Chondrocyte	Chondrocyte Differentiation Tool	ATCC, PCS-500-051	
Osteocyte	Osteocyte Differentiation Tool	ATCC, PCS-500-052	
	Component	Maker, reference	Concentration
Tenocyte ³	DMEM + Glucose + L-Glutamine	Gibco, 41965-039	Base medium
	Fetal Bovine Serum (FBS)	Gibco, 10270106	10% v/v
	Sodium pyruvate	Gibco, 11360-039	1 mM
	Growth Differentiation Factor 5 (GDF-5)	R&D Systems, 8340-G5-050	100 ng/ml

2.4. Live imaging

Prior to imaging, hMSCs at passage 3-4 were rinsed gently with PBS and incubated in growth medium with SiR-actin (Tebu-bio, SC001) at 200 nM for 4 h, or 750 nM for 1.5 h. The medium was removed and cells were then incubated in growth medium with Hoechst (Invitrogen, H3570) 1:1000 for 5 min. Cells were rinsed with PBS, trypsinised and seeded on the substrate at a density of 38200 cells/cm² in a glass-bottom microscopy dish (VWR, 734-2906H) in chondrogenesis-inducing medium. SiR-actin 100 nM was added in the medium to prevent loss of staining during imaging. The sample was immediately transferred to the microscope setting, pre-conditioned to 37°C and 5% CO₂. Live imaging was performed in a Nikon Eclipse Ti2-E inverted microscope with a Prime 95B sCMOS camera (Photometrics) and an Okolab Cage Incubator, with a 10X objective. Images were taken every 6 minutes for the phase contrast, blue and far red (Cy5) channels, for 40 hours. Samples were kept from ambient light during staining and imaging. Two independent samples were imaged and analysed for each condition.

2.5. Protrusion measurements

Filopodia were measured from phase contrast images at 8 h of live imaging. Images were scouted for any visible filopodia, which were manually measured along their longitudinal axis on Image J.

2.6. Single and collective cell segmentation and tracking

Live imaging stacks of Hoechst staining were analysed for cell movement. The first 17 frames (96 minutes) were removed to omit drifting prior to cell adhesion. Cell nuclei were tracked with the TrackMate plugin in ImageJ (version 2.0.0). Nuclei were segmented with the LoG Detector setting an estimated blob diameter of 15 μm and a threshold of 4 μm . No further filters were applied. The LAP Tracker was used with a maximum frame-to-frame linking distance of 50 μm and allowing gap closing to maximum 50 μm over 1 frame. For analysis, frame depth was not limited.

Analysis of collective cell migration in multicellular condensates was performed on the second half (20 to 40 hours) of live imaging Hoechst stacks as described above for single cells, except for the following parameters: Condensates were segmented with an estimated blob diameter of 70 μm and a threshold of 40 μm , and gap closing was allowed over 3 frames. All subsequent steps in track analysis were performed in the same way for single cells and condensates.

2.7. Trajectory graphs

Cell and condensate trajectories were graphed with GraphPad Prism 8.0.2. Twenty tracks were randomly selected and the trajectories were obtained from the Spots Statistics output in the TrackMate analysis. The coordinates of the first spot were subtracted from all spots in each track to reference the start to the origin (0,0) in a Cartesian system.

2.8. Track analysis

Tracks with a duration under 3 hours were excluded to avoid skewed results due to artificially short tracks. Track net displacement and duration were extracted from the Track Statistics output file of TrackMate. Sum trajectory was calculated with R Studio (version 4.0.2) from the Links Statistics output file by adding the displacements of all links in each track. Mean track velocity was calculated by dividing track trajectory (in μm) by track duration (in minutes).

To analyse track directionality, tortuosity was obtained as the division between the net displacement and the sum trajectory of each track. Turning angles were calculated from the Spots Statistics output of TrackMate: Vector components were found by subtracting particle coordinates at the start of each 6-minute link from those at the start of the next one (two consecutive spots) within each track. The angles between pairs of consecutive vectors were then found as (Eq. 2.1):

$$\alpha = \cos^{-1}\left(\frac{\mathbf{u} * \mathbf{v}}{\|\mathbf{u}\| * \|\mathbf{v}\|}\right)$$

Equation 2.1. Angle α between vectors u and v .

Angles with values equal to 0° or 180° were excluded to account for static cells. Angles were categorized into 15-degree sections according to their value, section percentages were calculated and plotted in polar histograms with the Plotly package in R Studio.

For single cell migration, the number of merge events (cell-cell collisions) per track was obtained by running a second TrackMate analysis with the settings as above but allowing track merging when nuclei collided at a distance under 30 μm . The number of merge events of each track was divided by its duration to obtain an hourly rate of cell-cell collisions.

2.9. Actin spread analysis

Actin was stained in live imaging experiments with SiR-actin as described above. A threshold was applied to select for actin staining area, with pixel intensity values from approximately 117 (manually adjusted according to staining intensity in each live imaging file) to 255. Actin area in each frame was automatically measured with the Analyze Particles tool in Image J, selecting for particles above 10 μm^2 .

The number of nuclei or condensates in each frame was measured from Hoechst staining. An automatic threshold was applied and particles from 3 to 3000 μm^2 were counted in each frame with the Analyze particles tool. Total actin area was then normalised to nuclei or condensate number in each frame to obtain the relative area of cell spreading over time. Actin spread was quantified in two independent samples for each condition and the average was calculated.

The mean value (from two independent samples) of actin spread per cell over time was fit into a linear model with R Studio, from 2 to 15 h of imaging.

2.10. Blocking of cell-substrate interactions with dendrimers in solution

For integrin blocking, RGD-Cys-D1 dendrimers were added to the medium to a final concentration of 4×10^{-9} % w/w. We selected this dendrimer concentration because it yields S_{18} substrates. During substrate functionalization, equilibrium is reached between dendrimer concentration in solution and adsorbed dendrimer density; hence, use of the concentration corresponding to the substrates with the lowest density prevents further adsorption mid-assay.

Additional dendrimers will then not adsorb on S_{90} substrates but rather attach to free integrin receptors, blocking their interactions with dendrimers on the surface.

For integrin blocking during live imaging (Chapter 3), dendrimers were included in the chondrogenic medium from the start of imaging. For integrin blocking at day 6 of chondrogenesis (Chapter 4), dendrimers were added with a medium change at day 5, 24 h prior to sample fixation.

2.11. Blocking cell-cell interactions through N-cadherin and gap junctions

To block N-cadherin or induce gap junction disassembly, we added ADH1 (Abmole, M5202) 300 μ M or 18 β GA (Sigma-Aldrich, G10105) 20 μ M, respectively, to the chondrogenic medium at the start of imaging. We selected these concentrations based on literature^{4,5} and after observing milder effects at lower concentrations (ADH1 200 μ M and 18 β GA 5-10 μ M) but substantial cell death at higher concentrations (ADH1 1000 μ M and 18 β GA 120 μ M).

2.12. Immunostaining

At the appropriate time point of differentiation induction, cells were carefully rinsed with PBS, fixed with Formalin Solution (Sigma, HT5011) for 20 min at room temperature, and rinsed again twice with PBS. Aldehyde groups were blocked with 50 mM ammonium chloride (Sigma, A9434) in PBS for 20 min. Samples were permeabilized with saponin (Sigma, 47036) 0.1% m/v in Blocking Solution (BSA (Sigma, A3059) 1% m/v in PBS) for 10 min.

Samples were stained with primary antibodies (Table 2.3) in Blocking Solution for 1 to 2 h at room temperature. For integrin β 1, samples were stained overnight at 4°C. Samples were washed with PBS and treated with fluorophore-conjugated secondary antibodies (according to the organism of the primary antibody): anti-rabbit Alexa 568 (LifeTech, A11036) and/or anti-mouse Alexa 488 (LifeTech, A10667) 1 μ g/mL in BSA 1% m/v in PBS for 1 h at room temperature, covered from light. For nuclei and actin observation, Hoechst 33342 (Invitrogen, H3570) 1:1000 and CytoPainter 488 (Abcam, ab176753) 1:1000 or Sir-actin (Tebu-bio, SC001) 1:3000 were included in the secondary antibody solution. Samples were washed with PBS and left to dry on air for 5-10 min, then placed on a Corning® 7.5 x 2.5 cm microscopy slide. One drop (50 μ l) of Fluoromount mounting medium (Sigma, HT5011) was added, and a Corning® 1.8 x 1.8 cm coverslip (Sigma-Aldrich, 2845-18) was placed on the sample avoiding the formation of bubbles. Mounted samples were stored at 4°C covered from light. At least 16 h were left to elapse before sample imaging.

Table 2.3. Primary antibodies

Type	Target protein	Reference	Organism	µg/ml
Focal adhesions	Integrin subunit β 1	ab30394	Mouse	8
	Paxillin (PXN)	ab32084	Rabbit	5
		ab23510	Mouse	5
Focal adhesions, adherens junctions	Vinculin (VCL)	ab130007	Mouse	5
Gap junctions	Connexin 43 (Cx43)	ab63851	Rabbit	5
Mechanotransduction	Yes-Associated Protein (YAP)	sc-101199	Mouse	0.5
Tenogenesis marker	Scleraxis (SCX)	ab58655	Rabbit	5
	Tenomodulin (TNMD)	ab203676	Rabbit	5
Extracellular matrix	Collagen-I (COL-I)	ab90395	Mouse	2.5
Osteogenesis marker	Osterix (OSX)	ab22552	Rabbit	2.5
	Alkaline phosphatase (ALP)	ab126820	Mouse	5

2.13. Analysis of integrin clustering

Cells were seeded on three S_{90} replicates as described above, either in unaltered chondrogenic medium (control samples) or with added RGD dendrimers at 4×10^{-9} %. After 40 hours in culture, samples were fixed and stained as described above with anti-integrin β 1 antibody (Table 2.3) overnight at 4°C. Samples were imaged in a Leica SPE Upright Confocal Microscope (Leica Microsystems) with a 63X objective. The distance between imaged slices (z-size) was set to 0.7 μ m.

Images were analysed with ImageJ software. For integrin cluster size, a Z-projection of maximum intensity slides was created and a threshold was applied to select for staining areas (pixel intensity values 110 to 255). The staining threshold was processed with the Analyze Particles feature in ImageJ, selecting for particles of 0.1 to 5 μ m². For the histograms of integrin clustering, large areas of staining in non-processed images were selected and analysed. Histogram lists for each sample were converted to percentage values and the mean percentage value was calculated for each intensity value from 0 to 255.

2.14. Cell viability in condensates

Cells were cultured on nanopatterned or fibronectin-coated substrates as described. A commercial viability/cytotoxicity cell labelling kit was used for the assay (ThermoFisher, L3224). At day 7 of chondrogenesis, samples were washed twice with PBS and stained with calcein AM and ethidium homodimer-1 at 4 μ M in non-serum containing medium for 40 min at 37°C and 5% CO₂. Samples were washed twice with PBS, mounted on microscopy slides, and immediately imaged in a Leica SPE Upright Confocal Microscope with a 40X objective. Z-projections of cell condensates were produced with Fiji software.

To test the cell viability after a freeze-thaw cycle, condensates at day 6 of chondrogenesis on S₉₀ substrates were carefully washed with PBS and removed from the substrates by rinsing with freezing medium (differentiation medium with 10% dimethyl sulfoxide (DMSO)), to avoid a centrifugation step. Condensates were directly transferred to freezing vials, left at -80°C in a container with isopropanol for 24 h and then transferred to a liquid nitrogen tank for storage. Three days later, one vial was thawed, centrifuged 5 min at 200 rcf, resuspended in chondrogenic medium and seeded on S₉₀. A cell viability assay was performed after another two days.

2.15. Analysis of internuclear distance

Samples were seeded in chondrogenic medium and stained with Hoechst as described. They were imaged in a Leica SPE or a LSM780 Confocal Microscope with a 40X or 63X objective. Slides in the central region of condensates were selected for analysis and the straight-line horizontal distances between the centres of adjacent cells were measured. Condensates from at least 3 substrates were analysed for each experimental condition.

2.16. Western blot assay

At day 6 of chondrogenesis, samples were rinsed with PBS and cells were lysed for 45 min on ice with RIPA buffer: 150 mM NaCl, 5 mM EDTA, 50 mM Tris-HCl (Tris base adjusted to pH=7.4), 1% m/v Triton X-100, 0.1% m/v SDS in MQ water, and 1 pill of EDTA-free Protease Inhibitor Cocktail (Roche, 4693159001) added just before use. Cell lysate solutions were transferred to Eppendorf tubes and centrifuged at 16100 g for 10 min at 4°C. The pellet was discarded and the supernatant was transferred to a new tube and stored short-term at -20°C. Total protein concentration was quantified with a Pierce TM BCA Protein Assay Kit (Thermo Fisher Scientific, 23227) in a Benchmark Plus Microplate Reader (Bio-Rad).

Chapter 2

Sample protein (5 μg , volume calculated according to each sample's total protein concentration) was mixed with 6.67 μl of loading buffer: 6% m/v SDS, 15% m/v 2-mercaptoethanol, 30% v/v glycerol, 0.006% m/v Bromophenol blue, 0.125M Tris-HCl in MQ water. The volume was adjusted to 20 μl with MQ water and samples were briefly vortexed and spun. Samples were heated to 96°C for 10 min and loaded in each well of an SDS-PAGE gel (Mini-Protean TGX Precast Gel 12%, Bio-Rad, 456-1045) along with a protein weight ladder. Protein electrophoresis was performed in a vertical cell (Mini-Protean System, Bio-Rad) filled with running buffer: 25 mM Tris base, 250 mM glycine, 0.8% m/v SDS in MQ water. Voltage was set at 50 V until samples transitioned from the stacking to the running section of the gel, then at 60 V for 1.5-2 h.

The resulting gel was transferred to a PVDF membrane (Amersham Hybond, 10600023). Membranes were first activated with methanol for 1 min, then washed with transfer buffer: 25 mM Tris base, 250 mM glycine, 20% methanol in MQ water. The gel and membrane were mounted adding transfer buffer between layers and keeping them always wet. They were placed in the vertical cell filled with transfer buffer at 4°C and a freezer-cold block, and transferred for 2 h at 60 V in a cold room at 4°C.

After the transfer, the membrane was reactivated with methanol for 30 s, washed with MQ water and stained with Ponceau solution: 0.1% m/v Ponceau S, 1% v/v acetic acid in MQ water, to observe total transferred protein. The membrane was imaged to quantify total protein amount in each lane. Gels and membranes were always manipulated with tweezers around the edges, to avoid damaging the protein samples.

For immunostaining, the membrane was washed twice with Tris Buffer Saline (TBS: 0.1 M Tris-HCl, 1% m/v NaCl in MQ water) and twice with TBS-T (TBS with 1% Tween 20), 5 min with light shaking per wash, then blocked with 5% m/v dry milk in TBS-T for 1 h. The membrane was sealed in a plastic folder and probed overnight shaking lightly at 4°C with 1:300 (3.3 $\mu\text{g}/\text{ml}$) mouse anti-VCL (Abcam, ab18058) primary antibody in 3% BSA in TBS-T. The membrane was washed three times (10 minutes with light shaking per wash) with TBS-T and incubated with IgG HRP-linked secondary antibody anti-mouse (Cell Signaling, 7076) in 3% BSA in TBST for 1 h at room temperature. The immunoblot was developed using Clarity ECL Western substrate (Bio-Rad, 1705060). Bands were visualized in an ImageQuant LAS 4000 imager (GE Healthcare).

The integrated density of bands was measured with Fiji. Background signal was measured in empty areas of the blot and subtracted from the corresponding values. Protein production in each lane was normalized to the integrated density of total protein staining.

2.17. RNA extraction and retrotranscription

Reverse transcription real-time PCR (RT-qPCR) was performed to measure *CDH2*, *VCL* and *GJA1* expression. All working surfaces and tools were treated with RNase Zap decontamination solution (Thermo Fisher Scientific, AM9780) prior to any steps involving RNA. After 6 and 9 days of differentiation, mRNA was extracted from the samples and purified with an RNeasy Micro Kit (Qiagen, 74004). Three cell culture replicates of each condition were obtained, with their RNA extracted and retrotranscribed. Extracted mRNA of each replicate was quantified in a Nanodrop ND-1000 Spectrophotometer (Thermo Fisher Scientific). The same amount of mRNA (75 ng) was retrotranscribed for each sample. Reverse transcription for cDNA production was performed with an iScript Advanced cDNA Synthesis Kit (Bio-Rad, 1725037) in a T100 Thermal Cycler (Bio-Rad). The resulting cDNA samples were diluted by adding 10 μ l of water. The same procedure was performed on undifferentiated human mesenchymal stem cells (hMSCs) as a reference.

2.18. qPCR and data analysis

qPCR was performed with the Sso Advanced Universal SYBR Green Supermix kit (Bio-Rad, 1725271) in an Applied Biosystems StepOnePlus Real-Time PCR Machine (Thermo Fisher Scientific). Commercial primer pairs were used for *CDH2* (Bio-Rad, qHsaCID0015189), *VCL* (Bio-Rad, qHsaCID0020885), *GJA1* (Bio-Rad, qHsaCID0012977) and *SOX9* (Bio-Rad, qHsaCED0044083), as well as *B2M* (Bio-Rad, qHsaCID0015347) and *RPL24* (Bio-Rad, qHsaCID0038677) as housekeeping genes. To prevent amplification of non-transcribed genomic DNA (gDNA), intron-spanning primer pairs were selected and a DNase digestion step was included during RNA extraction.

All qPCRs were performed on the same amount of cDNA per sample (2.5 ng). The amplification program consisted of an initial activation step of 30 s at 95°C, followed by 50 cycles of 10 s at 95°C for denaturation and 1 min at 60°C for annealing and extension, and a final denaturation step of 15 s at 95°C. Melt curves were performed from 65°C to 95°C in steps of 0.5°C. Technical duplicates of each sample were performed in the qPCR.

qPCR data were analysed with qBase+ software version 3.1 (Biogazelle, Zwijnaarde, Belgium). The expression of each gene was calculated by the $2^{-\Delta\Delta C_t}$ method, normalized to that of

undifferentiated hMSCs or to S_0 samples (assigned value 1) and presented as relative mRNA expression levels.

2.19. Analysis of condensate area and Cx43 GJIC

Three replicates of each condition were fixed at the appropriate time points as specified in the results section (Chapter 3), immunostained for Cx43 as described above and imaged with a Leica SPE Upright Confocal Microscope (Leica Microsystems) with a 40x/1.15 NA objective. The distance between imaged slices (z-size) was set at 1 μm . At least 3 cell condensates were imaged for each sample.

Images were analysed with ImageJ software. For condensate size measurements, a z-projection of each condensate was created, and the whole condensate area was manually selected and measured. For the measurement of Cx43 production, confocal z-projections were used (maximum stained area per sample). The background of z-projections was removed, and a threshold was applied to select areas of Cx43 staining. The obtained total area was normalised against the area of the corresponding condensate.

For the analysis of Cx43 network connectivity, a threshold was applied to the Cx43 confocal stack and then it was skeletonized with the Skeletonize ImageJ plugin. The resulting Cx43 network was analysed with the Analyze Skeleton plugin to retrieve the number of end-point voxels and the mean branch length in each condensate, which were normalised to the Cx43 expression area and the number of slices taken for analysis. Cx43 connectivity was calculated as the inverse value of the end-point voxels (Fig. 2.2).

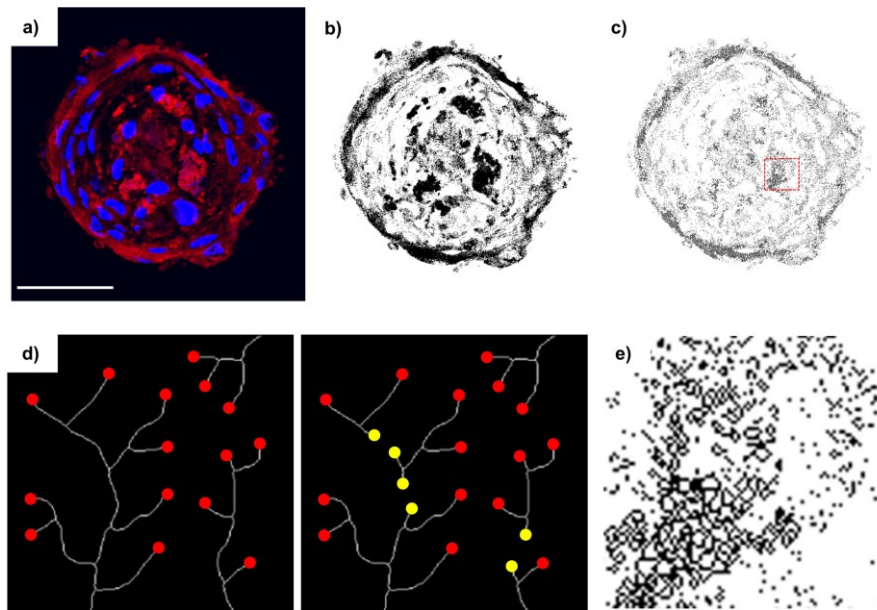


Figure 2.2. Analysis of Cx43 intercellular communication network architecture. **a)** Representative chondrogenic cell condensate stained for Cx43 (red) and cell nuclei (blue). Scale bar = 50 μm . **b)** Threshold selecting Cx43 expression. **c)** Skeletonizing of the Cx43 network, from which end-point voxels and mean branch length were quantified. **d)** Schematic of network connectivity quantification as the inverse of end-point voxels number. White lines represent theoretical networks. Red dots indicate end-point voxels, yellow dots indicate new end-point voxels as a results of network splitting. The network on the left is more extensively connected than that on the right, and thus contains fewer end-point voxels. **e)** Zoomed-in section from the red square in **c**.

2.20. Neurobiotin assay

A tracer assay was performed to analyse the functionality of GJIC networks. Four replicates of each condition were seeded in chondrogenesis-inducing medium, as described above. After 6 days of differentiation, samples were washed with HBSS buffer without calcium or magnesium (Life Technologies, 14175095) and treated with neurobiotin 2% m/v (Vector, SP-1120) in HBSS for 90 s at 37°C. Samples were then washed with HBSS, fixed with Formalin Solution, permeabilised with saponin and stained with Streptavidin-Texas Red conjugate (Life Technologies, S872) and Hoechst in BSA 1% m/v in PBS for 1 h at room temperature.

Samples were imaged with a Leica SPE Upright Confocal Microscope with a 40X objective. Images were analysed with ImageJ software. A z-projection of each condensate was created, selecting slices only in the central region of condensates, excluding basal and apical slices. The background was removed. Distance of neurobiotin spread was measured in a straight line from the outer rim of the condensates inwards, in at least two separate locations for each condensate.

2.21. Condensate transplantation

A transplantation assay was performed to study the effects of RGD nanopatterned substrates on formed condensates and the propagation of the adhesive information from the substrate into cell condensates. Nanopatterns with 18% (S_{18}) and 90% (S_{90}) of local surface adhesiveness were used. Cells were cultured on the nanopatterns in chondrogenesis-inducing medium as described above. After 3 days, cell condensates formed on the nanopatterns of S_{90} were removed by pipetting and transferred to new S_{90} or S_{18} substrates. Transplanted condensates were cultured on the new substrates for another 3 days, to a total of 6 days of differentiation. Six substrates were seeded for each S_{18} and S_{90} , and condensates from three substrates of each origin were transplanted to three fresh S_{18} or S_{90} substrates. For each original sample, around half of the condensates were transplanted, whereas the other half were kept on the original substrate (not transplanted) as a control of unaltered differentiation.

All samples were fixed at day 6, immunostained, imaged and analysed for Cx43 as described above. Cx43 staining of each transplanted substrate was calculated relative to its non-transplanted substrate of origin. Results were normalised to control S_{90} condensates (assigned value 1) and presented as relative values.

To visualise condensates from the side, Z-stacks were resliced and one image from the centre of the condensate was selected.

2.22. Myosin inhibition

Three replicates of each condition were seeded in chondrogenesis-inducing medium as described above. Medium was changed to fresh medium with 50 $\mu\text{g}/\text{mL}$ blebbistatin (Sigma, B0560) 6 h before fixation. Samples were fixed at day 6 of chondrogenesis, immunostained with anti-Cx43 antibody, Hoechst for nuclei and Sir-actin for the cytoskeleton, and imaged with a Zeiss LSM780 Confocal Microscope (Zeiss Microscopy) with a 40X objective. Cx43 in condensates was quantified as described above and normalised to corresponding non-treated samples.

2.23. Analysis of focal adhesions and nuclear shape

Three replicates of each condition were seeded in chondrogenesis-, tenogenesis- or osteogenesis-inducing medium. Samples were fixed at 24 h of culture and immunostained for paxillin as described above, with Hoechst and CytoPainter 488. Samples under chondrogenic induction were imaged with a Leica SPE Upright Confocal Microscope (for mesenchymal

condensates) or a Nikon E1000 microscope (for S_{FN} samples) with a 40X objective. Samples under tenogenic or osteogenic induction were imaged with a Nikon E600 upright manual microscope with a 40X objective and an Olympus DP72 colour digital camera. At least three representative images were taken of each sample.

Images were analysed with Fiji. Each fluorescence image was converted to an 8-bit file, the background was removed, and the resulting image was converted to binary by setting a threshold. Analysis was conducted with the Analyze Particles plugin. In the case of confocal stacks, analysis was conducted at the slice closest to the substrate (basal region of the condensate). A lower limit of $1 \mu\text{m}^2$ was set both for FAs area and nuclei quantification. For FAs area quantification, also an upper limit of $30 \mu\text{m}^2$ was applied (Fig. 2.3).

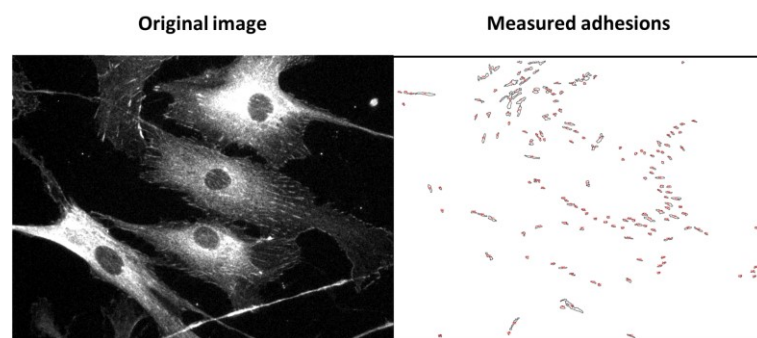


Figure 2.3. Analysis of focal adhesions. Paxillin-immunostained images were treated and adhesions between 1 to $30 \mu\text{m}^2$ were selected to measure their area.

The nuclear shape index (NSI) was calculated as previously described⁶ (Eq. 2.2), with the Circularity measurement in Fiji.

$$\text{NSI} = \frac{4\pi * \text{Nuclear area}}{\text{Nuclear perimeter}^2}$$

Equation 2.2 Nuclear shape index

2.24. Analysis of YAP nuclear translocation

Three replicates of each condition were seeded in chondrogenesis-inducing medium as described above. Samples were fixed after 6 hours and 3 days culture, immunostained for YAP and imaged with a Zeiss LSM780 Confocal Microscope with a 63X objective. YAP nuclear translocation ratios were quantified in Fiji by measuring the average staining intensity in two areas of the same size, inside and just beside the nucleus of each cell.

2.25. Analysis of differentiation to tendon and bone

Three replicates of each condition were seeded in tenogenesis- or osteogenesis-inducing medium. Samples were fixed at the corresponding time of culture as stated in the Results section, and immunostained for the corresponding differentiation markers (Table 2.3). Samples were imaged with a Nikon E600 upright manual microscope with a 40X objective and an Olympus DP72 colour digital camera. At least three representative images were taken of each sample.

Images were analysed with Fiji. Each image was converted to an 8-bit file, background was removed, brightness–contrast was adjusted, and a threshold was applied to select the areas of marker expression (Fig. 2.4). These areas were quantified as the percentage of area relative to the image, and normalised by the number of visible cell nuclei.

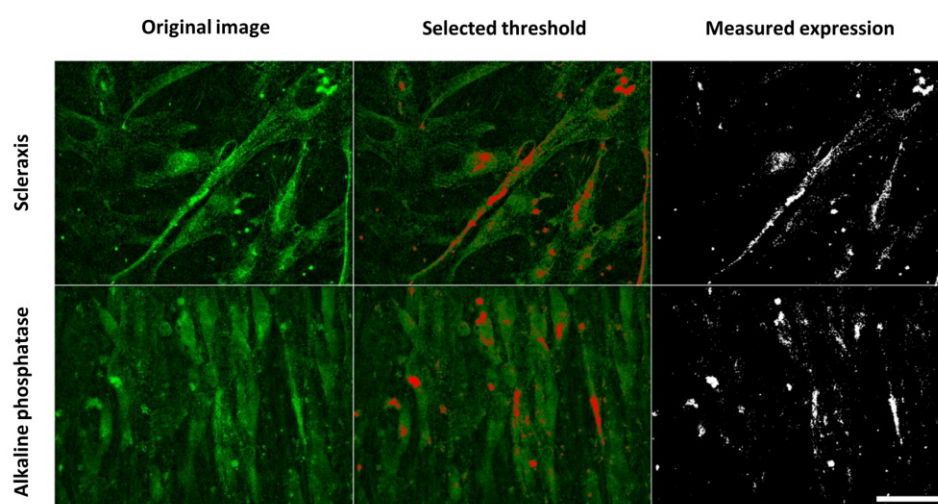


Figure 2.4. Analysis of differentiation markers for tenogenesis and osteogenesis. Immunostaining images of differentiation markers were treated, the corresponding area of expression was selected and measured. Scale bar = 50 μm .

2.26. Statistics

Graphs were generated in GraphPadPrism 8.3. Quantitative data are displayed, showing average and standard deviation (SD) or standard error of the mean (SEM) as indicated. n is the sample size. Data was subjected to a Kolmogorov-Smirnov normality test. For data following a normal distribution, significant differences were judged using the One-way ANOVA with Fisher LSD post-hoc test, or T-test when only two groups were compared. Where data did not pass a normality test, a Kruskal-Wallis test with Dunn means comparison was applied. Statistics were performed with OriginPro 8.5 and GraphPadPrism 8.3.

2.27. References

1. Lagunas, A. *et al.* Tailoring RGD local surface density at the nanoscale toward adult stem cell chondrogenic commitment. *Nano Res.* **10**, 1959–1971 (2017).
2. Casanellas, I. *et al.* Dendrimer-based uneven nanopatterns to locally control surface adhesiveness: A method to direct chondrogenic differentiation. *J. Vis. Exp.* **131**, e56347 (2018).
3. Park, A. *et al.* Adipose-Derived Mesenchymal Stem Cells Treated with Growth Differentiation Factor-5 Express Tendon-Specific Markers. *Tissue Eng. Part A* **16**, 2941–2951 (2010).
4. Guan, X., Wilson, S., Schlender, K. K. & Ruch, R. J. Gap-junction disassembly and connexin 43 dephosphorylation induced by 18 β -glycyrrhetic acid. *Mol. Carcinog.* **16**, 157–164 (1996).
5. Li, H., Price, D. K. & Figg, W. D. ADH1, an N-cadherin inhibitor, evaluated in preclinical models of angiogenesis and androgen-independent prostate cancer. *Anticancer. Drugs* **18**, 563–568 (2007).
6. Versaevel, M., Grevesse, T. & Gabriele, S. Spatial coordination between cell and nuclear shape within micropatterned endothelial cells. *Nat. Commun.* **3**, 671 (2012).

Chapter 3

Dynamics of stem cell migration and condensation

3.1. Introduction

Single and collective cell migration are an essential part of biological processes such as development, wound healing and disease progression^{1,2}. Through single migration, cells *in vivo* are able to traverse different regions of the body with little disruption, as is the case of immune cells, or position themselves in the two- and three-dimensional locations required at the onset of tissue formation³. In collective migration, variable numbers of cells –from just a few up to the hundreds of thousands– move in a synchronized manner as a cluster, sheet or stream^{3–5}. This mode of migration is therefore particularly relevant in the formation of tissue-level structures, be it for development or regeneration, and wound closure⁶. It is also an important mechanism of cancer invasion and metastasis^{7–9}. Importantly, cells in collective migration behave as a coordinated unit, rather than as multiple single cells undergoing similar processes in parallel¹⁰. For instance, cells can exercise different roles depending on their location within the group: selected cells at the front edge of mesenchymal migration, known as leader cells^{11,12}, sense the environment through protrusions and chemotactic signals. Follower cells maintain close contacts with their neighbours and move in the direction and velocity established by leaders, while executing other functions such as matrix remodelling^{3,5}. Multicellular groups of collective migration exhibit coordinated morphology and polarization, driven by supracellular organization of the actin cytoskeleton and mechanical coupling⁶. Notably, another mode of collective migration can also occur without stable cell-cell junctions, if cells coordinate through transient contacts or by chemotaxis through soluble factors^{1,13}.

In vivo studies on collective migration provide key observations on cell behaviour during development but do not allow for precise control of the environmental conditions that cells experience^{14–17}. On the other hand, *in vitro* systems provide a platform to simplify and modulate these conditions, as well as facilitating direct measurements on the sample; however, previous works on collective cell migration *in vitro* generally verse on sheets of cancer or epithelial cell lines^{8,10,12,18,19} rather than stem cell dynamics during tissue formation. In this chapter we live-image migration in a model of early development, starting with single undifferentiated mesenchymal stem cells and progressing towards the formation of multicellular aggregates, or condensates.

Mesenchymal condensation is a crucial step in early cartilage formation, in which mesenchymal stem cells (MSCs) gather together into tight multicellular structures²⁰ (see Chapter 1, section 1.5). Cell density increases locally at the condensation sites by means of extracellular

matrix (ECM)-driven active cell movement²⁰, with an important role of the ECM ubiquitous protein fibronectin (FN), which is upregulated in mesenchymal condensation^{21,22}. This process is therefore dependent on the capacity of cells to migrate towards condensation centres and establish the initial cell-cell contacts. Cell condensates then progressively evolve into cartilaginous nodules, setting the architectural foundations for tissue development.

Cell migration is affected by extracellular environmental cues such as substrate stiffness, viscoelasticity, adhesiveness or topography^{23–29}. Cell-substrate interactions are driven largely by integrin receptors at the plasma membrane (see Chapter 1); integrin-mediated adherence with extracellular RGD ligands is a paramount factor modulating cell migration^{30–32}.

Cells make use of diverse mechanisms to migrate on a substrate or through matrix. When cultured on adherent substrates, mesenchymal cells continually extend actin-rich membrane protrusions to probe their surroundings and interact with other cells^{33,34}. Protrusions can be categorized into filopodia, finger-like long and narrow extensions; and lamellipodia, thin sheet-like structures that cover large surfaces^{35,36}. In the mesenchymal mode of migration, cells produce lamellipodia at the front edge of movement, containing cell-substrate adhesions that serve as traction points. Actin flows back from front-edge protrusions towards the cell centre and the generated tensions reach the cell body, which contracts to propel forward as the rear edge detaches and retracts^{27,35,37–39}. A second mode of migration, known as amoeboid, entails cells producing filopodia rather than lamellipodia, while largely retaining a round morphology and producing weak transient adhesions with the substrate, instead of focal adhesions (Fig. 3.1). The mesenchymal and amoeboid modes of migration each include a range of sub-modes^{40,41}. Cells can quickly switch between mesenchymal and amoeboid migration as a response to environmental and signalling cues^{42–44}.

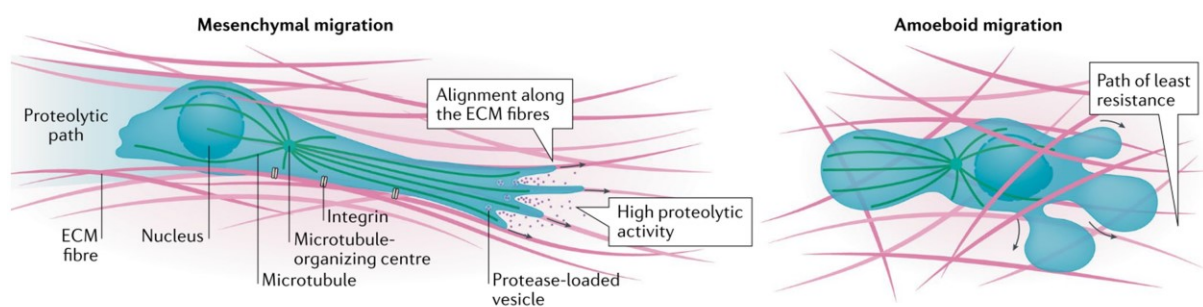


Figure 3.1. The mesenchymal and amoeboid modes of cell migration. Adapted with permission from Yamada and Sixt (2019)⁴⁴

During early development, as cells differentiate into lineages and secrete ECM components, they position themselves in relation to other cells to form the structural bases of tissues. They navigate this process by physical membrane-membrane contacts (juxtacrine communication) and by sensing morphogen concentration gradients secreted by other cells (paracrine communication)⁴⁵. The main forms of juxtacrine communication include adherens junctions and gap junctions. The former are mechanical adhesions mediated by cadherin proteins (in the case of mesenchymal cells, N-cadherin)⁴⁶. They are particularly important in collective dynamics, as they allow cells to coordinate their shape, speed and direction by coupling tensions driven through the cytoskeleton^{15,47-50}. Gap junctional transmembrane channels mediate molecule exchange between coupled cells (juxtacrine communication)⁵¹ and also improve the mechanical stability of the cell-cell junction⁵². Non-apposed hemichannels allow the release of chemotactic signals outside the cell (paracrine communication)^{53,54}, thus also contributing to multicellular coordination during migration^{55,56}.

The concept of nematicity is traditionally applied in materials science to liquid crystals, to describe a system where multiple elongated molecules adopt a parallel disposition (orientational order), although their spatial locations are not organized (Fig. 3.2a). Nematic systems can contain topological defects, where the supramolecular orientation is locally disturbed⁵⁷. As a dense population of particles outside of thermodynamic equilibrium, confluent monolayers or systems of cells can be described as an active nematic, with cells retaining an orientational order while they migrate⁵⁸⁻⁶¹. In active nematic systems, topological defects can spontaneously emerge as supracellular structures; defects are assigned a topological charge according to their organization features. Round, 360-degree polar defects carry an integer charge of +1 or -1, whereas partial defects weight +1/2 or -1/2. The plus and minus signs indicate whether cells present a net flow towards or outwards of the defect⁶² (Fig. 3.2a). Active nematics can thus be applied to describe collective cell motion. Our own fingertips present a paradigmatic example of topological defects, as they contain easily observable +1, +1/2 and -1/2 defects that confer each finger with its unique pattern⁶³. In morphogenesis, topological defects provide a base for the formation of structures from nematic multicellular pools⁶⁴ (Fig. 3.2b).

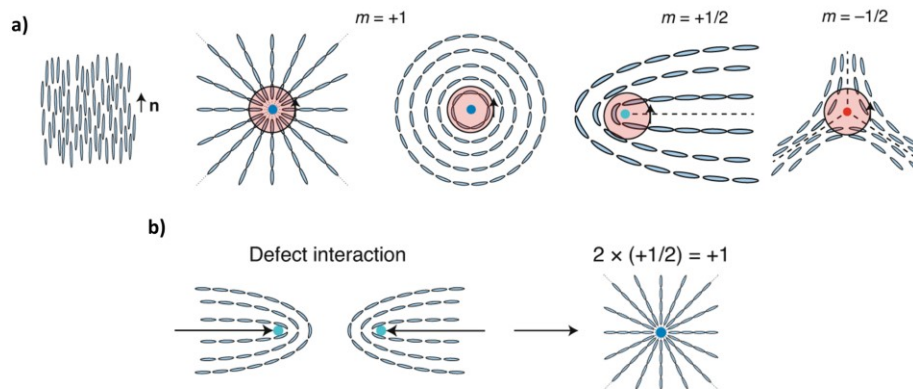


Figure 3.2. Topological defects in nematic systems. a) Orientation and director field, n , of a nematic liquid crystal. Typical director fields near the topological defects in a two-dimensional nematic liquid crystal can be classified according to the value of the integral of the director field along an imaginary loop enclosing the defect: $m = +1$, $m = +1/2$ and $m = -1/2$. **b)** Interaction between two $+1/2$ defects leading to the formation of a $+1$ defect. Adapted with permission from Fardin and Ladoux (2021)⁶³.

In this chapter we employ RGD dendrimer nanopatterns (see Chapter 1, section 1.4) to study the influence of local ligand density on single and collective MSC migration and condensation dynamics at the onset of chondrogenesis. Throughout this process, cells migrate while extending and retracting membrane protrusions to probe both the substrate and other cells. We observe mesenchymal and amoeboid migration, depending on whether cells are cultured on RGD-nanopatterned or fibronectin-coated substrates. The latter also support faster spreading, cell division and the establishment of a supracellular nematic order with half-integer defects. We find that nanopatterns of intermediate ligand density lead to faster movement and more cell-cell collisions, whereas high homogenous adherence impedes it by making cells slower and highly directional. Collective migration as multicellular condensates similarly depends on ligand density. We pharmacologically block cell-cell interactions mediated by cadherin and gap junctions, to investigate their role in the regulation of single and collective cell migration. We pose that nanopatterns of high ligand density represent an intersection between nanoscale local adherence and full protein coatings. Finally, we propose a model for the regulation of cell migration and condensation through an interplay of Contact Inhibition and Contact Following of Locomotion. Whenever two cells come into contact, they can either form stable cell-cell unions, leading to further condensation, or detach to resume single migration.

3.2. Results

Human adipose-derived MSCs were seeded on non-patterned substrates (S_0), nanopatterned substrates with increasing ligand densities (S_{18} , S_{45} and S_{90}) and fibronectin-coated substrates (S_{FN}) in chondrogenic culture medium. Samples were imaged for 40 hours.

3.2.1. Cell morphology

Cells started migrating immediately after seeding; live nuclei and actin staining were specific and stable over the time frame of imaging. Cell density at the start of imaging increased progressively with substrate adherence, with the highest density of initial cells on S_{FN} , although differences were not statistically significant (Fig. 3.3a).

Cell morphology is tightly linked to migration and is regulated by cell-substrate adherence⁶⁵. We characterised cell morphology in response to nanoscale surface ligand density. Since live imaging started soon after cell seeding on the substrates, most cells presented a round morphology and small size at the beginning. Cell spreading is governed by actin as weak adhesions form at the cell periphery prior to the establishment of mature, force-conducting adhesions⁶⁶. We thus quantified cell spreading from live actin staining over time. Within the first two hours of imaging, cells on S_{FN} substrates spread and triplicated their mean projected area, whereas cells on S_0 and nanopatterned substrates retained a similar size (Fig. 3.3b).

Differences in cell spreading conditioned the motility mode, with cells on S_0 and nanopatterned substrates presenting mostly round morphologies with expansion and contraction cycles and filopodia, indicative of amoeboid migration, whereas cells on S_{FN} displayed elongated spindle-like morphologies with lamellipodia, typical of mesenchymal migration (Fig. 3.3c).

Live staining also allowed for observation of actin dynamics. On S_0 and nanopatterned substrates these were governed by pulses of cortical actin, whereas on S_{FN} cells developed clearly defined actin fibres with rearward actin flows (Fig. 3.3d, Videos 3.1-3.5).

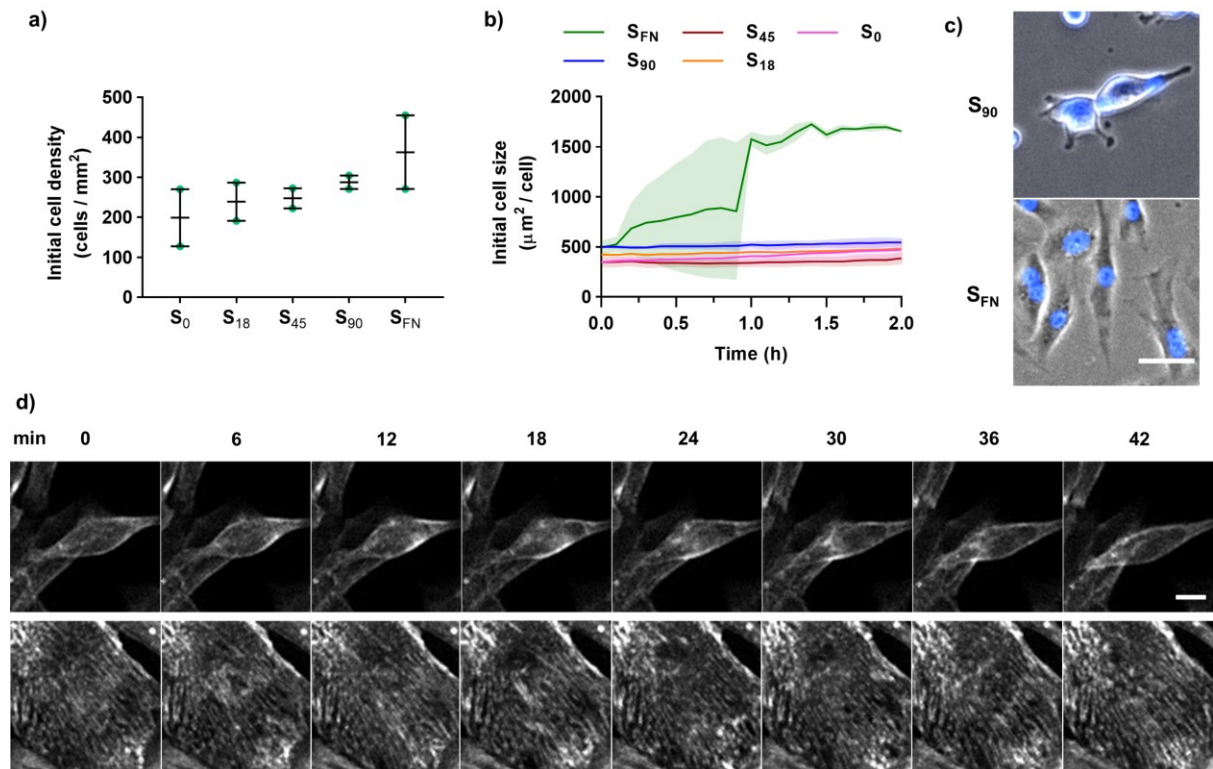


Figure 3.3. Initial cell morphology. **a)** Number of cell nuclei per area unit segmented for tracking at 96 min of imaging in each analysed substrate. Data points with the mean \pm SEM. **b)** Projected area of actin staining per cell during the first 2 h of imaging. Mean (solid line) \pm SEM (colour area) ($n = 2$). **c)** Representative phase contrast images of cells with stained nuclei (blue) on S₉₀ and S_{FN}, showing the distinct morphologies. Scale bar = 50 μ m. **d)** Time lapse sequences of a cortical actin pulse on S₉₀ (top) and flow of actin fibres on S_{FN} (bottom) over 42 minutes. Scale bar = 20 μ m.

To investigate how substrate conditions affect protrusion formation, we measured the length of filopodia at 8 hours of imaging (Fig. 3.4a). We found that cells on S_0 , S_{18} and S_{45} all had filopodia shorter than $8\ \mu\text{m}$ on average, whereas those on S_{90} presented filopodia of double the length at $16\ \mu\text{m}$. It should be noted that cells sometimes retained a fully round morphology for several hours before developing visible protrusions towards the end of the experiment; in other cases, protrusions retracted mid-imaging and did not reappear. Cells on S_{FN} presented filopodia-like structures, mainly as extensions of the protruding leading edge, with a size similar to that of S_{90} filopodia ($18\ \mu\text{m}$) (Fig. 3.4b).

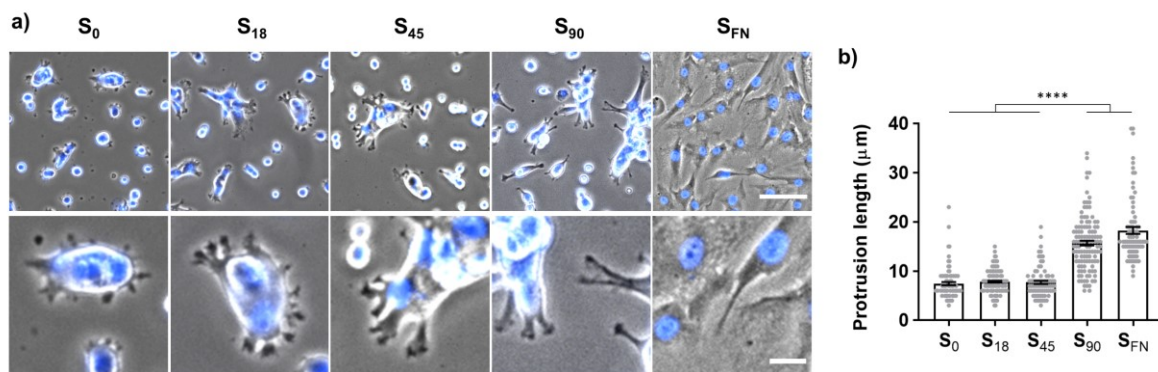


Figure 3.4. Protrusion size. **a)** Phase contrast images of cells stained for nuclei (blue) at 8 h of live imaging (top, scale bar = $100\ \mu\text{m}$) and zoomed-in sections displaying filopodia (bottom, scale bar = $25\ \mu\text{m}$). **b)** Length of protrusions at 8 h. All data points with the mean \pm SEM; **** $p < 0.0001$

3.2.2. Single cell migration

As cells attached and spread on the substrates, they started migrating. Cells on S_0 , S_{18} and S_{45} migrated either as single cells or in clusters, whereas cells on S_{90} aggregated but also spread at certain sections of the substrate, forming a local monolayer alongside three-dimensional clusters. Conversely, cells on S_{FN} quickly developed a compact monolayer from which no clusters appeared within the 40 hours of imaging (Fig. 3.5a,b, Videos 3.6-3.10). Moreover, S_{FN} was the only substrate on which cell proliferation was observed (Fig. 3.5c).

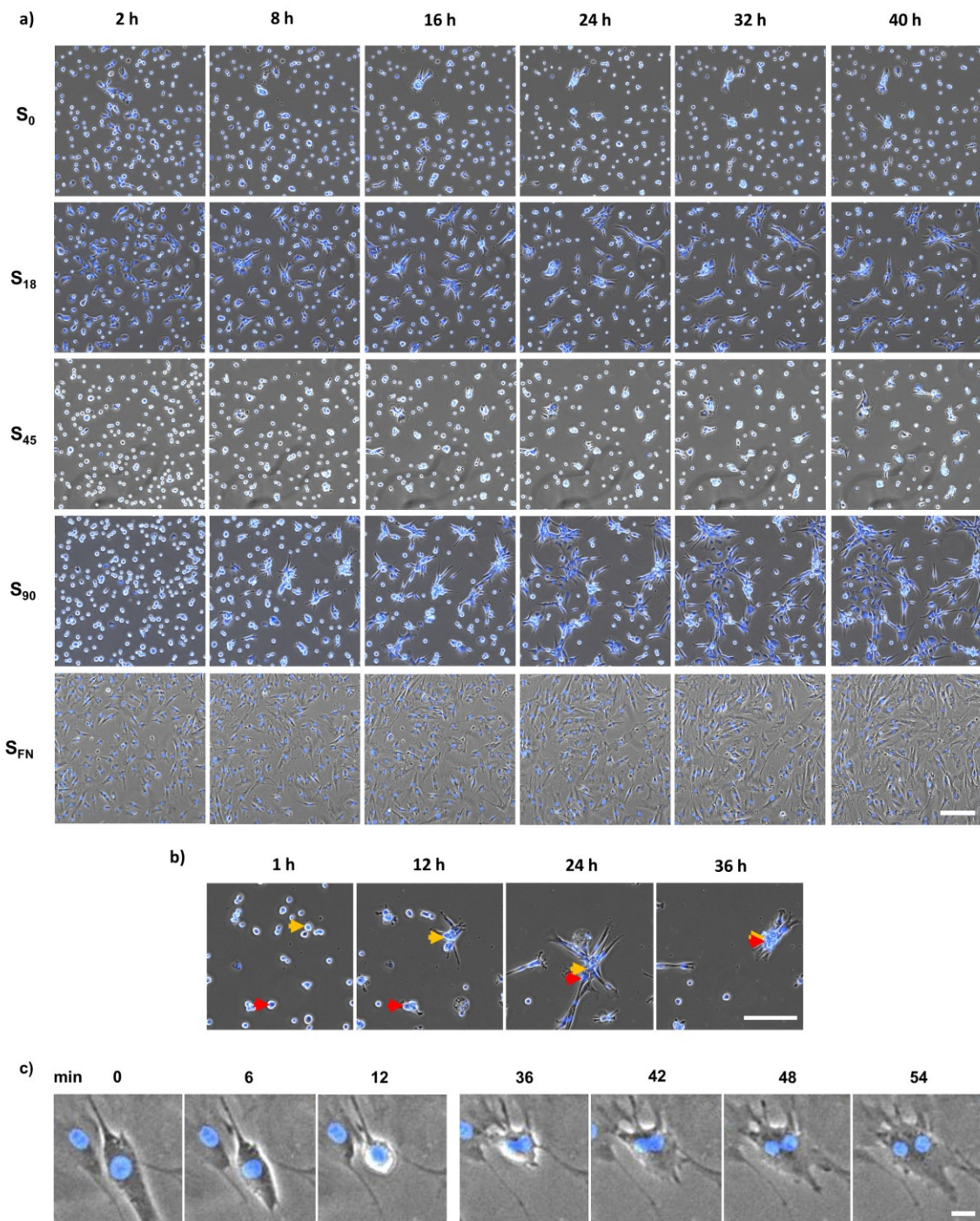


Figure 3.5. Live imaging of cell migration and condensation. a) Time lapse phase contrast images superimposed with fluorescence live images of cell nuclei (Hoechst, blue). Scale bar = 200 μm . **b)** Example sequence of cell condensation. The same two cells are marked with a red and a yellow arrow in each frame. Scale bar = 200 μm . **c)** Example sequence of cell division over 54 minutes on S_{FN} . Scale bar = 20 μm .

Cell nuclei were segmented as single objects (Fig. 3.6a) and tracked. For an initial evaluation of cell migration, random tracks were selected from each condition and graphed, setting the start of each track at the origin of Cartesian coordinates (0,0). Tracks were generally isotropic on S_0 and nanopatterned substrates, whereas on S_{FN} most tracks presented a directional component (Fig. 3.6b).

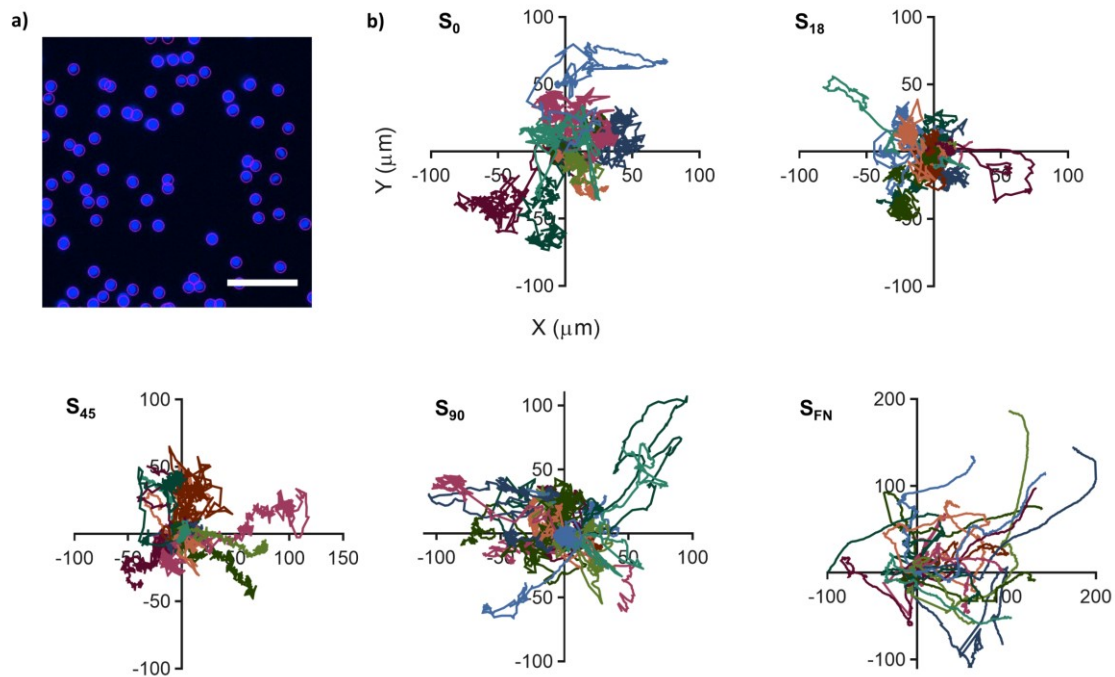


Figure 3.6. Single cell trajectories. **a)** Representative image of nuclei (blue) segmented for tracking at 96 min of imaging. Purple circles indicate segmented objects. Scale bar = 100 μm . **b)** Migratory trajectories of cell nuclei (20 tracks per substrate). All tracks have a duration of 38.2 h. Trajectories of different cells are shown in different colours. The start of each trajectory has been tied to the origin of the Cartesian coordinate system.

To characterise the dynamics of cell migration on the substrates, we analysed tracks with durations above 3 hours. We first measured net track displacement (the straight-line distance from start to end positions of the cell nucleus). Track displacement increased with substrate adherence, from 23 μm for S_0 to 72 μm for S_{FN} (Fig. 3.7a). This could be due to cells migrating faster or in a more directional manner, or a combined effect of both parameters.

To test whether larger displacements were due to speed, we quantified the mean linear velocity of cell migration. Mean track velocity was similar for low-adherence pristine and nanopatterned substrates (S_0 and S_{18}) and high-adherence nanopatterns (S_{90}), with means of 0.40

to 0.45 $\mu\text{m}/\text{min}$, but higher for mid-adherence nanopatterns (S_{45}) with 0.57 $\mu\text{m}/\text{min}$ and lower for high-adherence homogeneous substrates (S_{FN}) with 0.28 $\mu\text{m}/\text{min}$. (Fig. 3.7b).

We quantified track tortuosity as the relation between track net displacement and the total trajectory covered by the cell. A value of tortuosity closer to 1 indicates more directional movement, whereas lower values reveal a more winding path (values equal to 0 are due to static cells). We found the same or similar values of tortuosity for S_0 , S_{18} and S_{45} (means of 0.12 to 0.14); higher for S_{90} (0.21), and a clear maximum for S_{FN} (0.43) (Fig. 3.7c).

To further assess cell directionality, we calculated the turning angles between consecutive 6-minute links in each track and categorized them into 15-degree ranges. For S_0 , S_{18} and S_{45} , no more than 11% of all angles were contained in the minimum 0-15° range, similar to 9% in the maximum 165-180° range, indicating a non-directional mode of migration. For S_{90} , the two values shifted slightly to 14% and 8%, respectively. Finally, for S_{FN} , 24% of angles were in the 0-15° range, whereas only 6% were in the 165-180° range. The intermediate angle ranges of 75° to 120° contained the minimum number of turns for all conditions, with values from 4.5% (for S_{FN}) to 7.4% (for S_0) (Fig. 3.7d).

The first limiting factor in the formation of multicellular condensates is the rate at which cells collide with each another. The speed and directionality of migration in a multicellular environment will affect the number of cell-cell encounters and thus the chances for condensation to ensue. We quantified merge events, defined as instances of two tracks reaching a nucleus-nucleus distance lower than 30 μm . The hourly rate of merge events per track was equal or very similar for S_0 , S_{18} and S_{90} (means of 0.22-0.23 events/h), but higher for S_{45} (0.35 events/h) and lower for S_{FN} (0.06 events/h) (Fig. 3.7e).

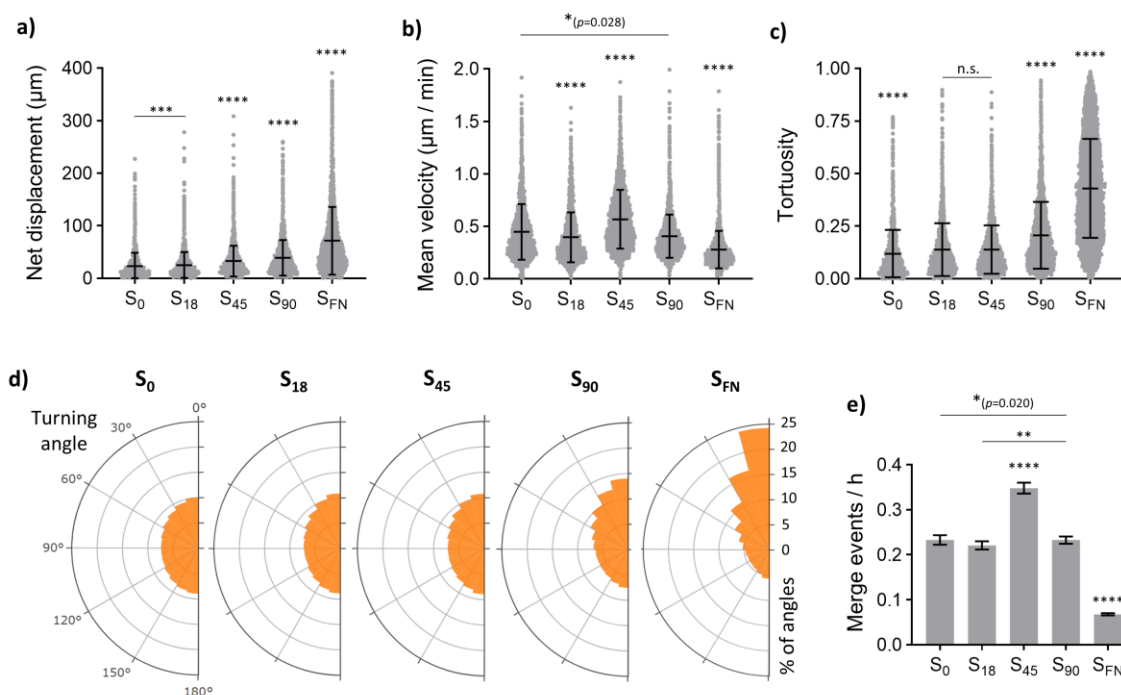


Figure 3.7. Dynamics of single cell migration and collisions. **a)** Net cell displacement. **b)** Mean instant velocities. **c)** Track tortuosity. **a-c):** $2387 \leq n \leq 7424$. All data points with the mean \pm SD. **d)** Polar histograms of turning angles in single-cell tracks ($309555 \leq n \leq 980940$). **e)** Rate of merge events (cell-cell collisions) in cell tracks ($941 \leq n \leq 2183$). Mean \pm SEM, ** $p < 0.01$, *** $p < 0.001$, **** $p < 0.0001$

3.2.3. Mesenchymal condensation

As cells attached to the substrates, they started spreading, migrating and, in the case of S₀ and nanopatterned substrates, coalescing into condensates. We analysed actin morphology during this time (20 hours). Actin staining allowed for observation of cells and condensates on S₀ and nanopatterned substrates, whereas cells on S_{FN} developed a monolayer that filled most of the imaging field (Fig. 3.8a). We thus quantified actin spread (normalised to the number of cells or condensates over time) on S₀ and nanopatterned substrates. After the initial two hours, actin area progressively increased on all substrates until hour 15, when it plateaued (Fig. 3.8b). Since this time frame corresponds with the formation of most condensates (see Fig. 3.5a), we can liken the rate of area growth to the process of condensation, shifting from a system where nearly all cells migrate as single cells to one with a substantial presence of multicellular aggregates.

To quantify the rate of actin expansion, we fitted the data of actin area from 2 to 15 h to a linear model and extracted the coefficient, or the slope in the area vs. time function. We found

that the rate of actin spreading was lowest on S_{18} , followed by similar rates for S_0 and S_{45} and steeper for S_{90} (Table 3.1).

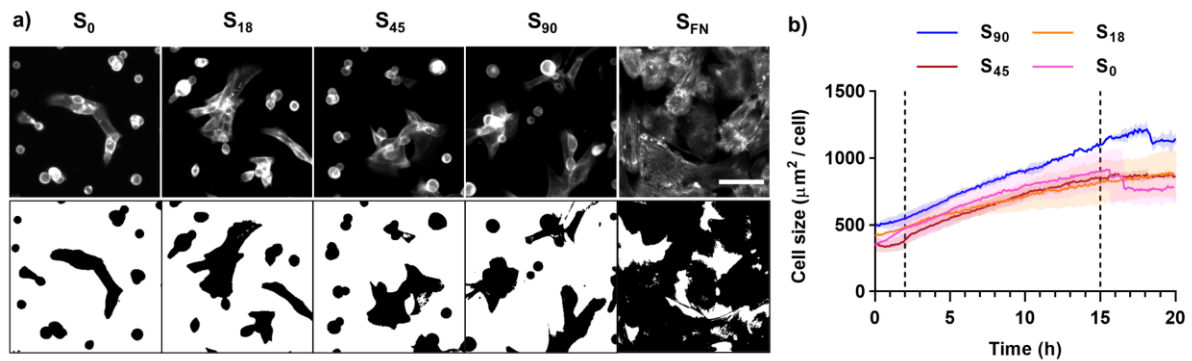


Figure 3.8. Actin dynamics during condensation. a) Actin staining at 20 h of condensation (top) and corresponding thresholds measured as actin spread area in black (bottom). Scale bar = 100 μm . b) Quantification of actin area per cell or cluster over time ($n = 2$). Mean (solid line) \pm SEM (colour area). Spreading from 2 to 15 h (section between dotted lines in the graph) was fit into a linear model.

Table 3.1. Fitting of actin area over time in a linear model. Parameters of linear models describing actin spreading ($\mu\text{m}^2 / \text{h}$) from 2 to 15 h of imaging ($n = 2$).

		S_0	S_{18}	S_{45}	S_{90}
Slope	Value	33.1	24.8	34.4	41.7
	SEM	0.5	0.2	0.4	0.3
Y-intercept	Value	439.0	459.5	370.8	487.1
	SEM	4.4	2.2	3.4	2.8
	R^2	0.97	0.99	0.99	0.99

3.2.4. Supracellular organization on protein coatings

Compared with other substrates, cells on S_{FN} proliferate, form a monolayer, migrate at a much slower speed but with much higher directionality, and present very few cell-cell collisions. No 3D condensates were observed on S_{FN} within the 40-hour frame of live imaging. We thus hypothesized that the mechanism of condensate formation on S_{FN} differs from that of nanopatterned substrates, rendering fewer condensates at a slower rate. We assessed whether observed differences could be explained based on order regime of cells on substrates.

Cells on nanopatterned substrates were not confluent, partly due to a smaller projected area and partly due to the absence of cell division. They thus migrated randomly and progressively converged as multicellular clusters. On the other hand, cells on S_{FN} established a nematic order, sliding past one another without clustering, and progressively developed $+1/2$ and $-1/2$ defects (Fig. 3.9). These two behaviours were very different and could account for differences in condensate formation.

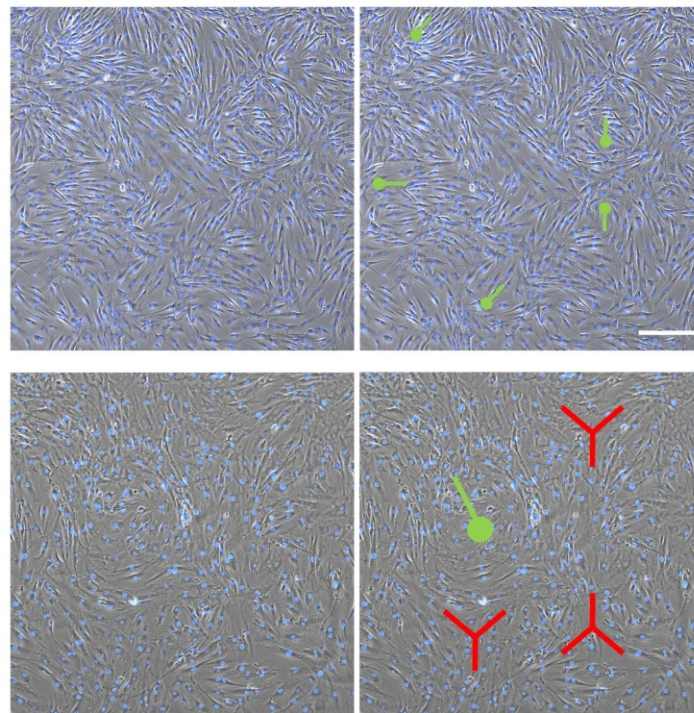


Figure 3.9. Topological defects in the nematic order of protein coatings. Examples of supracellular order in phase contrast images superimposed with nuclei staining (blue) showing $+1/2$ (green) and $-1/2$ (red) defects after 40 h of imaging. Scale bar = 300 μm .

3.2.5. Collective cell migration

After condensation, cells migrated collectively rather than as single cells. We quantified the migration dynamics of multicellular condensates present on S_0 and nanopatterned substrates. Whole condensates were segmented and tracked as single objects starting at 20 hours of imaging (Fig. 3.10a,b). Track displacement increased with ligand density, with a leap from S_{18} to S_{45} . Condensate speed was higher on S_{45} ($0.40 \mu\text{m}/\text{min}$), although significant only when compared to S_{18} ($0.31 \mu\text{m}/\text{min}$). Tortuosity was equal for S_0 , S_{18} and S_{45} (0.12 to 0.14) but presented a two-fold increase for S_{90} (0.24) (Fig. 3.10c-e). Finally, 13% to 14% of turning angles were in the minimum $0-15^\circ$ range for S_0 , S_{18} and S_{45} but this percentage increased to 19% for S_{90} , indicating a more directional mode of migration (Fig. 3.10f).

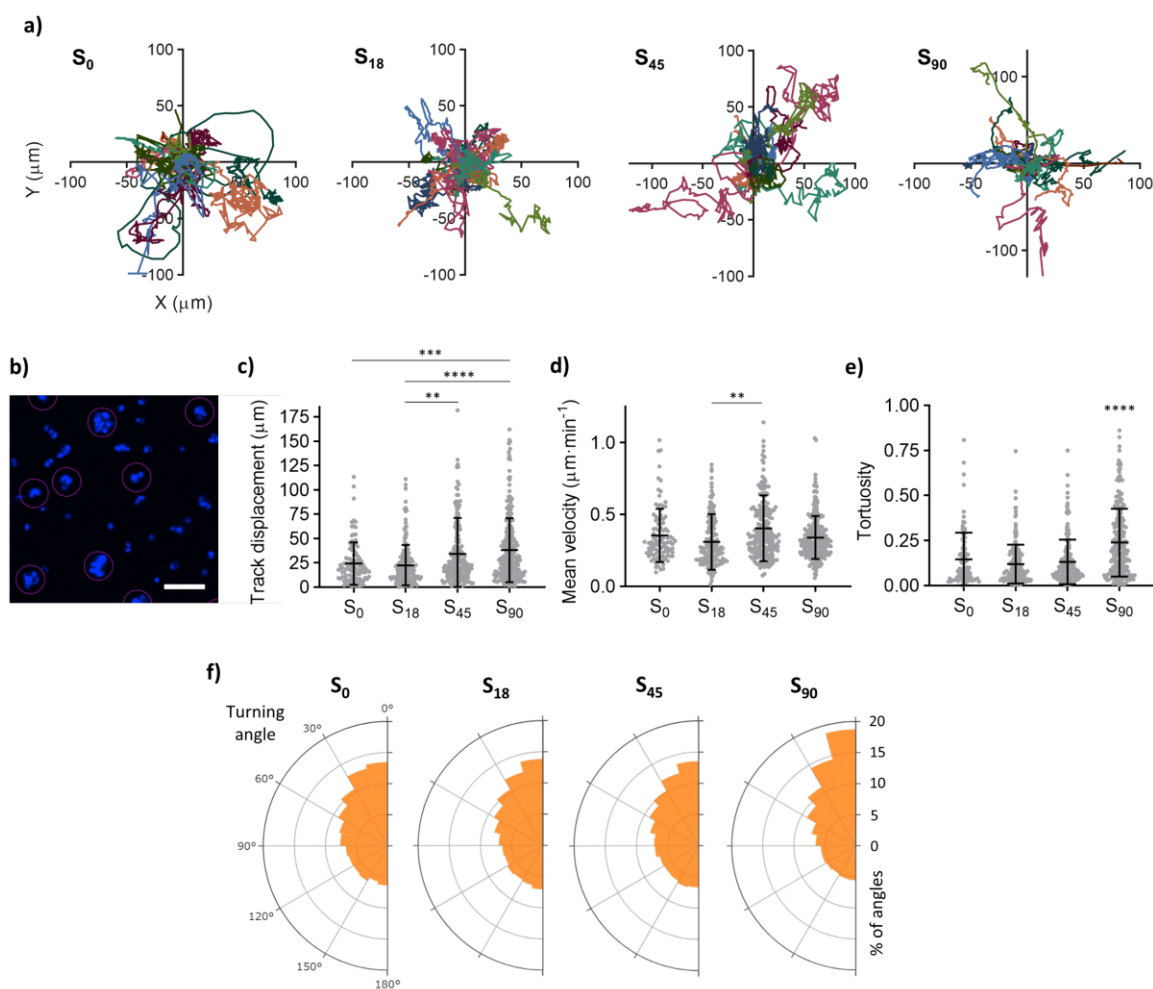


Figure 3.10. Dynamics of multicellular condensates. **a)** Migratory trajectories for condensates (20 tracks per condition). The beginning of each trajectory has been tied to the origin of the Cartesian coordinate system. Trajectories of different clusters are shown in different colours. **b)** Representative image of nuclei (blue) showing condensates segmented for tracking at 20 h of imaging (contained in purple circles). Scale bar = $100 \mu\text{m}$. **c)** Net track displacement. **d)** Mean instant velocities. **e)** Track tortuosity. **c-e):** $2387 \leq n \leq$

7424; all data points with mean \pm SD, ** $p < 0.01$, *** $p < 0.001$, **** $p < 0.0001$. **f)** Polar histograms of turning angles in condensate tracks ($11526 \leq n \leq 26786$).

3.2.6. Blocking cell-substrate and cell-cell interactions

We analysed migration and condensation under three types of pharmacological interventions impairing certain cell-substrate and cell-cell interactions: in-solution RGD dendrimers, ADH1 peptides and 18β -glycyrrhetic acid (18β GA). Addition of RGD peptides in culture medium impairs integrin clustering^{67,68}; we thus expected that RGD dendrimers in solution would have a similar effect, hampering integrin interaction with substrate-adsorbed ligands by competition. ADH1 is a cyclic pentapeptide that contains the HAV sequence that binds to adherens junction protein cadherin^{69,70}, thus blocking it when added in cell culture⁷¹⁻⁷³. Phosphorylation of gap junctional connexin proteins regulates several aspects of GJIC, including GJ formation, gating and turnover⁷⁴⁻⁷⁶; 18β GA is a saponin that induces disassembly of GJ plaques through connexin dephosphorylation⁷⁷⁻⁷⁹.

To test whether cell-substrate adhesion could indeed be affected by adding dendrimer in solution, we immunostained integrin subunit $\beta 1$ at the end of live imaging (Fig. 3.11a). Subunit $\beta 1$ is present in integrins related to substrate sensing, adhesion formation and migration, such as $\alpha 5\beta 1$ and $\alpha v\beta 1$ ⁸⁰⁻⁸³. Integrin-mediated adhesion and mechanotransduction are limited by integrin clustering at adhesion sites^{82,84}. We thus analysed whether RGD in solution affected integrin clustering. We used RGD dendrimers at the lowest concentration used in the production of nanopatterned substrates (4×10^{-9} % w/w, corresponding to S_{18}) to ensure that dendrimers would not adsorb on the S_{90} substrates and alter the surface configuration mid-imaging (see Chapter 2, section 2.10). We measured the size of integrin clusters at 40 h and found that adding RGD in solution did lead to smaller adhesions (Fig. 3.11b). Moreover, a histogram analysis was performed where low fluorescence intensity values represent diffuse integrins and high fluorescence values indicate clustered integrins⁶⁸. The distribution of staining intensities shifted toward a higher fraction of pixels at lower intensity values when adding RGD in solution, indicating less clustering (less area with high levels of staining) and a more homogeneous or diffuse integrin distribution (more area containing similar levels of staining at low values), and therefore, that integrin clustering was successfully impaired by dendrimers in solution (Fig. 3.11c).

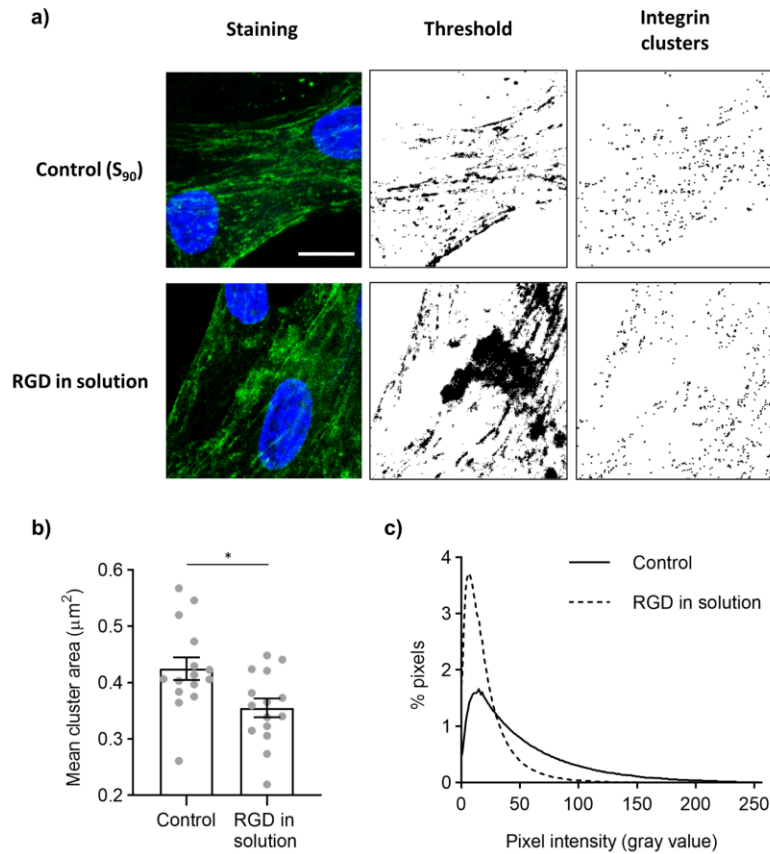


Figure 3.11. RGD dendrimers in solution impair integrin clustering. **a)** Representative fluorescence images showing merged integrin $\beta 1$ immunostaining (green) and cell nuclei (blue) at 40 h of chondrogenesis, with the corresponding thresholds selected for analysis and the measured integrin clusters, on S₉₀ in control conditions and with addition of RGD dendrimers in solution. Scale bar = 10 μm . **b)** Mean cluster area per image. All data points with the mean \pm SEM; * $p < 0.05$. **c)** Distributions of mean pixel intensity values in integrin staining.

We imaged single-cell and condensate dynamics on S_{90} substrates under each of the three pharmacological interventions. Observing the live imaging sequences, all interventions appeared to have a dramatic impact on migration and condensation (Fig. 3.12). Unlike in control S_{90} substrates, most cells with impaired cell-cell or cell-substrate interactions did not aggregate.

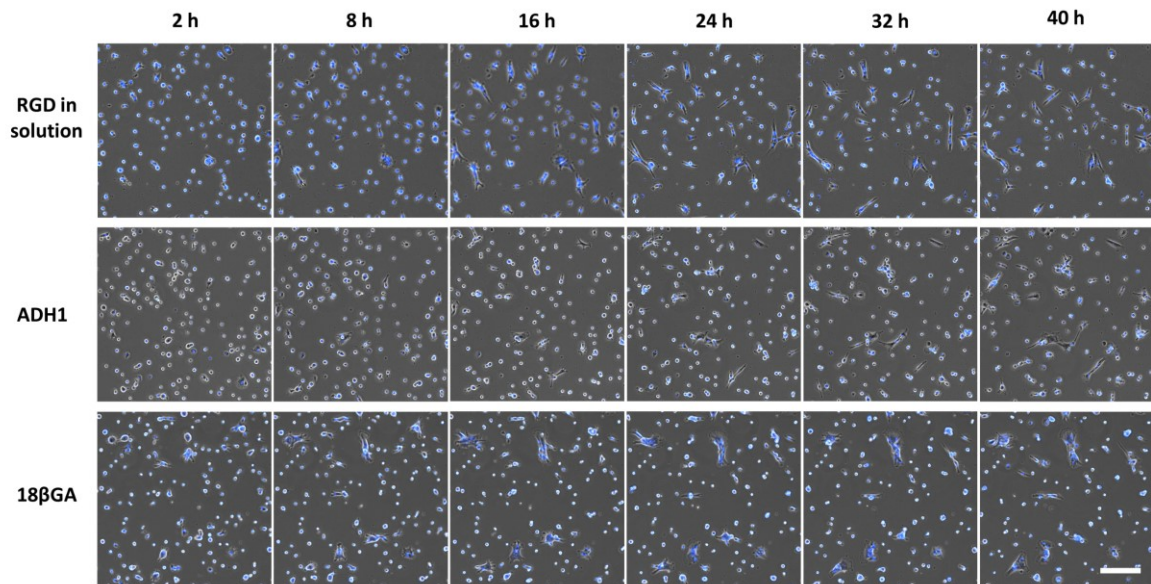


Figure 3.12. Cell migration blocking cell-substrate and cell-cell interactions. Time lapse phase contrast images superimposed with fluorescence images of cell nuclei (blue). Scale bar = 200 μm .

Compared to control S_{90} , blocking integrin receptors in single cells caused large reductions in both speed (28% slower) and directionality (52% lower tortuosity), whereas N-cadherin inhibition with ADH1 decreased mean velocity by 13% and tortuosity by 27%. Finally, uncoupling gap junctions with 18β GA affected speed as much as integrin blocking did (25%) but caused a comparatively smaller reduction in tortuosity (20%) (Fig. 3.13a,b). Both ADH1 and 18β GA reduced the hourly rate of merge events between tracks by 40%, while integrin blocking induced a maximum reduction of 55% (Fig. 3.13c).

We also analysed collective cell (condensate) dynamics in each condition. Integrin blocking led to a 41% decrease in tortuosity and a 23% decrease in speed. N-cadherin inhibition caused a stark 53% decrease of tortuosity but had no observable effect on condensate speed; on the other hand, gap junction disassembly had no effect on tortuosity but caused an 11% decrease in speed (Fig. 3.13d,e).

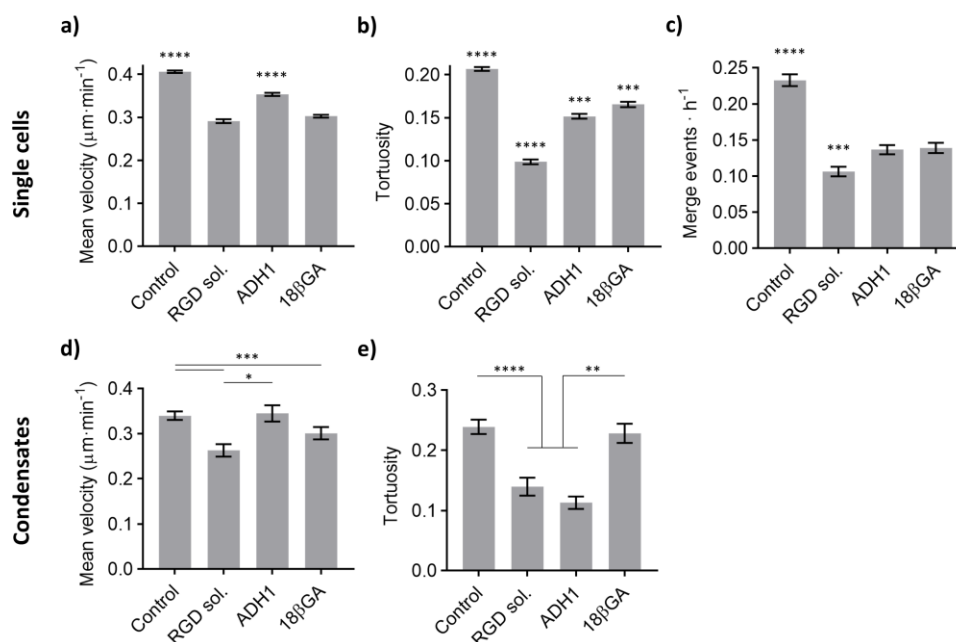


Figure 3.13. Effects of pharmacological inhibitors on single and collective cell migration. Control conditions are non-altered S_{90} substrates. **a)** Single cell mean instant velocities. **b)** Single cell tortuosity. **c)** Hourly rate of merge events (cell-cell collisions). **a-c):** $1574 \leq n \leq 5177$. **d)** Condensate mean instant velocities. **e)** Condensate tortuosity. **d, e):** $85 \leq n \leq 247$. All graphs presented as mean \pm SEM; * $p < 0.05$, ** $p < 0.01$, *** $p < 0.001$, **** $p < 0.0001$

3.3. Discussion

3.3.1. The intersection between nanopatterned ligands and a protein coating

Analysis of cell size over the first two hours of imaging showed that cells on S_{FN} spread faster and reached larger projection areas than those on nanopatterned substrates, as expected due to high homogeneous adherence and the complete biochemical signalling provided by fibronectin-coated substrates. S_{FN} was also the only substrate to support cell division. Given that proliferation is regulated by cell shape and promoted upon cell stretching^{85–87}, this could be due to S_{FN} prompting cells to spread more than other substrates. Moreover, cells are more prone to enter mitosis under high cell-cell tensions⁸⁸, which we expect would be the case in the monolayers that develop on S_{FN} . Finally, division of human cells in culture is dependent on the remodelling of pre-existing adhesions, as integrins attached to substrate ligands remain in place during mitosis and allow the daughter cells to quickly reattach⁸⁹. This process can be more easily supported in a high-adherence substrate such as S_{FN} .

Cells on S_{FN} clearly displayed the characteristic features of mesenchymal migration: large spreading, spindle morphologies and the formation of extensive lamellipodia. On the other hand, most cells on nanopatterned substrates generated filopodia while largely retaining a rounded morphology, typical of amoeboid migration. Amoeboid migration is generally observed in cells migrating on low-adherence substrates under spatial constraints, such as in microfluidic devices or in hydrogels⁹⁰. It has been recently reported on cancer and epithelial cells migrating freely on soft, viscoelastic substrates²⁴, as well as neural progenitors cultured at low density⁶⁰. Amoeboid migration is known to be faster than mesenchymal adherent migration^{91,92}, explaining why single cells moved slower on S_{FN} than in any other condition, as discussed below.

Cells use protrusions such as filopodia to probe the surrounding substrate before migrating there³⁴. Expansion of cell protrusions is a mechanosensitive process that is promoted on substrates facilitating adhesion, such as stiff surfaces⁶⁶. This explains why cells developed longer protrusions on high-adherence substrates S_{90} and S_{FN} . Moreover, filopodia were equally long for S_0 , S_{18} and S_{45} , meaning that nanoscale local substrate adherence had no effect on protrusion size within a large range of 0% to 45% of adherent area. Protrusion length was also equal for S_{90} and S_{FN} . This behaviour coincides with the described binary model of protrusion growth in relation to surface stiffness, by which large protrusions are stable only on surfaces with a Young's modulus

above a threshold of 5-8 kPa⁶⁶. In our case, large protrusions are supported only on surfaces with a percentage of adherent area above an undetermined threshold between 45% and 90%.

Analyses of cell spreading and filopodia length show that cells on S_{90} exhibit behaviours selectively similar to those on other conditions. The fact that cells on S_{90} present a relative size (as measured by actin spreading area) closer to S_{45} than to S_{FN} suggests that they retained their overall morphology without spreading further on the substrate; however, they developed filopodia as large as those of S_{FN} . This reveals an interesting system where certain features of S_{90} cells behave as those of other nanopatterns with lower ligand densities, whereas other features resemble those of high-adherence protein-coated substrates. Nanopatterns of high local ligand density thus provide particular conditions at the intersection of these two settings.

3.3.2. Nanoscale ligand density modulates stem cell migration

Higher substrate adherence allowed cells to migrate farther from their initial position. This could be due to differences in either track directionality or migration velocity. We found that cells migrate faster on S_{45} , showing that velocity follows a biphasic relation with substrate adhesiveness. Cell speed increased with ligand density up to a maximum found at an intermediate value, after which it decreased. This was first experimentally described on fibronectin-coated substrates with smooth muscle cells⁹³ and hamster ovary cells³⁰ and was recently demonstrated across cancer, epithelial and keratocyte lines²⁵. Recent studies show that RGD ordered nanopatterns also promote maximum speed of endothelial and keratocyte cells at intermediate interparticle spacings, rather than larger or shorter spacings, with the optimal spacing value varying with cell type^{32,94}. Hence, our results confirm and expand these conclusions to include MSCs migrating during morphogenesis on disordered RGD nanopatterns. The biphasic adherence-speed relation can be explained by substrates of intermediate adherence allowing cells to move freely without sticking to the surface while also finding enough adhesion sites on which to base their movement. Cells on S_0 and S_{18} would face difficulty establishing adhesions on a surface with low ligand density, whereas cells on S_{90} and S_{FN} would need to enact higher forces to detach and move. Cells on S_{45} would experience an intermediate ligand density, favourable for speedy migration⁹⁵.

The analyses of turning angles and tortuosity both reveal that movement on S_{90} is more directional than on S_0 , S_{18} and S_{45} , which we attribute to the higher percentage of adherent surface area enabling cells to migrate without needing to explore other neighbouring regions to find

points of attachment on which to proceed. The straightest cell movement is found on S_{FN} , with stark difference to those of non-adherent and nanopatterned substrates. The large shift in directionality from S_{90} to S_{FN} cannot be explained by ligand density alone, as they present a relatively small difference in the percentage of area covered with RGD groups at less than 70 nm: from 90% for S_{90} to presumably 100% for S_{FN} , given the fibronectin molecule size of 15.5 x 8.8 nm⁹⁶. However, it should be considered that the spatial positioning of RGD groups on native fibronectin would differ from that of nanopatterned RGD dendrimers, generating different sets of cell-substrate interactions and differently affecting cell adhesion and migration⁹⁷. Moreover, integrin binding to fibronectin is also modulated by the synergy sites at the protein, which are absent in isolated RGD dendrimers⁹⁸. Finally, a coating of whole fibronectin protein does not engage all the same integrin types that isolated RGD motifs do^{99,100}, which can also contribute to a difference in cell behaviour if the activated integrins have different parallel biological functions¹⁰¹.

Our results point to the importance of directionality, rather than speed, to determine how far a cell will migrate. While moving at greater speed allows cells on S_{45} to cover a longer sum trajectory, their lack of directionality means that net track displacement remains lower than those of S_{90} and S_{FN} . On the other hand, moving in straighter paths allows cells on S_{FN} to migrate farther, even with a lower velocity than all other conditions. Tellingly, S_0 , S_{18} and S_{90} have very similar mean velocities (lower than S_{45}), but a more directed movement allows S_{90} to migrate slightly farther than S_0 , S_{18} and S_{45} .

On S_0 and nanopatterned substrates, mid-range turns (75° to 120°) are less frequent than high-range ones (closer to 180°). This speaks to a migration system governed by cortical actin dynamics, in which a symmetrical actin flow from the front to the rear edge across both sides of the membrane can be less costly than redirecting cortical actin from one side to the other to generate a new leading edge.

3.3.3. Nanoscale ligand density modulates condensation

While migrating in a more directional way allows cells to move farther from their initial position, mesenchymal condensation requires that they reduce intercellular distances and eventually come into contact. Because cells are cultured on the substrates in chondrogenesis-inducing medium, they will tend to aggregate and form prechondrogenic condensates; however, this is limited by the number of times cells meet or collide on the surface. We thus measured the

rate of merge events between tracks in each condition. It should be noted that condensation involves not only merging, but also splitting events in which cells that established transient adhesions come apart. In live imaging, single cells sometimes probe a condensate and join it for only a few minutes before exiting; other times, a cell is seemingly pulled from a condensate by those in another one nearby. Hence, while the rate of merge events does not directly correlate with the number of cells present in the final constructs, it reveals S_{45} as a more dynamic system, in which cells come into contact more often than those on other substrates. This follows with the results described above, in which cells on S_{45} move faster but not straighter, which would facilitate their collisions. In contrast, cells on S_{FN} move slowly and more directionally, decreasing the chances for cell-cell encounters.

The curves of actin area on S_0 and nanopatterned substrates presented a similar trend to previous studies, with an initial expansion phase followed by a plateau¹⁰². The spreading phase, from 2 to 15 h, fit precisely within a simple linear model. Actin spreading depends on substrate adherence, but is also concurrent with condensation in our system. Therefore, the slope of the linear models would be influenced by the rate of cell spreading as well as condensate formation over time. The higher slope of S_{90} might thus indicate that these condensates were formed faster than on other substrates, despite the higher rate of cell-cell collisions on S_{45} . Merge events on S_{90} would then have a higher probability of resulting in stable cell-cell adherence.

After the onset of condensation, substrate ligand density affected the migration of multicellular clusters in a similar manner as that of single cells. This indicates that principles governing the dynamics of single hMSCs can generally be applied also to aggregates such as the ones here analysed. Recent studies on cancer cells also showed that multicellular spheroids follow the same migration modes as single cells, and that this occurs in absence of actin stress fibres within the spheroids, as is the case in prechondrogenic condensates¹⁰³. A “collective amoeboid” mode of migration has been described on non-adhesive substrates, independent of focal adhesions but dependent on integrin-mediated friction with the substrate¹⁰⁴.

3.3.4. Condensation on fibronectin as the emergence of topological defects

On S_0 and dendrimer-nanopatterned substrates, cells migrate until they collide and quickly generate large aggregates. On the other hand, cells on S_{FN} form a monolayer with no clear condensation sites within the time frame of live imaging. This corresponds with the previously described behaviour of hepatocyte cells, which aggregate if cultured on low-concentration

Matrigel but form a monolayer on high-concentration substrates, depending on the strength of cell-substrate adherence¹⁰⁵. In our case however, sparse and small condensates do appear on S_{FN} after several days of culture (see Chapter 4, Fig. 4.5). We thus investigated whether condensates on S_{FN} are formed through a different mechanism than those on S_0 and nanopatterned substrates.

Upon contact on S_0 and nanopatterned substrates, single cells approach other cells or condensates deploying front-rear polarity, with one end pointing towards the centre of the other cell and the other end outwards. This mode of condensation can be compared to the one recently described for precursors of skeletal muscle confined in small fibronectin-coated surfaces: Myoblasts in these conditions proliferate while establishing vortex-shaped +1 topological defects. As cell density increases, vortices develop into asters from which three-dimensional mounds emerge at the centre, with a similar height and structure to condensates in our system¹⁰⁶. This suggests that condensation through a localized increase of cell density is a general trait of development in musculoskeletal tissues such as muscle and cartilage. Front-rear polarity pointed towards the condensation site (therefore aster-shaped if cells approach the centre from all sides simultaneously) allows cells to quickly form three-dimensional condensates.

Instead, cells on S_{FN} slide next to each other without condensation. We pose that condensation on S_{FN} starts with the formation of $\pm 1/2$ topological defects in the nematic order of the confluent cell monolayer. In *Hydra* development, pairs of +1/2 defects progressively fuse into a +1 defect that can then emerge into the third dimension⁶⁴. We thus expect that condensates are formed slowly on S_{FN} through a similar mechanism, rather than the fast transition from random collisions to condensation sites observed on nanopatterned substrates. This is also supported by bacterial cells tending to form new 3D layers on +1/2 defects but creating holes from -1/2 defects⁶². Live imaging of +1/2 defects on S_{FN} after 40 h would be necessary to confirm this hypothesis.

3.3.5. Condensation through contact inhibition and following of locomotion

Cell migration is modulated by the chemical and mechanical interactions of cells with their substrate and, especially in collective migration, with other cells moving synchronously^{12,15,48,49,107}. To explore the role of these regulatory mechanisms on stem cell behaviour during tissue formation, we blocked integrin receptors (through in-solution RGD dendrimers), N-cadherin adhesions (with ADH1) and gap junction assembly (with 18 β GA). Integrin and gap junction blocking equally affected single cell speed but the former had a greater impact

on directionality, explaining the larger reduction it caused on merge events. Integrin blocking also affected both parameters more than cadherin blocking did. ADH1 and 18 β GA reduced either tortuosity (the former) or velocity (the latter) to a greater extent, leading to an equal reduction in cell-cell merge events, although this reduction was still lower than the one caused by dendrimers in solution.

We had indeed expected that single cell migration would be more affected by impairing integrin clustering than by interventions targeting cell-cell interactions, given that cell-substrate adhesion is the main modulator of this mode of migration. However, the fact that targeting cadherin junctions significantly reduced velocity and tortuosity shows that single cell migration within a multicellular setting (composed of multiple cells migrating separately) is also mediated by the contacts that occur between cells⁴⁸. In other words, cells use these transient interactions to guide their movement across the substrate. This phenomenon was theoretically proposed by Rørth¹ and can be related to the mechanisms of Contact Inhibition of Locomotion (CIL) and Contact Following of Locomotion (CFL). In CIL, first described by Abercrombie and Heaysman in fibroblast monolayers^{108,109}, cells coming into contact repel each other to avoid stacking into more than one layer. Studies on mesenchymal cells have shown that CIL is initiated by the retraction of protrusions near the cell-cell interface¹¹⁰. As cell-substrate adhesions disassemble, cytoskeletal tensions are transferred to cell-cell contacts¹¹¹, leading cells to repolarize and resume single migration in another direction¹¹². Hence, full cadherin adhesions are formed and quickly disassembled during CIL^{14,48}.

Contact Inhibition of Locomotion would be akin to single cells probing other cells or condensates in our system, without initiating condensation. However, cells cultured in chondrogenic medium tend to aggregate, rendering CIL as an incomplete or partial description of cell behaviour in these conditions. Alternatively, Contact Following of Locomotion is a more recently described mechanism by which a cell actively migrates towards the tail end of a neighbouring cell, coupling their trajectories and velocities^{113,114}. Prechondrogenic condensation is an example of CFL, in which contact between two single cells – or between a single cell and a forming condensate – results in a new cohesive unit of movement. This model would explain why blocking cadherin interactions led to a decrease in velocity and especially in directionality, as cells unable to form stable junctions would tend to experience CIL (repolarization and further single migration) rather than CFL (condensation).

Since gap junctions contribute to the overall reinforcement of cell-cell junctions¹⁰⁷, their disassembly would also affect adhesion stability and promote CIL over CFL. Moreover, Cx43 is also a transcriptional regulator of N-cadherin through its carboxyl terminal¹¹⁵. Given that treatment with 18 β GA induces a conformational change precisely in the carboxyl terminal (making it more widely exposed and an easier target for dephosphorylation)¹¹⁶, 18 β GA might cause a decrease in N-cadherin expression, which would in turn affect cell migration as described above.

The interplay between CIL and CFL would allow cells to migrate on nanopatterned substrates while sensing the environment and surrounding cells, as well as converging into condensates. While most contacts in live imaging did result in a stable cell-cell unit, we observed several instances of cells exiting multicellular aggregates minutes or hours after joining them. It has been reported that CIL can indeed coexist with collective cell migration in a population of rat kidney cells. In that case, the formation of stable multicellular chains depends on the circumstances of collision as well as the probability of each cell to repolarize: Attachment ensues more frequently in head-to-tail collisions or if only one of the two cells repolarizes, whereas head-to-head collisions tend to result in CIL¹¹⁷ (Fig. 3.14). The specific mechanism that determines whether a cell repolarizes or not upon collision remains unknown.

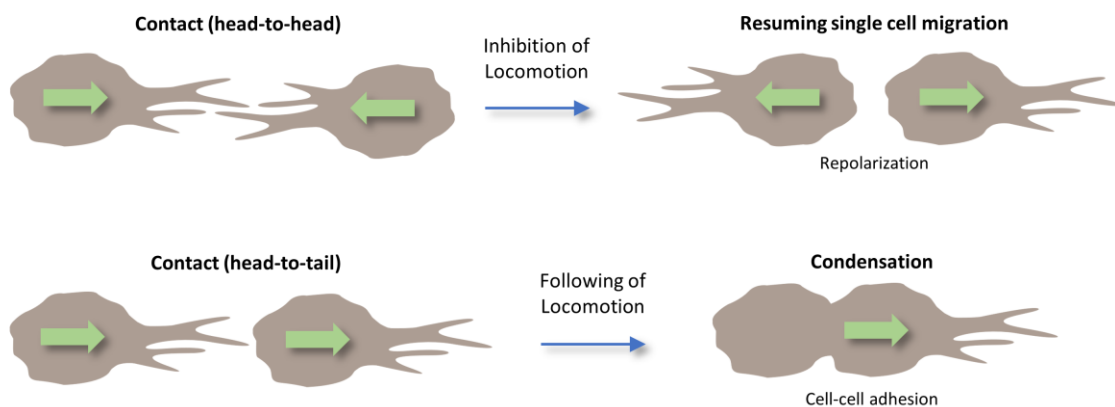


Figure 3.14. Schematic of condensation regulation. Cells are drawn displaying amoeboid migration, with filopodia at the front edge. Green arrows indicate the direction of movement. Upon cell-cell contact, inhibition of locomotion (CIL) results in cytoskeletal repolarization and cells resuming single migration, whereas following of locomotion (CFL) implies the establishment of stable cell-cell adhesions and therefore the formation of a new multicellular unit of migration, progressing towards condensation.

Non-apposed connexons or hemichannels at the plasma membrane are a gateway for cytoplasmic materials to be released into the extracellular medium^{53,56}. Growth factors and other chemotactic signals are sensed by cells in the vicinity and guide migration. Thus, impairing the

assembly of connexin plaques would hinder this mode of intercellular communication, providing an additional explanation as to why 18 β GA affected single cell directionality and velocity differently than ADH1 did. Further experiments would be required to unveil which of these mechanisms are prevalent in the effects of 18 β GA on single cell migration.

Moving on to collective migration, the trends in the effects of soluble RGD on condensate migration were comparable to those on single cell movement. Inhibiting N-cadherin and blocking gap junctions had different effects on condensate tortuosity and speed, each leaving one parameter unaltered while impairing the other. It was previously shown that downregulation of N-cadherin and Cx43 had different effects in cell migration outwards of mouse neural tube explants¹¹⁸. The effects of ADH1 on multicellular condensates largely correspond with studies performed on epithelial and cancer cells, where cadherin knockdown resulted in loss of directionality in strings or layers of cells^{48,49}. In sheets of epithelial cells, E-cadherin regulates the directionality but not the rate of migration¹¹⁹. In the *Drosophila* ovary, border cells migrating as a cluster rely on E-cadherin to communicate direction from the lead cell to follower cells in the group¹⁵. Our results confirm these observations as independent of cell type and extend the notion that cadherin-mediated adhesions are required for coordinated modulation of cell direction in collective migration, also during mesenchymal development.

Studies on neural progenitor cells (NPCs) showed that N-cadherin adhesions are required for maintaining cell stemness, expression levels of co-activator Yes-Associated Protein (YAP) and β -catenin signalling^{72,73,120}. This could have major impacts on cartilage formation, when loss of stemness would artificially speed up differentiation without necessarily allowing cells to appropriately position themselves in condensates or establish stable adhesions with neighbouring cells, altering the structure and functionality of the forming tissue.

Communication through gap junctions has not been as extensively studied as that of adherens junctions in the context of collective cell migration, especially for cell clusters and for mesenchymal stem cells, although they could be important for cell coupling and coordination⁵⁵. Moreover, given the tight and complex interplay between connexins and other proteins, including N-cadherin and cytoskeletal proteins, it is recognized that they play a role in migration beyond gap junctional communication¹²¹. We thus expected that connexin phosphorylation would also affect condensate motility. Surprisingly, while 18 β GA did reduce condensate velocity, it did not affect directionality.

Besides their role as membrane-crossing channels for soluble molecules, fully assembled gap junctions also act as points of adherence between adjacent cells⁵⁶. This facet of gap junctions was first described in malignant cancer cells and involves the cysteine residues of the extracellular connexon loops as adhesion points between membranes⁵². Cell-cell adhesion through gap junctions can regulate collective migration independently of channel activity or interactions of the connexin C-terminal with cytoplasmic proteins. For instance, neurons with knocked-down Cx43 or Cx26 fail to migrate from the intermediate zone towards the cortical plate in the developing cerebral cortex of rats, and this movement is not rescued by channel activity or C-terminal interactions alone¹²². Interneurons with the same knockdowns do move towards the plate but fail to transition from tangential to radial migration upon contact as in the wild type¹²³. The role of Cx43 in mechanical adhesions is also known because its knockdown alters the organization of epithelial monolayers, destabilizing them¹²⁴. Hence, this mechanism of cell-cell adherence through gap junctions helps explain the results observed here regarding 18 β GA effects on condensate migration, as the disassembly of gap junction plaques would result in unstable or loose condensates with difficulty to migrate as a cohesive unit.

3.4. References

1. Rørth, P. Collective cell migration. *Annu. Rev. Cell Dev. Biol.* **25**, 407–429 (2009).
2. Qu, F., Guilak, F. & Mauck, R. L. Cell migration: implications for repair and regeneration in joint disease. *Nat. Rev. Rheumatol.* **15**, 167–179 (2019).
3. Friedl, P. & Gilmour, D. Collective cell migration in morphogenesis, regeneration and cancer. *Nat. Rev. Mol. Cell Biol.* **10**, 445–457 (2009).
4. Weijer, C. J. Collective cell migration in development. *J. Cell Sci.* **122**, 3215–3223 (2009).
5. Mayor, R. & Etienne-manneville, S. The front and rear of collective cell migration. *Nat. Publ. Gr.* **17**, (2016).
6. Haeger, A., Wolf, K., Zegers, M. M. & Friedl, P. Collective cell migration: guidance principles and hierarchies. *Trends Cell Biol.* **25**, 556–566 (2015).
7. Alexander, S., Koehl, G. E., Hirschberg, M., Geissler, E. K. & Friedl, P. Dynamic imaging of cancer growth and invasion: a modified skin-fold chamber model. *Histochem. Cell Biol.* **130**, 1147–1154 (2008).
8. Sunyer, R. *et al.* Collective cell durotaxis emerges from long-range intercellular force transmission. *Science* **353**, 1157–1161 (2016).
9. Labernadie, A. *et al.* A mechanically active heterotypic E-cadherin/N-cadherin adhesion enables fibroblasts to drive cancer cell invasion. *Nat. Cell Biol.* **19**, 224–237 (2017).
10. Jain, S., Ladoux, B. & Mège, R.-M. Mechanical plasticity in collective cell migration. *Curr. Opin. Cell Biol.* **72**, 54–62 (2021).
11. Riahi, R. *et al.* Notch1–Dll4 signalling and mechanical force regulate leader cell formation during collective cell migration. *Nat. Commun.* **6**, 6556 (2015).
12. Vishwakarma, M. *et al.* Mechanical interactions among followers determine the emergence of leaders in migrating epithelial cell collectives. *Nat. Commun.* **9**, 3469 (2018).
13. Etienne-manneville, S. Neighborly relations during collective migration. *Curr. Opin. Cell Biol.* **30**, 51–59 (2014).
14. Theveneau, E. *et al.* Chase-and-run between adjacent cell populations promotes directional collective migration. *Nat. Cell Biol.* **15**, 763–772 (2013).

15. Cai, D. *et al.* Mechanical feedback through E-cadherin promotes direction sensing during collective cell migration. *Cell* **157**, 1146–1159 (2014).
16. Shellard, A., Szabó, A., Trepát, X. & Mayor, R. Supracellular contraction at the rear of neural crest cell groups drives collective chemotaxis. *Science* **362**, 339–343 (2018).
17. Grimaldi, C. *et al.* E-cadherin focuses protrusion formation at the front of migrating cells by impeding actin flow. *Nat. Commun.* **11**, 1–15 (2020).
18. Reffay, M. *et al.* Orientation and polarity in collectively migrating cell structures: Statics and dynamics. *Biophys. J.* **100**, 2566–2575 (2011).
19. Versaevel, M. *et al.* Collective migration during a gap closure in a two-dimensional haptotactic model. *Sci. Rep.* **11**, 5811 (2021).
20. DeLise, A. M., Fischer, L. & Tuan, R. S. Cellular interactions and signaling in cartilage development. *Osteoarthr. Cartil.* **8**, 309–334 (2000).
21. Christley, S., Alber, M. S. & Newman, S. A. Patterns of mesenchymal condensation in a multiscale, discrete stochastic model. *PLoS Comput. Biol.* **3**, 743–753 (2007).
22. Singh, P. & Schwarzbauer, J. E. Fibronectin and stem cell differentiation - lessons from chondrogenesis. *J. Cell Sci.* **125**, 3703–3712 (2012).
23. Charras, G. & Sahai, E. Physical influences of the extracellular environment on cell migration. *Nat. Rev. Mol. Cell Biol.* **15**, 813–824 (2014).
24. Adebowale, K. *et al.* Enhanced substrate stress relaxation promotes filopodia-mediated cell migration. *Nat. Mater.* **20**, 1290–1299 (2021).
25. Schreiber, C., Amiri, B., Heyn, J. C. J., Rädler, J. O. & Falcke, M. On the adhesion–velocity relation and length adaptation of motile cells on stepped fibronectin lanes. *Proc. Natl. Acad. Sci. U. S. A.* **118**, e2009959118 (2021).
26. Elosegui-artola, A. & Oria, R. Cell Migration: Deconstructing the Matrix. *Curr. Biol.* **30**, R1266–R1268 (2020).
27. Shellard, A. & Mayor, R. All Roads Lead to Directional Cell Migration. *Trends Cell Biol.* **30**, 852–868 (2020).
28. Clark, A. G., Maitra, A., Simon, A. & Carlos, P. Viscoelastic relaxation of collagen networks provides a self-generated directional cue during collective migration. *bioRxiv Prepr.* 1–38

- (2020).
29. SenGupta, S., Parent, C. A. & Bear, J. E. The principles of directed cell migration. *Nat. Rev. Mol. Cell Biol.* (2021) doi:10.1038/s41580-021-00366-6.
 30. Palecek, S. P., Loftus, J. C., Ginsberg, M. H., Lauffenburger, D. A. & Horwitz, A. F. Integrin-ligand binding properties govern cell migration speed through cell-substratum adhesiveness. *Nature* **385**, 537–540 (1997).
 31. Slater, J. H. *et al.* Modulation of Endothelial Cell Migration via Manipulation of Adhesion Site Growth Using Nanopatterned Surfaces. *Appl. Mater. Interfaces* **7**, 4390–4400 (2015).
 32. Di Russo, J. *et al.* Integrin $\alpha 5 \beta 1$ nano-presentation regulates collective keratinocyte migration independent of substrate rigidity. *bioRxiv* (2021) doi:10.1101/2021.03.08.434437.
 33. Heckman, C. A. & Plummer III, H. K. Filopodia as sensors. *Cell. Signal.* **25**, 2298–2311 (2013).
 34. Wong, S., Guo, W. H. & Wang, Y. L. Fibroblasts probe substrate rigidity with filopodia extensions before occupying an area. *Proc. Natl. Acad. Sci. U. S. A.* **111**, 17176–17181 (2014).
 35. Mitchison, T. J. & Cramer, L. P. Actin-based cell motility and cell locomotion. *Cell* **84**, 371–379 (1996).
 36. Xue, F., Janzen, D. M. & Knecht, D. A. Contribution of Filopodia to Cell Migration : A Mechanical Link between Protrusion and Contraction. *Int. J. Cell Biol.* **2010**, 507821 (2010).
 37. Pollard, T. D. & Borisy, G. G. Cellular motility driven by assembly and disassembly of actin filaments. *Cell* **112**, 453–465 (2003).
 38. Ridley, A. J. *et al.* Cell Migration: Integrating signals from front to back. *Science* **302**, 1704–1710 (2003).
 39. Webb, D. J., Parsons, J. T. & Horwitz, A. F. Adhesion assembly, disassembly and turnover in migrating cells – over and over and over again. *Nat. Cell Biol.* **4**, E97–E100 (2002).
 40. Lämmermann, T. & Sixt, M. Mechanical modes of ‘amoeboid’ cell migration. *Curr. Opin. Cell Biol.* **21**, 636–644 (2009).
 41. Shafqat-Abbasi, H. *et al.* An analysis toolbox to explore mesenchymal migration heterogeneity reveals adaptive switching between distinct modes. *Elife* **5**, e11384 (2015).
 42. Wolf, K. *et al.* Compensation mechanism in tumor cell migration: mesenchymal – amoeboid transition after blocking of pericellular proteolysis. *J. Cell Biol.* **160**, 267–277 (2003).

43. Panková, K., Rösel, D. & Novotný, M. The molecular mechanisms of transition between mesenchymal and amoeboid invasiveness in tumor cells. *Cell. Mol. Life Sci.* **2010**, 63–71 (2010).
44. Yamada, K. & Sixt, M. Mechanisms of 3D cell migration. *Nat. Rev. Mol. Cell Biol.* **20**, 738–752 (2019).
45. Toda, S., Frankel, N. W. & Lim, W. A. Engineering cell–cell communication networks: programming multicellular behaviors. *Curr. Opin. Chem. Biol.* **52**, 31–38 (2019).
46. Loh, C. Y. *et al.* *The E-Cadherin and N-Cadherin Switch in Epithelial-to-Mesenchymal Transition: Signaling, Therapeutic Implications, and Challenges.* *Cells* vol. 8 (2019).
47. Ganz, A. *et al.* Traction forces exerted through N-cadherin contacts. *Biol. Cell* **98**, 721–730 (2006).
48. Theveneau, E. & Mayor, R. Cadherins in collective cell migration of mesenchymal cells. *Curr. Opin. Cell Biol.* **24**, 677–684 (2012).
49. Shih, W. & Yamada, S. N-cadherin-mediated cell–cell adhesion promotes cell migration in a three-dimensional matrix. *J. Cell Sci.* **125**, 3661–3670 (2012).
50. Li, L. *et al.* E-cadherin plays an essential role in collective directional migration of large epithelial sheets. *Cell. Mol. Life Sci.* **69**, 2779–2789 (2012).
51. Hervé, J. C. & Derangeon, M. Gap-junction-mediated cell-to-cell communication. *Cell Tissue Res.* **352**, 21–31 (2013).
52. Lin, J. H. C. *et al.* Connexin 43 Enhances the Adhesivity and Mediates the Invasion of Malignant Glioma Cells. *J. Neurosci.* **22**, 4302–4311 (2002).
53. Goodenough, D. A. & Paul, D. L. Beyond the gap: Functions of unpaired connexon channels. *Nat. Rev. Mol. Cell Biol.* **4**, 285–294 (2003).
54. Ribeiro-Rodrigues, T. M., Martins-Marques, T., Morel, S., Kwak, B. R. & Girão, H. Role of connexin 43 in different forms of intercellular communication - gap junctions, extracellular vesicles and tunnelling nanotubes. *J. Cell Sci.* **130**, 3619–3630 (2017).
55. Lorraine, C., Wright, C. S. & Martin, P. E. Connexin43 plays diverse roles in co-ordinating cell migration and wound closure events. *Biochem. Soc. Trans.* **43**, 482–488 (2015).
56. Kotini, M. & Mayor, R. Connexins in migration during development and cancer. *Dev. Biol.* **401**, 143–151 (2015).

57. Mušević, I. Nematic liquid-crystal colloids. *Materials (Basel)*. **11**, 24 (2017).
58. Duclos, G., Erlenkämper, C., Joanny, J. F. & Silberzan, P. Topological defects in confined populations of spindle-shaped cells. *Nat. Phys.* **13**, 58–62 (2017).
59. Saw, T. *et al.* Topological defects in epithelia govern cell death and extrusion. *Nature* **544**, 212–216 (2017).
60. Kawaguchi, K., Kageyama, R. & Sano, M. Topological defects control collective dynamics in neural progenitor cell cultures. *Nature* **545**, 327–331 (2017).
61. Comelles, J. *et al.* Epithelial colonies in vitro elongate through collective effects. *Elife* **10**, 1–49 (2021).
62. Copenhagen, K., Alert, R., Wingreen, N. S. & Shaevitz, J. W. Topological defects promote layer formation in *Myxococcus xanthus* colonies. *Nat. Phys.* **17**, 211–215 (2021).
63. Fardin, M.-A. & Ladoux, B. Living proof of effective defects. *Nat. Phys.* **17**, 164–173 (2021).
64. Maroudas-Sacks, Y. *et al.* Topological defects in the nematic order of actin fibres as organization centres of Hydra morphogenesis. *Nat. Phys.* **17**, 251–259 (2021).
65. Barnhart, E. L., Lee, K. C., Keren, K., Mogilner, A. & Theriot, J. A. An adhesion-dependent switch between mechanisms that determine motile cell shape. *PLoS Biol.* **9**, e1001059 (2011).
66. Oakes, P. W. *et al.* Lamellipodium is a myosin-independent mechanosensor. *Proc. Natl. Acad. Sci. U. S. A.* **115**, 2646–2651 (2018).
67. Wang, Z. *et al.* RGD-independent cell adhesion via a tissue transglutaminase-fibronectin matrix promotes fibronectin fibril deposition and requires syndecan-4/2 and $\alpha 5\beta 1$ integrin co-signaling. *J. Biol. Chem.* **285**, 40212–40229 (2010).
68. Cluzel, C. *et al.* The mechanisms and dynamics of $\alpha\beta 3$ integrin clustering in living cells. *J. Cell Biol.* **171**, 383–392 (2005).
69. Williams, E., Williams, G., Gour, B. J., Blaschuk, O. W. & Doherty, P. A novel family of cyclic peptide antagonists suggests that N-cadherin specificity is determined by amino acids that flank the HAV motif. *J. Biol. Chem.* **275**, 4007–4012 (2000).
70. Erez, N., Zamir, E., Gour, B. J., Blaschuk, O. W. & Geiger, B. Induction of apoptosis in cultured endothelial cells by a cadherin antagonist peptide: Involvement of fibroblast growth factor receptor-mediated signalling. *Exp. Cell Res.* **294**, 366–378 (2004).

71. Shintani, Y. *et al.* ADH-1 suppresses N-cadherin-dependent pancreatic cancer progression. *Int. J. Cancer* **77**, 71–77 (2008).
72. Madl, C. M. *et al.* Maintenance of neural progenitor cell stemness in 3D hydrogels requires matrix remodelling. *Nat. Mater.* **16**, 1233–1242 (2017).
73. Madl, C. M., LeSavage, B. L., Dewi, R. E., Lampe, K. J. & Heilshorn, S. C. Matrix Remodeling Enhances the Differentiation Capacity of Neural Progenitor Cells in 3D Hydrogels. *Adv. Sci.* **6**, 1801716 (2019).
74. Solan, J. L. & Lampe, P. D. Specific Cx43 phosphorylation events regulate gap junction turnover in vivo. *FEBS Lett.* **588**, 1423–1429 (2014).
75. Solan, J. L. & Lampe, P. D. Spatio-temporal regulation of connexin43 phosphorylation and gap junction dynamics. *Biochim. Biophys. Acta* **1860**, 83–90 (2018).
76. Pogoda, K., Kameritsch, P., Retamal, M. A. & Vega, J. L. Regulation of gap junction channels and hemichannels by phosphorylation and redox changes : a revision. *BMC Cell Biol.* **17**, 137–150 (2016).
77. Guan, X., Wilson, S., Schlender, K. K. & Ruch, R. J. Gap-junction disassembly and connexin 43 dephosphorylation induced by 18 β -glycyrrhetic acid. *Mol. Carcinog.* **16**, 157–164 (1996).
78. Goldberg, G. *et al.* Evidence That Disruption of Connexon Particle Arrangements in Gap Junction Plaques Is Associated with Inhibition of Gap Junctional Communication by a Glycyrrhetic Acid Derivative. *Exp. Cell Res.* **53**, 48–53 (1996).
79. Böhmer, C., Kirschner, U. & Wehner, F. 18- β -Glycyrrhetic Acid (BGA) as an electrical uncoupler for intracellular recordings in confluent monolayer cultures. *Eur. J. Physiol.* **442**, 688–692 (2001).
80. Grose, R. *et al.* A crucial role of β 1 integrins for keratinocyte migration in vitro and during cutaneous wound repair. *Dev. Dis.* **129**, 2303–2315 (2002).
81. Rossier, O. *et al.* Integrins β 1 and β 3 exhibit distinct dynamic nanoscale organizations inside focal adhesions. *Nat. Cell Biol.* **14**, 1057–1067 (2012).
82. Roca-Cusachs, P., Gauthier, N. C. & Sheetz, M. P. Clustering of α 5 β 1 integrins determines adhesion strength whereas α v β 3 and talin enable mechanotransduction. *Proc. Natl. Acad. Sci.* **106**, 16245–16250 (2009).
83. Schiller, H. B. *et al.* β 1- and α v-class integrins cooperate to regulate myosin II during rigidity

- sensing of fibronectin-based microenvironments. *Nat. Cell Biol.* **15**, 625–636 (2013).
84. Cheng, B. *et al.* Nanoscale integrin cluster dynamics controls cellular mechanosensing via FAKY397 phosphorylation. *Sci. Adv.* **6**, eaax1909 (2020).
85. Streichan, S. J., Hoerner, C. R., Schneidt, T., Holzer, D. & Hufnagel, L. Spatial constraints control cell proliferation in tissues. *Proc. Natl. Acad. Sci. U. S. A.* **111**, 5586–5591 (2014).
86. Benham-Pyle, B. W., Pruitt, B. L. & Nelson, W. J. Mechanical strain induces E-cadherin-dependent Yap1 and β -catenin activation to drive cell cycle entry. *Science* **348**, 1024–1027 (2015).
87. Gudipaty, S. A. *et al.* Mechanical stretch triggers rapid epithelial cell division through Piezo1. *Nature* **543**, 118–121 (2017).
88. Uroz, M. *et al.* Regulation of cell cycle progression by cell-cell and cell-matrix forces. *Nat. Cell Biol.* **20**, 646–654 (2018).
89. Dix, C. L. *et al.* The Role of Mitotic Cell-Substrate Adhesion Re-modeling in Animal Cell Division. *Dev. Cell* **45**, 132–145 (2018).
90. Liu, Y.-J. *et al.* Confinement and Low Adhesion Induce Fast Amoeboid Migration of Slow Mesenchymal Cells. *Cell* **160**, 659–672 (2015).
91. Pandya, P., Orgaz, J. L. & Sanz-Moreno, V. Modes of invasion during tumour dissemination. *Mol. Oncol.* **11**, 5–27 (2017).
92. Graziani, V., Rodriguez-Hernandez, I., Maiques, O. & Sanz-Moreno, V. The amoeboid state as part of the epithelial-to-mesenchymal transition programme. *Trends Cell Biol.* **xx**, (2021).
93. DiMilla, P. A., Stone, J. A., Quinn, J. A., Albelda, S. M. & Lauffenburger, D. A. Maximal migration of human smooth muscle cells on fibronectin and type IV collagen occurs at an intermediate attachment strength. *J. Cell Biol.* **122**, 729–737 (1993).
94. Liu, Q. *et al.* Cell migration regulated by RGD nanospacing and enhanced under moderate cell adhesion on biomaterials. *Biomaterials* **263**, 120327 (2020).
95. Gupton, S. L. & Waterman-Storer, C. M. Spatiotemporal Feedback between Actomyosin and Focal-Adhesion Systems Optimizes Rapid Cell Migration. *Cell* **125**, 1361–1374 (2006).
96. Kotliansky, V. E., Bejanian, M. V. & Smirnov, V. N. Electron microscopy study of fibronectin structure. *FEBS Lett.* **120**, 283–286 (1980).

97. Cavalcanti-Adam, E. A. *et al.* Cell spreading and focal adhesion dynamics are regulated by spacing of integrin ligands. *Biophys. J.* **92**, 2964–2974 (2007).
98. Brown, A. C., Dysart, M. M., Clarke, K. C., Stabenfeldt, S. E. & Barker, T. H. Integrin $\alpha 3\beta 1$ binding to fibronectin is dependent on the ninth type III repeat. *J. Biol. Chem.* **290**, 25534–25547 (2015).
99. Humphries, J. D., Byron, A. & Humphries, M. J. Integrin ligands at a glance. *J. Cell Sci.* **119**, 3901–3903 (2006).
100. Moreno-Layseca, P., Icha, J., Hamidi, H. & Ivaska, J. Integrin trafficking in cells and tissues. *Nat. Cell Biol.* **21**, 122–132 (2019).
101. Elosegui-Artola, A. *et al.* Rigidity sensing and adaptation through regulation of integrin types. *Nat. Mater.* **13**, 631–637 (2014).
102. Paknikar, A. K., Eltzner, B. & Köster, S. Direct characterization of cytoskeletal reorganization during blood platelet spreading. *Prog. Biophys. Mol. Biol.* **144**, 166–176 (2019).
103. Beaune, G. *et al.* Spontaneous migration of cellular aggregates from giant keratocytes to running spheroids. *Proc. Natl. Acad. Sci. U. S. A.* **115**, 12926–12931 (2018).
104. Pagès, D. L. *et al.* Cell clusters adopt a collective amoeboid mode of migration in confined non-adhesive environments. *bioRxiv* (2020) doi:10.1101/2020.05.28.106203.
105. Powers, M. J., Rodriguez, R. E. & Griffith, L. G. Cell-substratum adhesion strength as a determinant of hepatocyte aggregate morphology. *Biotechnol. Bioeng.* **53**, 415–426 (1997).
106. Guillamat, P., Blanch-Mercader, C., Kruse, K. & Roux, A. Integer topological defects organize stresses driving tissue morphogenesis. *bioRxiv Prepr.* (2020).
107. Friedl, P. & Mayor, R. Tuning collective cell migration by cell-cell junction regulation. *Cold Spring Harb. Perspect. Biol.* **9**, a029199 (2017).
108. Abercrombie, M. & Heaysman, J. E. M. Observations on the social behaviour of cells in tissue culture I. Speed of movement of chick heart fibroblasts in relation to their mutual contacts. *Exp. Cell Res.* **5**, 111–131 (1953).
109. Abercrombie, M. & Heaysman, J. E. M. Observations on the social behaviour of cells in tissue culture II. 'Monolayering' of fibroblasts. *Exp. Cell Res.* **6**, 293–306 (1954).
110. Carmona-Fontaine, C. *et al.* Contact inhibition of locomotion in vivo controls neural crest

- directional migration. *Nature* **456**, 957–961 (2008).
111. Roycroft, A. *et al.* Redistribution of Adhesive Forces through Src/FAK Drives Contact Inhibition of Locomotion in Neural Crest. *Dev. Cell* **45**, 565–579 (2018).
 112. Scarpa, E. *et al.* A novel method to study contact inhibition of locomotion using micropatterned substrates. *Biol. Open* **2**, 901–905 (2013).
 113. Li, D. & Wang, Y. L. Coordination of cell migration mediated by site-dependent cell-cell contact. *Proc. Natl. Acad. Sci. U. S. A.* **115**, 10678–10683 (2018).
 114. Brückner, D. B. *et al.* Learning the dynamics of cell-cell interactions in confined cell migration. *Proc. Natl. Acad. Sci.* **118**, e2016602118 (2021).
 115. Kotini, M. *et al.* Gap junction protein Connexin-43 is a direct transcriptional regulator of N-cadherin in vivo. *Nat. Commun.* **9**, 3846 (2018).
 116. Guan, X., Wilson, S., Schlender, K. K. & Ruch, R. J. DONT DONT DONT Gap-junction disassembly and connexin 43 dephosphorylation induced by 18 β -glycyrrhetic acid. *Mol. Carcinog.* **16**, 157–164 (1996).
 117. Desai, R. A., Gopal, S. B., Chen, S. & Chen, C. S. Contact inhibition of locomotion probabilities drive solitary versus collective cell migration. *J. R. Soc. Interface* **10**, 20130717 (2013).
 118. Xu, X. *et al.* Modulation of mouse neural crest cell motility by N-cadherin and connexin 43 gap junctions. *J. Cell Biol.* **154**, 217–229 (2001).
 119. Borghi, N., Lowndes, M., Maruthamuthu, V., Gardel, M. L. & Nelson, W. J. Regulation of cell motile behavior by crosstalk between cadherin- and integrin-mediated adhesions. *Proc. Natl. Acad. Sci.* **107**, 13324–13329 (2010).
 120. Zhang, J. *et al.* Cortical Neural Precursors Inhibit Their Own Differentiation via N-Cadherin Maintenance of b-Catenin Signaling. *Dev. Cell* **18**, 472–479 (2010).
 121. Kameritsch, P., Pogoda, K. & Pohl, U. Channel-independent influence of connexin 43 on cell migration. *Biochim. Biophys. Acta - Biomembr.* **1818**, 1993–2001 (2012).
 122. Elias, L. A. B., Wang, D. D. & Kriegstein, A. R. Gap junction adhesion is necessary for radial migration in the neocortex. *Nature* **448**, 901–907 (2007).
 123. Elias, L. A. B., Turmaine, M., Parnavelas, J. G. & Kriegstein, A. R. Connexin 43 mediates the tangential to radial migratory switch in ventrally derived cortical interneurons. *J. Neurosci.* **30**,

7072–7077 (2010).

124. Bazellères, E. *et al.* Control of cell-cell forces and collective cell dynamics by the intercellular adhesive. *Nat. Cell Biol.* **17**, 409–420 (2015).

Chapter 4

Condensate structure and intercellular communication

4.1. Introduction

In the previous chapter we have observed the onset of multicellular aggregates through active migration of mesenchymal stem cells cultured in chondrogenic medium. *In vivo*, these anlagen are an essential stage in the development of articular cartilage, but also of skeletal bone¹. Condensates were initially described as a “membranous skeleton” to stress their importance in skeletal development^{2,3}. Thus, the condensation step determines the distribution and morphology of later morphogenetic structures (Fig. 4.1).

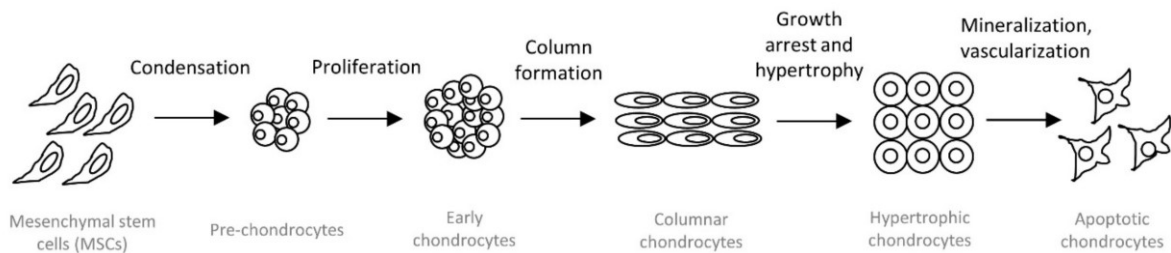


Figure 4.1. Osteochondral development, with mesenchymal condensation as the first stage. Adapted with permission from Shimizu, Yokoyama and Asahara (2007)⁴

During morphogenesis, cells cooperate to form functioning tissues and organs. This level of complex coordination entails intricate mechanisms of intercellular communication. In osteochondral development, mesenchymal cell condensation is concurrent with the formation of an extensive network of gap junctions (GJs)⁵, plasma membrane channels that link the cytoplasm of adjacent cells. GJs are present in almost all animal tissues, allowing cells to exchange ions, nucleotides and other small molecules through a gated mechanism⁶. Since they bring the membranes of neighbouring cells closer together, they also improve the mechanical stability at cell-cell junctions⁷. Moreover, gap junctions can act as cell-adhesive structures themselves⁸⁻¹⁰. An efficient network of GJs is an extremely versatile communication system that mediates the rapid synchronization between cells¹¹. GJs established during embryonic patterning allow multicellular groups to coordinate towards the formation of supracellular, tissue-level structures^{12,13}. Connective tissues, such as cartilage, particularly rely on this form of intercellular communication for successful development and homeostasis¹⁴⁻¹⁶. For instance, mature chondrocytes in articular cartilage employ GJ networks to exchange glucose, amino acids and nucleotides¹⁵.

Connexins, the building blocks of gap junctions, are ubiquitous proteins comprised of four transmembrane domains, two extracellular domains (the loops between the first and second, and the third and fourth, transmembrane domains) and three cytoplasmic domains (the N- and the C-terminals and a loop between the second and third transmembrane domains)¹⁷. These transmembrane domains shape the channel pore. Gap junctions are formed by two connexons or hemichannels, one at the membrane of each connecting cell; each connexon is comprised of six connexins. Connexons accumulate to form dense GJ plaques, which are continuously regenerated by the addition of connexon subunits at the edges and internalization from the centre of the plaques^{18,19}. Besides constituting cell-cell junctions, non-aposed hemichannels also allow the release of ions and molecules into the interstitial space, propagating signals such as calcium waves^{10,20,21} (Fig. 4.2).

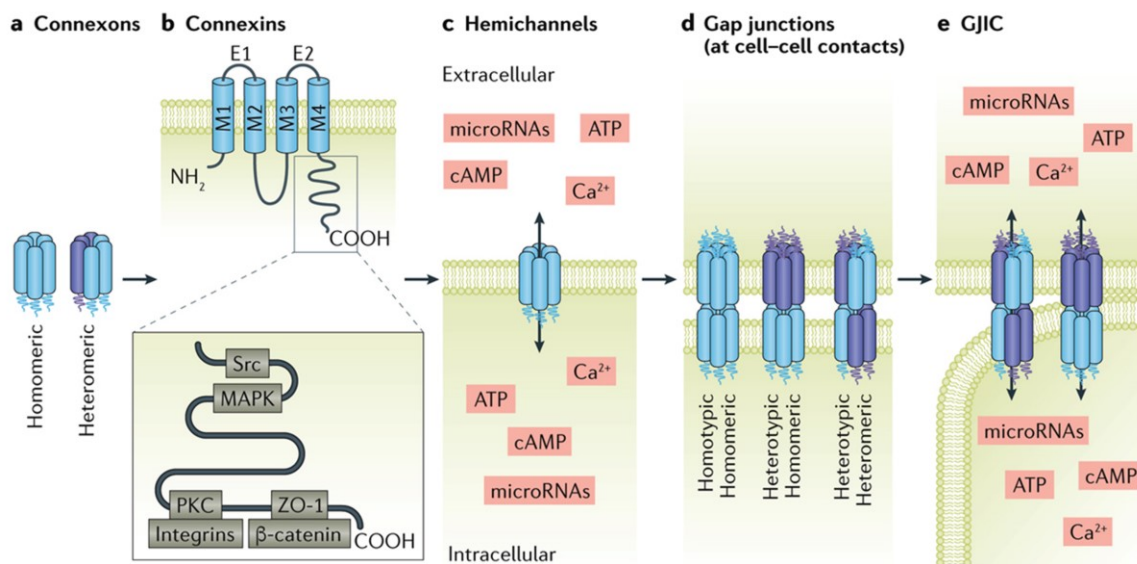


Fig. 4.2. Schematics of gap junction structure. **a)** Connexons are formed from the oligomerization of six connexins; connexons can be homomeric (formed from six monomers of the same connexin) or heteromeric (made up of different connexins). **b)** Each connexin has four transmembrane domains (M1, M2, M3 and M4) and two extracellular loops (E1 and E2); the intracellular carboxyl terminus of a connexin can interact with proto-oncogene tyrosine-protein kinase Src, mitogen-activated protein kinase (MAPK), protein kinase C (PKC), β-catenin and integrins. **c)** Connexon hemichannels facilitate the flux of small molecules such as cyclic AMP (cAMP), ATP, microRNAs and calcium ions across the plasma membrane. **d)** Hemichannels from adjacent cells form gap junctions by engaging in homotypic or heterotypic coupling. **e)** Varied gap junction composition mediates permeability, selectivity and gating in gap junctional intercellular communication (GJIC). Adapted with permission from Donahue, Qu and Genetos (2018)¹⁶

Connexin 43 (Cx43), also known as gap junction alpha 1 (GJA1), is a widely studied connexin. It is a building block of gap junctions and also mediates paracrine communication systems between non-adjacent cells, such as tunnelling nanotubes and extracellular vesicles²². Cx43 is one of the most abundant connexins in both cartilage and bone cells and is an important regulator of tissue formation and limb development^{23–27}. Inhibition of Cx43 expression in developing cartilage impairs cell differentiation²⁸. In mouse osteoblasts, altered ratios of Cx43 lead to decreased transcription of differentiation markers and subsequently impair bone mineralization; Cx43-null osteoblasts are not functional^{29–31}.

Like other connexins, Cx43 exerts functions through interaction of its cytoplasmic C-terminal tail (CT-Cx43) with cell-cell junction proteins as well as with several cytoskeletal proteins, including α -tubulin, β -tubulin, actin, vimentin and vinculin^{15,32,33}. In turn, gap junction formation and gating are regulated by cytoskeletal inputs^{32,34,35}. The assembly of gap junctions from Cx43 connexons is modulated by tight junction protein zonula occludens-1 (ZO-1) interacting with the CT-Cx43³⁶. In cartilage and bone development, the CT-Cx43 determines cell phenotype, nanoscale tissue structure and mechanical properties such as resistance to fracture^{37–40}; cleavage of the CT in pathological conditions contributes to the progression of joint diseases such as osteoarthritis³⁷.

Previous studies have related gap junction intercellular communication (GJIC) with extracellular inputs. Integrins $\alpha 5\beta 1$ and $\alpha 3\beta 1$ regulate Cx43 assembly, hemichannel opening and the resulting GJIC functionality^{41,42}. Adhesome protein vinculin (VCL) and ZO-1 both closely interact with Cx43 to stabilize gap junctions in heart development⁴³. Conversely, Cx43 influences matrix-dependent processes; in particular, cell migration during morphogenetic events such as wound closure^{44–48}.

Integrin-mediated cell-matrix interactions regulate many biological processes such as cell shape, proliferation, migration, differentiation and cell death^{49–51}. During morphogenesis, dynamic adhesion mechanisms, together with the associated signalling pathways, define tissue differentiation and architecture, and modulate collective cell behaviour^{11,52–57}. Here we employ RGD dendrimer nanopatterns to control local substrate adhesiveness (see Chapter 1, section 1.4).

In this chapter we follow up with multicellular aggregates after the initial stages of condensation. Taking chondrogenesis as a model⁵⁸, we study how substrate ligand density progressively modulates the formation of tissue during mesenchymal condensation. We first analyse condensate structure and mechanical stability and find that substrates of high local ligand

Chapter 4

density (S_{90}) facilitate tissue compaction and stability in culture. These phenomena are not explained by expression patterns of proteins traditionally linked to mechanical cell-cell and cell-matrix interactions, such as N-cadherin and vinculin. We then analyse Cx43 expression, employ confocal microscopy to image the protein in condensates, and analyse the image stacks to quantify the architectural connectivity of the intercellular connexin networks. We find that the S_{90} substrate condition induces an improvement in connexin expression and architectural connectivity, which leads to an increase in GJIC, as assessed by a tracer uptake assay. We then design an assay in which we transplant condensates from their original substrate to a new one, with either the same or a different ligand density, to evaluate whether changing matrix inputs induce a remodelling of connexin expression across the condensates. Finally, we employ integrin blocking and myosin inhibition to confirm that substrate effects are sensed by integrin adhesions and propagated into condensates by cytoskeletal contractility.

4.2. Results

4.2.1. Condensate structure and stability

Human mesenchymal stem cells (hMSCs) were cultured in chondrogenic medium on non-patterned S_0 ; RGD dendrimer-nanopatterned S_{18} , S_{45} and S_{90} ; and fibronectin-coated S_{FN} substrates. Samples were then observed at various time points of chondrogenic induction.

Several condensates formed quickly on pristine and nanopatterned substrates, whereas cells on S_{FN} remained mostly as a monolayer, with a reduced number of condensates appearing after 3 to 5 days in culture (Fig. 4.3a,b). As a control aimed to discern whether condensate formation was in fact due to chondrogenic induction, we seeded MSCs on S_{90} in growth medium instead of chondrogenic medium. In this case, cells generated a monolayer rather than undergoing mesenchymal condensation, proving that the observed multicellular aggregates were indeed the result of soluble signals in the differentiation medium (Fig. 4.3c).

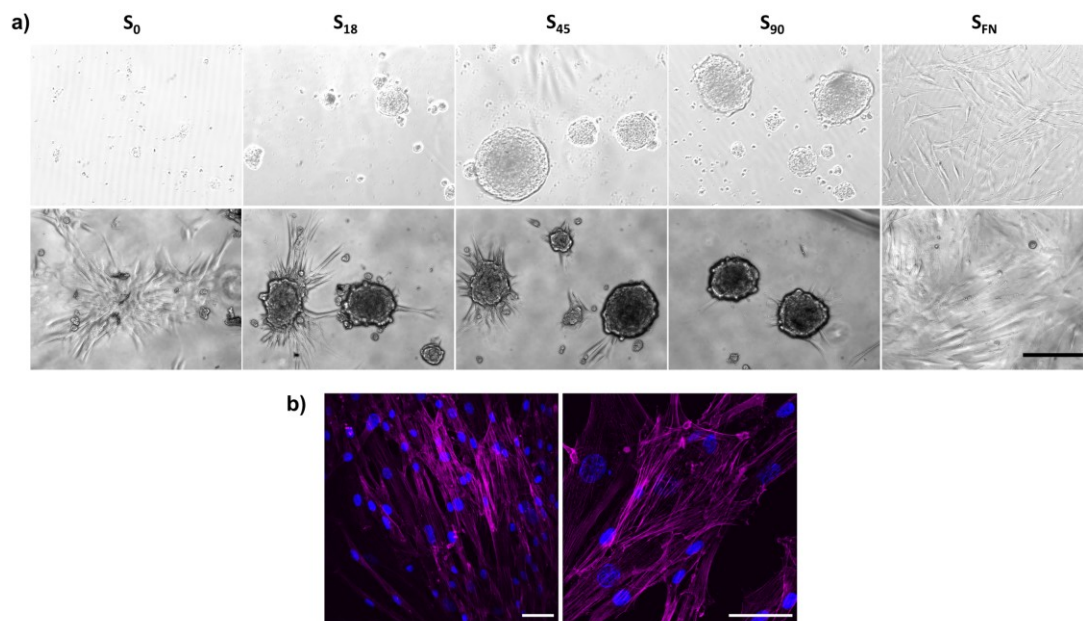


Figure 4.3. Chondrogenic medium induces mesenchymal condensation. a) Bright field (top) and phase contrast (bottom) images of cells after 3 days of chondrogenic induction. Scale bar = 100 μm . **b)** Confocal images showing actin (magenta) stress fibres and nuclei (blue) in cells after 6 days on S_{90} in growth medium. Scale bars = 50 μm .

Due to the quasi-hemispherical structure of condensates, we were concerned that cell viability at the centre might be impaired from a potential lack of nutrients or slower gas exchange with the medium. To assess viability, we conducted an assay to visualize esterase activity and

nucleic acids. Esterase activity was assessed with calcein AM, a cell-permeant dye that turns fluorescent upon enzymatic cleaving. Since esterase enzymes are ubiquitous in animal cells, an absence of fluorescence would indicate inactive or dead cells. Nucleic acids were stained with ethidium homodimer-1, a non-permeant dye; thus, cytoplasmic fluorescence would indicate significant membrane damage and non-viability of the cell⁵⁹. At day 7 of chondrogenesis, nearly all cells in condensates were alive (Fig. 4.4).

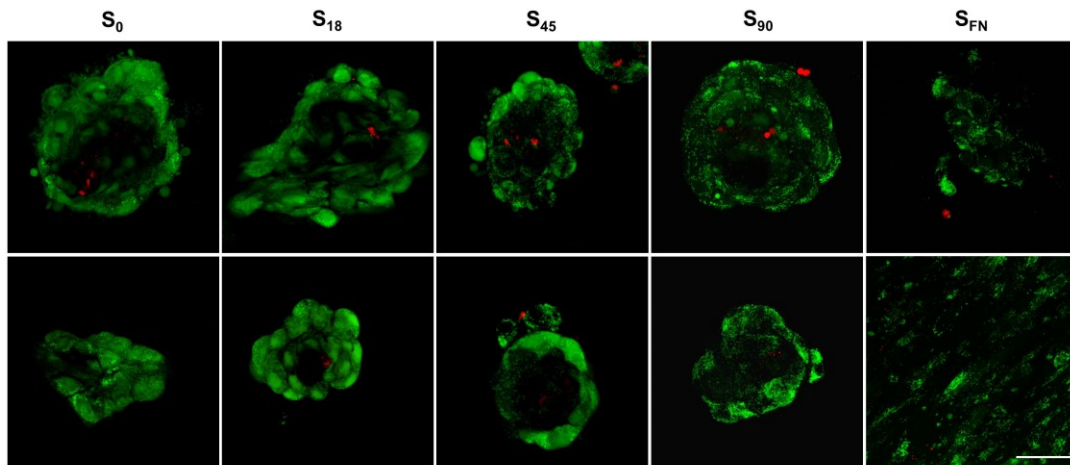


Figure 4.4. Live/Dead assay in condensates. Samples at day 7 of chondrogenic induction stained for intracellular esterase activity, indicating live cells (green), and for nucleic acids in membrane-damaged cells (red). Scale bar = 50 μm .

In the early stages of cartilage formation, prechondrogenic condensates provide the structural basis for subsequent development, as long as they are able to achieve an adequate size. Cartilage formation may be delayed or stopped due to small condensates, whereas excessively large condensates can lead to the formation of tissue with an anomalous morphology¹. While multicellular aggregates formed abundantly across S_0 and dendrimer-nanopatterned substrates, they may differ in size or structure. We measured the projected longitudinal area of condensates at different time points of chondrogenesis (Fig. 4.5a). Cells did aggregate into large condensates by day 6 on S_{45} and S_{90} , and to a smaller extent on S_0 . By day 9, condensates on S_{18} and S_{FN} also reached a similar area (around and above 10,000 μm^2 , or 0.01 mm^2), thus presenting a slower condensation rate that eventually resulted in condensates of the same size. However, by day 14, condensates on all substrates other than S_{90} had collapsed, with cells migrating out of them and spreading back on the substrate with a fibroblast-like morphology (Fig. 4.5b). Condensates on S_{90} at day 14 remained within the same size range as in previous time points, and were significantly larger than those on all other substrates.

To investigate which mechanisms could contribute to the increased stability of S_{90} cell condensates, we evaluated the structural compaction of condensates. We measured the distance between adjacent cell nuclei as a proxy for cell-cell cohesion at day 6 of chondrogenesis. We found that condensates on high-adherence substrates S_{90} and S_{FN} were spatially distributed closer together than those on S_0 , S_{18} and S_{45} (Fig. 4.5c).

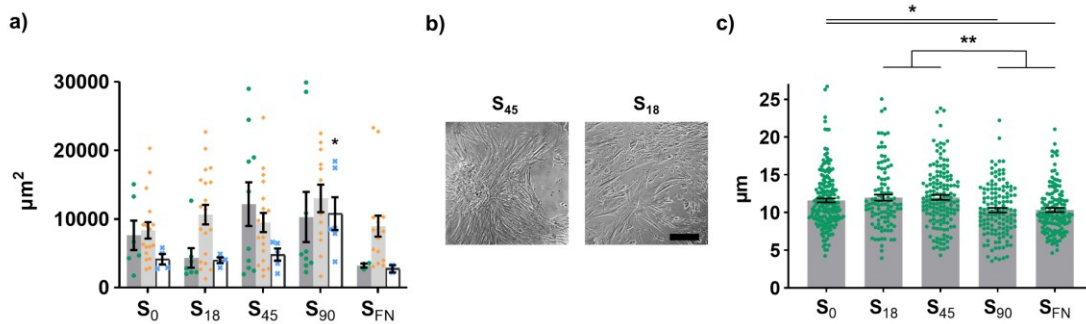


Figure 4.5. Condensate size and stability. **a)** Area of mesenchymal condensates at days 6, 9 and 14 of chondrogenic induction. Green dots with dark gray bars correspond to day 6; orange rhomboids with light gray bars correspond to day 9; blue asterisks with white bars correspond to day 14. **b)** Phase contrast images of condensates collapsing in S_{45} and S_{18} nanopatterns. Scale bar = 250 μm . **c)** Horizontal distance between adjacent cell's nuclei in condensates at day 6. **a, c)** Symbols represent single sample values, bars indicate the mean \pm SEM, * $p < 0.05$, ** $p < 0.01$

The process of mesenchymal cell condensation encompasses precise cell shape deformations, which are primarily driven by changes in the organization of the actin cortex⁶⁰. The actin cortex is a thin actomyosin network bound to the cell membrane that is found in most animal cells and that has a pivotal role in the mechanics of cell migration, cell division and morphogenesis⁶¹. A typical cortical actin disposition was observed in all the cell condensates while cells on S_{FN} substrates, arranged mostly in a 2D configuration, showed a stress-fibre organization of the actin network (Fig. 4.6).

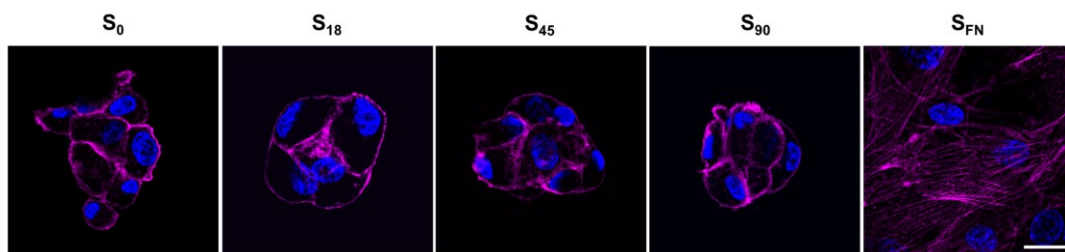


Figure 4.6. Actin structure in condensates. Confocal images showing actin (magenta) and nuclei (blue) in cell condensates or monolayers after 6 h of chondrogenic induction. Scale bar = 20 μm .

Supracellular mechanical cohesion and coordination are mainly regulated through adherens junctions^{62–64}, formed by N-cadherin (CDH2) in mesenchymal cells⁶⁵. Given the results in internuclear distance and long-term stability, we wondered if condensates on S_{90} might present higher levels of N-cadherin expression, which we examined by RT-qPCR (Fig. 4.7a). *CDH2* was more expressed on S_0 , S_{45} and S_{FN} at day 6, with no significant differences at day 9; moreover, expression in all conditions was downregulated to a half of undifferentiated hMSCs.

To further evaluate the role of mechanical junctions, we also measured expression of adhesome protein vinculin (VCL), present at cell-cell as well as cell-matrix adhesions (Fig. 4.7a). Surprisingly, *VCL* at 6 and 9 days was upregulated on substrates of low adherence (S_0 and S_{18}) with respect to S_{FN} , where expression levels were equal to undifferentiated hMSCs. A Western blot of VCL indicated equal amounts of protein production on S_0 , S_{18} and S_{45} , and lower for S_{90} and S_{FN} (Fig. 4.7b). Immunofluorescence images (Fig. 4.7c) showed that VCL accumulated mainly at the rim of cell condensates, wrapping cells in a compacted structure.

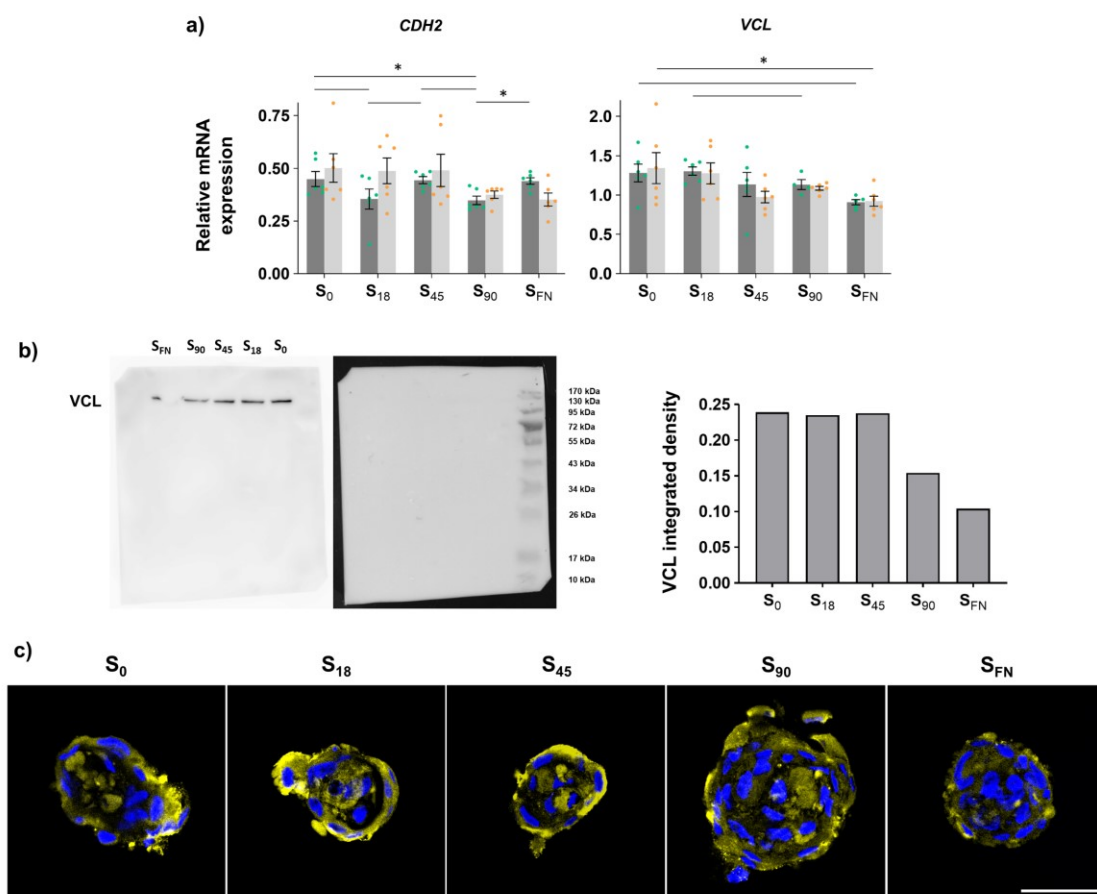


Figure 4.7. N-cadherin and vinculin expression. a) Expression of N-cadherin (*CDH2*) and vinculin (*VCL*) mRNA, relative to that of undifferentiated hMSCs (assigned value 1, not shown) at day 6 (dark bars with green dots) and day 9 (light bars with orange rhomboids) of chondrogenesis. Dots and rhomboids represent

single sample values, bars indicate the mean \pm SEM, $*p < 0.05$. **b)** Western blot of VCL at day 6, and corresponding quantification of integrated density normalized to total protein staining. **c)** Representative confocal microscopy images of condensates stained for VCL (yellow) and Hoechst (blue) at day 6. Scale bar = 40 μ m.

Observations in *CDH2* and *VCL* did not explain how condensate assembly, mechanical stability, and structural compaction were promoted on S_{90} over the other substrates.

4.2.2. Gap junction intercellular communication

Gap junctions (GJs) are the main modulators of molecule exchange between adjacent cells. Intercellular communication through gap junctions is crucial for correct cartilage development^{24,36}; we wondered if ligand density could affect cartilage formation through its impact on intercellular communication. To examine intercellular connectivity through GJs in chondrogenic condensates, we analysed the expression of *GJA1*, the gene encoding Cx43, at days 6 and 9 of culture in chondrogenesis-inducing medium (Fig. 4.8a). At day 6, *GJA1* was overexpressed on S_{90} to over twice the level of undifferentiated hMSCs, and downregulated to a half on S_{FN} . However, expression on S_{90} levelled off at day 9 with that of other nanopattern configurations. S_0 , S_{18} and S_{45} presented equal *GJA1* expression levels at both time points of chondrogenic induction.

We performed protein immunostaining to observe Cx43 production. Quantification of the percentage of immunofluorescent area showed higher values on S_{90} when compared to most other substrates at day 6 and a slight decrease at day 9, mirroring mRNA expression (Fig. 4.8b). The fact that Cx43 production on S_{90} was not as high as mRNA expression at day 6 could be explained by a rapid turnover of the protein as it accumulates at the plaques^{19,43}. Confocal z-projections (Fig. 4.8c) of immunostaining show that Cx43 plaques were unevenly distributed within the cell condensates, with a tendency to accumulate in the outer cell layers, although not as evident as seen above for VCL.

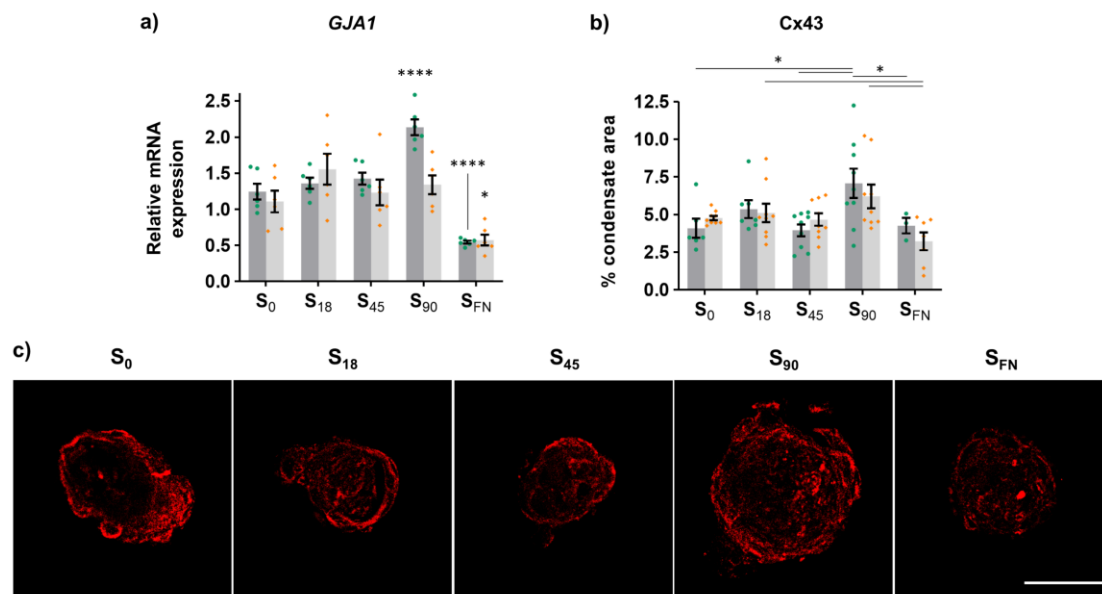


Figure 4.8. Ligand density modulates connexin expression. **a)** Expression of connexin 43 (*GJA1*) mRNA, relative to that of undifferentiated hMSCs (assigned value 1, not shown). **b)** Quantification of Cx43 production from immunostaining in cell condensates. **a, b)** Results at day 6 (dark bars with green dots) and day 9 (light bars with orange rhomboids) of chondrogenesis. Dots and rhomboids represent single sample values, bars indicate the mean \pm SEM, * $p < 0.05$, **** $p < 0.0001$. **c)** Confocal z-projections of Cx43 immunostaining at day 6 of chondrogenesis. Scale bar = 40 μ m.

After observing the effects of substrate ligand density on connexin expression, we aimed to discern whether the level of intercellular connectivity was also altered; in other words, if Cx43 overexpression in S₉₀ translates to the protein network architecture in the developing tissue. We employed Fiji plugins to skeletonize the Cx43 immunostaining images (Fig. 4.9a, top; Video 4.1). Observation of the resulting network skeletons suggested a higher degree of architectural connectivity on S₉₀ when compared to S₀ (Fig. 4.9a, zoomed-in images).

Given an entangled complex network of interconnected branches, shorter branches and fewer branch terminations indicate an architecture based on more intricate connections (see Chapter 2, Fig. 2.2). We first measured the average branch length in Cx43 protein networks; while S₉₀ condensates presented the lowest mean values, there were no significant differences other than S₀ condensates having longer branches at day 9 (Fig. 4.9b).

We then quantified the number of branch terminations (labelled as end-point voxels). Once normalised to the amount of Cx43 present in each condensate (measured by the immunostaining area and number of slides in the confocal stack), we took this value as the inverse index for architectural connectivity, given that more branch terminations within a same amount of protein

would indicate a lower degree of connectivity in the network (Fig. 4.9c). At days 6 and 9 of chondrogenic induction, Cx43 architectural connectivity progressively increased with local surface adhesiveness up to S_{90} and decreased for S_{FN} . At day 9, S_{90} presented significantly higher connectivity than all other conditions except for S_{45} .

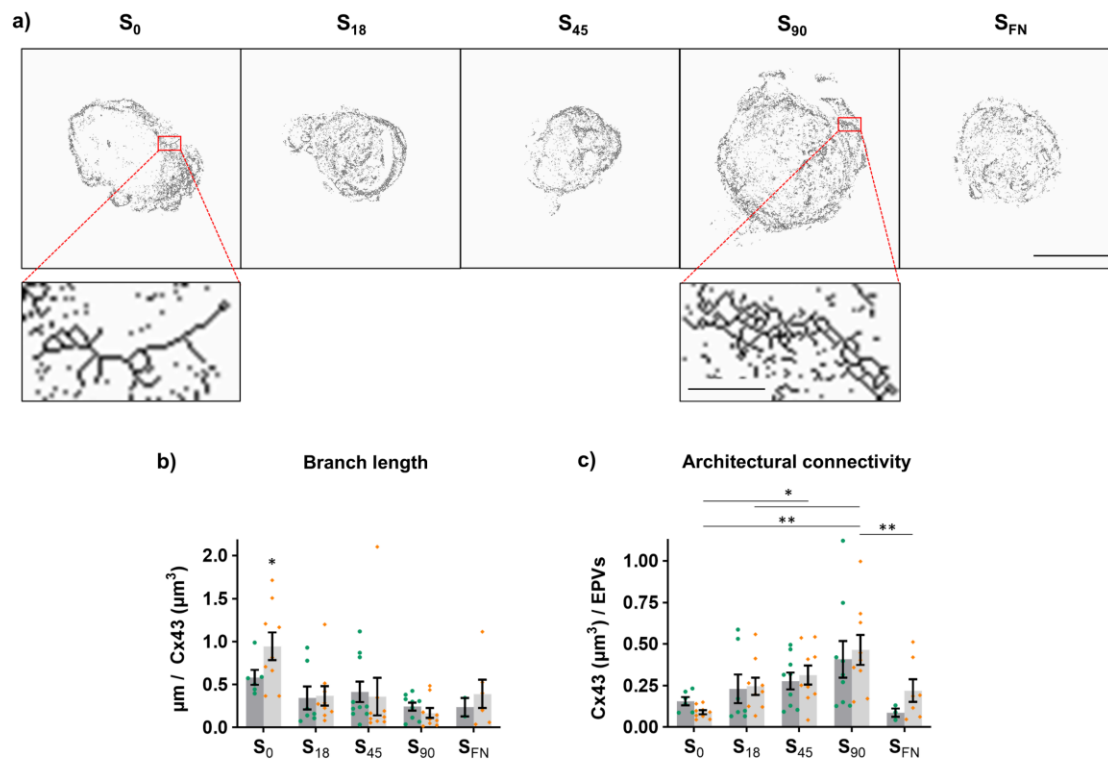


Figure 4.9: Ligand density modulates gap junction network architecture. **a)** Top: Skeletonized z-projections of Cx43 immunostaining reveal the branched architecture of the intercellular connectivity network. Scale bar = 40 μm . Bottom: Zoomed-in sections of S_0 and S_{90} highlight observable differences in the network architecture. Scale bar = 3 μm . **b)** Average length of Cx43 branches from skeletonized images, normalized to Cx43 protein staining. **c)** Cx43 network architectural connectivity calculated as the inverse of the number of end-point voxels (EPVs), normalized to protein staining. Dots and rhomboids represent single sample values, bars indicate the mean \pm SEM, * $p < 0.05$, ** $p < 0.01$

Next, we set out to determine whether substrate ligand density effects on both Cx43 expression and its spatial organization had repercussions in the functionality of intercellular communication, an important factor during cartilage development. Observation of the uptake of biotinylated or fluorescent tracers is one of the most common methods of demonstrating gap junction network coupling; blocking GJIC impairs the transfer of tracers such as calcein or neurobiotin (NB)^{66,67}. Dyes can permeate through the exposed Cx43 connexons and diffuse inwards across the GJIC network when Ca^{2+} is maintained below physiological levels (open channel conformation)⁶⁸. Therefore, to assess the functionality of GJIC networks, we conducted a

neurobiotin tracer uptake assay in cell condensates. In this assay, samples at day 6 of chondrogenic induction were exposed to a buffer (without Ca^{2+} , to induce channel opening) containing NB for a set amount of time before staining with a corresponding fluorophore. Assuming hemichannel permeability to not be rate-limiting⁶⁹, the measured uptake of NB should be representative of the GJIC efficiency in tracer spreading within mesenchymal cell condensates.

We first exposed the samples for 10 minutes to ensure that the tracer would permeate the condensates; however, this resulted in condensates on all conditions almost filled with tracer, which made any differences in the uptake distance unobservable (Fig. 4.10a). This was solved by reducing the time of exposure to 90 seconds, which rendered condensates only partially filled with tracer and thus allowed for observation of the uptake distance (Fig. 4.10b). Quantification of NB diffusion into cell condensates showed uptake was higher in S_{90} nanopatterns (mean value of 11.5 μm) while statistically equal on all other substrates (mean values of 6.8 to 8.1 μm) (Fig. 4.10c). Given the 90-second exposure time, the mean uptake speed of NB in condensates ranged from 4.5 $\mu\text{m}/\text{min}$ on S_{FN} to 7.7 $\mu\text{m}/\text{min}$ on S_{90} .

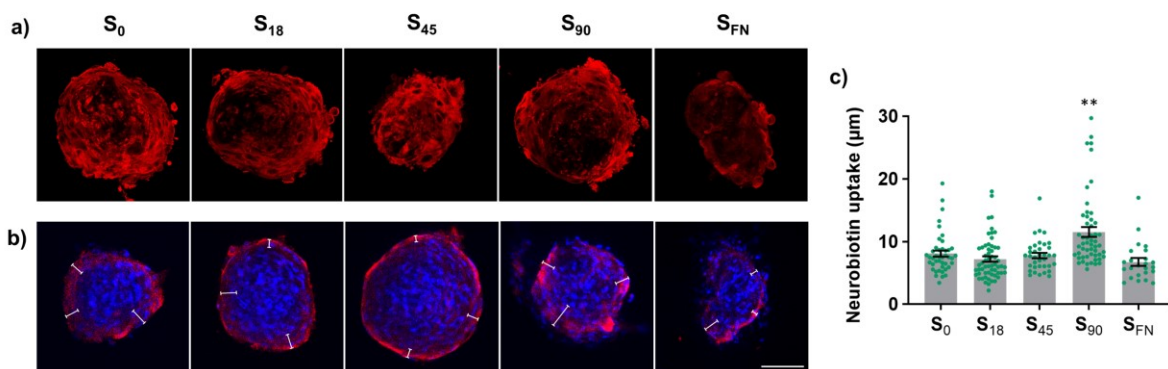


Figure 4.10. Gap junction intercellular communication network functionality. **a)** Confocal z-projections showing neurobiotin tracer (red) after 10 min of exposure on condensates at day 6 of chondrogenic induction. **b)** Confocal z-projections showing neurobiotin tracer (red) and cell nuclei (blue) after 90 s of exposure. White lines are examples of tracer uptake measured distances. **a, b)** Scale bar = 80 μm . **c)** Quantification of tracer uptake after 90 s of exposure. Dots represent single sample values, bars indicate the mean \pm SEM, ** $p < 0.01$

4.2.3. Condensate transplantation assay

Results showed an effect of local surface adhesiveness on intercellular communication network architecture and functionality of pre-cartilaginous cell condensates. We then questioned whether substrate adhesion is relevant only at the beginning of condensation, as a memory effect, or if it continuously influences the tissue as it forms. To consider these two possibilities, we designed a transplantation assay in which condensates formed on S_{90} and S_{18} were collected at day 3, plated on new S_{90} and S_{18} substrates and maintained for 3 more days in culture (Fig. 4.11a). The percentage of area immunostained for Cx43 was assessed at day 6 for the transplanted and non-transplanted condensates. Transplantation from S_{90} or S_{18} to fresh S_{90} substrates caused a significant increase in Cx43 production, of $71 \pm 21\%$ and $61 \pm 19\%$ (mean \pm SEM) in each case. On the other hand, transplantation of either S_{90} or S_{18} condensates to fresh S_{18} substrates did not render significant changes in Cx43 production (Fig. 4.11b).

Condensates formed on one substrate and then transplanted to another will sense the new input only from the basal side, which is in direct contact with the new substrate. We investigated if effects derived from changing substrate conditions would be confined to cells at the basal layer of condensates or instead propagate thorough the forming tissue to the apical layer of condensates. Lateral projections of transplanted condensates presented increased Cx43 production at all heights (Fig. 4.11c), showing that fresh substrate inputs spread through cells and modulated protein expression within the whole forming tissue. Moreover, the proportion of Cx43 between the basal versus apical regions was equal in control and transplanted condensates, indicating that transplantation did not alter the ratios of protein distribution between condensate layers (Fig. 4.11d).

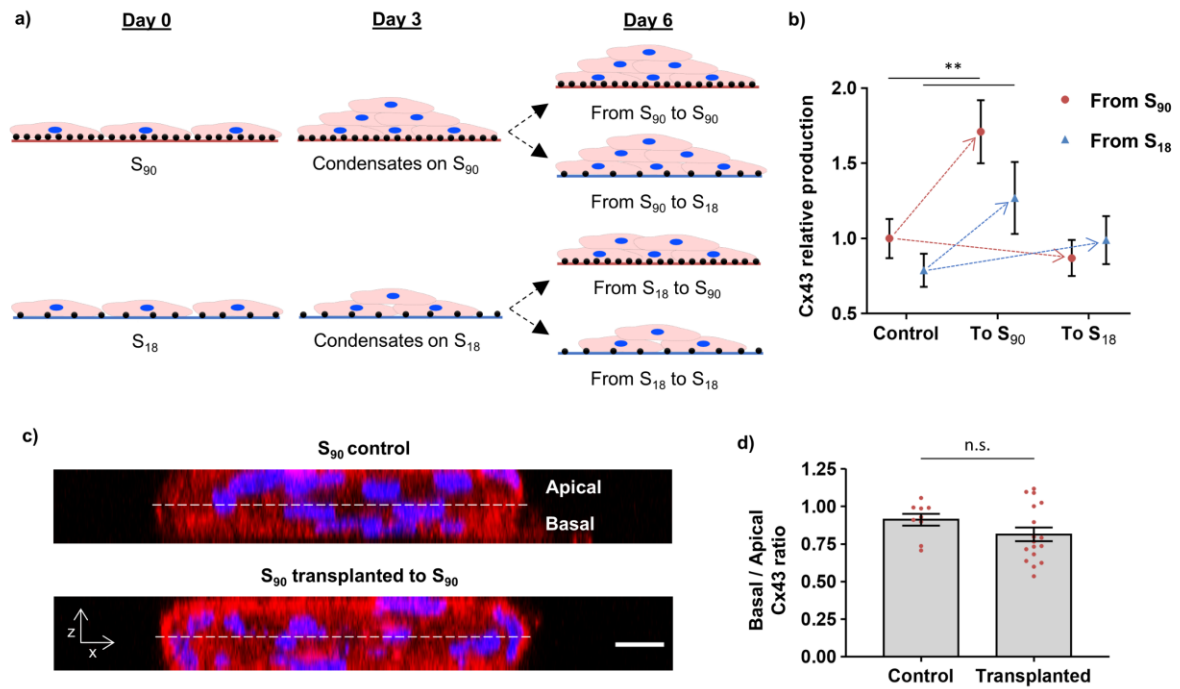


Figure 4.11. Cell condensates adapt to changing ligand density. **a)** Schematics of the transplantation experiment. Cell condensates formed on S_{90} and S_{18} substrates were collected at day 3 and plated on fresh S_{90} or S_{18} substrates for 3 more days of chondrogenic induction. Black dots represent dendrimers (not to scale). **b)** Quantification of Cx43-stained percentage area for non-transplanted and transplanted condensates at day 6, $**p < 0.01$. **c)** Confocal lateral projections of control and transplanted S_{90} condensates, stained for Cx43 (red) and Hoechst (blue). Scale bar = 10 μm . **d)** Ratio between Cx43 staining intensity at the basal and apical regions of S_{90} condensates, in control substrates or transplanted to fresh S_{90} . Dots represent single sample values, bars indicate the mean \pm SEM, n.s.: not significant.

4.2.4. Integrin blocking and myosin inhibition

Integrin adhesions are the main mediators of cell-matrix adhesion and mechanotransduction^{70,71}. To evaluate their role in modulating GJIC during mesenchymal condensation, we performed an assay intended to impair integrin-dendrimer interactions. We cultured MSCs on nanopatterned substrates, allowing them to form multicellular condensates, and then added dendrimers in solution to block integrin receptors at the cell membrane. The presence of new binding ligands in solution would compete with substrate-adsorbed ligands and hinder integrin clustering (see Chapter 3, Fig. 3.11). If substrate effects on Cx43 expression were indeed due to ligand density, this treatment would mask them. Disturbance of cell-substrate adherence led to a decrease in Cx43 on S_{90} but not on S_{18} (Fig. 4.12a). This indicates that integrin-mediated cell adhesion is responsible for the transduction and regulation of substrate information that affects GJIC, and that cell response is maximized when integrins are engaged by the RGD configuration provided by S_{90} nanopatterns.

Since perturbations at the cell membrane are transduced into chemical responses by propagation from integrins through the cytoskeleton^{51,72}, the mechanism by which substrate information diffuses within the cell condensates to establish the GJIC network may involve the actin cortex. The actomyosin cell cortex, attached to the cytoplasmic side of the cell membrane, provides mechanical cohesiveness at the cellular level⁷³. Cortical tension gradients are responsible for mesenchymal cell rearrangement during tissue formation and are essential in driving tissue morphogenesis^{74–76}. Myosin-II pulls on actin filaments and generates tension⁷⁷; inhibition of myosin-II activity can cause a decrease in cortical tension of up to 80%⁷⁵. We observed cortical actin structures in mesenchymal condensates on nanopatterned substrates, as described above (Fig. 4.6). Treatment of day-6 condensates with the myosin-II inhibitor blebbistatin significantly decreased the percentage of area immunostained for Cx43 in S_{90} condensates but not in S_{18} ones, as described above also for integrin blocking (Fig. 4.12a).

To evaluate the impact of both treatments on cytoskeletal conformation, we stained condensates in each case for actin. Control condensates presented the expected cortical actin disposition. In-solution dendrimers and blebbistatin affected cytoskeletal conformation in a similar manner, inducing a more diffuse distribution of actin in condensates instead of concentrating in clearly defined cortical structures as in control conditions (Fig. 4.12b). This indicates that cytoskeletal conformation in mesenchymal condensates was dependent of cytoskeletal tension, as expected, but also of cell-substrate integrin adhesions. We thus infer that

cells at the basal layer of condensates sense ligand inputs through integrins and propagate them by actin contractility to adjacent cells.

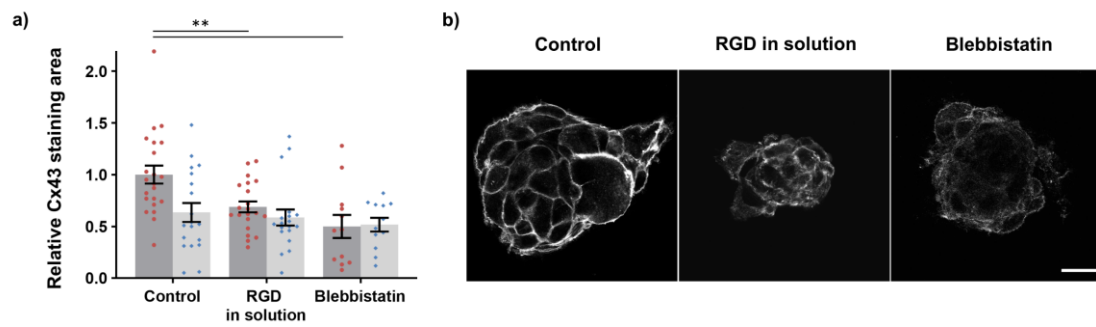


Figure 4.12. Effects of integrin blocking and myosin inhibition. a) Relative amount of Cx43 production on S₉₀ (dark bars with red dots) and S₁₈ (light bars with blue rhomboids). Dots and rhomboids represent single sample values, bars indicate the mean ± SEM; ***p* < 0.01. **b)** Actin staining for S₉₀ condensates at day 6 in control conditions, with RGD dendrimers in solution (integrin blocking) or with blebbistatin (myosin inhibition). Scale bar = 25 μm.

4.3. Discussion

4.3.1. Ligand density regulates condensate structure, stability and GJIC

We studied the effects of the nanoscale adhesiveness of the substrate on the establishment of GJIC during mesenchymal cell condensation, a prevalent morphogenetic transition⁷⁸. Because cells formed condensates only when cultured in differentiation medium, we can say that the observed multicellular aggregates are formed as a direct effect of chondrogenesis induction. Moreover, all substrates supported active cells up to at least day 7 of culture, both as a monolayer and in condensates. This shows that the present substrates are appropriate for long-term cell culture, and that the formation of three-dimensional structures did not subject cells to excessively straining conditions.

Larger and more stable cell condensates were obtained on S_{90} nanopatterns. Condensates on S_{18} took longer than those on the rest of nanopatterns to reach the same size (by day 9 of culture). While we expected that cells would condensate more slowly on S_{18} than on high-adherence nanopatterns, we were surprised to see that they were also slower than those on S_0 . This could be explained by cells tending to form stable cell-cell junctions with greater ease on S_0 than on S_{18} , given the lack of competing substrate adhesion sites in the non-patterned substrates. Previous works have revealed similar levels of paxillin expression on S_0 and S_{18} , showing that presenting cells with only 18% of surface area covered with ligands is not enough to facilitate adhesion formation^{79,80}. However, S_{18} substrates might provide enough adherence to make cell-cell attachment less favourable. Finally, condensates on S_{FN} are formed through a different mechanism than those on nanopatterned substrates (as discussed in Chapter 3, Fig. 3.9), explaining their slower rate of growth.

S_{45} condensates at day 6 were generally larger than S_{90} ones (with 5 out of 10 measured condensates larger than $10,000 \mu\text{m}^2$, compared to 3 out of 9), a difference that disappeared by day 9. This could be explained by cells aggregating in a more disorganized manner on S_{45} (supported by the results in the rate of cell-cell collisions in Chapter 3, Fig. 3.7), leading to assembled structures that are less stable long-term than those formed on S_{90} , at an optimal speed and on a substrate that retains basal cells in place rather than allowing them to migrate out of condensates. Only S_{90} condensates remained structurally stable until at least day 14 of differentiation, showcasing the importance of optimal tissue-matrix adherence to sustain the anlagen that are a crucial stage of cartilage development.

Nuclei in high-adherence substrates (S_{90} and S_{FN}) were closer together than those on low- and mid-adherence ones at day 6. This indicates a tighter spatial distribution, or packaging, of cells in those condensates. While this could be attributed to cells on S_{90} being more differentiated towards chondrocytes (see Chapter 5, Fig. 5.6), and thus possibly presenting a morphology more akin to mature cartilage, that is not the case on S_{FN} . Shorter intercellular distances in condensates at day 6 could be a factor explaining the resistance of large S_{90} condensates to collapse through day 14. In fact, previous studies demonstrated that applying pressure to physically constrain mesenchymal condensates is enough to induce odontogenesis, showing that condensate compaction is a regulator of tissue formation^{81,82}. Interestingly, the binary relation of condensate compactness with substrate adhesiveness is similar to the one we observed for filopodia length at 8 h of differentiation (see Chapter 3, Fig. 3.4): S_0 , S_{18} and S_{45} present the same mean intercellular distance between them, as do S_{90} and S_{FN} . This again points to S_{90} as an optimal condition bridging nanoscale local ligand density with high adhesiveness.

Mechanical inputs are propagated through cells mainly by adherens junctions⁵⁷. To address the increased stability and packed structure of S_{90} condensates, we measured expression of adherens junction protein N-cadherin (*CDH2*) and of cell-cell and cell-matrix junction protein vinculin (*VCL*). Substrate ligand density did not cause any clear variations in *CDH2*, leading to the conclusion that the increased stability and compactness of S_{90} condensates is not due to stronger cell-cell mechanical adhesions. Instead, S_{90} substrates would improve condensate stability through optimal high local adherence (90% of the surface area patterned with high-density ligands). A similar behaviour has been recently described in multi-layered epithelia, which can self-fold during morphogenesis through a mechanism entailing strong cell-substrate adhesions alongside weak cell-cell adhesions, allowing for expansion and subsequent buckling of the tissue⁸³.

Murine sarcoma cells cultured on fibronectin-coated substrates present a negative correlation between spreading and E-cadherin expression⁸⁴, showing that cell-matrix interactions can act as downregulators of cell-cell adhesions. Thus, the results in N-cadherin expression could be explained by intracellular interactions of integrins and cadherins^{85–87}. Downstream signalling of the integrin $\beta 1$ subunit modulates cadherin localization and the integrity of cell-cell junctions during angiogenesis⁸⁸, and regulates clustering of cytoplasmic cadherins into junctions in neural crest cells⁸⁹. In fibronectin-null mouse myofibroblasts, integrin $\alpha 5 \beta 1$ is linked to N-cadherin at cell-cell junctions; upon integrin recruitment to matrix adhesions, N-cadherin is also redistributed,

coordinating cell-cell and cell-matrix adherence⁹⁰. Given that substrate ligand density determines focal adhesion formation and thus integrin clustering⁸⁰, we hypothesize that similar levels of *CDH2* expression among substrates could still generate differently functional networks of cadherin-mediated cell-cell adhesions, affecting condensate cohesiveness.

Cadherin expression in tissue is also proportional to surface tension generated by cortical actin contractions⁶², which presents a second possible mechanism to explain condensate mechanical stability on S_{90} . As opposed to condensate cohesiveness being driven solely through cell-cell adhesions, an optimal balance of integrin adhesions and surface tension would allow condensates to achieve tensional homeostasis, improving their structural stability⁸⁷. Since S_{18} and S_{90} condensates show equal *CDH2* expression levels and thus a similar surface tension, but S_{90} condensates are more stable in culture, we pose that stronger cell-substrate adhesions at the basal layer of condensates on S_{90} provide an adequate balance to the existing tissue tension. This balance is lost in S_{FN} , where a full protein coating hinders condensation.

Finally, integrin adhesions can regulate tissue cohesion by attaching cells to each other through the secreted matrix in between^{91,92}. Therefore, and while further experiments would be required to unveil the specific mechanism behind condensate stability, we can conclude that local surface adhesiveness plays a decisive role in modulating the long-term structural resilience of multicellular condensates during chondrogenesis⁹³.

We had expected *VCL* expression to be higher in condensates of increased mechanical stability and under stronger cell-substrate adherence; counterintuitively, *VCL* was more expressed on low-adherence substrates (S_0 and S_{18} , compared to S_{FN}). We observed through immunostaining that *VCL* was mainly localized at the rim of cell condensates, similarly as observed in amnioserosa cells of embryos undergoing the late stages of dorsal closure, in which *VCL* confers cell cohesiveness and maintains tension⁹⁴. *VCL* also provides structural stability to embryonal carcinoma cell condensates obtained under non-adherent substrate conditions⁹⁵. Many cell types, such as fibroblasts or epithelial cells, tend to aggregate when cultured on low-adherence or soft substrates, but migrate out of explants if cultured on stiff substrates⁹⁶. Thus, we understand the pattern of *VCL* expression as a response of cells on low-adherence substrates to generate cell-cell junctions as an alternative source of stability during condensation, given the lack of cell-substrate adhesions. However, these inferred adhesions would appear not to provide the condensates with the mechanical stability found on S_{90} . *VCL* is a cytoplasmic component of cell-cell adhesion structures other than adherens junctions, meaning that further experiments would be required

to unveil whether *VCL* expression correlates with other proteins such as zonula occludens-1, present at tight junctions.

We then analysed the influence of substrate ligand density on the establishment of a gap junction intercellular communication (GJIC) network in cell condensates. We measured expression and production of Cx43, a connexin which is ubiquitously expressed in developing cartilage^{37,97}. Cx43 facilitates the formation of multicellular aggregates⁹ and mediates cell-cell adhesion during self-assembly of microtissues from human granulosa cells and fibroblasts⁹⁸, which would help explain the improved mechanical stability of S_{90} condensates. Indeed, we found that *GJA1* expression at day 6 of chondrogenesis increased with local surface adhesiveness in the nanopatterns. Cell condensates on S_{90} nanopatterns present increased Cx43 expression with a seemingly higher protein turnover rate, revealing a direct effect of substrate ligand density on gap junction protein regulation.

Besides protein expression, the establishment of a communication network requires an appropriate protein localization. We analysed the architectural connectivity of Cx43 in condensates to assess whether substrate ligand density modulates the development of gap junction networks. We found that S_{90} condensates contain a connexin network that is more intricate, with fewer end-point voxels and shorter branches, indicative of improved communication capacities. Therefore, beyond modulating gene expression profiles at the cellular level, we report an effect of substrate ligand density on the structure of protein networks in the developing tissue.

We evaluated the impact of protein network architecture on its functionality with a neurobiotin uptake assay and found that GJIC is more efficient on S_{90} condensates. The tracer speeds that we measured are similar to the range previously observed in HeLa cells, and which is affected by their levels of Cx43 expression³⁶. Given a mean condensate area of approximately $10,000 \mu\text{m}^2$ for S_{90} , and hence (assuming the circular projected shape that condensates generally present) an average radius of $56 \mu\text{m}$, the measured uptake rates also explain why an exposure time of 10 minutes resulted in condensates nearly filled with tracer.

Overall, these results show that local surface adhesiveness determines not only protein expression but also its spatial disposition during mesenchymal condensation in chondrogenesis, affecting the functionality of the forming tissue. Similarly, hMSCs from apical papilla respond to increasing substrate stiffness by assembling gap junction plaques, resulting in increased

transmission of lucifer yellow tracer, through a process regulated by FAK and paxillin binding to Cx43⁹⁹. This would correspond with increased paxillin expression previously observed on S_{90} substrates⁸⁰, and focal adhesion size in these mesenchymal condensates (Chapter 5, Fig. 5.4).

4.3.2. Substrate adhesion continually regulates GJIC across condensate layers

We designed a condensate transplantation assay to test whether cells in the condensate, previously in contact with the substrate during cell recruitment, retain initial substrate information (memory effect) or receive a continuous feedback of substrate input. Transplantation of cell condensates to a new S_{90} substrate caused a significant increase in Cx43, showing that cell condensates still preserve a certain level of mesenchymal plasticity at early stages of chondrogenic differentiation, allowing phenotype reconfiguration in response to the ECM input. In a non-developmental setting, hMSCs seeded on non-adherent substrates tend to aggregate, which induces an upregulation of stemness factors^{100–102}, allowing for a continuous renewal of cell response to changing environmental conditions.

The fact that condensate transplantation from S_{90} to fresh S_{90} caused a further increase in Cx43 suggests that cells exert a degree of substrate remodelling that masks the original substrate information after at least three days of culture. Cells could generate this effect either through matrix secretion, which would progressively cover the substrate and offer competing adhesion sites to the cells; or by altering the density and distribution of nanopatterned ligands, which is possible because RGD dendrimers are adsorbed but not covalently bound to the substrates. Upon transplantation to fresh substrates of the optimal ligand density (S_{90}), condensates sense the original signals again and respond with further connexin production. Since transplantation to a non-optimal substrate (S_{18}) does not induce any Cx43 production increase, the response observed on S_{90} is specifically due to its local ligand density. We thus conclude that cells continuously sense nanoscale substrate inputs and respond accordingly.

The effects of transplantation on Cx43 expression were observed at all heights within condensates, and transplanted condensates maintained the proportion of total protein contained at the basal and apical regions, indicating that substrate inputs are propagated into the third dimension, across cells to the top. We thus show that changing environmental conditions during morphogenesis continually modulate tissue properties, pointing to the importance of accounting for time variations in the design of biomaterials for tissue engineering.

We addressed the biological mechanism by which cells sense substrate ligand density. Blocking integrin-mediated interactions between the substrate and the basal layer in cell condensates caused a Cx43 decrease in S₉₀ but not in S₁₈. This observation, together with results of condensate stability and GJIC, demonstrates that the establishment of GJIC during mesenchymal condensation is an adhesion-gated mechanism, in which S₉₀ nanopattern configuration provides optimal local ligand density and distribution to trigger cell response.

To investigate the propagation of substrate information within cell condensates, we conducted a myosin-II inhibition assay. Blebbistatin caused a decrease of Cx43 production in S₉₀ cell condensates, in agreement with previous reports showing that connexin recruitment in gap junctions is modulated by their interactions with cytoskeletal structures^{35,103}. Once integrins are engaged, the adhesion information from the substrate is transduced and propagates through the actin filaments by myosin-II mediated contraction, which in turn can regulate GJ accretion through ZO-1⁴³. Cx43 accumulation into GJs and the subsequent GJIC network in a cell monolayer is dependent on myosin-VI¹⁰⁴. In human tenocytes, Cx43 co-localizes with actin only under myosin-II activity¹⁰⁵, showing that mechanical contractions are necessary for gap junctional regulation through cytoskeletal proteins. These results also agree with reports indicating that the dynamics of membrane proteins, such as connexins, are regulated by the cell's actin cortex¹⁰⁶.

Integrin adhesions at the basal plane of a cell monolayer are mechanically connected not only to the nucleus and cytoplasm of the cells^{107,108}, but also to their apical plane; strong cell-substrate adhesions thus stabilize oscillations originating in the apical region of the monolayer¹⁰⁹. In two-dimensional cell clusters, these tensions are propagated through cadherin cell-cell junctions until they are compensated either by cell-substrate adhesions or by cytoskeletal contractions¹¹⁰. Recent studies show that actomyosin tensions modulate tissue fluidity at the supracellular scale to allow for morphogenetic events such as wound closure^{57,111,112}. Therefore, we propose a contractility-based mechanism for the propagation of ECM adhesion information within the condensates, in which local substrate adhesiveness induces a rearrangement and adaptation of the actin cortex and cell-cell junctions in the first cell layers and propagates through the tissue by actomyosin contractions, regulating Cx43 expression and network architecture during mesenchymal condensation in early chondrogenesis¹¹³ (Fig. 4.13).

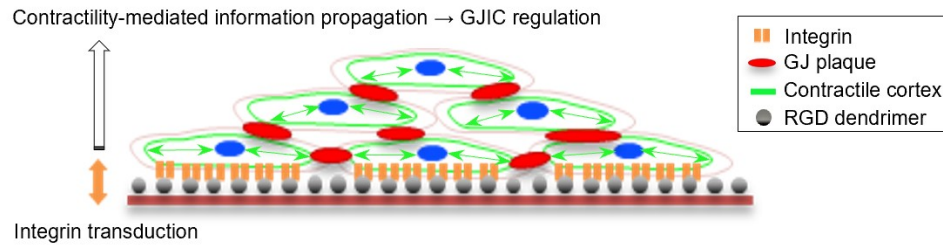


Fig. 4.13. Proposed model for substrate input sensing and propagation. Schematic representation of ligand density sensing through integrin adhesions, followed by actomyosin contraction-guided propagation of information in cell condensates.

The structural and mechanical properties of developing cartilage has been described in a mouse model¹¹⁴. AFM observation of the matrix secreted by cells at E13.5 showed that it is comprised by a meshwork of randomly oriented collagen fibrils. These fibrils contain integrin-binding sites, mostly located within the overlapping regions (axial D-periodicity of 67 nm), and the interfibrillar space could also contain other integrin-binding proteins^{115,116}. This indicates that *in vivo* cartilage development requires a highly adherent matrix surrounding the cells. Therefore, the S₉₀ configuration, in which 90% of the surface area contains adhesion sites with a local spacing lower than 70 nm, could be emulating the native disposition of integrin binding sites in the ECM of developing cartilage, favouring mesenchymal cell condensation and differentiation.

4.4. References

1. DeLise, A. M., Fischer, L. & Tuan, R. S. Cellular interactions and signaling in cartilage development. *Osteoarthr. Cartil.* **8**, 309–334 (2000).
2. Grüneberg, H. *The pathology of development: a study of inherited skeletal disorders in animals.* (Blackwells Scientific Publications, 1963).
3. Hall, B. K. & Miyake, T. The membranous skeleton: the role of cell condensations in vertebrate skeletogenesis. *Anat. Embryol. (Berl)*. **186**, 107–124 (1992).
4. Shimizu, H., Yokoyama, S. & Asahara, H. Growth and differentiation of the developing limb bud from the perspective of chondrogenesis. *Dev. Growth Differ.* **49**, 449–454 (2007).
5. Coelho, C. N. D. & Kosher, R. A. Gap junctional communication during limb cartilage differentiation. *Dev. Biol.* **144**, 47–53 (1991).
6. Hervé, J. C. & Derangeon, M. Gap-junction-mediated cell-to-cell communication. *Cell Tissue Res.* **352**, 21–31 (2013).
7. Xu, X. *et al.* Modulation of mouse neural crest cell motility by N-cadherin and connexin 43 gap junctions. *J. Cell Biol.* **154**, 217–229 (2001).
8. Lin, J. H. C. *et al.* Connexin 43 Enhances the Adhesivity and Mediates the Invasion of Malignant Glioma Cells. *J. Neurosci.* **22**, 4302–4311 (2002).
9. Cotrina, M. L., Lin, J. H.-C. & Nedergaard, M. Adhesive Properties of Connexin Hemichannels. *Glia* **56**, 1791–1798 (2008).
10. Kotini, M. & Mayor, R. Connexins in migration during development and cancer. *Dev. Biol.* **401**, 143–151 (2015).
11. Ho, K. Y. L., Khadilkar, R. J., Carr, R. L. & Tanentzapf, G. A gap-junction-mediated, calcium-signaling network controls blood progenitor fate decisions in hematopoiesis. *Curr. Biol.* **31**, 1–16 (2021).
12. Wei, C. J., Xu, X. & Lo, C. W. Connexins and cell signaling in development and disease. *Annu. Rev. Cell Dev. Biol.* **20**, 811–838 (2004).
13. Glen, C. M., McDevitt, T. C. & Kemp, M. L. Dynamic intercellular transport modulates the spatial patterning of differentiation during early neural commitment. *Nat. Commun.* **9**, 4111 (2018).
14. Plotkin, L. I. & Stains, J. P. Connexins and pannexins in the skeleton: gap junctions,

- hemichannels and more. *Cell. Mol. Life Sci.* **72**, 2853–2867 (2015).
15. Mayan, M. D. *et al.* Articular chondrocyte network mediated by gap junctions: Role in metabolic cartilage homeostasis. *Ann. Rheum. Dis.* **74**, 275–284 (2015).
 16. Donahue, H. J., Qu, R. W. & Genetos, D. C. Joint diseases: From connexins to gap junctions. *Nat. Rev. Rheumatol.* **14**, 42–51 (2018).
 17. Krysko, D. V., Leybaert, L., Vandenameele, P. & D’Herde, K. Gap junctions and the propagation of cell survival and cell death signals. *Apoptosis* **10**, 459–469 (2005).
 18. Piehl, M. *et al.* Internalization of Large Double-Membrane Intercellular Vesicles by a Clathrin-dependent Endocytic Process. *Mol. Biol. Cell* **18**, 337–347 (2007).
 19. Leithe, E., Sirnes, S., Fykerud, T., Kjenseth, A. & Rivedal, E. Endocytosis and post-endocytic sorting of connexins. *Biochim. Biophys. Acta - Biomembr.* **1818**, 1870–1879 (2012).
 20. Goodenough, D. A. & Paul, D. L. Beyond the gap: Functions of unpaired connexon channels. *Nat. Rev. Mol. Cell Biol.* **4**, 285–294 (2003).
 21. Fujii, Y., Maekawa, S. & Morita, M. Astrocyte calcium waves propagate proximally by gap junction and distally by extracellular diffusion of ATP released from volume- regulated anion channels. *Sci. Rep.* **7**, 13115 (2017).
 22. Ribeiro-Rodrigues, T. M., Martins-Marques, T., Morel, S., Kwak, B. R. & Girão, H. Role of connexin 43 in different forms of intercellular communication - gap junctions, extracellular vesicles and tunnelling nanotubes. *J. Cell Sci.* **130**, 3619–3630 (2017).
 23. Civitelli, R. *et al.* Connexin43 Mediates Direct Intercellular Communication in Human Osteoblastic Cell Networks. *The J. Clin. Investig.* **91**, 1888–1896 (1993).
 24. Richardson, R. R., Donnai, D., Meire, F. & Dixon, M. J. Expression of Gja1 correlates with the phenotype observed in oculodentodigital syndrome/type III syndactyly. *J. Med. Genet.* **41**, 60–67 (2004).
 25. Mayan, M. D., Carpintero-fernandez, P., Gago-fuentes, R., Martinez-de-ildaruya, O. & Wang, H. Human Articular Chondrocytes Express Multiple Gap Junction Proteins Differential Expression of Connexins in Normal and Osteoarthritic Cartilage. *Am. J. Pathol.* **182**, 1337–1346 (2013).
 26. Buo, A. M. & Stains, J. P. Gap Junctional Regulation of Signal Transduction in Bone Cells. *FEBS Lett.* **588**, 1315–1321 (2014).

27. Buo, A. M., Tomlinson, R. E., Eidelman, E. R., Chason, M. & Stains, J. P. Connexin43 and Runx2 Interact to Affect Cortical Bone Geometry, Skeletal Development, and Osteoblast and Osteoclast Function. *J. Bone Miner. Res.* **32**, 1727–1738 (2017).
28. Schrobback, K., Klein, T. J. & Woodfield, T. B. F. The Importance of Connexin Hemichannels During Chondroprogenitor Cell Differentiation in Hydrogel Versus Microtissue Culture Models. *Tissue Eng. Part A* **21**, 1785–1794 (2015).
29. Lecanda, F. *et al.* Gap Junctional Communication Modulates Gene Expression in Osteoblastic Cells. *Mol. Biol. Cell* **9**, 2249–2258 (1998).
30. Lecanda, F. *et al.* Connexin43 Deficiency Causes Delayed Ossification, Craniofacial Abnormalities, and Osteoblast Dysfunction. *J. Cell Biol.* **151**, 931–943 (2000).
31. McLachlan, E. *et al.* ODDD-Linked Cx43 Mutants Reduce Endogenous Cx43 Expression and Function in Osteoblasts and Inhibit Late Stage Differentiation. *J. Bone Miner. Res.* **23**, 928–938 (2008).
32. Hervé, J. C., Derangeon, M., Sarrouilhe, D., Giepmans, B. N. G. & Bourmeyster, N. Gap junctional channels are parts of multiprotein complexes. *Biochim. Biophys. Acta - Biomembr.* **1818**, 1844–1865 (2012).
33. Leithe, E., Mesnil, M. & Aasen, T. The connexin 43 C-terminus: A tail of many tales. *Biochim. Biophys. Acta - Biomembr.* **1860**, 48–64 (2018).
34. Thomas, T. *et al.* Mechanism of Cx43 and Cx26 transport to the plasma membrane and gap junction regeneration. *J. Cell Sci.* **118**, 4451–4462 (2005).
35. Olk, S., Zoidl, G. & Dermietzel, R. Connexins, cell motility, and the cytoskeleton. *Cell Motil. Cytoskeleton* **66**, 1000–1016 (2009).
36. Rhett, J. M., Jourdan, J. & Gourdie, R. G. Connexin 43 connexon to gap junction transition is regulated by zonula occludens-1. *Mol. Biol. Cell* **22**, 1516–1528 (2011).
37. Gago-Fuentes, R. *et al.* The C-terminal domain of connexin43 modulates cartilage structure via chondrocyte phenotypic changes. *Oncotarget* **7**, 73055–73067 (2016).
38. Pacheco-Costa, R. *et al.* Defective cancellous bone structure and abnormal response to PTH in cortical bone of mice lacking Cx43 cytoplasmic C-terminus domain. *Bone* **81**, 632–643 (2015).
39. Hammond, M. A. *et al.* Removing or truncating connexin 43 in murine osteocytes alters cortical geometry, nanoscale morphology, and tissue mechanics in the tibia. *Bone* **88**, 85–91 (2016).

40. Plotkin, L. I. & Bellido, T. Beyond gap junctions : Connexin43 and bone cell signaling. *Bone* **52**, 157–166 (2013).
41. Lampe, P. D. *et al.* Cellular interaction of integrin $\alpha 3\beta 1$ with laminin 5 promotes gap junctional communication. *J. Cell Biol.* **143**, 1735–1747 (1998).
42. Batra, N. *et al.* Mechanical stress-activated integrin $\alpha 5\beta 1$ induces opening of connexin 43 hemichannels. *Proc. Natl. Acad. Sci.* **109**, 3359–3364 (2012).
43. Zemljic-Harpf, A. E. *et al.* Vinculin directly binds zonula occludens-1 and is essential for stabilizing connexin-43-containing gap junctions in cardiac myocytes. *J. Cell Sci.* **127**, 1104–1116 (2014).
44. Mori, R., Power, K. T., Wang, C. M., Martin, P. & Becker, D. L. Acute downregulation of connexin43 at wound sites leads to a reduced inflammatory response, enhanced keratinocyte proliferation and wound fibroblast migration. *J. Cell Sci.* **119**, 5193–5203 (2006).
45. Mendoza-Naranjo, A. *et al.* Targeting Cx43 and N-Cadherin, Which Are Abnormally Upregulated in Venous Leg Ulcers, Influences Migration, Adhesion and Activation of Rho GTPases. *PLoS One* **7**, e37374 (2012).
46. Wright, C. S., Pollok, S., Flint, D. J., Brandner, J. M. & Martin, P. E. M. The Connexin Mimetic Peptide Gap27 Increases Human Dermal Fibroblast Migration in Hyperglycemic and Hyperinsulinemic Conditions In Vitro. *J. Cell. Biochem.* **227**, 77–87 (2012).
47. Lorraine, C., Wright, C. S. & Martin, P. E. Connexin43 plays diverse roles in co-ordinating cell migration and wound closure events. *Biochem. Soc. Trans.* **43**, 482–488 (2015).
48. Faniku, C. *et al.* The Connexin Mimetic Peptide Gap27 and Cx43-Knockdown Reveal Differential Roles for Connexin43 in Wound Closure Events in Skin Model Systems. *Int. J. Mol. Sci.* **19**, 604 (2018).
49. Gumbiner, B. M. Cell adhesion: The molecular basis of tissue architecture and morphogenesis. *Cell* **84**, 345–357 (1996).
50. Parsons, J. T., Horwitz, A. R. & Schwartz, M. A. Cell adhesion: Integrating cytoskeletal dynamics and cellular tension. *Nat. Rev. Mol. Cell Biol.* **11**, 633–643 (2010).
51. Bachmann, M., Kukkurainen, S., Hytönen, V. P. & Wehrle-Haller, B. Cell adhesion by integrins. *Physiol. Rev.* **99**, 1655–1699 (2019).
52. Van Essen, D. C. A tension-based theory of morphogenesis and compact wiring in the central

- nervous system. *Nature* **385**, 313–318 (1997).
53. Tada, M. & Concha, M. L. Vertebrate gastrulation: Calcium waves orchestrate cell movements. *Curr. Biol.* **11**, 470–472 (2001).
 54. Tseng, Q. *et al.* Spatial organization of the extracellular matrix regulates cell–cell junction positioning. *Proc. Natl. Acad. Sci.* **109**, 1506–1511 (2012).
 55. Shih, H. P., Panlasigui, D., Cirulli, V. & Sander, M. ECM signaling regulates collective cellular dynamics to control pancreas branching morphogenesis. *Cell Rep.* **14**, 169–179 (2016).
 56. Goodwin, K. & Nelson, C. M. Mechanics of Development. *Dev. Cell* **56**, 240–250 (2020).
 57. Clarke, D. N. & Martin, A. C. Actin-based force generation and cell adhesion in tissue morphogenesis. *Curr. Biol.* **31**, R667–R680 (2021).
 58. Bobick, B. E., Chen, F. H., Le, A. M. & Tuan, R. S. Regulation of the chondrogenic phenotype in culture. *Birth Defects Res. Part C - Embryo Today Rev.* **87**, 351–371 (2009).
 59. Papadopoulos, N. G. *et al.* An improved fluorescence assay for the determination of lymphocyte-mediated cytotoxicity using flow cytometry. *J. Immunol. Methods* **177**, 101–111 (1994).
 60. Chalut, K. J. & Paluch, E. K. The Actin Cortex: A Bridge between Cell Shape and Function. *Dev. Cell* **38**, 571–573 (2016).
 61. Chugh, P. & Paluch, E. K. The actin cortex at a glance. *J. Cell Sci.* **131**, 1–9 (2018).
 62. Foty, R. A. & Steinberg, M. S. The differential adhesion hypothesis: A direct evaluation. *Dev. Biol.* **278**, 255–263 (2005).
 63. Le Duc, Q. *et al.* Vinculin potentiates E-cadherin mechanosensing and is recruited to actin-anchored sites within adherens junctions in a myosin II-dependent manner. *J. Cell Biol.* **189**, 1107–1115 (2010).
 64. Charras, G. & Yap, A. S. Tensile Forces and Mechanotransduction at Cell–Cell Junctions. *Curr. Biol.* **28**, R445–R457 (2018).
 65. Cosgrove, B. D. *et al.* N-cadherin adhesive interactions modulate matrix mechanosensing and fate commitment of mesenchymal stem cells. *Nat. Mater.* **15**, 1297–1306 (2016).
 66. Achilli, T.-M., McCalla, S., Meyer, J., Tripathi, A. & Morgan, J. R. Multilayer Spheroids To Quantify Drug Uptake and Diffusion in 3D. *Mol. Pharm.* **11**, 2071–2081 (2014).

67. Jacoby, J., Nath, A., Jessen, Z. F. & Schwartz, G. W. A Self-Regulating Gap Junction Network of Amacrine Cells Controls Nitric Oxide Release in the Retina. *Neuron* **100**, 1149–1162.e5 (2018).
68. Thimm, J., Mechler, A., Lin, H., Rhee, S. & Lal, R. Calcium-dependent open/closed conformations and interfacial energy maps of reconstituted hemichannels. *J. Biol. Chem.* **280**, 10646–10654 (2005).
69. Sáez, J. C., Retamal, M. A., Basilio, D., Bukauskas, F. F. & Bennett, M. V. L. Connexin-based gap junction hemichannels: Gating mechanisms. *Biochim. Biophys. Acta* **1711**, 215–224 (2005).
70. Sun, Z., Guo, S. S. & Fässler, R. Integrin-mediated mechanotransduction. *J. Cell Biol.* **215**, 445–456 (2016).
71. Kechagia, J. Z., Ivaska, J. & Roca-Cusachs, P. Integrins as biomechanical sensors of the microenvironment. *Nat. Rev. Mol. Cell Biol.* **20**, 457–473 (2019).
72. Coravos, J. S., Mason, F. M. & Martin, A. C. Actomyosin Pulsing in Tissue Integrity Maintenance during Morphogenesis. *Trends Cell Biol.* **27**, 276–283 (2017).
73. Vignaud, T. *et al.* Stress fibres are embedded in a contractile cortical network. *Nat. Mater.* **20**, 410–420 (2021).
74. Nishikawa, M., Naganathan, S. R., Jülicher, F. & Grill, S. W. Controlling contractile instabilities in the actomyosin cortex. *Elife* **6**, e19595 (2017).
75. Tao, H. *et al.* Oscillatory cortical forces promote three dimensional cell intercalations that shape the murine mandibular arch. *Nat. Commun.* **10**, 1–18 (2019).
76. Kelkar, M., Bohec, P. & Charras, G. Mechanics of the cellular actin cortex: From signalling to shape change. *Curr. Opin. Cell Biol.* **66**, 69–78 (2020).
77. Truong Quang, B. A. *et al.* Extent of myosin penetration within the actin cortex regulates cell surface mechanics. *Nat. Commun.* **12**, 6511 (2021).
78. Thesleff, I., Vaahtokari, A. & Partanen, A. M. Regulation of organogenesis. Common molecular mechanisms regulating the development of teeth and other organs. *Int. J. Dev. Biol.* **39**, 35–50 (1995).
79. Lagunas, A. *et al.* Large-scale dendrimer-based uneven nanopatterns for the study of local arginine-glycine-aspartic acid (RGD) density effects on cell adhesion. *Nano Res.* **7**, 399–409 (2014).

Chapter 4

80. Lagunas, A. *et al.* Tailoring RGD local surface density at the nanoscale toward adult stem cell chondrogenic commitment. *Nano Res.* **10**, 1959–1971 (2017).
81. Hashmi, B. *et al.* Developmentally-Inspired Shrink-Wrap Polymers for Mechanical Induction of Tissue Differentiation. *Adv. Mater.* **26**, 3253–3257 (2014).
82. Hashmi, B. *et al.* Mechanical induction of dentin-like differentiation by adult mouse bone marrow stromal cells using compressive scaffolds. *Stem Cell Res.* **24**, 55–60 (2017).
83. Wang, S., Matsumoto, K., Lish, S. R., Cartagena-Rivera, A. X. & Yamada, K. M. Budding epithelial morphogenesis driven by cell-matrix versus cell-cell adhesion. *Cell* **184**, 1–15 (2021).
84. Al-Kilani, A., Freitas, O. De, Dufour, S. & Gallet, F. Negative Feedback from Integrins to Cadherins: A Micromechanical Study. *Biophys. J.* **101**, 336–344 (2011).
85. Yano, H. *et al.* Roles played by a subset of integrin signaling molecules in cadherin-based cell-cell adhesion. *J. Cell Biol.* **166**, 283–295 (2004).
86. Weber, G. F., Bjerke, M. A. & DeSimone, D. W. Integrins and cadherins join forces to form adhesive networks. *J. Cell Sci.* **124**, 1183–1193 (2011).
87. Mui, K. L., Chen, C. S. & Assoian, R. K. The mechanical regulation of integrin–cadherin crosstalk organizes cells, signaling and forces. *J. Cell Sci.* **129**, 1093–1100 (2016).
88. Yamamoto, H. *et al.* Integrin beta1 controls VE-cadherin localization and blood vessel stability. *Nat. Commun.* **6**, 6429 (2015).
89. Monier-Gavelle, F. & Duband, J. Cross Talk between Adhesion Molecules: Control of N-cadherin Activity by Intracellular Signals Elicited by beta1 and beta3 Integrins in Migrating Neural Crest Cells. *J. Cell Biol.* **137**, 1663–1681 (1997).
90. Lefort, C. T., Wojciechowski, K. & Hocking, D. C. N-cadherin Cell-Cell Adhesion Complexes Are Regulated by Fibronectin Matrix Assembly. *J. Biol. Chem.* **286**, 3149–3160 (2011).
91. Robinson, E. E., Zazzali, K. M., Corbett, S. A. & Foty, R. A. Alpha5beta1 integrin mediates strong tissue cohesion. *J. Cell Sci.* **116**, 377–386 (2003).
92. Caicedo-Carvajal, C. E., Shinbrot, T. & Foty, R. A. $\alpha 5 \beta 1$ integrin-fibronectin interactions specify liquid to solid phase transition of 3D cellular aggregates. *PLoS One* **5**, e11830 (2010).
93. Casanellas, I. *et al.* The Janus role of adhesion in chondrogenesis. *Int. J. Mol. Sci.* **21**, 5269 (2020).

94. Jurado, J., Navascués, J. de & Gorfinkiel, N. α -Catenin stabilises Cadherin-Catenin complexes and modulates actomyosin dynamics to allow pulsatile apical contraction. *J. Cell Sci.* **129**, 4496–4508 (2016).
95. Tozeren, A. *et al.* Vinculin and cell-cell adhesion. *Cell Adhes. Commun.* **5**, 49–59 (1998).
96. Guo, W., Frey, M. T., Burnham, N. A. & Wang, Y. Substrate Rigidity Regulates the Formation and Maintenance of Tissues. *Biophys. J.* **90**, 2213–2220 (2006).
97. Meyer, R. A. *et al.* Developmental regulation and asymmetric expression of the gene encoding Cx43 gap junctions in the mouse limb bud. *Dev. Genet.* **21**, 290–300 (1997).
98. Bao, B., Jiang, J., Yanase, T., Nishi, Y. & Morgan, J. R. Connexon-mediated cell adhesion drives microtissue self-assembly. *FASEB J.* **25**, 255–264 (2011).
99. Zhou, C. *et al.* Substrate mechanics dictate cell-cell communication by gap junctions in stem cells from human apical papilla. *Acta Biomater.* **107**, 178–193 (2020).
100. Su, G. *et al.* The effect of forced growth of cells into 3D spheres using low attachment surfaces on the acquisition of stemness properties. *Biomaterials* **34**, 3215–3222 (2013).
101. Follin, B. *et al.* Increased Paracrine Immunomodulatory Potential of Mesenchymal Stromal Cells in Three-Dimensional Culture. *Tissue Eng. Part B* **22**, 322–329 (2016).
102. Liu, Y., Muñoz, N., Tsai, A. C., Logan, T. M. & Ma, T. Metabolic Reconfiguration Supports Reacquisition of Primitive Phenotype in Human Mesenchymal Stem Cell Aggregates. *Stem Cells* **35**, 398–410 (2017).
103. Derangeon, M. *et al.* RhoA GTPase and F-actin Dynamically Regulate the Permeability of Cx43-made Channels in Rat Cardiac Myocytes. *J. Biol. Chem.* **283**, 30754–30765 (2008).
104. Waxse, B. J., Sengupta, P., Hesketh, G. G., Lippincott-Schwartz, J. & Buss, F. Myosin VI facilitates connexin 43 gap junction accretion. *J. Cell Sci.* **130**, 827–840 (2017).
105. Wall, M. E., Otey, C., Qi, J. & Banes, A. J. Connexin 43 is Localized With Actin in Tenocytes. *Cell Motil. Cytoskeleton* **64**, 121–130 (2007).
106. Gowrishankar, K. *et al.* Active remodeling of cortical actin regulates spatiotemporal organization of cell surface molecules. *Cell* **149**, 1353–1367 (2012).
107. Wang, N., Tytell, J. D. & Ingber, D. E. Mechanotransduction at a distance: Mechanically coupling the extracellular matrix with the nucleus. *Nat. Rev. Mol. Cell Biol.* **10**, 75–82 (2009).

Chapter 4

108. Huveneers, S. & Rooij, J. De. Mechanosensitive systems at the cadherin–F-actin interface. *J. Cell Sci.* **126**, 403–413 (2013).
109. Goodwin, K. *et al.* Basal Cell-Extracellular Matrix Adhesion Regulates Force Transmission during Tissue Morphogenesis. *Dev. Cell* **39**, 611–625 (2016).
110. Ng, M. R., Besser, A., Brugge, J. S. & Danuser, G. Mapping the dynamics of force transduction at cell – cell junctions of epithelial clusters. *Elife* **3**, e03282 (2014).
111. Tetley, R. J. *et al.* Tissue fluidity promotes epithelial wound healing. *Nat. Phys.* **15**, 1195–1203 (2019).
112. Jain, A. *et al.* Regionalized tissue fluidization is required for epithelial gap closure during insect gastrulation. *Nat. Commun.* **11**, 5604 (2020).
113. Casanellas, I. *et al.* Substrate ligand density modulates gap junction intercellular communication during mesenchymal cell condensation. *bioRxiv* (2021) doi:10.1101/2021.04.28.441739.
114. Prein, C. *et al.* Structural and mechanical properties of the proliferative zone of the developing murine growth plate cartilage assessed by atomic force microscopy. *Matrix Biol.* **50**, 1–15 (2016).
115. Erickson, B. *et al.* Nanoscale structure of type I collagen fibrils: Quantitative measurement of D-spacing. *Biotechnol. J.* **8**, 117–126 (2013).
116. Sweeney, S. M. *et al.* Candidate Cell and Matrix Interaction Domains on the Collagen Fibril, the Predominant Protein of Vertebrates. *J. Biol. Chem.* **283**, 21187–21197 (2008).

Chapter 5

Adhesion, nuclear shape and differentiation to musculoskeletal lineages

5.1. Introduction

Given the widespread interest for improved regenerative therapies of musculoskeletal tissues, different strategies have been explored in recent years. An implant intended to be inserted into a patient should mimic the host tissue's structure and mechanical properties, to promote integration. The scaffold must be biocompatible, not be immunologically rejected, allow cell infiltration and stand sterilization and surgery procedures. Scaffolds can be preloaded with cells that will differentiate and generate the target tissue, or be functionalized with particles such as growth factors to recruit cells from the host^{1,2}. On the other hand, *in vitro* systems that only aim to guide cells towards the desired fate, and then remove them for implantation (directly or in another carrier), can set some of these considerations aside. This approach can be particularly interesting for tissues that generate distinct early morphogenetic structures, such as mesenchymal condensates^{3,4}.

Cell-matrix interactions are driven by nanoscale phenomena, which mediate cell response including differentiation⁵⁻⁸. As such, *in vitro* platforms and biomaterials that aim to modulate cell behaviour should be designed taking nanoscale factors into account, helping optimize their properties for regenerative therapies^{9,10}. This includes cartilage, tendon and bone. Nanobiomaterials with different features have been developed to direct MSCs towards bone formation, including surfaces with nanotopographies, nanofibers, and RGD nanopatterns¹¹⁻¹⁷. PLLA scaffolds with carbon nanotubes were also employed¹⁸. In the case of cartilage, components such as nanofibers and nanoparticles can promote MSC differentiation to chondrogenesis¹⁹⁻²¹. Several materials have been applied to design chondrogenic platforms (such as PLLA, hyaluronic acid or collagen), but less attention has been paid to the nanoscale adherence of the substrate or scaffold²². Comparatively fewer studies have been published on nanobiomaterials for tendon regeneration²³.

During tissue patterning, cells induce extensive ECM remodelling that leads to a unique ECM composition, characteristic of the target tissue²⁴⁻²⁶. Stem cell proliferation and differentiation are in turn regulated by mechano-chemical inputs from the ECM which are sensed through cell membrane receptors, mainly integrins, and transduced into biological signals through mechanotransduction²⁷⁻³¹. Integrin-mediated cell-substrate adhesions thus modulate a range of cell behaviour parameters^{5,32-36}. Given that mechanotransduction is a nanoscale process (see Chapter 1, section 1.2), nanopatterned surfaces are used to study ECM–cell interactions and to identify the geometric cues that initiate and guide cell adhesion. The spatial distribution of ligands

is one of the main factors driving cell response to matrix inputs³⁷ and regulates cell spreading, migration or differentiation^{38–41}. Spatial sensing of ECM ligands is transduced at membrane adhesions into tensions⁴², which are transmitted across the cytoskeleton to the cell nucleus through the linkers of nucleoskeleton and cytoskeleton (LINC) complexes, regulating nuclear dynamics and gene expression^{43–45}. Nuclear morphology mediates cell response to the environment; as the nucleus is compressed or deformed, it activates corresponding signalling pathways and allows cells to adapt to the shape induced by their surroundings^{46–48}.

In addition to direct tension transmission from the membrane to the nucleus, mechanical signals directing the cell fate involve molecular factors from the Hippo pathway⁴⁹. This signalling pathway is a key regulator of organ size, controlling cell proliferation and apoptosis with an important role in the self-renewal and differentiation of both multipotent and tissue-specific progenitor cells. The core of the Hippo pathway is composed of a kinase cascade in which the STE20-family kinases MST1 and MST2, in complex with the adaptor proteins SAV1, MOBKL1A and MOBKL1B, phosphorylate and activate the NDR-family kinases LATS1 and LATS2. Phosphorylated LATS1 and LATS2, in turn, phosphorylate and inactivate the transcriptional regulators TAZ and Yes-associated protein (YAP), sequestering them in the cytosol, where they are degraded (inhibitory phosphorylation of YAP/TAZ)⁵⁰. Therefore, when the Hippo pathway is inactive, YAP translocates into the cell nucleus promoting cell proliferation and stem cell self-renewal, and apoptosis is inhibited (Fig. 5.1). Several upstream regulators of the Hippo pathway have been described. In particular SRC kinase, which is activated by cell adhesion, facilitates YAP nuclear translocation^{49,51}. As such, alterations in YAP activity are a predominant mechanism by which mechanotransduction influences cell fate^{34,52,53}.

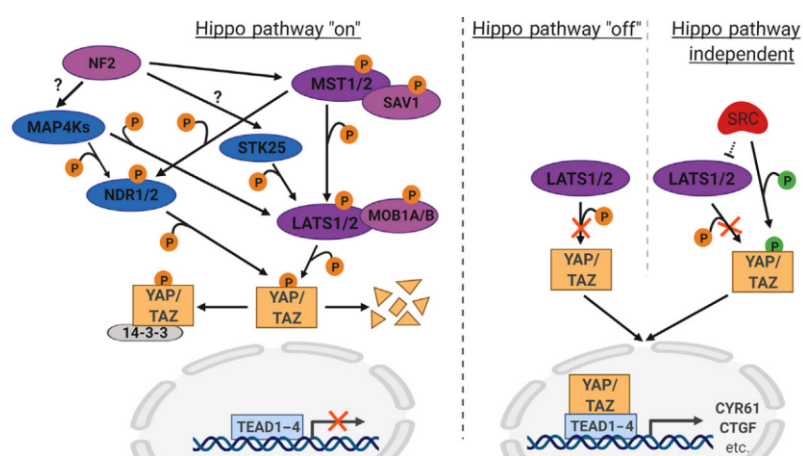


Figure 5.1. Regulation of YAP/TAZ nuclear translocation through the Hippo pathway. Adapted under a Creative Commons (CC BY 4.0) license from Rausch and Hansen (2020)⁴⁹.

The nuclear translocation of YAP is regulated through a complex interplay of parameters such as substrate stiffness and configuration, culture dimensionality and cellular and nuclear morphology^{48,54,55}. Cell-cell adhesions in MSCs cause a reduction in YAP activation, affecting the downstream signalling events. Thus, cell-cell interactions, which are progressively lost during limb development, may actuate as a regulatory mechanism to control tissue maturation⁵⁶. YAP activity levels then affect cell fate⁵². YAP expression is particularly regulated during chondrogenesis, with active YAP increasing within the first days of chondrogenesis and then decreasing during chondrocyte maturation^{57,58}. Matrix elasticity also affects the fate of chondrocytes through YAP regulation. Mature chondrocytes maintain their phenotype on soft substrates (4 kPa) but tend to de-differentiate on stiff substrates (40 kPa), coinciding with a higher translocation of YAP into the cell nuclei⁵⁹

In this chapter, we employ nanopatterns of the cell-adhesive peptide arginine–glycine–aspartic acid (RGD) that allow control of the local surface adhesiveness at the nanoscale (see Chapter 1, section 1.4) to unveil the adhesive requirements that guide MSCs towards the chondrogenic, tenogenic and osteogenic fates and explore the adhesive cues that play a role during early mesenchyme patterning. Finding the optimal ligand density to promote stem cell differentiation towards these tissues could later be applied in the design of biomaterials to regenerate fractured and extensively diseased tissue. From a perspective of cell biology, we were interested to see whether local ligand density effects on morphogenesis were confined to cartilage formation (as seen in Chapters 3 and 4) or could be expanded to other tissues, indicating a general mode of differentiation control during mesenchymal development. We find that chondrogenesis and osteogenesis are favoured by high local surface adhesiveness, while tenogenesis is not. For chondrogenesis, we analyse YAP localization within cells in condensates and find that high ligand density induces YAP nuclear translocation, confirming a mechanotransduction pathway that mediates the effects of ligand nanospacing on musculoskeletal tissue formation. We then analyse nuclear shape remodelling through FA assembly, and their influence on cell differentiation. In chondrogenesis, we identify a biphasic response of nuclear shape at low or high local ligand densities. In tenogenesis, tension applied from FAs appears to be homogeneously distributed along the cell perimeter independently of local surface adhesiveness, promoting a prevalent rounded nuclear morphology, while in osteogenesis, nuclear deformation increases linearly with decreasing cell–surface adherence. We find lineage commitment to be regulated by tension exerted as a combination of FAs size and distribution, in different manners according to each musculoskeletal lineage.

5.2. Results

5.2.1. Nuclear remodelling, cytoskeletal morphology and adhesion size

Up until this point, we have employed dendrimer-nanopatterned substrates to regulate stem cell behaviour in a context of cartilage development. We wanted to extend the work by exploring whether the same *in vitro* platform could be applied to other musculoskeletal tissues, namely tendon and bone.

To investigate whether the local surface adhesiveness could influence nuclear morphology, we cultured hMSCs under each of the differentiation media and stained them 24 h later for nuclei. We then calculated the nuclear shape index (NSI). Values close to 1 indicate nuclei with a nearly circular shape; the lower the NSI, the farther the nuclei shape is from a perfect circle. For chondrogenesis, nuclei on S_{FN} (NSI of 0.81) were rounder than the rest, while nuclei on S_0 and nanopatterned substrates, which were mostly contained in multicellular condensates, were more elongated. Nuclei of cells on S_{90} (NSI of 0.52) were less deformed than those on S_{18} and S_{45} (0.38 and 0.44, respectively) and statistically equal to those on S_0 (0.49).

Cells under tenogenic and osteogenic induction retained a two-dimensional configuration in all conditions. In general, osteogenic conditions led to slightly more elongated nuclei than tenogenic induction: the NSI mean values in the former ranged from 0.76 to 0.81, whereas in the latter they went from 0.79 to 0.83. Cells on S_0 substrates presented lower NSI values in both cases. We found that for each differentiation fate there was a different nanopattern ligand density that induced a high level of nuclear deformation, alongside non-patterned substrates: S_{45} for tenogenesis (NSI of 0.80) and S_{90} for osteogenesis (NSI of 0.77). In each case, the NSI mean values on these conditions were significantly lower than all others, except that of S_0 (Fig. 5.2).

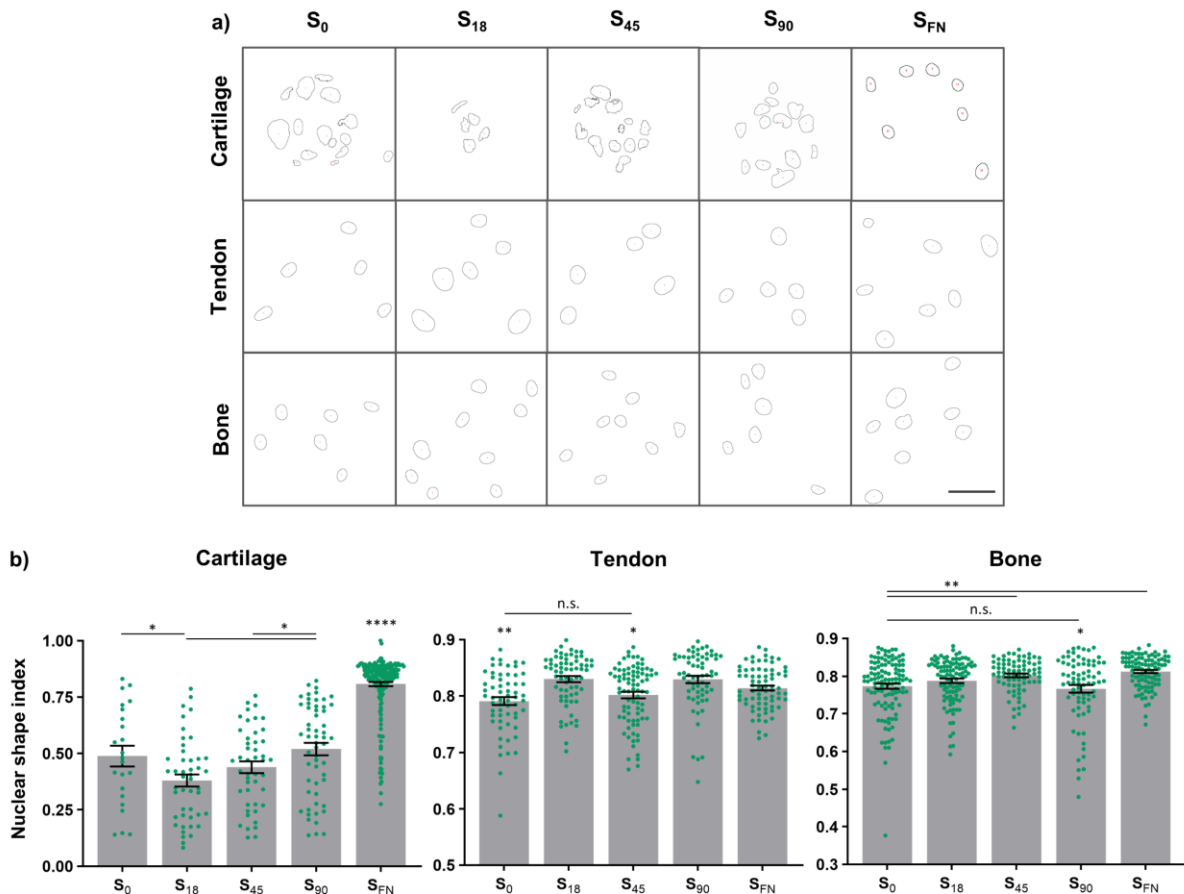


Figure 5.2. Nuclear shape depends on cell fate. **a)** Representative nuclei outlines after 24 h of chondrogenic (top), tenogenic (middle) and osteogenic (bottom) induction. Scale bar = 50 μ m. **b)** Nuclear shape index under cartilage, tendon and bone induction. Dots represent single data points, bars indicate the mean \pm SEM, * $p < 0.05$, ** $p < 0.01$, **** $p < 0.0001$

During random migration, cells continuously switch between elongated and rounded morphologies, remodelling nuclear shape through the lateral compressive forces exerted by actin filaments^{60–62}. Random movement alternates fast translocation with slow rotation, for which the nuclei switch from elongated to rounded shapes, respectively⁶³. Our results on nuclear morphology could indicate that cells on S₁₈ (for chondrogenesis), S₄₅ (for tenogenesis) and S₉₀ (for osteogenesis) were moving rapidly with a small contribution of rotation, which would explain their tendency towards more elongated shapes. To test this hypothesis, we stained cells for actin to observe spreading and morphology. Cells on S₀ and nanopatterned substrates under chondrogenic induction formed condensates with a cortical actin disposition, whereas on S_{FN} they were spread as a monolayer, similarly to those on the other two lineages. Cells on S₄₅ in tenogenesis and S₉₀ in osteogenesis looked similar to cells on S_{FN}: widely spread and with clearly defined actin fibres. In S₀, under both tenogenic and osteogenic induction, actin appeared more

punctuated and fibres were less defined (Fig. 5.3). Therefore, while nuclear shape was similar to S_0 in both cases, cell and cytoskeletal morphology were more akin to those of S_{FN} .

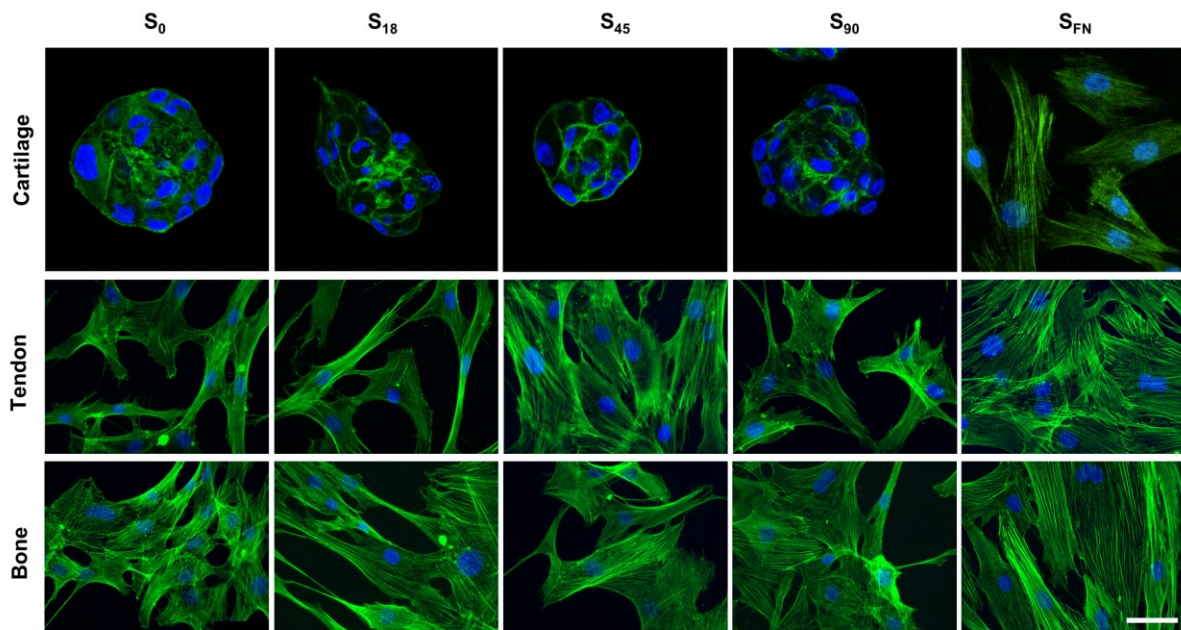


Figure 5.3. Cytoskeletal morphology. Representative images of cells stained for actin (green) and Hoechst (blue) at 24h of chondrogenic (top), tenogenic (middle) and osteogenic (bottom) induction. Scale bar = 50 μm .

Nuclear morphology is regulated by lateral compressive forces, which derive from the tension exerted on actomyosin filaments through focal adhesions (FAs)^{64,65}. Cytoskeletal tensions are known to depend on adhesion size; larger integrin clusters and their corresponding assembled adhesomes sustain higher forces inwards and outwards of the cell^{66,67}. We thus examined FA assembly on the substrates by immunostaining cells for adhesome protein paxillin (PXN) after 24 h in culture. Substantial amounts of diffuse protein could be observed alongside clearly defined PXN clusters, indicating the presence of focal adhesions. (Fig. 5.4a). We measured the mean area of stained FAs to evaluate whether substrate ligand density effects on adhesion formation depended on the fate towards which cells were differentiating. In the case of prechondrogenic condensates imaged with confocal microscopy, PXN was examined at the basal layer of condensates, in contact with the substrate. PXN clusters in this case appeared rounder and more diffuse than in other conditions, where cells formed a monolayer and presented more elongated FAs. For chondrogenesis, FA size increased with substrate adhesiveness: PXN clusters were 1.7 μm^2 on S_0 , 2.1 μm^2 on S_{18} and S_{45} , and significantly larger (2.8 μm^2) on S_{90} and S_{FN} . Under tenogenic

conditions, FA area increased with local ligand density on nanopatterned substrates and was significantly larger for cells on S_{45} and S_{90} ($3.7\text{-}3.8\ \mu\text{m}^2$), but decreased for S_{FN} ($3.2\ \mu\text{m}^2$). Surprisingly, for osteogenesis, no direct correlation between FA size and local surface adhesiveness was found, as the largest FAs were observed on S_{18} and S_{45} ($4.0\ \mu\text{m}^2$) rather than S_{90} ($3.6\ \mu\text{m}^2$). As in tenogenesis, the smallest adhesions were found on S_{FN} ($3.4\ \mu\text{m}^2$) (Fig. 5.4b).

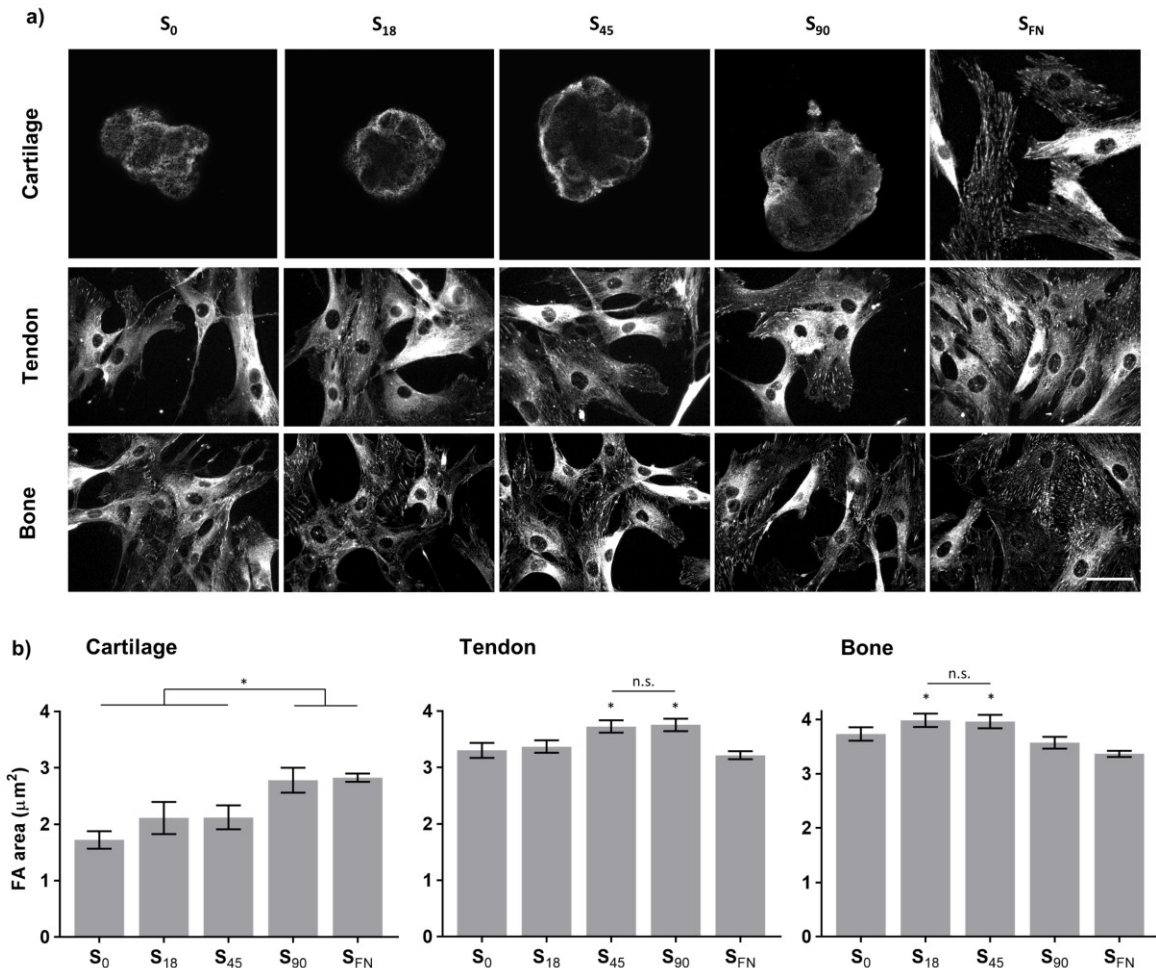


Figure 5.4. Focal adhesion (FA) size depends on cell fate. a) Representative epifluorescence images of hMSCs after 24 h of culture under chondrogenic (top), tenogenic (middle) and osteogenic (bottom) induction, immunostained for the FA protein paxillin. Scale bar = $50\ \mu\text{m}$. **b)** Quantification of FAs area in hMSCs after 24 h of culture under chondrogenic, tenogenic and osteogenic induction. Bars indicate the mean \pm SEM, * $p < 0.05$, n.s.: not significant.

We assessed whether there was a correlation between nuclear shape and focal adhesion size in each differentiation path (Fig. 5.5a). Under chondrogenic induction, an increase in FA area was not clearly linked to nuclear deformation: For instance, cells on S_{90} and S_{FN} , with equally sized FAs, presented very different NSIs, whereas cells on S_{90} and S_0 , with differently sized FAs, presented equal NSIs. However, a multiphasic trend was observed in condensates on nanopatterned substrates, by which NSI initially decreased with increasing FA size (from S_0 to S_{18}), then remained equal (from S_{18} to S_{45}) and finally increased alongside FA size (from S_{45} to S_{90}). FA area did not correlate with the NSI under tenogenic stimuli, while in osteogenesis, the NSI linearly increased with FA size within nanopatterned substrates. The results in tenogenesis might seem counterintuitive, as larger FAs would be expected to exert higher forces on the nuclei and cause more deformation, as seen for osteogenesis. However, since nanopatterns provide an uneven distribution of RGD, cells adhere to the substrates without a preferential direction. Following this premise, FAs could be homogeneously distributed around the cell perimeter even as their size increased, thus applying similar forces from all directions and preserving the rounded shape of the nuclei⁶⁵. Observing the distribution of FAs around cell nuclei suggested that this was the case: in tenogenic conditions FAs were distributed around nuclei on all conditions, whereas in osteogenic conditions we observed that FAs on S_{90} and S_0 appeared to be polarized at two opposite sides of each nucleus (Fig. 5.5b).

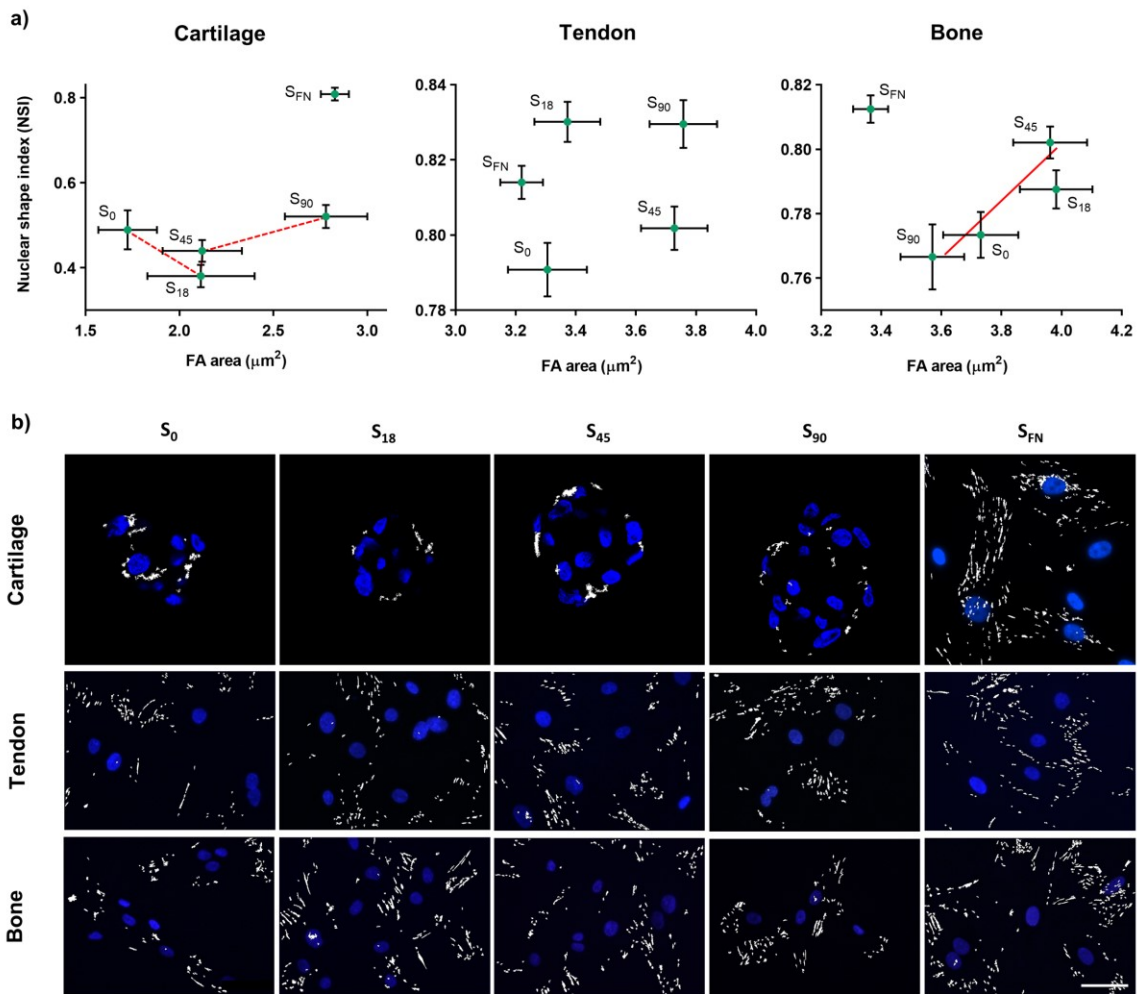


Figure 5.5. Focal adhesion (FA) size influence on nuclear remodelling. a) Correlation of the nuclear shape index with focal adhesion area under chondrogenic, tenogenic or osteogenic induction on each substrate. Green dots with bars show the mean \pm SEM. Solid red lines indicate trends in graphs. Dashed red lines are visual guides following substrates in order of adhesiveness. **b)** Images of cell nuclei (blue) with the clusters in paxillin staining measured as focal adhesions (white). Scale bar = 50 μ m.

5.2.2. Differentiation to cartilage, tendon and bone

Previous work at the Nanobioengineering group indicated that S_{90} ligand density promotes cell differentiation towards cartilage at day 5 of culture⁶⁸. To further confirm these results, we seeded hMSCs on the nanopatterned substrates in chondrogenic medium and measured the expression levels of chondrogenic marker *SOX9* at days 6 and 9 of culture. *SOX9* is a transcription factor characteristic of cartilage development, both during mesenchymal condensation, when it induces cell differentiation and matrix secretion, and in later stages, when it prevents adult chondrocytes from becoming hypertrophic^{69–71}. Mutations in the *SOX9* gene lead to severe skeletal defects in mice⁷². *SOX9* was significantly upregulated on S_{90} at days 6 (relative to all other conditions) and 9 (relative to S_0 and S_{FN}) of chondrogenic induction (Fig. 5.6):

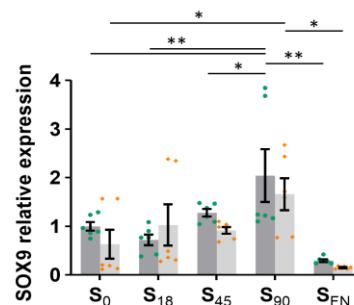


Figure 5.6. Effect of substrate nanopatterning on cartilage differentiation. Expression of *SOX9* mRNA, relative to that of S_0 , at days 6 (dark bars with green dots) and 9 (light bars with orange rhomboids) of chondrogenesis. Dots and rhomboids represent single data points, bars indicate the mean \pm SEM; * $p < 0.05$, ** $p < 0.01$

To examine the impact of mechanotransduction on how local surface adhesiveness regulates chondrogenesis, we examined YAP localization at two early time points of differentiation. Observation of immunostained YAP in mesenchymal condensates showed that most nuclei were devoid of the protein or contained small amounts of it, compared to the surrounding cytosol (Fig. 5.7a). We measured the ratio of nuclear versus cytoplasmic staining for all conditions at 6 hours of culture; and for S_{18} and S_{90} at 72 hours. YAP was mostly cytoplasmic in all experimental conditions (all mean ratios were lower than 0.5). At 6 h of culture, S_{45} and S_{90} presented higher ratios of nuclear translocation than all other substrates, with mean values of 0.35 and 0.38, compared to 0.25–0.26 found on S_0 , S_{18} and S_{FN} . After 3 days, YAP nuclear translocation increased for both S_{18} (0.39) and S_{90} (0.47), with the latter still presenting the highest translocation ratio (Fig. 5.7b).

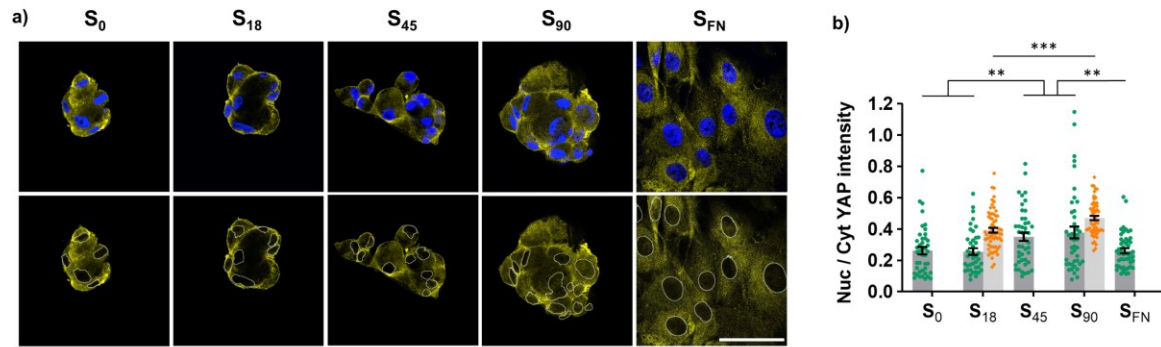


Fig. 5.7. YAP nuclear translocation in chondrogenesis. **a)** Confocal images showing YAP at 6 h of chondrogenesis. Top: merged nuclei (Hoechst, blue) and YAP staining (yellow). Bottom: cell nuclei perimeters superimposed on YAP staining. Scale bar = 50 μ m. **b)** Quantification of YAP localization at 6 hours (dark bars with green dots) and 3 days (light bars with orange rhomboids) of chondrogenesis. Dots and rhomboids represent single data points, bars indicate the mean \pm SEM, ** $p < 0.01$, *** $p < 0.001$

We seeded hMSCs in tenogenesis- or osteogenesis-inducing media and measured the area immunostained for specific differentiation protein markers. To quantify tenogenesis, cultures were immunostained for scleraxis (SCX, Fig. 5.8a) and collagen-I (COL-I, Fig. 5.8b) after three days, and for tenomodulin (TNMD) after six days. These are three markers commonly used to assess tendon formation *in vitro*^{73–75}. Scleraxis is a transcription factor specifically expressed in tendon across development stages, from early progenitors to mature tissue⁷⁶. It subsequently mediates the expression of COL-I, one of the main components of the extracellular matrix in tendon and other musculoskeletal tissues⁷⁷. We observed a similar pattern for SCX and COL-I, with protein staining levels tending to increase from S_0 to S_{45} and then decrease until S_{FN} , although there were no significant differences between the means of different conditions. Tenomodulin (TNMD) is a transmembrane glycoprotein that is a specific marker of later tenogenesis stages, appearing several days after peak SCX expression^{23,78}. We measured TNMD staining at day 6 of tenogenesis and observed no differences between substrates, although there was a trend for protein staining to slightly decrease with increasing substrate adhesiveness (Fig. 5.8c).

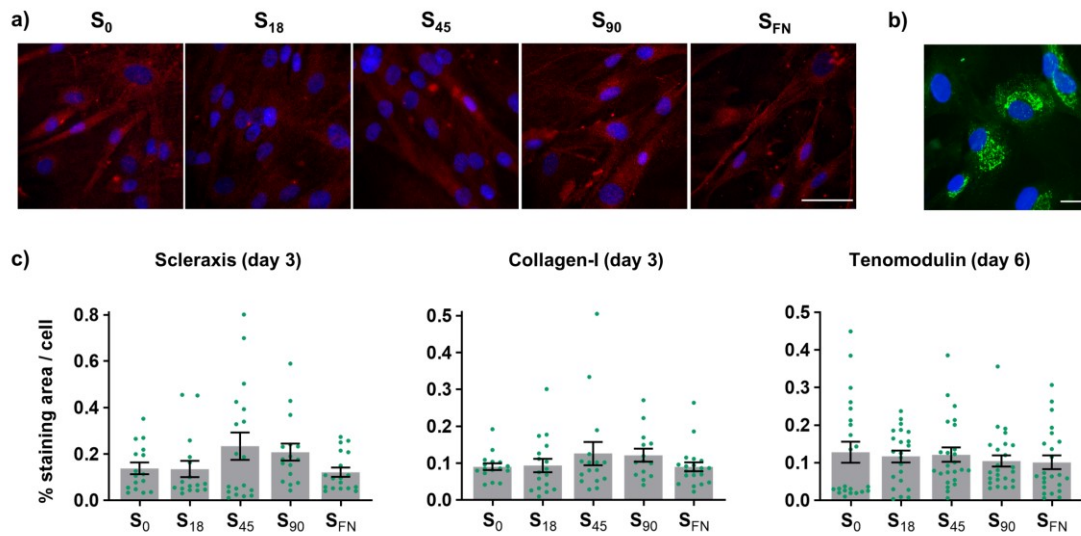


Figure 5.8. Effect of substrate nanopatterning on tendon differentiation. a) Fluorescence images of cells immunostained for scleraxis (red) at day 3 of tenogenesis. Scale bar = 50 μm . **b)** Representative fluorescence image of cells immunostained for collagen-I (green) at day 3 of tenogenesis. Scale bar = 25 μm . **c)** Quantification of area stained for scleraxis, collagen-I and tenomodulin at days 3 and 6 of tenogenesis. Dots represent single data points, bars indicate the mean \pm SEM.

To assess osteogenesis, cultures were immunostained for osterix (OSX) after 48 h and for alkaline phosphatase (ALP) after six days of osteogenic induction. Osterix is a transcription factor that is activated and translocates to the nucleus during the very first stages of differentiation, where it activates downstream osteogenic genes⁷⁹. It is a necessary protein for bone development: in *OSX*-null mice, MSCs do not deposit bone matrix and bone formation is impaired⁸⁰. We first counted the proportion of cells containing any amount of OSX visible upon first observation of the nucleus (Fig. 5.9a). In most S₉₀ images (14 out of 24), at least 75% of cells presented nuclear OSX, whereas in other nanopatterned substrates most single values were below this threshold, and on S_{FN} all were lower than 70%. Overall, S₉₀ substrates presented the highest proportion of cells with visible nuclear OSX (61%), almost double than S₁₈ (32%). S₀, S₄₅ and S_{FN} presented mean values between 39% and 48%, statistically equal to all others (Fig. 5.9b).

To quantify OSX nuclear translocation, indicative of cells having initiated osteogenic differentiation, we measured staining intensity in equal areas inside and just outside of the nucleus (Fig. 5.9c). While most of the protein was contained in the cytoplasm, cells on S₉₀ presented a significantly higher level of OSX translocation with a nuclear-cytoplasmic ratio of 0.62, compared to 0.47-0.54 for other conditions (Fig. 5.9d).

Alkaline phosphatase is a dephosphorylating enzyme and its activity significantly increases during bone formation^{81,82}. We immunostained ALP at day 6 of osteogenic induction (Fig. 5.9e). The highest values of ALP staining were reached on S₀ and S₉₀ nanopatterns, both of which were significant when compared to S₁₈ (Fig. 5.9f). Altogether, our results point to the requirements of local surface adhesiveness depending on the lineage commitment.

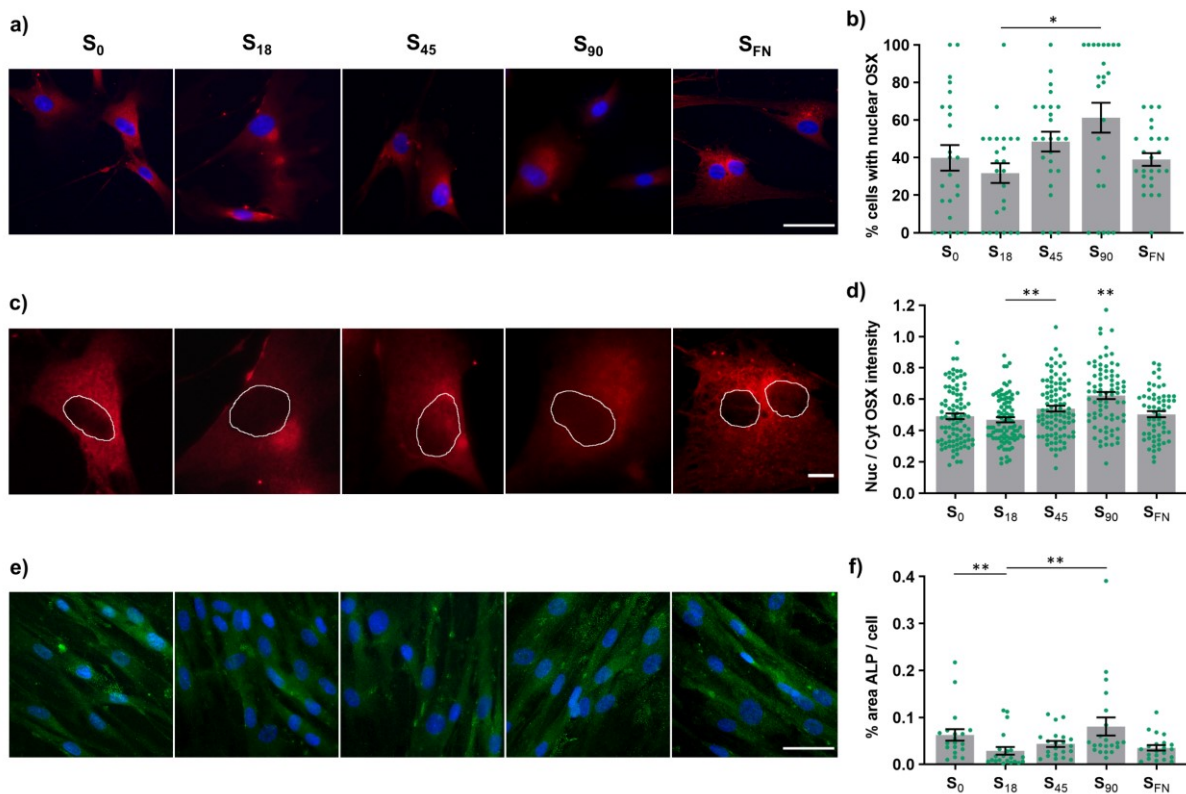


Figure 5.9. Effect of substrate nanopatterning on bone differentiation. **a)** Fluorescence images of cells immunostained for osterix (red) and nuclei (blue) at 48 h of osteogenesis. Scale bar = 50 μ m. **b)** Percentage of nuclei containing visible osterix. **c)** Zoomed-in areas of osterix staining with nuclei contours in white. Scale bar = 10 μ m. **d)** Quantification of osterix translocation by relative intensity in the nucleus and the cytosol. **e)** Fluorescence images of alkaline phosphatase staining (green) at day 7 of osteogenesis. Scale bar = 50 μ m. **f)** Quantification of area stained for alkaline phosphatase. Dots represent single data points, bars indicate the mean \pm SEM, * p < 0.05, ** p < 0.01.

5.2.3. Lineage commitment through adherence and nuclear shape

Focal adhesions at the cell-substrate interface are the main form of mechanical signal sensing between the cell and the ECM^{83–85}. We analysed whether FA area at 24 h of culture could account for the measured levels of selected differentiation markers at later time points (Fig. 5.10a). This was the case for chondrogenesis, where *SOX9* expression increased with FA area on nanopatterned substrates. Under tenogenic induction, the levels of SCX staining increased progressively with the size of FAs, whereas under osteogenic induction, ALP staining showed the opposite relation to FA size: higher levels of ALP were obtained with decreasing cell–substrate adhesion area, except on S_{FN} .

Focal adhesion tensions propagate through the cytoskeleton to influence nuclear morphology⁸⁶, regulating gene transcription^{65,87}. Therefore, we analysed whether marker expression in each differentiation path could be linked to the NSI of cells according to substrate adhesiveness. Chondrogenesis again improved with increasing NSI (rounder nuclei), except for S_{FN} . For tenogenesis, no correlation was found between SCX staining and the NSI. In contrast, for osteogenesis, ALP staining increased with nuclear elongation (Fig. 5.10b).

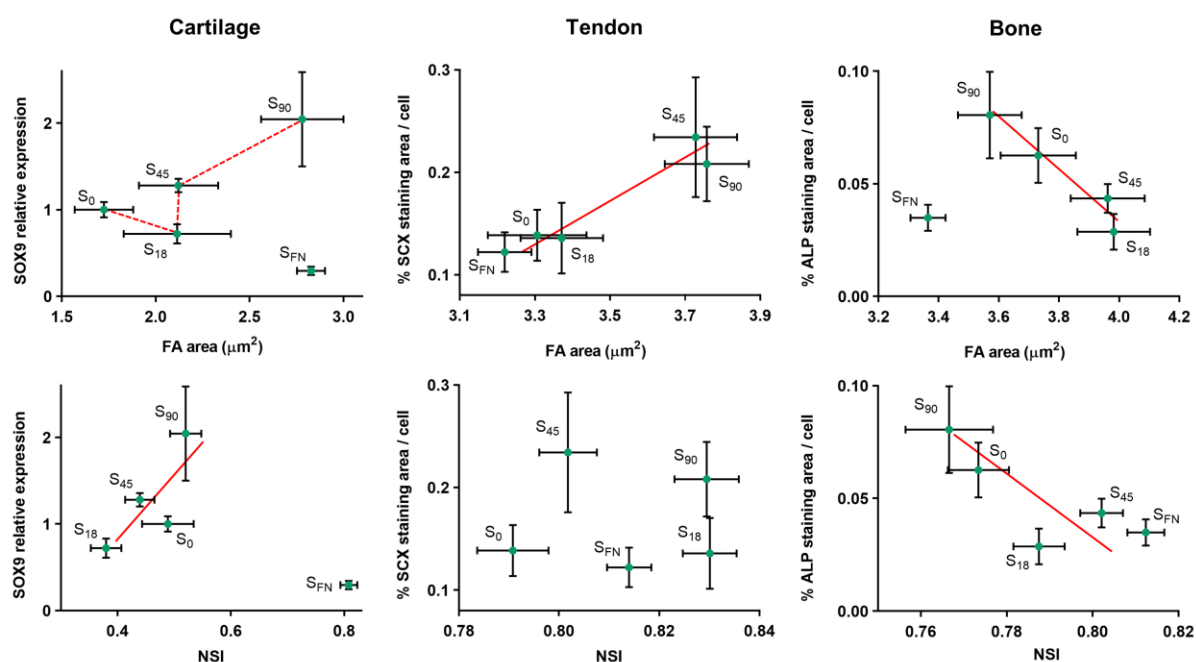


Figure 5.10. Adherence and nuclear remodelling mediate differentiation. Correlation of selected differentiation markers with adhesion area (top) and nuclear shape index (bottom) under chondrogenic, tenogenic and osteogenic conditions on each substrate. Green dots with bars show the mean \pm SEM. Solid red lines indicate trends in graphs. Dashed red lines are visual guides following substrates in order of adhesiveness.

Nuclear morphology has also been linked to the degree of chromatin condensation, affecting gene expression in response to environmental inputs^{65,87,88}. We observed cell nuclei stained with Hoechst to assess whether observable differences were present. No relevant changes were observed in chromatin condensation among the different tested conditions of substrate adhesiveness and differentiation commitment, and more condensed or more diffuse chromatin configurations could not be assigned to any particular behaviour (Fig. 5.11a). In tenogenesis and osteogenesis, nuclei on substrates inducing more nuclear deformation presented a similar appearance to their respective fibronectin-coated substrates (Fig. 5.11b).

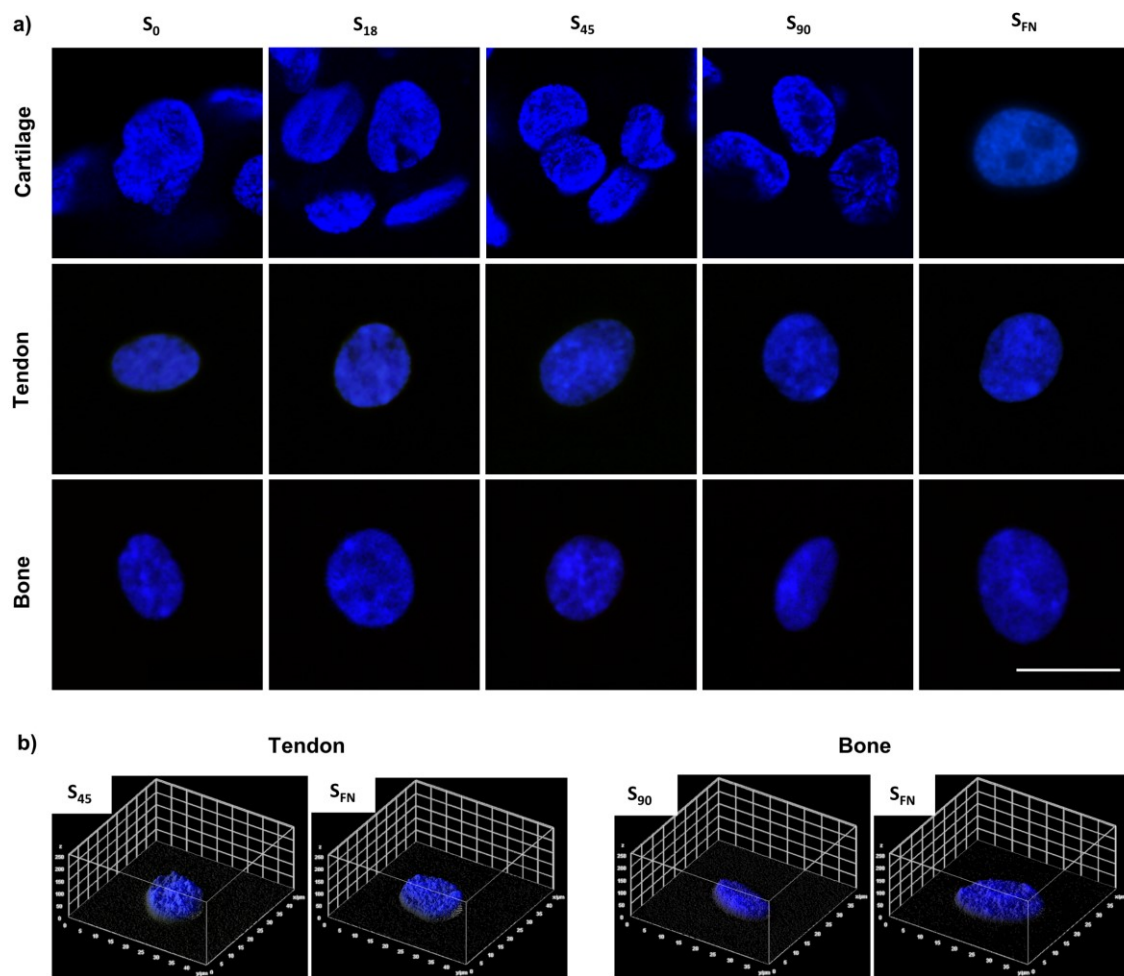


Figure 5.11. Chromatin condensation. a) Representative confocal (for cartilage) or epifluorescence (for tendon and bone) images of cell nuclei in hMSCs cultured under chondrogenic (top), tenogenic (middle) or osteogenic (bottom) induction for 24 h. Scale bar = 20 μm . b) Comparison of three-dimensional surface plots showing chromatin condensations obtained on nanopatterns with highest nuclear elongation versus their respective S_{FN} , in tenogenesis and osteogenesis.

5.2.4. Freezing mesenchymal condensates

The ultimate goal of nanobiomaterials is to improve the current state of the art in regenerative therapies of the target tissue. Previous *in vivo* assays in a sheep model showed that PLLA/chitosan scaffolds, loaded with MSCs and implanted into osteochondral defects, promote articular cartilage regeneration to a higher degree if they are functionalized with RGD dendrimers. To test a further application of dendrimer-nanopatterned substrates in musculoskeletal regenerative therapies, current studies at the Nanobioengineering Group aim to load mesenchymal condensates onto chondrogenesis- and osteogenesis-inducing carriers, to engineer optimal osteochondral precursor constructs that will promote articular regeneration. In that regard, we analysed whether mesenchymal condensates could be stored frozen for use at a later desired time. We removed formed condensates from S_{90} substrates at day 6 of chondrogenic differentiation, froze them, thawed them back and seeded them on new substrates. After another 2 days in culture, condensates retained their general size and structure. We then conducted a Live/Dead assay on thawed condensates, showing that most cells in them were alive (Fig. 5.12).

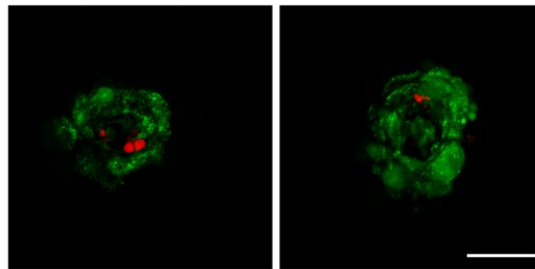


Fig. 5.12. Live/Dead assay in condensates after a freeze-thaw cycle. Representative confocal images of frozen and thawed S_{90} condensates, stained for intracellular esterase activity, indicating live cells (green), and for nucleic acids in membrane-damaged cells (red). Scale bar = 50 μm .

5.3. Discussion

We have discussed in the previous chapters how substrate ligand density modulates the early steps of mesenchymal condensation and cartilage development. In this chapter we seeded mesenchymal stem cells on dendrimer nanopatterns under chondrogenic, tenogenic or osteogenic stimulation, to evaluate their morphological and differentiation responses to substrate adhesiveness.

5.3.1. Adhesion area modulates nuclear morphology

Nuclear positioning and remodelling are necessary for mesenchymal cells to migrate and differentiate^{47,63}. Nuclear dynamics are controlled by tension exerted from adhesions and propagated through the cytoskeleton to the nuclear actin cap^{44,65}. We examined nuclear morphology on the nanopatterns and observed that hMSCs nuclei behaved differently depending on the differentiation stimuli: Cells under chondrogenic stimuli on S_0 and nanopatterned substrates aggregated into condensates, which induced nuclear elongation, although S_0 and S_{90} condensates presented slightly higher NSI values. Under tenogenic induction, the lowest values of NSI were found for cells cultured on S_{45} , and on S_{90} for osteogenesis. In both cases, they were comparable to the values of the respective non-adherent substrates (S_0). Therefore, an interesting pattern emerges by which each lineage induces distinctly shaped nuclei on both S_0 and one of the nanopatterned substrates. Nuclei on S_0 and S_{90} are rounder during chondrogenesis, whereas nuclei on S_0 and S_{45} for tenogenesis, or S_0 and S_{90} for osteogenesis, are more elongated. As discussed below, S_{90} is also the substrate condition that promotes differentiation towards both cartilage and bone.

Cytoskeletal staining in chondrogenesis showed the expected cortical structure for mesenchymal condensates, or a monolayer disposition for S_{FN} . For tenogenesis and osteogenesis, while cytoskeletal staining of cells on S_0 showed punctuated and poorly defined actin fibres and distorted cell morphology, cells on S_{45} and S_{90} (for each lineage respectively) were spread and presented clearly defined actin fibres, similar to those on S_{FN} . Therefore, we conclude that nuclear distortion on the nanopatterns is related to tension applied through the cytoskeleton due to substrate ligand density. This is supported by the fact that osteogenesis is generally promoted through morphological changes in cells subjected to high cytoskeletal tensions^{89,90}.

Since cytoskeletal tension is mostly governed by integrin-mediated cell adhesion²⁷, we examined FA assembly. In chondrogenesis, adhesion size increased with substrate adhesiveness.

The same was true for tenogenic conditions excluding S_{FN} , with the largest adhesions found on S_{45} and S_{90} nanopatterns. However, for osteogenesis, larger FAs were formed on S_{45} and S_{18} nanopatterns. This was surprising, since we expected FA assembly to be favoured at higher ligand densities, as observed for chondrogenesis and tenogenesis. It is well established that cells seeded on ordered RGD nanopatterns attach more efficiently and develop larger FAs at shorter interparticle nanopacings within the 58 nm (corresponding to S_{90} , see Chapter 1, Table 1.1) to 70 nm (corresponding to S_{18}) range on stiff substrates³⁷. Importantly, substrates in our setup present an uneven distribution of RGD, meaning that surfaces with lower ligand densities also contain local nanopacings below 70 nm, promoting adhesion at these regions⁹¹. However, this characteristic of disordered patterns does not explain why cells undergoing osteogenesis form larger FAs on substrates of low and medium ligand densities, rather than high. This points to a mechanism by which, under osteogenic stimuli, cell-substrate adhesion maturation is impaired at high ligand densities. A previous theoretical model states that very large stresses prevent the growth of adhesion complexes, and that the tension threshold beyond which maturation is impaired depends on cell type and matrix composition¹⁵. Given that FAs in osteogenesis were generally larger than in chondrogenesis and tenogenesis, this could be the situation on S_{90} under osteogenic induction and would explain why different behaviours are observed depending on lineage commitment. Indeed, adhesions under osteogenic stimuli on S_{18} and S_{45} were nearly $4.0 \mu\text{m}^2$ on average, whereas on S_{90} they decreased to $3.6 \mu\text{m}^2$, smaller than on S_0 . On the other hand, the largest adhesions under chondrogenesis (sustained on S_{90} and S_{FN}) were only $2.8 \mu\text{m}^2$, while under tenogenesis (sustained on S_{45} and S_{90}) they were smaller than $3.8 \mu\text{m}^2$. It is therefore possible that adhesions around or above $4.0 \mu\text{m}^2$ would have formed on S_{90} during osteogenesis, but collapsed before reaching that value due to the excessive tensions exerted on them.

The observed cell behaviour regarding adhesion size would also agree with the molecular clutch model by which very high tensions lead to adhesion collapse. The model states that cells cultured on soft substrates experience tension build-up and subsequent adhesion disassembly at short interparticle nanopacings, whereas stiff substrates promote adhesion growth with increasing ligand density⁴². Since our substrates are rigid (they consist of a thin polymer coating on glass), we would expect to observe the behaviour described for stiff substrates, as indeed occurs for chondrogenesis and tenogenesis. However, disordered ligand distributions (as is the case here) reduce the rigidity threshold under which large adhesions would require larger ligand nanopacings in order not to collapse⁴². This threshold appears to be breached under osteogenic conditions, explaining the counterintuitive results regarding larger adhesions on S_{18} and S_{45} than

on S₉₀. Therefore, according to the molecular clutch model, cells undergoing osteogenesis on S₉₀ would require stiffer substrates to form larger adhesions capable of sustaining higher tensions.

5.3.2. Optimal ligand densities to promote differentiation

We analysed cell commitment induced by the differentiation media as influenced by substrate nanoscale ligand density. We find that high local ligand density nanopatterns (S₉₀) induce an increase in early chondrogenic differentiation^{68,92}. This relates to a study linking high ligand density with improved chondrogenesis: gold nanoparticles functionalized with RGD ligands are endocytosed into hMSCs, with the highest RGD density resulting in increased cellular uptake and improved chondrogenesis in cell pellets²⁰. Authors suggested that high RGD density promotes chondrogenesis by facilitating integrin activation alongside cell-cell interactions, which would also explain results in our system given the increased mechanical cohesiveness and gap junctional communication of S₉₀ condensates (as seen in Chapter 4). Another study employing PEG hydrogels with hexagonal RGD nanopatterns found an opposite trend, with chondrogenesis being promoted at large nanospacings (161 nm) rather than small ones (63 nm). However, in this case MSCs did not form three-dimensional condensates⁹³. Authors did note that chondrogenic differentiation occurred on substrates where cells retained a round rather than spread morphology, corresponding with our results on nuclear deformation in chondrogenesis, which show that S₉₀ nuclei are rounder than those on S₁₈ and S₄₅. Therefore, chondrogenic differentiation is probably linked to the distinct structure and mechanical properties of condensates on this substrate, and to the morphology that cells adopt in them. Cell shape and tissue compaction are indeed regulators of differentiation^{87,89,94}.

We find no clear effects of ligand density on tendon formation. This could be due to shortfalls of the experimental setup, or to tendon formation being less susceptible to local ligand density than cartilage and bone. It should be noted that published literature on the modulation of tendon formation through substrate engineering is not nearly as abundant as on the other two tissues, possibly indicating a higher degree of difficulty to obtain positive results. Instead, induction of tendon differentiation seems to require mechanical stimulation such as cell stretching cycles that promote cell alignment^{74,95-99}.

For osteogenesis, differentiation at day 3 was favoured on S₉₀. A recent study showed that streptavidin substrates promote osteogenesis when functionalized with a high concentration of cyclic RGD, which increases integrin clustering and upregulates BMP2 signalling¹⁷. By day 6 of

differentiation, S_{90} but also S_0 presented higher levels of differentiation than S_{18} . Optimal ligand density requirements thus depend on the developing cell lineage and possibly also on the time point of differentiation.

Previous reports indicated that osteogenesis is promoted on RGD nanopatterns with large interparticle spacings (between 87 and 124 nm) on PEG hydrogels^{40,100}. While this would seem to contradict our results, these studies found the expected relation between interparticle spacing and FA size, with larger adhesions forming on substrates of higher ligand density, which was not the case on our nanopatterned substrates under osteogenic conditions. This difference could be due to the different stiffness of PEG hydrogels versus PLLA-coated glass substrates, as discussed above; and to the different effects of ordered versus disordered nanopatterns on cell adhesion⁹¹. Hence, our results match other reports in that a higher degree of osteogenic differentiation is observed on substrates that promote smaller adhesions; in our case, S_0 but also S_{90} .

5.3.3. YAP-mediated mechanotransduction in chondrogenesis

We analysed the intracellular localization of YAP transcription coactivator in chondrogenesis and found that it was influenced by the local surface adhesiveness of the nanopatterns. YAP localization in three-dimensional prechondrogenic condensates was predominantly cytosolic in all conditions, corresponding with previous reports of YAP activity in 3D and in which cells also present a cortical actin disposition¹⁰¹. Moreover, high-density cultures (such as packed multicellular condensates) undergo activation of the Hippo pathway and YAP cytosol sequestering through a mechanism known as contact inhibition of proliferation, explaining the cytosolic-leaning ratios of YAP localization that we observe^{102–104}. Contraction of perinuclear actin fibres in 2D cultures on stiff substrates flattens the nucleus and opens the nuclear pores, thereby facilitating YAP import¹⁰⁵, which would seemingly be the case of fibronectin-coated substrates. Epithelial cells plated at low density on fibronectin substrates also experience an increase in YAP nuclear translocation via the FAK-Src-PI3K pathway¹⁰⁶; however, the high-density monolayer disposition that hMSCs adopt on S_{FN} would hinder YAP translocation as discussed above.

Although still mainly located in the cytosol, YAP translocation to the nucleus was higher in S_{45} and S_{90} , correlating with substrate ligand density. Interestingly, while S_{45} condensates displayed YAP translocation values at 6 h similar to those of S_{90} , this did not result in increased chondrogenic differentiation. Hence, while YAP-mediated mechanotransduction is possibly a

necessary step of cartilage formation, it is not enough to induce chondrogenesis by itself within the time frames analysed here.

Active YAP in the condensates increased after three days of chondrogenic induction, indicating that prolonged culture led to higher levels of mechanotransduction. This corresponds with the described YAP nuclear translocation in the early stages of chondrogenesis: in micromass cultures of chondroprogenitor cells, nuclear Yap peaks at day 5 and then gradually decreases, becoming mainly cytosolic after day 10, coinciding with the expression levels of chondrogenic markers Col2a1 and Col10a1^{57,58}. Therefore, we can link YAP nuclear translocation with increased differentiation on S_{90} nanopatterns. While it is possible that cells on other substrates also undergo chondrogenesis, this process would in any case be substantially slower without the appropriate nanoscale ligand configuration conferred by S_{90} substrates. In conclusion, controlling nanoscale local surface adhesiveness during the first chondrogenic steps is crucial to modulate YAP-mediated mechanotransduction and direct the fate of MSCs towards cartilage¹⁰⁷.

5.3.4. Local ligand density modulates differentiation through adhesion size and distribution

As nanopatterned surfaces provide an isotropic distribution of ligands, there is no preferential direction for cell adhesion, which would therefore result in a homogeneous distribution of the applied tension and favour a round nuclear morphology. Accordingly, no correlation was found between FA size and NSI under tenogenic conditions at 24 h, indicating that the applied tension was distributed around the cell perimeter, independently of adhesion size. We report a distinct biphasic behaviour in chondrogenesis, by which cells initially respond to increasing FA area by deforming their nuclei; as adhesion area increases, nuclear morphology becomes rounder again. We thus hypothesise that tension under chondrogenic induction is exerted through of a combination of adhesion size and distribution, regulating nuclear elongation. By this model, as adhesion assembly progresses, their location shifts in two stages: smaller and larger adhesions are distributed around the nucleus more evenly than medium-sized adhesions, which are more polarized. The former would induce nuclear roundness, while the latter would promote elongation. Because cells under chondrogenic stimuli aggregate into packed multicellular condensates, it cannot be determined from confocal microscopy images of paxillin staining whether this is the case. Cells on S_{FN} do present a distribution of paxillin clusters around nuclei similar to those in tenogenesis and osteogenesis, explaining the equal NSI values of 0.81 in all three lineages on this substrate.

In the case of osteogenesis, we find a clear trend for cell nuclei to become rounder as the FA area increases on nanopatterned substrates (which means that nuclei are rounder on S_{18} and S_{45} than on S_{90} , because cells on these substrates generate larger adhesions, as discussed above). As with chondrogenesis, this suggests that nuclear shape is regulated through both adhesion size and spatial distribution. Paxillin immunostaining in osteogenesis does show more polarized adhesions on the nanopatterned substrates where cells form smaller adhesions. Therefore, we conclude that during osteogenesis on nanopatterned substrates, smaller FAs are more polarized at two opposite sides of each nucleus, whereas larger FAs are more heterogeneously distributed. This varying distribution of FAs as they grow mediates nuclear morphology in the differentiating cells (Fig. 5.13).

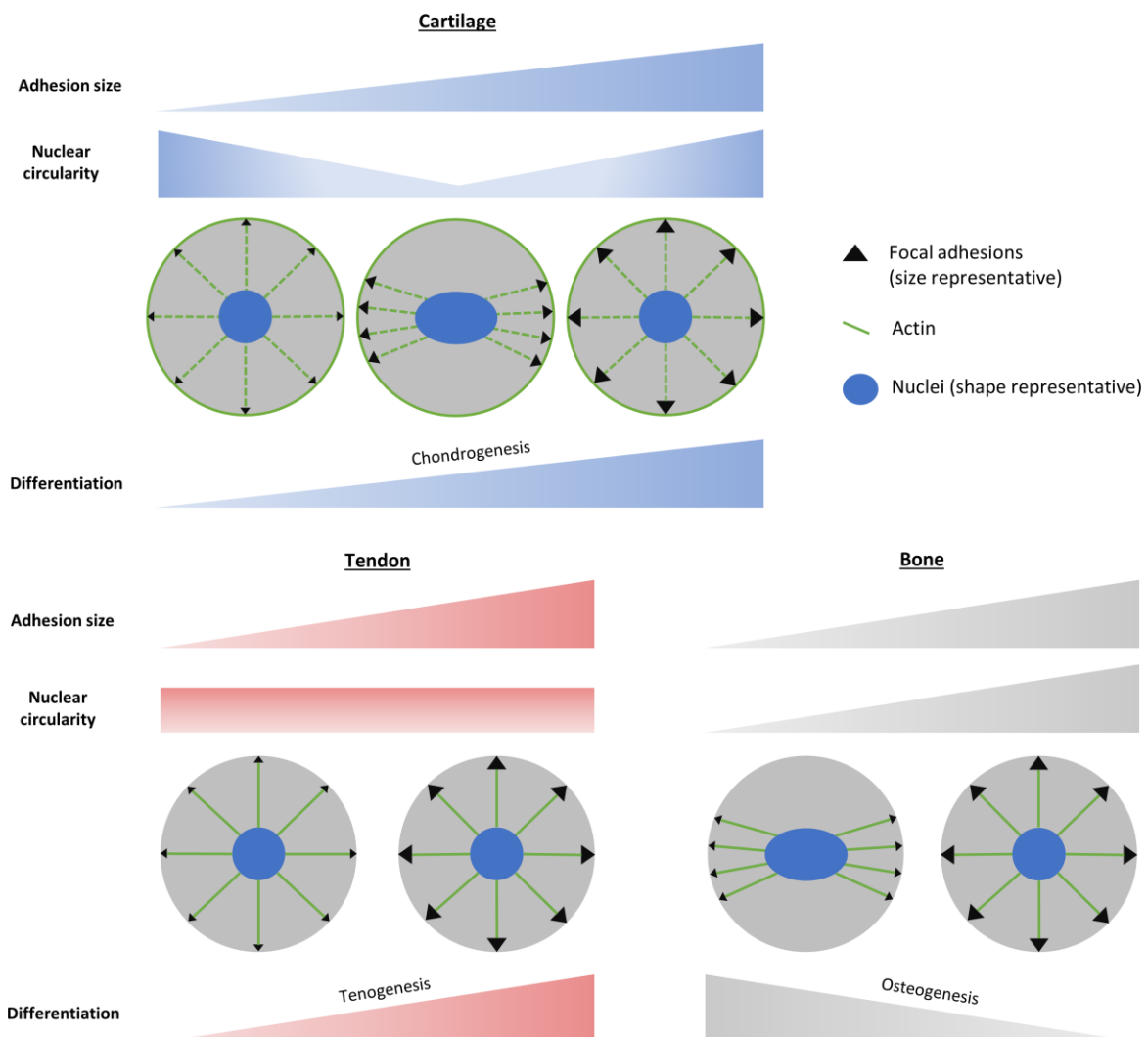


Figure 5.13. Nuclear morphology is modulated by focal adhesion size and distribution according to cell fate. Differentiation of hMSCs is regulated by the tension applied, which depends on FA size (tension module) and distribution (tension orientation) on nanopatterned substrates. Cell response varies according to the musculoskeletal lineage that is the fate of differentiation.

Finally, we analysed the relation between cell differentiation to each of the three musculoskeletal lineages with adhesion size and nuclear shape. We find that differentiation does depend on FA size and NSI, although in a different manner for each analysed cell fate. In chondrogenesis, marker expression increased when both FA size and the NSI also increased, excluding fibronectin-coated substrates. This again points to a close correlation between cell-substrate adhesion, the resulting cell shape in mesenchymal condensates, and subsequent differentiation towards chondrocytes. In tenogenesis, larger FAs evenly positioned around the nucleus seem to correlate with higher expression levels of the early tenogenic marker, supported by the described round morphology observed in tendon precursor cells¹⁰⁸. Cells under osteogenic conditions presented an opposite trend to the other lineages: smaller adhesions and elongated nuclei promoted differentiation. Thus, tension exerted through a combination of adhesion size and distribution regulates nuclear morphology and the subsequent osteogenic commitment, which is favoured by nuclear elongation¹⁰⁹.

5.4. References

1. Casanellas, I., García-Lizarribar, A., Lagunas, A. & Samitier, J. Producing 3D biomimetic nanomaterials for musculoskeletal system regeneration. *Front. Bioeng. Biotechnol.* **6**, 128 (2018).
2. Bouyer, M. *et al.* 3D-printed scaffold combined to 2D osteoinductive coatings to repair a critical-size mandibular bone defect. *Mater. Today Bio* **11**, 100113 (2021).
3. Wang, Y.-H. *et al.* Characterization and evaluation of the differentiation ability of human adipose-derived stem cells growing in scaffold-free suspension culture. *Cytotherapy* **16**, 485–495 (2014).
4. Staubli, F., Stoddart, M. J., D’Este, M. & Schwab, A. Pre-Culture of Human Mesenchymal Stromal Cells in Spheroids Reduces Hypertrophic Differentiation in vitro and Facilitates Chondrogenesis at a Low Total Cell Count Upon Embedding in Biomaterials. *SSRN Electron. J.* (2021) doi:10.2139/ssrn.3943650.
5. Bressan, E. *et al.* Nanotechnology to drive stem cell commitment. *Nanomedicine* **8**, 469–486 (2013).
6. Donnelly, H., Salmeron-sanchez, M. & Dalby, M. J. Designing stem cell niches for differentiation and self-renewal. *J. R. Soc. Interface* **15**, 20180388 (2018).
7. Wang, P. Y., Thissen, H. & Kingshott, P. Modulation of human multipotent and pluripotent stem cells using surface nanotopographies and surface-immobilised bioactive signals: A review. *Acta Biomater.* **45**, 31–59 (2016).
8. Migliorini, E., Guevara-Garcia, A., Albiges-Rizo, C. & Picart, C. Learning from BMPs and their biophysical extracellular matrix microenvironment for biomaterial design. *Bone* **141**, 115540 (2020).
9. Dalby, M. J., Gadegaard, N. & Oreffo, R. O. C. Harnessing nanotopography and integrin-matrix interactions to influence stem cell fate. *Nat Mater* **13**, 558–569 (2014).
10. Cross, L. M., Thakur, A., Jalili, N. A., Detamore, M. & Gaharwar, A. K. Nanoengineered biomaterials for repair and regeneration of orthopedic tissue interfaces. *Acta Biomater.* **42**, 2–17 (2016).
11. Dalby, M. J. *et al.* The control of human mesenchymal cell differentiation using nanoscale symmetry and disorder. *Nat. Mat* **6**, 997–1003 (2007).

12. Ye, K. *et al.* Matrix Stiffness and Nanoscale Spatial Organization of Cell-Adhesive Ligands Direct Stem Cell Fate. *Nano Lett.* **15**, 4720–4729 (2015).
13. Dobbenga, S., Fratila-apachitei, L. E. & Zadpoor, A. A. Nanopattern-induced osteogenic differentiation of stem cells – A systematic review. *Acta Biomater.* **46**, 3–14 (2016).
14. Gugutkov, D. *et al.* Osteogenic differentiation of mesenchymal stem cells using hybrid nanofibers with different configurations and dimensionality. *J. Biomed. Mater. Res. - Part A* **105**, 2065–2074 (2017).
15. Allan, C. *et al.* Osteoblast response to disordered nanotopography. *Cell Eng. Micro/Nanoscale* **9**, 1–7 (2018).
16. Ho-Shui-Ling, A. *et al.* Bone regeneration strategies: Engineered scaffolds, bioactive molecules and stem cells current stage and future perspectives. *Biomaterials* **180**, 143–162 (2018).
17. Sefkow-Werner, J. *et al.* Heparan sulfate co-immobilized with cRGD ligands and BMP2 on biomimetic platforms promotes BMP2-mediated osteogenic differentiation. *Acta Biomater.* **114**, 90–103 (2020).
18. Vozzi, G., Corallo, C. & Daraio, C. Pressure-activated microsyringe composite scaffold of poly(L-lactic acid) and carbon nanotubes for bone tissue engineering. *J. Appl. Polym. Sci.* **129**, 528–536 (2013).
19. Forget, J. *et al.* Differentiation of Human Mesenchymal Stem Cells Toward Quality Cartilage Using Fibrinogen-Based Nanofibers. *Macromol. Biosci.* **16**, 1348–1359 (2016).
20. Li, J., Li, X., Zhang, J., Kawazoe, N. & Chen, G. Induction of Chondrogenic Differentiation of Human Mesenchymal Stem Cells by Biomimetic Gold Nanoparticles with Tunable RGD Density. *Adv. Healthc. Mater.* **6**, 1700317 (2017).
21. Maturavongsadit, P. *et al.* Promotion of In Vitro Chondrogenesis of Mesenchymal Stem Cells Using In Situ Hyaluronic Hydrogel Functionalized with Rod-Like Viral Nanoparticles. *Biomacromolecules* **17**, 1930–1938 (2016).
22. Eftekhari, A. *et al.* The use of nanomaterials in tissue engineering for cartilage regeneration; current approaches and future perspectives. *Int. J. Mol. Sci.* **21**, 536 (2020).
23. Iannone, M. *et al.* Nanoengineered surfaces for focal adhesion guidance trigger mesenchymal stem cell self-organization and tenogenesis. *Nano Lett.* **15**, 1517–1525 (2015).
24. Bonnans, C., Chou, J. & Werb, Z. Remodelling the extracellular matrix in development and

- disease. *Nat. Rev. Mol. Cell Biol.* **15**, 786–801 (2014).
25. Assis-Ribas, T., Forni, M. F., Winnischofer, S. M. B., Sogayar, M. C. & Trombetta-Lima, M. Extracellular matrix dynamics during mesenchymal stem cells differentiation. *Dev. Biol.* **437**, 63–74 (2018).
 26. Madl, C. M., LeSavage, B. L., Dewi, R. E., Lampe, K. J. & Heilshorn, S. C. Matrix Remodeling Enhances the Differentiation Capacity of Neural Progenitor Cells in 3D Hydrogels. *Adv. Sci.* **6**, 1801716 (2019).
 27. Ingber, D. E., Wang, N. & Stamenović, D. Tensegrity, cellular biophysics, and the mechanics of living systems. *Reports Prog. Phys.* **77**, 1–42 (2014).
 28. Sun, Z., Guo, S. S. & Fässler, R. Integrin-mediated mechanotransduction. *J. Cell Biol.* **215**, 445–456 (2016).
 29. Vogel, V. & Sheetz, M. Local force and geometry sensing regulate cell functions. *Nat. Rev. Mol. Cell Biol.* **7**, 265–275 (2006).
 30. Watt, F. M. & Huck, W. T. S. Role of the extracellular matrix in regulating stem cell fate. *Nat. Rev. Mol. Cell Biol.* **14**, 467–473 (2013).
 31. Vogel, V. Unraveling the Mechanobiology of Extracellular Matrix. *Annu. Rev. Physiol.* **80**, 353–387 (2018).
 32. Rahil, Z. *et al.* Nanoscale mechanics guides cellular decision making. *Integr. Biol.* **8**, 929–935 (2016).
 33. Goetzke, R., Sechi, A., De Laporte, L., Neuss, S. & Wagner, W. Why the impact of mechanical stimuli on stem cells remains a challenge. *Cell. Mol. Life Sci.* **75**, 3297–3312 (2018).
 34. Dalby, M. J., García, A. J. & Salmeron-Sanchez, M. Receptor control in mesenchymal stem cell engineering. *Nat. Rev. Mater.* **3**, 17091 (2018).
 35. Wolfenson, H., Yang, B. & Sheetz, M. P. Steps in Mechanotransduction Pathways that Control Cell Morphology. *Annu. Rev. Physiol.* **81**, 585–605 (2019).
 36. Loebel, C., Mauck, R. L. & Burdick, J. A. Local nascent protein deposition and remodelling guide mesenchymal stromal cell mechanosensing and fate in three-dimensional hydrogels. *Nat. Mater.* **18**, 883–891 (2019).
 37. Arnold, M. *et al.* Activation of integrin function by nanopatterned adhesive interfaces.

- ChemPhysChem* **5**, 383–388 (2004).
38. Cavalcanti-Adam, E. A. *et al.* Lateral spacing of integrin ligands influences cell spreading and focal adhesion assembly. *Eur. J. Cell Biol.* **85**, 219–224 (2006).
 39. Cavalcanti-Adam, E. A. *et al.* Cell spreading and focal adhesion dynamics are regulated by spacing of integrin ligands. *Biophys. J.* **92**, 2964–2974 (2007).
 40. Wang, X. *et al.* Effect of RGD nanospacing on differentiation of stem cells. *Biomaterials* **34**, 2865–2874 (2013).
 41. Polini, A. *et al.* Mesenchymal Stem Cell Fate: Applying Biomaterials for Control of Stem Cell Behavior. *Front. Bioeng. Biotechnol* **4**, 383389–38 (2016).
 42. Oria, R. *et al.* Force loading explains spatial sensing of ligands by cells. *Nature* **552**, 219–224 (2017).
 43. Thomas, C. H., Collier, J. H., Sfeir, C. S. & Healy, K. E. Engineering gene expression and protein synthesis by modulation of nuclear shape. *Proc. Natl. Acad. Sci.* **99**, 1972–1977 (2002).
 44. Kim, D. H., Chambliss, A. B. & Wirtz, D. The multi-faceted role of the actin cap in cellular mechanosensation and mechanotransduction. *Soft Matter* **9**, 5516–5523 (2013).
 45. Tsimbouri, P. *et al.* Nanotopographical effects on mesenchymal stem cell morphology and phenotype. *J. Cell. Biochem.* **115**, 380–390 (2014).
 46. Lomakin, A. J. *et al.* The nucleus acts as a ruler tailoring cell responses to spatial constraints. *Science* **370**, eaba2894 (2020).
 47. Venturini, V. *et al.* The nucleus measures shape changes for cellular proprioception to control dynamic cell behavior. *Science* **370**, (2020).
 48. Luciano, M. *et al.* Cell monolayers sense curvature by exploiting active mechanics and nuclear mechanoadaptation. *Nat. Phys.* (2021) doi:10.1038/s41567-021-01374-1.
 49. Rausch, V. & Hansen, C. G. The Hippo Pathway, YAP/TAZ, and the Plasma Membrane. *Trends Cell Biol.* **30**, 32–48 (2020).
 50. Hiemer, S. E. & Varelas, X. Stem cell regulation by the Hippo pathway. *Biochim. Biophys. Acta - Gen. Subj.* **1830**, 2323–2334 (2013).
 51. Si, Y. *et al.* Src Inhibits the hippo tumor suppressor pathway through tyrosine phosphorylation of Lats1. *Cancer Res.* **77**, 4868–4880 (2017).

Chapter 5

52. Dupont, S. *et al.* Role of YAP/TAZ in mechanotransduction. *Nature* **474**, 179–184 (2011).
53. Stanton, A. E., Tong, X., Lee, S. & Yang, F. Biochemical Ligand Density Regulates Yes-Associated Protein Translocation in Stem Cells through Cytoskeletal Tension and Integrins. *ACS Appl. Mater. Interfaces* **11**, 8849–8857 (2019).
54. Dasgupta, I. & McCollum, D. Control of cellular responses to mechanical cues through YAP/TAZ regulation. *J. Biol. Chem.* **294**, 17693–17706 (2019).
55. Scott, K. E., Fraley, S. I. & Rangamani, P. A spatial model of YAP/TAZ signaling reveals how stiffness, dimensionality, and shape contribute to emergent outcomes. *Proc. Natl. Acad. Sci.* **118**, e2021571118 (2021).
56. Cosgrove, B. D. *et al.* N-cadherin adhesive interactions modulate matrix mechanosensing and fate commitment of mesenchymal stem cells. *Nat. Mater.* **15**, 1297–1306 (2016).
57. Karystinou, A. *et al.* Yes-associated protein (YAP) is a negative regulator of chondrogenesis in mesenchymal stem cells. *Arthritis Res. Ther.* **17**, 1–14 (2015).
58. Deng, Y. *et al.* Yap1 Regulates Multiple Steps of Chondrocyte Differentiation during Skeletal Development and Bone Repair. *Cell Rep.* **14**, 2224–2237 (2016).
59. Zhong, W. *et al.* YAP-mediated regulation of the chondrogenic phenotype in response to matrix elasticity. *J. Mol. Histol.* **44**, 587–595 (2013).
60. Sims, J. R., Karp, S. & Ingber, D. E. Altering the cellular mechanical force balance results in integrated changes in cell , cytoskeletal and nuclear shape. **103**, 1215–1222 (1992).
61. Jean, R. P., Gray, D. S., Spector, A. A. & Chen, C. S. Characterization of the nuclear deformation caused by changes in endothelial cell shape. *J. Biomech. Eng.* **126**, 552–558 (2004).
62. Köppen, M., García Fernández, B., Carvalho, L., Jacinto, A. & Heisenberg, C. P. Coordinated cell-shape changes control epithelial movement in zebrafish and *Drosophila*. *Development* **133**, 2671–2681 (2006).
63. Kim, D., Cho, S. & Wirtz, D. Tight coupling between nucleus and cell migration through the perinuclear actin cap. *J. Cell Sci.* **127**, 2528–2541 (2014).
64. Galbraith, C. G. & Sheetz, M. P. A micromachined device provides a new bend on fibroblast. *Proc. Natl. Acad. Sci.* **94**, 9114–9118 (1997).
65. Versaevel, M., Grevesse, T. & Gabriele, S. Spatial coordination between cell and nuclear shape

- within micropatterned endothelial cells. *Nat. Commun.* **3**, 671 (2012).
66. Balaban, N. Q. *et al.* Force and focal adhesion assembly: a close relationship studied using elastic micropatterned substrates. *Nat. Cell Biol.* **3**, 466–472 (2001).
 67. Kim, D. & Wirtz, D. Focal adhesion size uniquely predicts cell migration. *FASEB J.* **27**, 1351–1361 (2013).
 68. Lagunas, A. *et al.* Tailoring RGD local surface density at the nanoscale toward adult stem cell chondrogenic commitment. *Nano Res.* **10**, 1959–1971 (2017).
 69. DeLise, A. M., Fischer, L. & Tuan, R. S. Cellular interactions and signaling in cartilage development. *Osteoarthr. Cartil.* **8**, 309–334 (2000).
 70. Bobick, B. E., Chen, F. H., Le, A. M. & Tuan, R. S. Regulation of the chondrogenic phenotype in culture. *Birth Defects Res. Part C - Embryo Today Rev.* **87**, 351–371 (2009).
 71. Chen, S., Fu, P., Cong, R., Wu, H. S. & Pei, M. Strategies to minimize hypertrophy in cartilage engineering and regeneration. *Genes Dis.* **2**, 76–95 (2015).
 72. Bi, W. *et al.* Haploinsufficiency of Sox9 results in defective cartilage primordia and premature skeletal mineralization. *Proc. Natl. Acad. Sci.* **98**, 6698–6703 (2001).
 73. Park, A. *et al.* Adipose-Derived Mesenchymal Stem Cells Treated with Growth Differentiation Factor-5 Express Tendon-Specific Markers. *Tissue Eng. Part A* **16**, 2941–2951 (2010).
 74. Brown, J. P., Galassi, T. V., Stoppato, M., Schiele, N. R. & Kuo, C. K. Comparative analysis of mesenchymal stem cell and embryonic tendon progenitor cell response to embryonic tendon biochemical and mechanical factors. *Stem Cell Res. Ther.* **6**, 1–8 (2015).
 75. Nam, H. Y., Pinguan-Murphy, B., Amir Abbas, A., Mahmood Merican, A. & Kamarul, T. The proliferation and tenogenic differentiation potential of bone marrow-derived mesenchymal stromal cell are influenced by specific uniaxial cyclic tensile loading conditions. *Biomech. Model. Mechanobiol.* **14**, 649–663 (2015).
 76. Schweitzer, R. *et al.* Analysis of the tendon cell fate using Scleraxis, a specific marker for tendons and ligaments. *Development* **128**, 3855–3866 (2001).
 77. Tan, S.-L. *et al.* Identification of Pathways Mediating Growth Differentiation Factor5-Induced Tenogenic Differentiation in Human Bone Marrow Stromal Cells. *PLoS One* **10**, e0140869 (2015).

Chapter 5

78. Shukunami, C., Takimoto, A., Oro, M. & Hiraki, Y. Scleraxis positively regulates the expression of tenomodulin, a differentiation marker of tenocytes. **298**, 234–247 (2006).
79. Tai, G., Christodoulou, I., Bishop, A. E. & Polak, J. M. Use of green fluorescent fusion protein to track activation of the transcription factor osterix during early osteoblast differentiation. **333**, 1116–1122 (2005).
80. Nakashima, K. *et al.* The Novel Zinc Finger-Containing Transcription Factor Osterix Is Required for Osteoblast Differentiation and Bone Formation. *Cell* **108**, 17–29 (2002).
81. Zhang, W., Yang, N. & Shi, X. Regulation of Mesenchymal Stem Cell Osteogenic Differentiation by Glucocorticoid-induced Leucine Zipper (GILZ). *J. Biol. Chem.* **283**, 4723–4729 (2008).
82. Lagunas, A. *et al.* Continuous bone morphogenetic protein-2 gradients for concentration effect studies on C2C12 osteogenic fate. *Nanomedicine Nanotechnology, Biol. Med.* **9**, 694–701 (2013).
83. Chen, C. S., Mrksich, M., Huang, S., Whitesides, G. M. & Ingber, D. E. Geometric control of cell life and death. *Science* **276**, 1425–1428 (1997).
84. Clark, E. A. & Brugge, J. S. Integrins and signal transduction pathways: The road taken. *Science* **268**, 233–239 (1995).
85. Miyamoto, S., Akiyama, S. K. & Yamada, K. M. Synergistic roles for receptor occupancy and aggregation in integrin transmembrane function. *Science* **267**, 883–885 (1995).
86. Maniotis, A. J., Chen, C. S. & Ingber, D. E. Demonstration of mechanical connections between integrins, cytoskeletal filaments, and nucleoplasm that stabilize nuclear structure. *Proc. Natl. Acad. Sci.* **94**, 849–854 (1997).
87. Vergani, L., Grattarola, M. & Nicolini, C. Modifications of chromatin structure and gene expression following induced alterations of cellular shape. *Int. J. Biochem. Cell Biol.* **36**, 1447–1461 (2004).
88. Seelbinder, B. *et al.* Nuclear deformation guides chromatin reorganization in cardiac development and disease. *Nat. Biomed. Eng.* (2021) doi:10.1038/s41551-021-00823-9.
89. McBeath, R., Pirone, D. M., Nelson, C. M., Bhadriraju, K. & Chen, C. S. Cell Shape, Cytoskeletal Tension, and RhoA Regulate Stem Cell Lineage Commitment. *Dev. Cell* **6**, 483–495 (2004).
90. Kilian, K. A., Bugarija, B., Lahn, B. T. & Mrksich, M. Geometric cues for directing the differentiation of mesenchymal stem cells. *Proc. Natl. Acad. Sci.* **107**, 4872–4877 (2010).

91. Huang, J. *et al.* Impact of order and disorder in RGD nanopatterns on cell adhesion. *Nano Lett.* **9**, 1111–1116 (2009).
92. Casanellas, I. *et al.* Dendrimer-based uneven nanopatterns to locally control surface adhesiveness: A method to direct chondrogenic differentiation. *J. Vis. Exp.* **131**, e56347 (2018).
93. Li, Z. *et al.* Effects of RGD nanospacing on chondrogenic differentiation of mesenchymal stem cells. *J. Mater. Chem. B* **3**, 5197–5209 (2015).
94. Hashmi, B. *et al.* Mechanical induction of dentin-like differentiation by adult mouse bone marrow stromal cells using compressive scaffolds. *Stem Cell Res.* **24**, 55–60 (2017).
95. Kuo, C. K. & Tuan, R. S. Mechanoactive Tenogenic Differentiation of Human Mesenchymal Stem Cells. *Tissue Eng. Part A* **14**, 1615–1627 (2008).
96. Teh, T. K. H., Toh, S. & Goh, J. C. H. Aligned Fibrous Scaffolds for Enhanced Mechanoresponse and Tenogenesis of Mesenchymal Stem Cells. *Tissue Eng. Part A* **19**, 1360–1372 (2013).
97. Morita, Y., Watanabe, S., Ju, Y. & Xu, B. Determination of optimal cyclic Uniaxial stretches for stem cell-to-tenocyte differentiation under a wide range of mechanical stretch conditions by evaluating gene expression and protein synthesis levels. *Acta Bioeng. Biomech.* **15**, 71–79 (2013).
98. Burk, J. *et al.* Induction of Tenogenic Differentiation Mediated by Extracellular Tendon Matrix and Short-Term Cyclic Stretching. *Stem Cells Int.* **2016**, 7342379 (2016).
99. Testa, S. *et al.* Combination of biochemical and mechanical cues for tendon tissue engineering. *J. Cell. Mol. Med.* **21**, 2711–2719 (2017).
100. Wang, X., Li, S., Yan, C., Liu, P. & Ding, J. Fabrication of RGD micro/nanopattern and corresponding study of stem cell differentiation. *Nano Lett.* **15**, 1457–1467 (2015).
101. Lee, J. Y. *et al.* YAP-independent mechanotransduction drives breast cancer progression. *Nat. Commun.* **10**, 1–9 (2019).
102. Zhao, B. *et al.* Inactivation of YAP oncoprotein by the Hippo pathway is involved in cell contact inhibition and tissue growth control. *Genes Dev.* **21**, 2747–2761 (2007).
103. Silvis, M. R. *et al.* α -Catenin Is a Tumor Suppressor That Controls Cell Accumulation by Regulating the Localization and Activity of the Transcriptional Coactivator Yap1. *Sci. Signal.* **4**, ra33 (2011).

Chapter 5

104. Kim, N., Koh, E., Chen, X. & Gumbiner, B. M. E-cadherin mediates contact inhibition of proliferation through Hippo signaling-pathway components. *Proc. Natl. Acad. Sci.* **108**, 11930–11935 (2011).
105. Elosegui-Artola, A. *et al.* Force Triggers YAP Nuclear Entry by Regulating Transport across Nuclear Pores. *Cell* **171**, 1397–1410 (2017).
106. Kim, N. G. & Gumbiner, B. M. Adhesion to fibronectin regulates Hippo signaling via the FAK–Src–PI3K pathway. *J. Cell Biol.* **210**, 503–515 (2015).
107. Casanellas, I. *et al.* The Janus role of adhesion in chondrogenesis. *Int. J. Mol. Sci.* **21**, 5269 (2020).
108. Chen, J. *et al.* Characterization and comparison of post-natal rat Achilles tendon-derived stem cells at different development stages. *Sci. Rep.* **6**, 22946 (2016).
109. Casanellas, I. *et al.* Matrix nanopatterning regulates mesenchymal differentiation through focal adhesion size and distribution according to cell fate. *Biomimetics* **4**, 43 (2019).

Chapter 6

Conclusions

Injuries and conditions of musculoskeletal tissues such as cartilage, tendon and bone are among the main causes of disability worldwide and there is a wide need for improved regenerative therapies. *In vitro* platforms and biomaterials that aim to guide stem cell differentiation should be designed considering that cells interact with their surroundings through nanoscale receptors at the membrane, attaching to ligands in the extracellular matrix. We have successfully employed uneven dendrimer-nanopatterned substrates to modulate local cell-surface adherence in cells undergoing differentiation towards cartilage, tendon and bone. We elucidate nanoscale adherence cues driving stem cell behaviour and differentiation during the formation of these musculoskeletal tissues, and the corresponding mechanisms of signal sensing and transduction:

- Mesenchymal stem cells (MSCs) adapt their motility mode to substrate local adherence during early cartilage formation. While cells on low-adherence substrates migrate in an amoeboid manner, cells on protein coatings behave as fully mesenchymal.
- Mesenchymal condensation on pristine and nanopatterned substrates is regulated by an equilibrium between contact inhibition of locomotion and contact following of locomotion, whereas condensation on protein coatings entails the formation of topological defects in the nematic order of the established monolayer.
- Nanopatterns of high local ligand density represent an intersection between tailored local ligand density and full protein coatings. Cells on this condition present behaviours selectively similar to those on low-density nanopatterned substrates and protein coatings: While they migrate as single round cells and quickly form condensates, they also develop local monolayer-like structures and extend large protrusions.
- The response of MSCs to substrate local adherence on nanopatterns can be linear or biphasic, depending on the parameter. Linear parameters include net displacement and directionality during migration, mechanical cell-cell adherence in condensates and bone differentiation. Biphasic parameters include protrusion size, migration velocity, the rate of cell-cell collisions, condensate compaction, gap junction intercellular communication (GJIC), the nuclear translocation of Yes-associated protein and cartilage differentiation.
- Cell sensing and response to local ligand density is a continuous process that influences gap junction protein production during and after condensation. Substrate adherence is sensed by integrin adhesions and propagated to adjacent cells through cytoskeletal contractions.

- The formation of cell-substrate adhesions depends on the musculoskeletal lineage that cells are differentiating to. Cells undergoing osteogenesis form larger adhesions on substrates of lower local ligand density, contrary to cells under chondrogenic or tenogenic induction. We attribute this behaviour to the specific requirements of each tissue and to the relation between ligand spacing and substrate stiffness.
- Nuclear elongation holds a different relation with adhesion size in each of the analysed tissues, showcasing the role of the nucleus as a transducer of substrate adherence. We attribute these differences to the developmental characteristics of each tissue and the varying distribution of adhesions around the nucleus in each case.
- Nanopatterns of high local ligand density provide MSCs with optimal conditions to promote cartilage development (as seen through condensate structure and stability, GJIC and cell differentiation) and osteogenic differentiation. Mesenchymal condensates from this condition can be removed from the substrate, frozen and thawed again without loss of structure or cell viability, indicating their potential adequacy for cell-based regenerative therapies.

Our findings reflect the impact that the fine tuning of materials interfaces has in cell response. By tailoring the nanopattern configuration of the cell-adhesive motif RGD, we exerted control over the formation, architecture and function of a complex dynamic biological system such as mesenchymal condensates. Moreover, we demonstrate that substrate functionalization should be designed according to the specific nanoscale requirements of the target tissue. The results have an immediate application to *in vitro* engineering of musculoskeletal tissues, but they are also extensible to the study of other biological processes in which active ECM remodelling and thus, changes in the adhesion requirements play an active role.

Resum en català (Summary in Catalan)

Extracte introductori

Tradicionalment descrites com la unitat més petita de la vida, les cèl·lules modulen contínuament el seu comportament segons l'ambient on es troben i la companyia que mantenen. Aquest comportament és també inherent als éssers humans, ja que percebem el nostre entorn mitjançant sistemes altament especialitzats (els cinc sentits) que fan de sensors i transductors de senyals. A través d'aquests sistemes podem experimentar el món que ens envolta, interactuar amb ell i, en la mesura de les nostres capacitats, intentar remodelar-lo per adaptar-lo als nostres propòsits, tal com fan les cèl·lules que ens componen.

La pregunta de com les cèl·lules perceben el seu entorn (inclosa la matriu extracel·lular i les cèl·lules veïnes) i hi responen ha fascinat la comunitat científica des de fa dècades. Se sap que les indicacions que reben del seu ambient poden portar les cèl·lules per camins diferents com ara la divisió, la diferenciació i fins i tot la malignitat, essent un regulador primordial de la funció cel·lular en moltes situacions fisiològiques. Per tant, aprofundint en la nostra comprensió fonamental de les interaccions cèl·lula-matriu, els investigadors també contribueixen al desenvolupament de teràpies o dispositius per fer front a lesions i malalties del nostre cos. En aquest treball explorem les interaccions cèl·lula-matriu que regulen el desenvolupament de teixits musculoesquelètics, que són alguns dels més freqüentment lesionats i entre les principals causes de discapacitat al món.

Com que les cèl·lules tenen una mica micromètrica, les seves interaccions amb la matriu del seu voltant tenen lloc principalment a escala nanomètrica. Els receptors de proteïnes de la membrana cel·lular s'uneixen als lligands presents a les proteïnes extracel·lulars; aquestes adhesions tenen repercussions intracel·lulars i regulen paràmetres com la forma cel·lular, l'organització del citoesquelet o l'expressió gènica. En aquesta tesi produïm nanopatrons de lligands adherents per a les cèl·lules, i els utilitzem com a plataformes *in vitro* on cultivem cèl·lules mare mesenquimals, en medis de cultiu inductors de diferenciació cap a cartílag, tendó o os, tres teixits musculoesquelètics. També emprem substrats totalment coberts de fibronectina (proteïna de la matriu extracel·lular) com a condició d'alta adherència amb senyalització biològica completa. Analitzem la dinàmica del moviment cel·lular, la formació de les primeres estructures de teixits i les seves propietats mecàniques i estabilitat, la comunicació intercel·lular i la

diferenciació cel·lular a cadascun dels tres llinatges. També explorem mecanismes de mecanotransducció que poden explicar les nostres observacions.

Extractes dels capítols

La tesi s'estructura en tres capítols centrals on presentem resultats sobre diferents aspectes del desenvolupament de teixits musculoesquelètics, i com es regulen a partir de l'adhesió a escala nanomètrica que aporten els substrats de cultiu nanopatronats:

- Capítol 3: Dinàmica de la migració i la condensació cel·lular

La migració cel·lular aïllada (cada cèl·lula per separat) i col·lectiva (grups de cèl·lules en conjunt) és una part essencial dels processos biològics com la formació de teixits, la cicatrització de ferides i el desenvolupament de malalties. Durant les primeres etapes de formació de cartílag, les cèl·lules mare mesenquimals s'agrupen en estructures multicel·lulars que estableixen les bases estructurals del teixit. Aquest procés de condensació mesenquimal està limitat per la capacitat de les cèl·lules per migrar a través de la matriu extracel·lular i establir els primers contactes cèl·lula-cèl·lula. En aquest capítol fem vídeos de cèl·lules a l'inici de la condrogènesi sobre nanopatrons de lligand de matriu adhesiu, i trobem que la densitat de lligand al substrat modula la direccionalitat i la velocitat de migració de cèl·lules mare individuals i col·lectives. La transició progressiva de cèl·lules individuals a condensats multicel·lulars també està guiada pels contactes cèl·lula-cèl·lula. Les cèl·lules cultivades sobre substrats amb nanopatrons presenten un mode de migració ameboide amb morfologia arrodonida, mentre que les dels substrats coberts de proteïna mostren morfologies mesenquimals i tendeixen a formar una monocapa en lloc de condensacions. Plantejem que, quan dues cèl·lules xoquen, la condensació mesenquimal està regulada per l'equilibri entre la inhibició de locomoció per contacte (cada cèl·lula reprèn la migració de manera aïllada) i el seguiment de locomoció per contacte (les cèl·lules estableixen una nova unitat de condensació).

- Capítol 4: Estructura dels condensats i comunicació intercel·lular

La comunicació intercel·lular per unions *gap* (GJIC, en anglès) proporciona un flux continu i eficient d'informació biològica durant la formació de teixits i és essencial per mantenir l'homeòstasi i la funció tissular. Aquest mode de comunicació intercel·lular és especialment important en teixits avasculars com el cartílag. Aquí utilitzem substrats amb nanopatrons per estudiar com la densitat local de lligands modula l'estructura, l'estabilitat mecànica i l'arquitectura de la xarxa de proteïnes dins de condensats mesenquimals multicel·lulars durant la condrogènesi.

Mostrem que els nanopatrons d'alta densitat de lligand faciliten el creixement de condensats i generen condensats que són més estables i més compactes. Després demostrem que els nanopatrons d'alta densitat de lligand promouen l'expressió de proteïna d'unió *gap* i milloren l'arquitectura de la xarxa intercel·lular que forma la proteïna, generant una xarxa més eficient de GJIC en condensats mesenquimals. A continuació dissenyem un assaig de trasplantament de condensats i mostrem que les cèl·lules detecten la densitat de lligand al substrat de manera contínua, amb cèl·lules que responen a les condicions canviants del substrat encara que no hi estiguin en contacte directe. Finalment, confirmem que la informació del substrat és detectada per les adhesions cèl·lula-substrat i es propaga pel condensat mitjançant contraccions del citoesquelet.

- Capítol 5: Adhesió, forma cel·lular i diferenciació a llinatges musculoesquelètics

Les lesions i malalties dels teixits musculoesquelètics com el cartílag, el tendó i l'os es troben entre les principals causes de discapacitat a tot el món; hi ha una necessitat urgent de millorar les teràpies de regeneració d'aquests teixits. Com a aplicació dels substrats amb nanopatrons per guiar les cèl·lules mare cap a destins musculoesquelètics, aquí induïm la diferenciació cel·lular a cadascun d'aquests tres llinatges per averiguar la densitat de lligand local òptima que la promou. Els nanopatrons d'alta densitat de lligand promouen la diferenciació condrogènica mitjançant la translocació nuclear d'un activador transcripcional mecanosensible. La mateixa configuració de nanopatró també afavoreix l'osteogènesi, encara que en aquest cas les cèl·lules formen adhesions més petites que en substrats de baixa i mitjana densitat. La tenogènesi no sembla veure's afectada per la densitat de lligand del substrat. Atès que la tensió exercida des dels receptors de la membrana cel·lular es transmet pel citoesquelet al nucli cel·lular, analitzem la morfologia nuclear de cada condició segons el destí de diferenciació cel·lular. Per a la condrogènesi, trobem que les cèl·lules responen als augments inicials de la mida d'adhesió amb nuclis allargats; a mesura que augmenta la mida d'adhesió, els nuclis recuperen una forma circular. En el cas de la tenogènesi, no hi ha cap relació entre la mida de l'adhesió i la circularitat nuclear, cosa que indica que les adhesions es distribueixen al voltant de la cèl·lula de manera similar a tots els substrats. Per a l'osteogènesi, trobem que la deformació nuclear augmenta amb la disminució de la mida d'adhesió. Plantegem que la resposta cel·lular a la densitat de lligand a la nanoescala depèn tant de la mida com de la distribució de les adhesions al voltant de la cèl·lula, d'una manera diferent per a cadascun dels tres llinatges analitzats, i que l'estirament nuclear modula els efectes observats sobre la diferenciació.

Conclusions

Les plataformes *in vitro* i els biomaterials que tenen com a objectiu guiar la diferenciació de cèl·lules mare s'han de dissenyar tenint en compte que les cèl·lules interaccionen amb el seu entorn mitjançant receptors a la nanoescala de la membrana, que s'uneixen als lligands de la matriu extracel·lular. Hem emprat amb èxit substrats amb nanopatrons de lligand adherent per modular l'adhesió local de les cèl·lules que s'estan diferenciant cap al cartílag, el tendó i l'os. Esbrinem les conformacions d'adhesió nanomètrica que regulen el comportament i diferenciació de cèl·lules mare durant la formació d'aquests teixits musculoesquelètics, i els mecanismes corresponents de detecció i transducció del senyal. Les principals conclusions que n'extreiem són les següents:

- Les cèl·lules mare mesenquimals adapten el seu mode de migració a l'adherència local del substrat durant la formació de cartílag. Mentre que les cèl·lules de substrats de baixa adherència migren de manera ameboide, les cèl·lules en recobriments de proteïnes es comporten com a totalment mesenquimals.

- La condensació mesenquimal en nanopatrons està regulada per un equilibri entre la inhibició de contacte de la locomoció i el seguiment de contacte de la locomoció, mentre que la condensació en els recobriments de proteïnes comporta la formació de defectes topològics en l'ordre nemàtic de la monocapa establerta.

- Els nanopatrons d'alta densitat local de lligand representen una intersecció entre la presència de lligand regulada localment a escala nanomètrica i els recobriments de proteïnes completes. Les cèl·lules en aquesta condició presenten comportaments selectivament similars als dels substrats amb nanopatrons de baixa densitat i recobriments de proteïnes: migren com a cèl·lules rodones individuals i formen condensats ràpidament, però també desenvolupen estructures locals semblants a una monocapa i estenen grans protuberàncies.

- La resposta cel·lular a l'adherència local del substrat en nanopatrons pot ser lineal o bifàsica, depenent del paràmetre. Els paràmetres lineals inclouen el desplaçament net i la direccionalitat durant la migració, l'adhesió mecànica cèl·lula-cèl·lula en els condensats i la diferenciació òssia. Els paràmetres bifàsics inclouen la mida de les protrusions, la velocitat de migració, el ritme de col·lisions cèl·lula-cèl·lula, la compactació del condensat, la comunicació intercel·lular per unions *gap* (GJIC), la translocació nuclear de proteïna mecanosensible i la diferenciació a cartílag.

- La detecció i la resposta a la densitat de lligand és un procés continu que influeix en la producció de proteïnes d'unió *gap* durant i després de la condensació. Les cèl·lules detecten l'adherència al substrat mitjançant les adhesions d'integrines, i es propaga a les cèl·lules adjacents per contraccions del citoesquelet.

- La formació d'adhesions cèl·lula-substrat depèn del llinatge musculoesquelètic al qual s'estan diferenciant les cèl·lules. Les cèl·lules que realitzen osteogènesi formen adhesions més grans sobre substrats de densitat de lligand més baixa, al contrari que les cèl·lules sota inducció condrogènica o tenogènica. Atribuïm aquest comportament als requisits específics de cada teixit i a la relació entre l'espaiat de lligands i la rigidesa del substrat.

- L'allargament nuclear té una relació diferent amb la mida d'adhesions en cadascun dels teixits analitzats, mostrant el paper del nucli com a transductor de l'adherència al substrat. Atribuïm aquestes diferències a les característiques de desenvolupament de cada teixit i a la distribució variable de les adhesions al voltant del nucli en cada cas.

- Els nanopatrons d'alta densitat de lligand proporcionen a les cèl·lules condicions òptimes per al desenvolupament del cartílag (com es veu a través de l'estructura i l'estabilitat dels condensats, la GJIC i la diferenciació cel·lular) i la diferenciació osteogènica. Els condensats mesenquimals d'aquesta condició es poden extreure del substrat, congelar i descongelar de nou sense pèrdua d'estructura o viabilitat cel·lular, cosa que indica la seva potencial adequació per a teràpies regeneratives.

Les nostres conclusions reflecteixen l'impacte que té l'ajust precís de les interfícies de materials en la resposta cel·lular. Adaptant la configuració del nanopatró de lligand adhesiu cel·lular, controlem la formació, l'arquitectura i la funció d'un sistema biològic dinàmic complex com són els condensats mesenquimals. A més, demostrem que la funcionalització del substrat s'ha de dissenyar segons els requisits específics a nanoescala del teixit objectiu. Els resultats tenen una aplicació immediata a l'enginyeria *in vitro* de teixits musculoesquelètics, però també són extensibles a l'estudi d'altres processos biològics en els quals la remodelació activa de la matriu extracel·lular i, per tant, els canvis en els requisits d'adhesió, tinguin un paper rellevant.

List of Figures

Chapter 1

1.1. Types and ligands of integrin receptors	23
1.2. Integrin conformational states	24
1.3. Nanoscale architecture of focal adhesions	26
1.4. Proposed mechanisms of nuclear mechanotransduction	27
1.5. Dendrimer surface adsorption	32
1.6. Uneven nanopatterns of RGD dendrimers	34
1.7. Mesenchymal condensation	38

Chapter 2

2.1. Steps of substrate coating and nanopatterning	60
2.2. Analysis of Cx43 intercellular communication network architecture	71
2.3. Analysis of focal adhesions	73
2.4. Analysis of differentiation markers for tenogenesis and osteogenesis	74

Chapter 3

3.1. The mesenchymal and amoeboid modes of cell migration	80
3.2. Topological defects in nematic systems	82
3.3. Initial cell morphology	84
3.4. Protrusion size	85
3.5. Live imaging of cell migration and condensation	86
3.6. Single cell trajectories	87
3.7. Dynamics of single cell migration and collisions	89
3.8. Actin dynamics during condensation	90
3.9. Topological defects in the nematic order of protein coatings	91

3.10. Dynamics of multicellular condensates	92
3.11. RGD dendrimers in solution impair integrin clustering	94
3.12. Cell migration blocking cell-substrate and cell-cell interactions	95
3.13. Effects of pharmacological inhibitors on single and collective cell migration	96
3.14. Schematic of condensation regulation	103

Chapter 4

4.1. Osteochondral development, with mesenchymal condensation as the first stage	119
4.2. Schematics of gap junction structure	120
4.3. Chondrogenic medium induces mesenchymal condensation	123
4.4. Live/Dead assay in condensates	124
4.5. Condensate size and stability	125
4.6. Actin structure in condensates	125
4.7. N-cadherin and vinculin expression	126
4.8. Ligand density modulates connexin expression	128
4.9. Ligand density modulates gap junction network architecture	129
4.10. Gap junction intercellular communication network functionality	130
4.11. Cell condensates adapt to changing ligand density	132
4.12. Effects of integrin blocking and myosin inhibition	134
4.13. Proposed model for substrate input sensing and propagation	141

Chapter 5

5.1. Regulation of YAP/TAZ nuclear translocation through the Hippo pathway	154
5.2. Nuclear shape depends on cell fate	157
5.3. Cytoskeletal morphology	158
5.4. Focal adhesion (FA) size depends on cell fate	159

5.5. Focal adhesion (FA) size influence on nuclear remodelling	161
5.6. Effect of substrate nanopatterning on cartilage differentiation	162
5.7. YAP nuclear translocation in chondrogenesis	163
5.8. Effect of substrate nanopatterning on tendon differentiation	164
5.9. Effect of substrate nanopatterning on bone differentiation	165
5.10. Adherence and nuclear remodelling mediate differentiation	166
5.11. Chromatin condensation	167
5.12. Live/Dead assay in condensates after a freeze-thaw cycle	168
5.13. Nuclear morphology is modulated by focal adhesion size and distribution according to cell fate	174

List of Tables

Chapter 1

1.1. Nanopatterns characterization	34
------------------------------------	----

Chapter 2

2.1. Preparation of RGD-Cys-D1 dendrimer solutions	60
--	----

2.2 Differentiation media	62
---------------------------	----

2.3. Primary antibodies	66
-------------------------	----

Chapter 3

3.1. Fitting of actin area over time in a linear model	90
--	----

List of Videos

Chapter 3

- 3.1. Live imaging of actin on S_0 .
- 3.2. Live imaging of actin on S_{18} .
- 3.3. Live imaging of actin on S_{45} .
- 3.4. Live imaging of actin on S_{90} .
- 3.5. Live imaging of actin on S_{FN} .
- 3.6. Live imaging of cells and nuclei on S_0 .
- 3.7. Live imaging of cells and nuclei on S_{18} .
- 3.8. Live imaging of cells and nuclei on S_{45} .
- 3.9. Live imaging of cells and nuclei on S_{90} .
- 3.10. Live imaging of cells and nuclei on S_{FN} .

Chapter 4

- 4.1. 3D structure of connexin 43 in a mesenchymal condensate.

List of Equations

Chapter 2

2.1. Angle α between vectors \mathbf{u} and \mathbf{v}	63
2.2. Nuclear shape index	73